

**Titre:** Contribution to Assessment Methods for Low-Frequency Interactions  
in Inverter Dominated Power Systems

**Auteur:** Aramis Schwanka Trevisan  
Author:

**Date:** 2020

**Type:** Mémoire ou thèse / Dissertation or Thesis

**Référence:** Schwanka Trevisan, A. (2020). Contribution to Assessment Methods for Low-Frequency Interactions in Inverter Dominated Power Systems [Thèse de doctorat, Polytechnique Montréal]. PolyPublie. <https://publications.polymtl.ca/5470/>  
Citation:

 **Document en libre accès dans PolyPublie**  
Open Access document in PolyPublie

**URL de PolyPublie:** <https://publications.polymtl.ca/5470/>  
PolyPublie URL:

**Directeurs de recherche:** Jean Mahseredjian, Richard Gagnon, & Angelo Mendonça  
Advisors:

**Programme:** génie électrique  
Program:

**POLYTECHNIQUE MONTRÉAL**

affiliée à l'Université de Montréal

**Contribution to Assessment Methods for Low-Frequency Interactions in  
Inverter Dominated Power Systems**

**ARAMIS SCHWANKA TREVISAN**

Département de génie électrique

Thèse présentée en vue de l'obtention du diplôme de *Philosophiæ Doctor*

Génie Électrique

Octobre 2020

# **POLYTECHNIQUE MONTRÉAL**

affiliée à l'Université de Montréal

Cette thèse intitulée:

## **Contribution to Assessment Methods for Low-Frequency Interactions in Inverter Dominated Power Systems**

présentée par **Aramis SCHWANKA TREVISAN**

en vue de l'obtention du diplôme de *Philosophiæ Doctor*

a été dûment acceptée par le jury d'examen constitué de :

**Houshang KARIMI**, président

**Jean MAHSEREDJIAN**, membre et directeur de recherche

**Richard GAGNON**, membre et codirecteur de recherche

**Ângelo MENDONÇA**, membre et codirecteur de recherche

**Ilhan KOCAR**, membre

**Reza IRAVANI**, membre externe

## **DEDICATION**

*To my family, especially my parents and wife,  
for being a constant source of inspiration and motivation.*

## ACKNOWLEDGEMENTS

My journey as a Ph.D. student has been an exciting and fruitful one, but required a huge amount of dedication and hard work. Throughout this process, I have received a great deal of support, assistance, and encouragement from several people who left a significant imprint on my life. Here, I would like to express my sincere gratitude to them.

To all my supervisors, Prof. Jean Mahseredjian, Richard Gagnon and Ângelo Mendonça, for accepting me as your PhD student, for your trust, encouragement, and guidance. To Martin Fecteau, for the valuable support all these years. To Amgad El-Deib, for having started this journey with me, for your support and advices. It has been an honor and a pleasure to work with you all.

To ENERCON for the opportunity of giving an academic perspective to my work. I should acknowledge especially Alfred Beekmann, Matthias Bartsch, Ingo Mackensen, and Markus Fischer for making it possible. Also, many thanks to all my friends and colleagues at ENERCON for your support, and for sharing your knowledge and experiences with me. The list is long.

To the people at IREQ with whom I had the honor to work with and exchange ideas during this project, and also for sharing their valuable knowledge and experiences with me: Jean Lemay, Olivier Tremblay, Dmitry Rimorov, Gilbert Sybille, Pierre Giroux, Eric Lemieux, Omar Saad, Jacques Brochu, Innocent Kamwa, and others.

To my friends and colleagues, but especially those at Polytechnique, for your support, for the interesting discussions, and for helping making this journey also a pleasant adventure: Aboutaleb Haddadi, Anton Stepanov, Diane Desjardins, Haoyan Xue, Henry Gras, Isabel Lafaia, Jesus Morales Rodrigues, Juan Miguel David Becerra Tobar, Masashi Natsui, Miguel Cervantes Martinez, Ming Cai, Reza Hassani, Thomas Kauffmann, Willy Nzale, Xiaopeng Fu, and others.

To my family, especially my parents, for their lessons, tireless support and guidance throughout life, and for always believing in me.

To my wife Anaïs for the constant encouragement, compassionate support, patience, and love.

Without you all, it would not have been possible to come this far.

Thank you.

## RÉSUMÉ

Dans le cadre de l'actuelle transition énergétique, les réseaux électriques ont connu un essor rapide du raccordement d'onduleurs de puissance, principalement motivé par l'intégration à grande échelle de production éolienne et solaire ainsi qu'à l'utilisation de systèmes de courant continu à haute tension (HVDC).

Même si les onduleurs couplés au réseau peuvent offrir des services réseaux avancés, leurs caractéristiques et dynamiques diffèrent de celles bien connues des composants du système classique. Par conséquent, l'accroissement rapide de leur utilisation change de façon significative la dynamique des réseaux électriques.

Plusieurs événements ont été signalés indiquant des interactions néfastes entre des onduleurs et les réseaux électriques sur lesquels ils sont connectés. Ces incidents, en particulier ceux survenus ces dernières années, démontrent de façon probante la nécessité de revoir substantiellement la planification et les méthodes d'analyse des réseaux électriques afin d'intégrer harmonieusement ces « nouveaux » dispositifs et d'évaluer leur impacts sur les réseaux.

Dans ce contexte, un des principaux défis rencontrés auxquels est confronté l'industrie des réseaux électriques est la nécessité de comprendre et d'évaluer correctement et efficacement les risques potentiels de telles interactions indésirables, même si en pratique, pour des raisons de protection de la propriété intellectuelle, peu d'information et des données sur les composants sont disponibles, notamment aussi à cause de l'utilisation de modèles « boîtes noires ».

Afin de relever ce défi, des méthodes rapides de détection d'interactions ont été présentées dans plusieurs études. Le recours à des représentations très simplifiées des onduleurs et les réseaux électriques dans ces études rendent toutefois difficile l'application de ces résultats à des cas réels.

À cette fin, cette thèse vise à proposer une analyse fondamentale de la stabilité à basse fréquence impliquant des onduleurs raccordés aux réseaux électriques, tout en considérant une représentation détaillé et réaliste des onduleurs et des réseaux.

Cette thèse donne une vue d'ensemble des modèles des réseaux de référence existants de type électromagnétique transitoire (EMT) pour ces études et propose un modèle de référence supplémentaire pour l'étude des interactions à basses fréquences des parcs éoliens reliés à des réseaux compensés série.

De plus, un modèle EMT générique représentant une éolienne spécifique d'un manufacturier est développé. Ce modèle est basé sur une génératrice synchrone à l'excitation externe, directement couplé à l'éolienne (sans boîte d'engrenage) et connecté à un convertisseur électronique à trois étages permettant le transit de toute la puissance produite par l'éolienne. Tous les systèmes de commande de cette éolienne sont développés et expliqués. La performance du modèle est validée par des essais dédiés réalisés sur une éolienne de type similaire raccordée au réseau.

En outre, basé sur cette représentation détaillée de l'éolienne, un modèle EMT hybride est également élaboré pour ce même système. Ce modèle hybride est composé de circuits équivalents représentant des valeurs moyennes et commutées des convertisseurs basés sur l'électronique de puissance.

Une étude analytique approfondie des phénomènes d'interactions à basse fréquence impliquant des onduleurs connectés au réseau est réalisée. Les équations d'état sont développées pour les systèmes linéarisés représentant les éoliennes de type III et type IV. Une analyse modale est réalisée afin d'étudier le comportement dynamique de ces systèmes et pour bien comprendre les phénomènes observés. Il est démontré que l'interaction découverte dans le cas d'un parc éolien de type III dans un réseau compensé série est principalement de nature électrique. Néanmoins, il est également démontré par l'analyse de sensibilité que les contrôleurs de ce type d'éoliennes, s'ils sont correctement réglés, peuvent atténuer, voire éliminer les problèmes d'interaction.

Une revue des méthodes d'évaluation de stabilité, en mettant l'accent sur les phénomènes de basse fréquence, est fournie. Les capacités d'une méthodologie, à savoir la technique dite *combined-scan*, qui est présentement largement utilisée dans l'industrie, sont explorées. Il est démontré que cette technique est capable de prédire correctement la stabilité dans un scénario impliquant un parc éolien de type III, mais n'y parvient pas dans le cas d'un système VSC simple et dans celui d'un parc éolien de type IV. Après une analyse détaillée de type petits signaux de ces cas particuliers, les

résultats sont expliqués par l'incapacité de cette technique à capturer correctement les caractéristiques asymétriques des admittances d'entrée des onduleurs. Ces observations viennent par conséquent renforcer l'argumentation quant à la nécessité de recourir à un cadre multi-variable pour évaluer précisément la stabilité des réseaux électriques modernes.

Une nouvelle technique d'extraction des caractéristiques d'entrée de type petits signaux des onduleurs et des réseaux électriques, à savoir la technique de « DQ-Scanning », est proposée pour évaluer les conditions de stabilité potentiellement critiques. Appuyée par des modèles analytiques rigoureusement développés, il est démontré que cette technique permet d'extraire précisément les admittances et impédances d'entrée des onduleurs et des réseaux électriques modernes comportant différents équipements munis d'électronique de puissance. Il est également expliqué comment le critère généralisé de Nyquist peut être appliqué aux matrices résultantes de l'application du *DQ-Scanning* pour évaluer la stabilité.

Des scénarios supplémentaires ont été élaborés afin d'illustrer de façon analytique l'effet des pôles à parties réelles positives des admittances- $dq$  et impédances- $dq$  d'entrée des onduleurs et des réseaux électriques. Il est démontré qu'il est possible de les considérer dans la méthodologie proposée, à condition que leur existence soit connue.

Enfin, la précision et l'efficacité de la méthodologie proposée sont testées dans plusieurs scénarios et systèmes de référence à grande échelle impliquant différents types d'onduleurs connectés au réseau. Tous les résultats d'analyse sont validés par rapport à ceux obtenus par simulation EMT détaillée des cas correspondants.

## ABSTRACT

In the framework of ongoing energy transition, power systems have experienced a rapid increase in the use of grid-connected inverters, mostly driven by large-scale integration of wind and solar power plants as well as the use of voltage-sourced converter-based high-voltage direct current (HVDC) transmission systems.

Although grid-connected inverters are capable of providing advanced grid services, their characteristics and dynamics differ from those well-known of classical system components and, thus, their rapid widespread application is significantly changing power system dynamics.

Several field events involving grid-connected inverters have been reported, indicating that these devices can adversely interact with existing grid infrastructure. These events, especially those of recent years, are convincing evidence that substantial revision of existing power system planning and study methodologies is required in order to properly address these “new” devices and their impacts in the grid.

In this context, one of the major challenges faced by the power system industry is the necessity of correctly and efficiently understanding and assessing potential risks of such adverse interactions, even when in practical cases, mostly due to intellectual property issues, not much information of components is available and protected (i.e., black-box) models are used.

Several studies have been reported and approaches for fast interaction screening have been proposed to address the aforementioned needs, however, these results mostly relied on oversimplified representations of grid-connected converters and electrical grids, thus, making it difficult to translate findings to practical cases.

To address these needs, this thesis aims to contribute with new analyses of low frequency stability phenomena involving grid-connected converters in power systems under detailed and realistic consideration of power equipment.

An overview of existing electromagnetic transient (EMT) type benchmark models is provided and an additional benchmark is proposed to address the investigation of low frequency interaction of wind farms connected to series compensated grids.

Additionally, a generic manufacturer specific EMT-type wind turbine model is developed. It focuses on a directly-coupled (gearless) externally-excited synchronous generator connected to a three-stage full-converter system. All wind turbine controllers are developed and explained. The model performance is validated against dedicated field tests conducted in a real wind turbine of similar type.

Moreover, an EMT-type hybrid model representation is also developed for the same system. It consists of average value and switched equivalent circuit representations for the power electronic stages. Their use allow for larger simulation time-steps and faster computation times under some acceptable assumptions, especially with focus on the investigation of low frequency phenomena.

An in-depth analytical analysis of low frequency interaction phenomena involving grid-connected inverters is made. Linearized state-space representations are developed for the investigated systems, with focus on type-III and type-IV wind turbines. Modal analysis is applied to support investigations and help understanding of the phenomena. It is demonstrated that the interaction found for the case of a type-III wind farm in a series compensated grid is mostly of electrical nature. Nevertheless, it is also shown through sensitivity analysis that the wind turbine controllers, if properly tuned, can support mitigating the interaction issue.

A review of existing stability assessment methods, with focus on low frequency phenomena, is provided. The capabilities of one methodology with current largest industrial relevance, namely, the combined scan technique, are investigated. It is demonstrated that this technique is capable of properly predicting stability in a scenario involving a type-III wind farm, however fails to predict in the cases of a simple VSC system and of a type-IV wind farm. Detailed analysis of these cases indicate that small-signal asymmetric input admittance characteristics of grid-connected inverters, which are not properly captured in the combined scan technique, contribute to these results. These findings corroborate therefore the argumentation that a multivariable framework is required to accurately allow for stability assessment of modern power systems.

A new screening technique, namely, the DQ-Scanning technique, is proposed for efficient assessment of potentially critical stability conditions. Supported by rigorously developed analytical models, it is demonstrated that this technique is capable of accurately extracting input admittances and impedances for grid-connected inverters and modern power system structures, respectively. It is

further outlined how the well-established generalized Nyquist criterion can be applied to the resulting frequency dependent matrices to assess stability.

To analytically illustrate the effect of right-half-plane poles in the frequency dependent input  $dq$ -admittances and  $dq$ -impedances of grid-connected inverters and power systems, additional scenarios were developed. It is demonstrated that, if the existence of right-half-plane poles is known a priori, the proposed methodology can properly handle them during stability assessment.

Finally, the accuracy and efficiency of the proposed methodology is tested in several scenarios and large-scale benchmark systems involving different types of grid-connected inverters. All analytical results are validated against the ones obtained through detailed EMT simulation of the corresponding cases.

## TABLE OF CONTENTS

DEDICATION .....	III
ACKNOWLEDGEMENTS .....	IV
RÉSUMÉ.....	V
ABSTRACT .....	VIII
TABLE OF CONTENTS .....	XI
LIST OF TABLES .....	XV
LIST OF FIGURES.....	XVI
LIST OF SYMBOLS AND ABBREVIATIONS.....	XXI
LIST OF APPENDICES .....	XXII
CHAPTER 1 INTRODUCTION.....	1
1.1 Context and Motivation.....	1
1.2 Overview Field Events Related to Low-Frequency Phenomena .....	3
1.3 Research Questions .....	8
1.4 Thesis Outline and Contributions.....	10
CHAPTER 2 GENERIC EMT WIND TURBINE MODELS .....	12
2.1 Motivation .....	12
2.2 Generic Type-III Wind Turbine Model for EMT Studies.....	13
2.3 Development of a Generic EMT Type-IV Wind Turbine Model .....	15
2.3.1 Aerodynamic System .....	16
2.3.2 Control of Synchronous Machine .....	18
2.3.3 Grid Side Converter Control .....	21
2.3.4 Current Controller and Output Filter.....	23
2.3.5 FRT Control Strategies and Protections.....	24

2.3.6	Hybrid Model Implementation.....	26
2.3.7	Model Performance Validation Against Field Tests.....	34
CHAPTER 3 LOW-FREQUENCY PHENOMENA IN WIND FARMS.....		38
3.1	Overview and Definitions .....	38
3.1.1	Power System Oscillations.....	38
3.1.2	Subsynchronous Oscillations .....	40
3.1.3	Low-Frequency Oscillation in Power Systems .....	43
3.2	Existing Models for the Study of Low-Frequency Phenomena .....	44
3.2.1	IEEE First Benchmark System for SSR Studies .....	44
3.2.2	IEEE Second Benchmark System for SSR Studies.....	46
3.2.3	Review of Benchmark System for SSO involving Wind Generation .....	47
3.3	Benchmark for Low-Frequency Studies involving Wind Farms .....	49
3.3.1	Impacts of Nonlinear Components in Low-Frequency Phenomena .....	52
3.4	Type-IV Wind Farm Behavior in Series-Compensated Grids .....	55
3.5	Type-III Wind Farm Behavior in Series-Compensated Grids .....	56
CHAPTER 4 MODAL ANALYSIS APPLIED TO GRID-CONNECTED CONVERTERS		58
4.1	Review of Modal Analysis Applied to Low-Frequency Phenomena.....	58
4.2	Modal Analysis of a Simple VSC System .....	60
4.2.1	Obtaining a Linear Time-Invariant Representation for Equations.....	64
4.2.2	RL-Grid .....	65
4.2.3	Phase-locked-loop (PLL) .....	66
4.2.4	VSC Output Filter .....	69
4.2.5	Current Controller .....	70
4.2.6	Transport Time-Delay.....	71

4.2.7	Current Measurement and Frame Rotation .....	72
4.2.8	Voltage Measurement .....	74
4.2.9	Reference frame conversion: from internal to global frame .....	75
4.3	Complete State-Space Representation of the VSC System.....	76
4.4	Validation of Complete VSC State-Space Representation .....	79
4.5	Eigenvalue Analysis Applied to VSC System .....	81
4.6	Modal Analysis Applied to the Type-IV Wind Farm Scenario .....	82
4.7	Modal Analysis Applied to the Type-III Wind Farm Scenario.....	84
4.7.1	Impact of Series Compensation.....	86
4.7.2	Participation Factor Analysis .....	87
4.7.3	Impact of RSC Current Regulator Gains.....	88
CHAPTER 5 STABILITY ASSESSMENT BASED ON BLACK-BOXES .....		92
5.1	Motivation .....	92
5.2	Review of Screening Techniques .....	93
5.3	Combined Scan Technique Applied to Type-III Wind Farm.....	102
5.4	Combined Scan Technique Applied to Type-IV Wind Farm .....	103
5.5	Combined Scan Predictions for Simple VSC System.....	104
5.6	Combined Scan Technique Limitations .....	109
5.7	Asymmetric Input Admittance Characteristics .....	114
CHAPTER 6 DQ-SCANNING TECHNIQUE .....		119
6.1	Multivariable Impedance-based Stability Assessment.....	119
6.2	Application of the DQ-Scanning Technique.....	121
6.3	Impact of Realistic Equipment Modeling .....	124
6.4	Enhanced Perturbation Signals for Realistic Systems.....	127

6.5	Analytical Validation of the DQ-Scanning Technique .....	131
6.6	Stability Assessment based on DQ-Scanning Results.....	133
6.7	DQ-Scanning based Stability Assessment of Simple VSC System .....	138
6.8	Stability Assessment of Type-III and Type-IV Wind Farms .....	140
6.9	Effects of Right-Half-Plane Poles .....	144
6.9.1	Right-Half-Plane Poles in the Admittance Representation .....	145
6.9.2	Right-Half-Plane Poles in the Impedance Representation .....	152
6.10	Application Cases: DQ-Scanning for Stability Assessment .....	161
6.10.1	Unstable Type-IV based Wind Farm in Weak Grid System.....	161
6.10.2	Offshore Type-III Wind Farm connection through an HVDC Link .....	164
6.10.3	Large-Scale Grid under n-1 Contingency Condition .....	167
6.10.4	Large-Scale Grid: Stability under High and Low Wind Conditions.....	170
CHAPTER 7 CONCLUSION AND RECOMMENDATIONS .....		174
7.1	Summary .....	174
7.2	Recommendations for Future Works .....	176
REFERENCES .....		179
APPENDICES.....		195

## LIST OF TABLES

Table 3.1 Electrical Parameters of the Proposed Benchmark Grid for SSO Studies .....	51
Table 3.2 Electrical Parameters of the Proposed Benchmark Grid for SSO Studies .....	52
Table 4.1 Electrical and Control Parameters of simple VSC system.....	62
Table 4.2 Thevenin grid parameters.....	62
Table 4.3 Participation factors for critical model of type-III wind farm case.....	88
Table 5.1 Modified controller gains of simple VSC system.....	105
Table 6.1 Grid parameters.....	145
Table 6.2 Eigenvalues of 230 kV grid (with PCC voltages as input).....	149
Table 6.3 Eigenvalues of 230 kV grid (with grid currents as input).....	151
Table 6.4 Grid parameters.....	152
Table 6.5 Eigenvalues of 100 V grid subsystem (with grid currents as system input).....	154
Table 6.6 Eigenvalues of 100 V grid subsystem (with grid voltages as system input).....	155
Table A.1 Power coefficient values .....	195
Table A.2 Wind Turbine Parameters.....	195
Table A.3 Synchronous machine parameters.....	195

## LIST OF FIGURES

Figure 1.1 IEA data: average action prices for period 2012-2022 [2]. .....	1
Figure 2.1 Typical structure of a type-III wind turbine (also known as DFIG wind turbine).....	14
Figure 2.2 Schematic control diagram of a type-III wind turbine.....	15
Figure 2.3 Type-IV wind turbine system used for the development of a generic EMT model. ....	16
Figure 2.4 Mechanical power as function of rotational speed for different wind speeds. ....	19
Figure 2.5 Optimal $VDC1$ as a function of rotor speed.....	20
Figure 2.6 Buck- and boost-converter controller schematic structures.....	20
Figure 2.7 DC-link and reactive power control topologies. ....	22
Figure 2.8 Implemented HCC scheme for two-level VSC system. ....	23
Figure 2.9 Bode diagram of grid-converter LCL-type output filter with damping circuit.....	24
Figure 2.10 FRT-strategies implemented in the generic EMT-type wind turbine model. ....	24
Figure 2.11 Switched equivalent representation of boost-converter circuit.....	28
Figure 2.12 Comparison between DM and HM of boost-converter with different time steps. ....	29
Figure 2.13 Switched equivalent circuit of buck-converter. ....	31
Figure 2.14 Average model representation of a two-level VSC with HCC.....	32
Figure 2.15 Wind turbine currents during FRT Mode 2: DM ( $T_s = 1 \mu s$ ) vs. HM ( $T_s = 50 \mu s$ ).....	33
Figure 2.16 E-82 2.3 MW test site at Seigneurie de Beaupré, Canada (courtesy of ENERCON). ....	34
Figure 2.17 FRT-Mode 1 with $k_{uvrt} = 3$ for phase-to-phase-to-ground and three-phase faults. ....	36
Figure 2.18 FRT-Mode 2 response for phase-to-phase-to-ground and three-phase fault. ....	36
Figure 3.1 IEEE FBM for subsynchronous resonance studies [64]. .....	45
Figure 3.2 Sys-1 (left) and Sys-2 (right) of the IEEE second benchmark for SSR studies [75]. ....	46
Figure 3.3 SSCI-Benchmark-I – Large-scale system [37]. .....	48

Figure 3.4 Benchmark for studies involving wind farms and series-compensated grids.....	51
Figure 3.5 Fault location and considered transformer saturation characteristic in EMTP.....	52
Figure 3.6 Comparison of voltages across the series capacitance for the investigated cases. ....	53
Figure 3.7 Type-IV wind farm: active power at the PCC (base power: 100 MVA). ....	56
Figure 3.8 Type-III wind farm: active power at the PCC (base power: 100 MVA). ....	57
Figure 4.1 Simple VSC system used in investigation studies. ....	60
Figure 4.2 Current regulator schematic diagram in $dq$ -frame. ....	61
Figure 4.3 Synchronous rotating frame PLL control scheme. ....	61
Figure 4.4 Thevenin grid equivalent with consideration of a shunt resistance. ....	65
Figure 4.5 PLL in $dq$ -frame.....	67
Figure 4.6 VSC output filter.....	69
Figure 4.7 Current measurements and $dq$ -transformation.....	72
Figure 4.8 Current measurement subsystem in $dq$ -frame. ....	73
Figure 4.9 Interconnection diagram of subsystems from the simple VSC system. ....	77
Figure 4.10 PLL validation: nonlinear model (blue) vs. linearized model (red). ....	80
Figure 4.11 Comparison: $i_{dq}$ , from nonlinear (blue) vs. linearized model (red).....	80
Figure 4.12 Comparison: $v_{dq,meas}$ from nonlinear (blue) vs. linearized model (red).....	80
Figure 4.13 Eigenvalues of linearized VSC system representation. ....	81
Figure 4.14 Comparison of PLL angle: detailed (blue) vs. linearized (red) models.....	83
Figure 4.15 PCC voltages: detailed (blue) vs. linearized (red) models.....	83
Figure 4.16 Transmission line currents: detailed (blue) vs. linearized (red) models. ....	83
Figure 4.17 Eigenvalue plot for type-IV wind farm in series-compensated benchmark grid. ....	84
Figure 4.18 Comparison of PLL angle: EMTP detailed (blue) vs. linearized (red) models. ....	85
Figure 4.19 PCC voltages: detailed (blue) vs. linearized (red) models.....	85

Figure 4.20 Transmission line currents: detailed (blue) vs. linearized (red) models. ....	86
Figure 4.21 Eigenvalue traces for varying series compensation level. ....	87
Figure 4.22 Eigenvalue traces for varying RSC current regulator gains (20% compensation). ....	89
Figure 4.23 EMTP results for reduced current regulator gains and 20 % series compensation. ....	90
Figure 5.1 Synchronous machine equivalent for SSO studies. ....	94
Figure 5.2 Representation used by Canay for conventional generator shaft systems. ....	95
Figure 5.3 Impedance-based small signal representation of a grid-connected inverter. ....	98
Figure 5.4 Combined scan technique applied to a wind farm interconnection [132]. ....	100
Figure 5.5 Combined scan results for type-III wind farm connected to benchmark grid. ....	102
Figure 5.6 Combined scan results for type-IV wind farm connected to benchmark grid. ....	104
Figure 5.7 Detailed EMT simulation of simple VSC system under different SCR levels. ....	106
Figure 5.8 Input impedances of simple VSC system for different grid strengths. ....	107
Figure 5.9 Combined scan results for simple VSC system for SCR of 10 and 3. ....	108
Figure 5.10 Combined scan results for simple VSC system for SCR of 2 and 1. ....	109
Figure 5.11 Analytical input $dq$ -admittances of type-IV wind farm. ....	112
Figure 5.12 Analytical input $dq$ -admittances of type-III wind farm. ....	113
Figure 5.13 PLL and current regulator control schemes of simple VSC system. ....	115
Figure 5.14 Input $dq$ -admittances of simple VSC system. ....	116
Figure 5.15 Reference angle calculation without PLL dynamics. ....	116
Figure 5.16 Input $dq$ -admittances of simple VSC system without PLL dynamics. ....	117
Figure 6.1 DQ-Scanning application to a wind power plant (WPP). ....	121
Figure 6.2 DQ-Scanning application to grid subsystem in EMTP. ....	122
Figure 6.3 Input $dq$ -admittances for type-III wind farm. ....	125
Figure 6.4 Perturbation signal characteristics applied by the DQ-Scanning technique. ....	127

Figure 6.5 Input $dq$ -admittances of type-III wind farm: DQ-Scanning vs. analytical. ....	131
Figure 6.6 Input $dq$ -admittances of type-IV wind farm: DQ-Scanning vs. analytical. ....	132
Figure 6.7 Input $dq$ -impedances of benchmark grid: DQ-Scanning vs. analytical formulation ..	133
Figure 6.8 Impedance-based circuit interpretation in the $dq$ -frame. ....	134
Figure 6.9 Block diagram representation of impedance-based source- and load-subsystems. ....	134
Figure 6.10 Steady-state condition obtained from a time-domain EMT simulation. ....	138
Figure 6.11 GNC diagrams for the VSC system in grids for different SCR levels. ....	139
Figure 6.12 GNC based on DQ-Scanning for type-III WF and 8 % series compensation. ....	140
Figure 6.13 GNC based on DQ-Scanning for type-III WF and 9% series compensation. ....	141
Figure 6.14 GNC based on DQ-Scanning for type-III WF and 10 % series compensation. ....	141
Figure 6.15 Unstable oscillatory frequencies estimated from GNC for type-III WF. ....	142
Figure 6.16 GNC based on DQ-Scanning for type-IV WF and 50% series compensation. ....	144
Figure 6.17 GNC based on DQ-Scanning for type-IV WF and 70% series compensation. ....	144
Figure 6.18 Simple grid structure to investigate effects of RHP poles in grid $dq$ -admittances. ...	145
Figure 6.19 (a) voltage perturbation based vs. (b) current perturbation based DQ-Scanning. ....	146
Figure 6.20 Voltage perturbation based DQ-Scanning application. ....	147
Figure 6.21 Interconnection diagram for grid (with voltage as input and current as output). ....	148
Figure 6.22 Current perturbation based DQ-Scanning application. ....	149
Figure 6.23 Interconnection diagram for grid (with current as input and voltage as output). ....	151
Figure 6.24 Simple three-phase 100 V grid structure. ....	152
Figure 6.25 (a) current perturbation based vs. (b) voltage perturbation based DQ-Scanning. ....	153
Figure 6.26 Grid subsystem with used current notations. ....	153
Figure 6.27 Nyquist diagram for stability assessment of the 100 V grid interconnection. ....	157
Figure 6.28 Measured $dq$ -currents through inductance $L1$ for small voltage perturbations. ....	158

Figure 6.29 GNC diagram for stability assessment of the new interconnection.....	159
Figure 6.30 Measured $dq$ -currents through inductance $L1$ for GCI resistance change.....	160
Figure 6.31 Modified benchmark system: case with unstable type-IV wind farm. ....	162
Figure 6.32 Positive sequence voltage, active and reactive powers measured at the PCC.....	162
Figure 6.33 Generalized Nyquist contour for scenario with load at the PCC.....	163
Figure 6.34 Generalized Nyquist contour for scenario without load at the PCC.....	163
Figure 6.35 Type-III wind farm offshore interconnection through HVDC link [163]. ....	164
Figure 6.36 Left: HVDC MMC $abc$ -currents; Right: Wind farm active and reactive powers. ...	165
Figure 6.37 GNC contour for the wind farm – HVDC interconnection with CCC active.....	166
Figure 6.38 GNC contour for the wind farm – HVDC interconnection with CCC deactivated. .	166
Figure 6.39 Large scale grid – investigation of new WF (WPP 1) under n-1 contingency. ....	168
Figure 6.40 Nyquist contour for WPP 1 interconnection under normal condition.....	169
Figure 6.41 Nyquist contour for WPP 1 interconnection under contingency condition. ....	169
Figure 6.42 Large-scale grid: effect of n-1 contingency at PCC of WPP 1. ....	170
Figure 6.43 Nyquist contour for WPP 5 interconnection considering nominal wind speed. ....	171
Figure 6.44 Nyquist contour for WPP 5 interconnection with low wind speed (8 m/s).....	171
Figure 6.45 Positive sequence voltage and powers at PCC after wind speed change.....	172

## LIST OF SYMBOLS AND ABBREVIATIONS

DFIG	Doubly-fed Induction Generator
CCM	Component Connection Method
GNC	Generalized Nyquist Criterion
GSC	Grid-side Converter
HCC	Hysteresis Current Control
HVDC	High-voltage Direct Current
IGBT	Insulated-gate bipolar transistor
IGE	Induction Generator Effect
MMC	Modular Multi-level Converter
OVRT	Overvoltage Ride-Through
PCC	Point of Common Coupling
PWM	Pulse Width Modulation
RSC	Rotor-side Converter
SCR	Short-circuit Ratio
SSCI	Subsynchronous Control Interaction
SSO	Subsynchronous Oscillation
SSR	Subsynchronous Resonance
SSTI	Subsynchronous Torsional Interaction
VSC	Voltage-sourced Converter
WF	Wind Farm
WPP	Wind Power Plant

## LIST OF APPENDICES

Appendix A	Generic Type-IV Wind Turbine Parameters .....	195
Appendix B	DQ-Transformation .....	196
Appendix C	Frame rotation in DQ-frame .....	199
Appendix D	Matlab code – State space development of simple VSC system .....	201

## CHAPTER 1 INTRODUCTION

### 1.1 Context and Motivation

There is a current worldwide socio-political trend in displacing fossil-fuel based conventional generation by distributed renewable energy generation as one measure of reducing our impact in the climate change. This has been recently ratified by most nations through the international Paris Agreement [1].

At the same time, competitive energy market structures and continuous development of the concerned technologies are pushing the energy prices of renewable energy sources to values below those practiced by conventional generation, thus, further accelerating their large-scale integration. An overview of the average auction price practiced in the last years worldwide is provided in Figure 1.1 based on data from the International Energy Agency [2]. The values are shown for wind (onshore and offshore) as well as solar power plants, which represent most of the new interconnected sources in recent years [3].

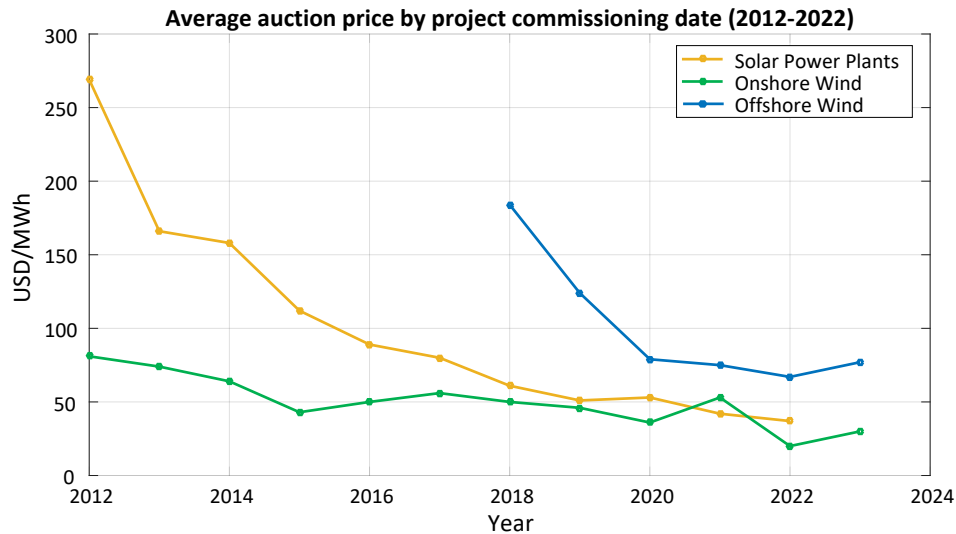


Figure 1.1 IEA data: average action prices for period 2012-2022 [2].

From a technical perspective, it is important to emphasize that the underpinning technology for this energy transition is the power-electronic based voltage-sourced converter (VSC). This is due to the fact that VSCs are not only an essential component in the integration of intermittent renewable generation into electrical grids, but they are also present in other grid-connected inverters as a mean

of improving transportation and end-use energy efficiency and reliability, for instance, through high-voltage direct current (HVDC) transmission lines and through power-electronic based loads.

These trends and observations put together corroborate the premise that power systems complexity is increasing. It is noted that, although grid-connected inverters are capable of providing advanced grid services, their inherent characteristics and dynamics differ from those of well-known and studied classical system components and conventional generating units.

Moreover, several field events involving grid-connected inverters have been reported, indicating that grid-connected inverters can adversely interact with existing grid infrastructure. The fact that the number of such events has not decreased in recent years is strong evidence that a substantial revision of existing power system planning and study methodologies is required in order to properly address these “new” devices.

In this context, one of the major challenges currently faced by the power system industry is the necessity of efficiently and accurately identifying potential risks in new interconnection projects, even when, mostly due to intellectual property issues, not much information on new devices is available and protected (i.e., black-box) models are used. For instance, as it will be demonstrated in this thesis, although internal controllers and parameters as well as nonlinear electrical devices’ characteristics of grid-connected inverters may significantly impact power system dynamics and, consequently, its stability, such detailed information are usually not accessible to power system engineers during interconnection studies. Even in the fewer cases in which they are available, strict project schedules as well as lack of efficient ways (i.e., methodologies) for properly taking this detailed information into account, limit their correct consideration in system studies.

At this point, it is important to note that the reported issues faced during integration of grid-connected inverters are not always of the same type and may involve different grid components and control structures. When it comes to interactions observed between grid-connected inverters and the electrical grid, the term *resonance* is often applied. Additionally, experience has shown that depending on the observed resonance frequencies, indication for potential root-causes as well as possible mitigations can be drawn. For this reason, it is helpful to categorize the observed phenomena in order to make their investigation more efficient.

The classification adopted in [4] is used as base for the terminology applied in this thesis. According to it, grid resonances involving grid-connected inverters can be classified in two categories: i) *Harmonic resonances*; and ii) *Near-synchronous resonances*. The former comprises resonances that are in the range from hundreds of hertz up to some kilohertz and are consequence of the inherent impedance characteristics of transmission lines and cables in conjunction with the VSC's input filters. The latter refers to resonances in the range from few hertz up to roughly twice the system nominal frequency, comprising, therefore, the so-called subsynchronous oscillations (SSO), resonances (SSR) and torsional interactions (SSTI). Also, the recent category of subsynchronous control interaction (SSCI) may fall in the near-synchronous range.

The current thesis focuses mostly on the phenomena addressed by the second category above. However, investigations conducted in the framework of this research indicated that these types of resonances can not only present very low frequencies, but as well as go to more than twice the nominal frequency. From this perspective, the term *near-synchronous* could become restrictive and generate confusion. For this reason, this thesis adopts a broader term, namely, *low-frequency* phenomena, to address these resonances ranging from very few hertz up to roughly ten times the system nominal frequency.

In the specific case of low-frequency phenomena, it is highlighted, as indicated previously, that events, which fall in this category, have been reported in literature both for conventional units and grid-connected inverters. Before diving into the detailed study of low-frequency phenomena, it is useful to obtain an overview of relevant field events to support further classification and understanding of the issue. This is provided in the next subchapter.

## **1.2 Overview Field Events Related to Low-Frequency Phenomena**

This subchapter describes low-frequency phenomena encountered in different jurisdictions and involving different components. They are listed in chronological order.

### ***The Mohave Incident***

This event did not involve an inverter-based device, however it is depicted here due to its importance to the field of SSR, since it is the first real case of this type reported in the literature [5].

Mohave is a power plant in Laughlin, Nevada, USA. It is one of the generating power plants of the so-called Navajo Project, which was a generation and transmission project of three 750 MW coal-fired units. The Navajo transmission system consisted of approximately 3000 km of 500 kV transmission lines, all equipped with series capacitor, where the highest compensation level was as high as 70 %.

On October 26<sup>th</sup>, 1971, a shaft failure was reported at the Mohave plant. The electromechanical system of the turbine-generator system interacted with the series-compensated system. Two turbine-generator shaft systems were damaged. The event was later categorized of the SSR type and several mitigations approaches have been investigated for the issue.

### ***The Square-Butte Event***

In the beginning of the 80's, Bahrman et al. reported about interaction phenomena seen between conventional generating units and a new HVDC system [6]. The report from October 1977 indicated that the newly commissioned HVDC terminal was interacting adversely with an 11.5 Hz torsional mode of an adjacent turbine-generator unit. To the author's knowledge, this is the first reported case of interaction between a power electronic based device and conventional units.

The Square Butte Project began its commercial operation in May of 1977. It consisted of a  $\pm 250$  kV, 500 MW DC line and a 438 MW steam turbine-generator. The power coming from the generating units located in North Dakota is transmitted through this system for approximately 750 km to serve load in the northeastern of Minnesota. The studies and reports at the time accurately stated that this was not a case of standard SSR, since there is absence of series compensated lines in the vicinity of the HVDC terminals. Linear techniques were applied to investigate the phenomena and propose mitigation through control and parameter adjustments of the HVDC terminal controllers [6].

### ***ASDEX Upgrade (AUG) tokamak***

The ASDEX Upgrade (AUG) tokamak is a nuclear fusion experiment of the Max Planck Institute for Plasma Physics, in Germany, that requires electrical power ramp up to a few hundred megawatts in short period of times (typically about ten seconds) to feed some loads, which are interfaced by inverter-based devices [7]. Three separate networks based on flywheel generators are used to provide the power and energy for such experiments [7], [8].

Shaft damages were encountered in the flywheel generator systems in routine checks performed in 1999 and 2002. Due to the fact that the active load of each generator in service was of about 100 MW and is well below the design value of their shafts, which is more than 800 MW, the damages could only be explained by a torsional resonance of the shaft.

Detailed investigations indicated that the natural frequency of the shaft assemblies were 23.8 Hz and 26 Hz. It was also seen that the spectrum of the load curves from the ASDEX Upgrade were between 10 and 30 Hz. The phenomenon has been explained as an interaction between the turbine-generator shaft systems and the power-electronic interface loads. It is noted that, although no series compensation was used in any of lines, these events were still classified as being of SSR type in [7] and [8]. Several mitigation approaches have been investigated, but, finally, dedicated SSR damping has been developed to solve this specific issue [8].

### ***South Central Minnesota Wind Plant Substation***

In 2007 a SSO event happened involving a wind plant in South Central Minnesota, USA. This event was, however, only reported years later, in 2011, in [9]. To the author's knowledge, this may be the first ever SSO event reported involving wind turbines.

More specifically, this event involved a 100 MW wind farm based on type-III wind turbines, i.e., with doubly-fed induction generators (DFIG) based systems, connected to a series compensated 345 kV transmission grid. Due to a sequence of breaker operations that were opened as part of a regular system switching procedure for the installation of a bypass scheme, the wind farm was finally found in radial connection with a series compensated transmission line with approximately 60% compensation level. Undamped oscillations with relatively high magnitude in the frequency range of 9 to 13 Hz were observed. Also some other low magnitude frequency components in the frequency range of 37 to 43 Hz were seen. Wind turbine components were damaged during this event [9]. As a mitigation measure, the concerned utility company decided to install protective relays to monitor the currents fed by the wind farm.

### ***The 2009 Event in ERCOT***

In 2009 an event occurred involving DFIG-based wind farms connected to a 345 kV transmission system through the Ajo substation in the jurisdiction of ERCOT, in Texas, USA. More specifically, two 345 kV transmission lines derive from the Ajo substation.

In October 2009 a single line-to-ground fault tripped one of the transmission lines leaving the so-called Zorillo Gulf wind farm, totaling 485 MW of DFIG wind turbines, radially connected to the system through an effective series compensation level of around 80%. SSO in the range of 20 to 30 Hz rapidly built up and caused damage to both series capacitor and wind turbines [10]. Analyses and studies carried out after the event classified it as of a subsynchronous control interaction (SSCI) type [11]. After repairs were made, a SSR relay was installed as a temporary solution to trip the transmission line feeding the wind farms. Later, wind farm operators confirmed the installation of subsynchronous damping controllers and the relay was retired.

This 2009 event from ERCOT gained a lot of repercussion and has been since presented as convincing evidence, especially in the academic community, of real risks between grid-connected inverters and the existing grid infrastructure. Several research works have since been published motivated by this event, as it will be outlined later in this thesis.

#### ***Events in Hebei Province (China)***

SSO events have been recorded in the transmission networks of Hebei Province, which is located in the northwest of China and surrounds the Beijing area. The power of more than 20 wind farms is collected by 220 kV transmission lines and connected to centralized substation that steps up the voltage to 500 kV. By the end of 2012, the total installed capacity of wind turbines in this area already exceeded 3000 MW. Most of the turbines are of DFIG technology [12].

In the morning of December 25<sup>th</sup>, 2012, many wind turbines in the above described area suddenly tripped. According to the data from fault recorders, large magnitude subsynchronous currents with approximately 7 Hz were observed. Due to the existence of series-compensation in the upstream 500 kV transmission system, this event was deemed as of an unstable SSR type. Reference [12] confirmed expectation through linear analysis and detailed electromagnetic transient (EMT) simulation.

#### ***Events in the Xinjiang Uygur Autonomous Region (China)***

All aforementioned events involving wind farms were concentrated on the DFIG based technology. The events in the Xinjiang Uygur Autonomous Region, in China, were the first reported to involve subsynchronous oscillations for full-converter devices. More specifically, it involved type-IV wind turbines [13].

The installed capacity of wind generation increased rapidly in the Xinjiang Uygur Autonomous Region. Since 2014 sustained power oscillations at subsynchronous frequencies have been repeatedly captured by the wide-area measurement system.

Investigations in [13] indicate that the oscillations happen due to interaction of the wind turbines and the electrical grid, which, in this particular case, is characterized by low short-circuit power (weak systems). Such phenomena was until then only known for type-IV wind turbines, and full converter systems in general, from theoretical investigations [14].

### ***BorWin1 HVDC System for Offshore Wind Farm***

BorWin1 is a project realized by TenneT (dutch and german transmission system operator) to connect the offshore wind farm Bard Offshore 1 to the shore of Germany with dc technology. In fact, it was the first project of this dimension to connect an offshore wind farm to the shore by means of an HVDC system [15]. The system was dimensioned for 400 MW, uses a two level converter and, thus, requires the use of a special filter at its shore station to absorb switching harmonics generated by the HVDC converter station.

During system commissioning BorWind1 sustained oscillations were measured. Differently than the aforementioned events, the biggest components were measured in the range of 400 to 500 Hz, i.e., up to ten times the system nominal frequency. However, as explained in [15], these “harmonics” are not of the standard type, which are generated by switching of power-electronic devices, and result from resonances between the converter station, converter filters and the grid from TenneT. Different mitigations approaches were proposed for the system in [15].

### ***The Case Involving Photovoltaic Inverters***

A publication dated from early 2018 reported low-frequency instabilities for Photovoltaic (PV) plants of different sizes [16]. Measurements are shown for PV plants under 500 kW indicating low- and high-order harmonic distortions. The first are concentrated in at 420 Hz, which correspond to the 7<sup>th</sup> harmonic of the analyzed system, and represented 20% of the PV plant nominal current. The latter focused on oscillations with frequencies around 2370 Hz.

Also, [16] presents measurement diagrams indicating the existence of subsynchronous oscillations for PV plants of 10 MW each. More specifically, weakly damped oscillations of around 20 Hz were

recorded at the PV plant connecting substation whenever a 30 MVar capacitor was energized at the substation. These cases are, to the author's best knowledge, the first ever reported from commercial PV units.

### *The 2017 Events in ERCOT*

Although the 2009 event in ERCOT (described above) resulted in several reviews of internal methodologies for planning studies and integration of new wind farms ([10], [17], [18]), three other events were reported in 2017 [19].

All of the three events involved series compensated transmission lines and type-III wind turbines. Moreover, all three events happened under n-1 contingencies that resulted in a radial connection of the concerned wind farms and the rest of the system. Subsynchronous oscillations of 20 to 30 Hz were seen in all three cases. Two of the events ended with the wind farms tripping off and/or the series compensation being bypassed. One of the oscillation events damped out by itself, probably due to the existence of a resulting small amount of positive damping in the system. No hardware damage has been reported for these events.

Nevertheless, these events are noteworthy, because after the 2009 event in ERCOT, the knowledge base and requirements regarding SSCI have been greatly improved [19]. Prior to being commissioned, all involved wind farms underwent detailed SSR studies and SSCI damping controllers were installed in the wind turbines.

## **1.3 Research Questions**

The previous subchapter highlighted real low-frequency phenomena events involving grid-connected inverters. They illustrate that such phenomena are not restricted to just one type of technology, but are convincing evidence that any integration of grid-connected inverter can be involved in such events.

Additionally, the fact that some of the outlined events are recent, for instance, the ones of 2017 in ERCOT, in China and the ones involving PV plants, indicate that existing methodologies applied for the integration of new generation should be revised. In fact, these events raise important concerns for the further integration of grid-connected inverters.

From a research perspective, however, these events yield the urgent need for better understanding the low-frequency phenomena in the context of “new” grid-connected inverters. Assuming that the aforementioned energy transition goals are further pursued, this is much required to help quantify how profound their impact is to be expected in modern (and future) power systems.

Moreover, the certainty provided by these events that grid-connected inverters may adversely interact with existing power system motivates the search for efficient assessment techniques for identification of such risks as early as possible during new interconnection projects.

Techniques have already been proposed to address the screening of potentially critical low-frequency interactions both in the context of conventional as well as modern power systems, i.e., involving grid-connected inverters. However, it is noted that for such techniques to achieve a mature status and consequent industrial application, detailed investigation based on practical cases about their limitations is required.

Additionally, still with regards to the applicability of these approaches in practical cases, industrial constraints need to be considered in the process of application of such techniques. A typical one concerns, for instance, the availability of information from both grid and grid-connected inverters during interconnection projects. It is noted at this point that grid planners do not have much details available on devices to be used in future interconnections. Moreover, even in the practical case of an interconnection project, it is very common that detailed studies are conducted based on protected (i.e., black-box) models, due to intellectual property concerns. Interestingly, the same applies for manufacturers and project developers, which on the other side of the project rarely have access to detailed information about the grid their devices are going to be connected to. From these perspectives, in order to achieve industrial acceptance, it is imperative that approaches proposed to efficiently screen out potentially critical scenarios be based on the information that is usually available in practical cases.

The ultimate goal of this thesis is to provide one of such approaches. However, to achieve this goal, the research work was led through following research questions, summarized below:

- 1) What are the currently available techniques used to address low-frequency interactions in the context of conventional and modern power systems?

- 2) Are the currently available techniques sufficient for their purpose? What are their limitations? When are they expected to fail?
- 3) Is it possible to circumvent the limitations found in existing techniques? Could one of the approaches be extended to address the limitations? Or should a new approach be proposed to address them?

Based on these research questions, work packages were derived for the current research work, which are reflected in the structure of this thesis. Throughout the work packages, new findings and contributions are present. These are listed in the next subchapter.

## **1.4 Thesis Outline and Contributions**

This thesis is structured in the following six chapters, which correspond to the different work packages, and four appendices.

Chapter 2 presents the wind turbine models that are used in the detailed investigations presented in the next chapters. A new generic electromagnetic transient (EMT) type manufacturer specific wind turbine model based on a directly-coupled and externally excited synchronous generator connected to a full-converter system is proposed and validated against field measurements.

In Chapter 3, definitions applicable to low-frequency power system oscillations are provided, supported by a literature review. A definition for low-frequency phenomena in modern power systems is proposed, which is then used throughout this thesis. A review of existing benchmark systems for the study of low-frequency phenomena is provided and a new benchmark study system is developed. The behavior of the wind turbines introduced in Chapter 2 is assessed in this system based on detailed EMT simulations.

Chapter 4 focuses on modal analysis of low-frequency phenomena. It starts by reviewing previous works, which applied modal analysis to assess low-frequency oscillations in power systems. Then, based on a simple VSC converter, it outlines the methodology used in this work to obtain a complete linearized state-space system of equations for the grid-connected converters and grids for modal analysis. Finally, this methodology is applied to the detailed representations of type-III and type-IV wind farms in conjunction with the proposed benchmark system. It is demonstrated that

the interactions in the type-III wind farm scenario are of electrical nature. Participation factor and sensitivity analysis are proposed to address mitigation.

Chapter 5 deals with the small-signal stability assessment of power systems, mostly based on black-box models. It provides a literature review of existing methodologies. Moreover, it gives an in-depth analysis of the capabilities of the currently most used technique, namely, the combined scan technique. Limitations are found and discussed.

In Chapter 6 a new methodology is proposed to extract the small-signal impedance characteristics of grid-connected inverters and power systems. The effectiveness of the methodology is demonstrated by validating its results against rigorous developed analytical models of the corresponding systems. It is shown how stability can be assessed based on the results. A discussion about the limitations of the technique in the presence of right-half-plane poles in the small-signal admittance or impedance representations, and how these can be properly considered, is provided. Finally, the accuracy of the proposed methodology is assessed based on previous investigated scenarios involving type-III and type-IV wind turbine systems as well as new ones involving multi-converter scenarios and large-scale grids.

Finally, Chapter 7 presents a summary of the contributions of this thesis as well as conclusions obtained throughout this research project. Also, recommendations for future works are provided. Additional information required to support analyses in this thesis is as well provided in four separate appendices at the end of the document.

## CHAPTER 2      GENERIC EMT WIND TURBINE MODELS

This chapter deals with generic electromagnetic (EMT) wind turbine models, which are later in this thesis used to study low-frequency phenomena in power systems. An existing type-III wind turbine model is briefly outlined. Additionally, a manufacturer specific type-IV wind turbine model is developed. It is emphasized that this work has been done in close collaboration with ENERCON, a German wind turbine manufacturer and official partner of this research project, which also allowed for the conduction of field tests in a real turbine to validate the proposed model. Results obtained in this work package were also published in [20].

### 2.1 Motivation

Operators of modern power systems are experiencing the integration of grid-connected inverters at fast pace in their systems. As indicated in [3], wind turbines represent a significant portion of the newly installed equipment. The resulting increased complexity of power systems is forcing reconsiderations on how these are studied, planned and operated.

In this context, as a response to the increasing complexity, the provision of detailed and validated manufacturer EMT models for new interconnection has become a requirement in different power system jurisdictions, notably in Canada, Australia and France [21]–[24].

Due to mostly confidentiality issues, however, such detailed manufacturer specific models are often provided as protected models (i.e., black-boxes), thus hindering access to internal parameters and control structures and, therefore, making it very difficult to understand and study the phenomena. Additionally, the application of analytical techniques becomes almost impossible.

To overcome some of these obstacles in specific cases, working groups and task forces have been created in recent years to propose so-called generic transient stability type models (in phasor-domain), also known as RMS models [25], [26]. However such models have an intrinsic limited frequency bandwidth consideration that, together with typical assumptions for grid model equations in phasor-domain, limits their application range.

To address these limitations, generic EMT-type models have been proposed. For instance, references [27]–[29] proposed detailed models for type-III wind turbines and references [30]–[32] pro-

vided as well valuable insights into the detailed modeling of type-IV wind turbines. Also, references [33] and [34] addressed the need and use of generic EMT-type model representations of wind turbines of type II, III and IV, although not to the same level of modeling detail.

In the framework of this thesis, low-frequency phenomena are investigated focusing mostly on wind turbines, before translating results to other systems. More specifically, detailed studies are conducted based on generic EMT-type models of type-III and type-IV wind turbines.

To allow for the application of analytical approaches, studies are conducted based on generic models. However, it is emphasized that these models are validated against real equipment. The used type-III wind turbine model is based on the work published in [33] and in [34] and, since details are readily available, its structure is briefly described in subchapter 2.2. On the other hand, the type-IV wind turbine model used in this thesis has been explicitly developed in the framework of this research and, therefore, detailed explanation is provided in subchapter 2.3.

## **2.2 Generic Type-III Wind Turbine Model for EMT Studies**

Prior to going into the details of a type-III wind turbine system, it is emphasized that most of the SSO events reported involved type-III wind turbines ([9]–[12], [19]), i.e., based on doubly-fed induction generator (DFIG) technology. For this reason, the consideration of type-III wind turbines is mandatory for this research work.

However, it is also noted that due to the relatively large amount of field events, the type-III technology has been already extensively addressed in previous studies and its characteristics outlined in detail, for instance, in [35], [36]. Additionally, generic EMT-type models have also been proposed, notably in [27]–[29], [33], [34], [37].

In the framework of this research, the model proposed in [33] and used in [34] will be investigated in detail. For convenience, its topology and controls are briefly outlined in the following.

A type-III wind turbine uses an induction generator, also known as asynchronous generator, to convert mechanical energy from the wind turbine into electrical energy, which is then injected into the grid. The induction generator has a wound rotor. The machine stator is directly connected to the grid, whereas the rotor is connected to the grid through an ac-dc-ac voltage source converter (VSC) with a rated capacity of approximately one third of the generator rated power. The VSC of

a type-III wind turbine is divided into a Rotor-Side Converter (RSC) and a Grid-Side Converter (GSC). A typical type-III wind turbine structure is depicted in Figure 2.1.

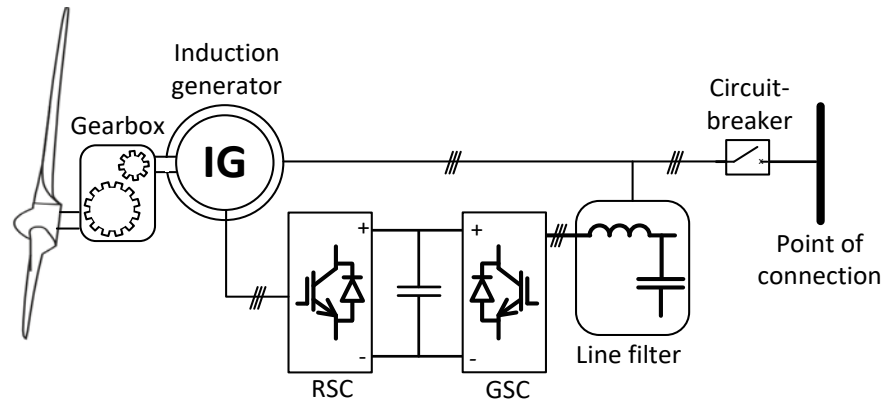


Figure 2.1 Typical structure of a type-III wind turbine (also known as DFIG wind turbine).

The RSC is responsible for controlling the generator speed and the reactive power flow through the turbine terminals. This control is typically done in the  $dq$ -frame, after transforming the measured  $abc$ -rotor currents by means of an  $abc$ -to- $dq$ -transformation using the rotor angle and the phase-locked loop (PLL) reference angle.

The generator speed is controlled through a pre-defined power-speed characteristic. For this, the active power injected into the grid is measured at the turbine terminals. Then, to achieve the corresponding reference speed, the speed regulator calculates an electromagnetic torque to be produced by the induction generator. This torque is then divided by an estimated  $q$ -axis flux of the generator in order to obtain a reference value for the  $d$ -component of the rotor currents.

Differently, the  $q$ -component of the rotor currents is used to control the reactive power injected into the grid. An integrator is used to generate a voltage reference from the error between reference and measured reactive powers. A cascaded integrator is then applied to calculate a reference value for the  $q$ -component of the rotor currents from the error between the resulting voltage reference and the measured voltage.

Both  $dq$ -current components are controlled by a two-level PWM-based VSC system using vector-control with feedforward in the  $dq$ -frame [38]. No inductive output filter is required on the rotor side, since the inductances of the machine rotor can be used for the same purpose.

The main function of the GSC is to regulate the dc-bus voltage to a constant value. As for the RSC, typically a control in  $dq$ -frame is used. For this, a phased-locked loop (PLL) is used to track the system phase based on the measured voltages at the turbine terminals. Then,  $d$ -component of the GSC currents is used to control the dc-link voltage to a constant value and the  $q$ -component is usually controlled to zero.

A high-level overview of RSC and GSC controls is provided in Figure 2.2. It is noted that in the interest of figure readability details are omitted, such as measurement filters, controller limitations and feedforward implementation. However, it is reinforced at this point that details can be extracted from [27], [33], [34].

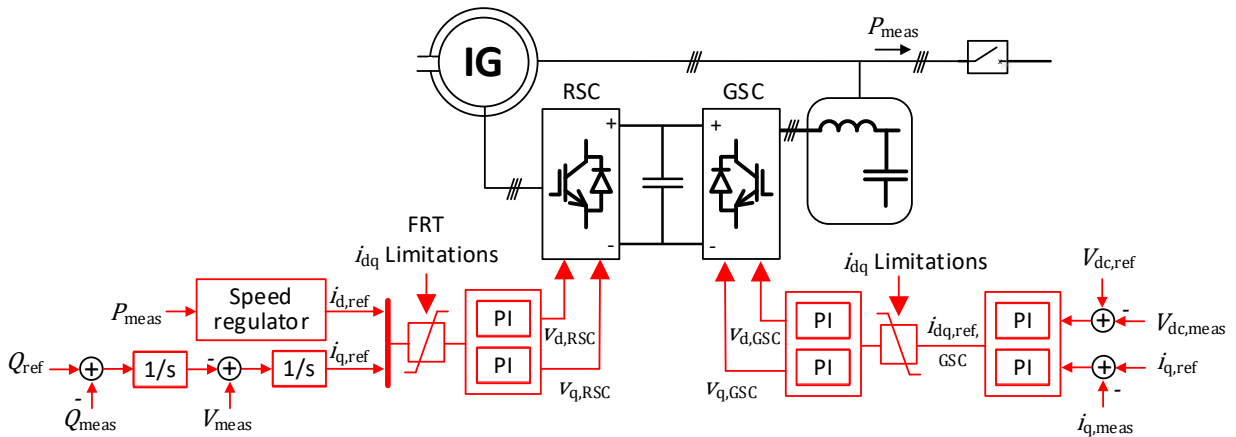


Figure 2.2 Schematic control diagram of a type-III wind turbine.

### 2.3 Development of a Generic EMT Type-IV Wind Turbine Model

Differently than a of a type-III wind turbine, there exist several implementation forms of wind turbines that could fall in a type-IV category, i.e., a wind turbine whose connection to the grid is done through a full-converter system. For instance, references [30]–[32] considered permanent magnet synchronous generators. It is emphasized, however, that the energy conversion is not limited to this type of generator. An asynchronous generator, as the one used in a type-III wind turbine system, could also be considered.

In this thesis, a new generic EMT-type wind turbine is proposed. It focuses on a system based on a 2-MW directly-coupled and externally-excited synchronous generator, which is connected to a three-stage full-converter system consisting of a six-pulse diode rectifier, a dc-dc boost converter

and an IGBT-based two-level voltage source converter (VSC). The considered wind turbine system is depicted in Figure 2.3.

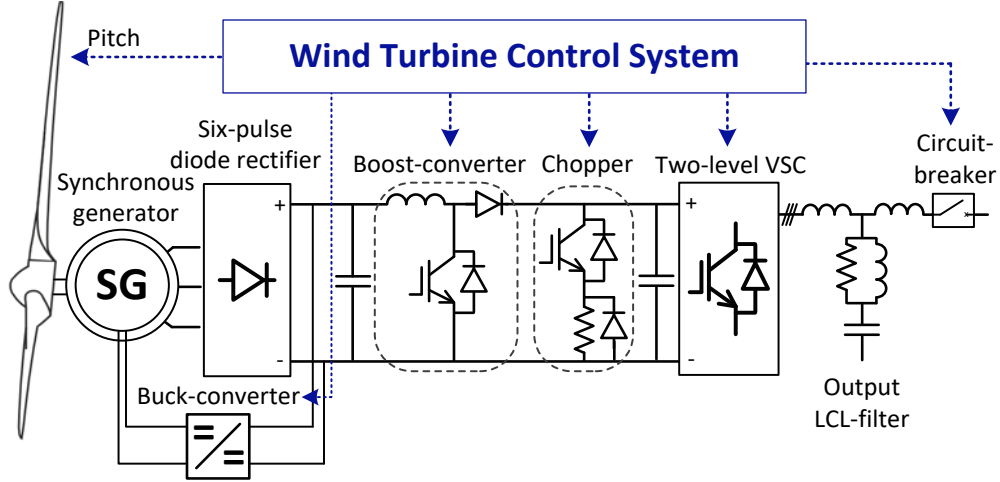


Figure 2.3 Type-IV wind turbine system used for the development of a generic EMT model.

In the next subchapters, the wind turbine structure shown in Figure 2.3 and its controllers are developed in detail and explained.

### 2.3.1 Aerodynamic System

The generic aerodynamic model used in the wind turbine model is based on [39] and uses well-known analytical formulations for the power extraction from wind, which are given in

$$P_m = \frac{\rho}{2} c_p(\lambda_{tip}, \theta_{pitch}) A_r v_{wind}^3 \quad (2.1)$$

where  $P_m$  is the mechanical power extracted through the wind turbine,  $\rho$  is air density (assumed equal to  $1.225 \text{ kg/m}^3$ ),  $A_r$  is the area swept by turbine blades in  $\text{m}^2$ ,  $v_{wind}$  is wind speed in  $\text{m/s}$ . The parameter  $c_p$  is known as the performance coefficient or power coefficient of the wind turbine, which is a function of tip-speed ratio,  $\lambda_{tip}$ , and of blade pitch angle,  $\theta_{pitch}$ . The tip-speed ratio is analytically given by

$$\lambda_{tip} = \frac{R_r \omega_r}{v_{wind}} \quad (2.2)$$

where  $R_r$  is the radius of the wind turbine rotor and  $\omega_r$  is the rotor rotational speed.

The power coefficient  $c_p$  is analytically assumed as

$$c_p = c_1 \left( \frac{c_2}{\lambda_i} - c_3 \theta_{pitch} - c_4 \theta_{pitch}^{c_5} - c_6 \right) e^{(-c_7/\lambda_i)} \quad (2.3)$$

where

$$\lambda_i = \left[ \left( \frac{1}{\lambda_{tip} + c_8 \theta_{pitch}} \right) - \left( \frac{c_9}{\theta_{pitch}^3 + 1} \right) \right]^{-1} \quad (2.4)$$

It is emphasized that the above equations are extracted from [39], however that their structures and relations originate from [40]. Moreover, it is noted that the values of the constants  $c_1$  to  $c_9$  have been adjusted to better match manufacturer data used as basis, which are from an Enercon E-82 2MW wind turbine. The values are provided in Table A.1, in Appendix A.

Moreover, similar to what is suggested in [39], this work also assumes high-frequency wind speed variations are a local phenomenon and, therefore, are considered even out over the rotor surface, especially in cases where swept area of wind turbines become larger. To approximate this effect, a rate limitation is included in the rotor model to limit the wind variations. A value of 5 m/s/s is assumed, which is based on experience obtained by field data.

It is noted that the rotor of the proposed wind turbine is assumed to be directly coupled (no gearbox) to the rotor of the synchronous machine. Furthermore, the blade system and the machine rotor are assumed to lie on the same plane and the resulting extremely short shaft is assumed to allow a single-mass type of representation for the mechanical system. Moreover, the three-phase stator system of the synchronous machine is assumed directly connected to a diode-based six-pulse bridge rectifier, as illustrated Figure 2.3. The proposed values for the representation of the wind turbine aerodynamics, mechanical components and synchronous machine are also given in Appendix A. It is emphasized that the values are for the representation of a 2 MW wind turbine.

At this point it is worth mentioning that, in the context of industrial applications of wind turbines, the directly-coupled nature of the turbine-generator system yields some specific requirements for the involved components. For instance, some of these requirements affect the electrical and mechanical design of the synchronous machine, resulting usually in the use of a large number of pole pairs and unusual proportions. As a result, electrical parameters of synchronous machines for wind

application may considerably differ from cases where the generator is directly connected to the grid, for instance, in hydro-power plants [20].

### 2.3.2 Control of Synchronous Machine

From a control perspective, different regulators could be conceived for the electromechanical system described above, depending on the primary objectives, pre-defined requirements and existing hardware constraints from wind applications. For the purposes of this research work, a maximum power tracking requirement is going to be assumed. This means that, for any given wind speed  $v_{wind}$ , the electromechanical system and its controls are expected to extract the maximum power possible from wind and, thus, allow the most efficient operating condition.

Due to the directly-coupled nature of the assumed type-IV wind turbine system, the optimal rotor rotational speed  $\omega_r$  of the synchronous machine is the one that also optimizes the mechanical power extraction,  $P_m$ , of the turbine. In other words, according to the assumed power coefficient characteristic, for each wind speed  $v_{wind}$  there is an optimal value of  $\omega_r$ . This is illustrated in Figure 2.4, where the mechanical power  $P_m$  is presented as a function of the wind speed and of the rotor rotational speed of the synchronous machine  $\omega_r$ . Also, the optimal rotor rotational speed characteristic is indicated in red dashed line as a function of the considered wind speeds.

This work assumes that the rotor rotational speed is controlled by means of the excitation of the synchronous machine. For each measured wind speed, an optimal rotor rotational  $\omega_{r\_opt}$  speed is calculated. To reduce control efforts,  $\omega_{r\_opt}$  is first filtered and, then, given as reference value  $\omega_{r\_ref}$  to the controller. The error between  $\omega_{r\_ref}$  and the measured rotational speed,  $\omega_{r\_meas}$ , is sent as input to the excitation controller.

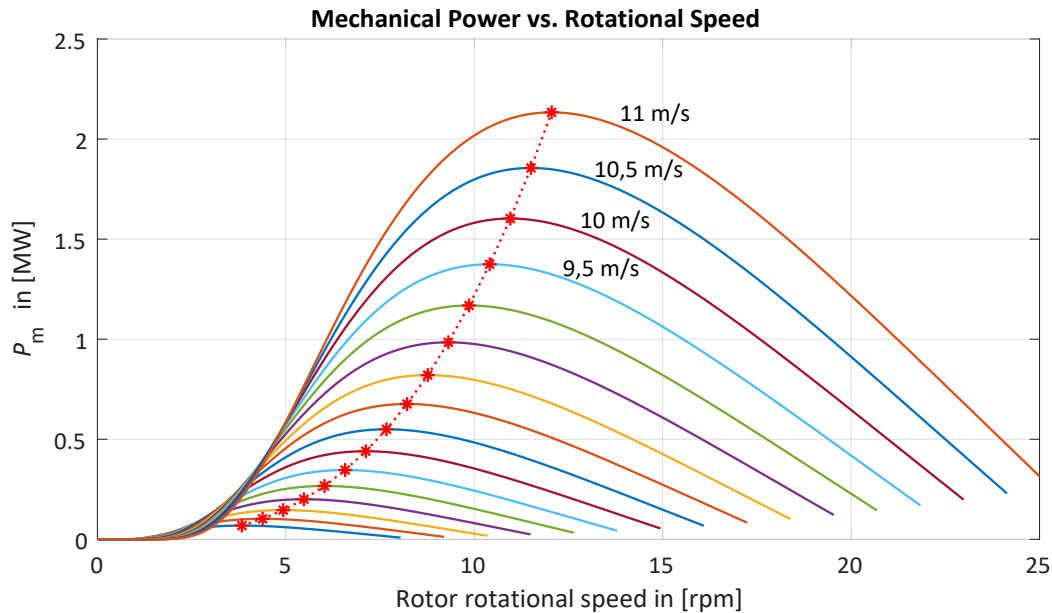


Figure 2.4 Mechanical power as function of rotational speed for different wind speeds.

The excitation controller is of proportional-integral (PI)-type with dynamic limitations and anti-windup capability. The upper and lower limiters are used to represent the real voltage constraints imposed by the dc-link voltage  $V_{DC1}$ , to which the buck-converter is connected (see Figure 2.3). A pulse-width modulator (PWM) generator is used to convert the controller output into gating signals, which are then applied to the IGBT of the buck-converter to generate the required synchronous machine excitation voltage.

Additionally, it is important to note that the rectified dc-link voltage  $V_{DC1}$  can be understood as a further degree of freedom for the system depicted above (i.e., synchronous machine connected to a diode rectifier). In that sense, it is further used in this work to help the system comply with the maximal power tracking requirements, i.e., for power losses minimization in the turbine-generator system. In other words, for each assumed rotor rotational speed  $\omega_r$  there is also an optimal combination of excitation voltage  $V_{SG\_field}$  and rectified voltage  $V_{DC1}$ . For the proposed model, this characteristic was extracted through simulation-based scanning, which looked for the maximal efficiency of the generator system through a broad range of rectified voltage values given different rotor rotational speeds. The result is illustrated in blue in Figure 2.5.

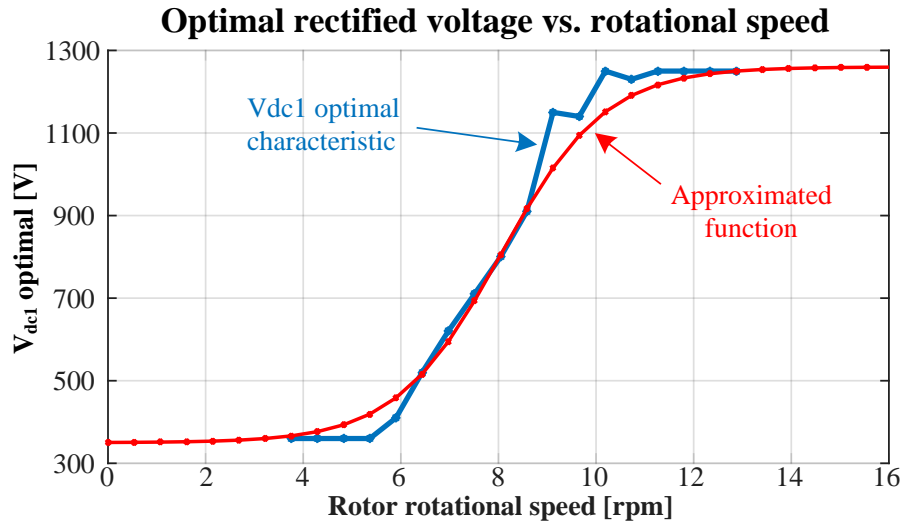


Figure 2.5 Optimal  $V_{DC1}$  as a function of rotor speed.

The characteristic illustrated in Figure 2.5 is used as base for the boost-converter controller law. It is assumed, as further explained later in this chapter, that the grid-side converter controls the second dc-link voltage,  $V_{DC2}$ , to a constant value of 1250 V. For its implementation in the controller model, an approximated function was obtained through polynomial fitting. The resulting function is illustrated in red in Figure 2.5. It is then further used to generate the boost-converter duty-cycle  $d_{boost}$  given a measured rotor speed. The approximated function is given by

$$d_{boost} = 1.5 - \frac{1.50005}{1 + e^{-(\omega_r + 0.1)^5}} \quad (2.5)$$

A block-diagram of the buck- and boost converter controller structures is depicted in Figure 2.6.

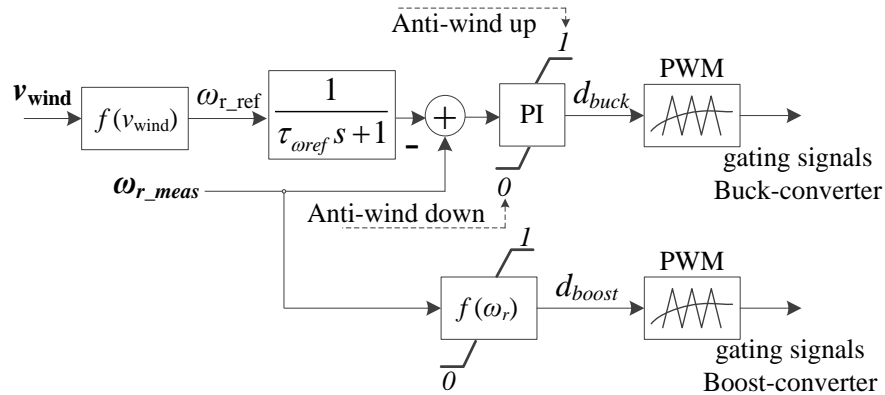


Figure 2.6 Buck- and boost-converter controller schematic structures.

Finally, it is reinforced that the model development aimed at a 2 MW wind turbine to match the system against which it has been validated with field measurement data. Although the controller development and the hardware parameters are made available in the per-unit system, it is emphasized that changes in the turbine rating resulting from a direct downscaling or upscaling of the system parts are prone to yield non-realistic components and/or operating conditions. This is mostly due to the directly-coupled and variable-speed nature of the turbine-generator system.

To exemplify one of the possible resulting issues, it suffices to observe that larger wind turbines, with larger rotor diameters, tend to have lower rotational speeds to reduce mechanical stress. For the wind turbine system considered in this thesis, depicted in Figure 2.3, lower rotational speeds are likely to yield some modifications in the turbine-generator system, such as different blade profiles and the number of generator pole pairs, that are not inherently changed through an upscaling by means of a simple definition of new ratings in the per-unit system. Therefore, to better address cases in which the model has to be used to represent larger generating units, for instance, wind farms, another model parameter was created that lumps (i.e., aggregates) the same model. Its use is recommended for such purposes, since the final representation still respects the realistic constraints considered throughout the model development.

### **2.3.3 Grid Side Converter Control**

The use of full-converter systems offers several advantages [38], [39], [41]. Its application, for instance, to wind turbines, solar plants and HVDC systems allows for fast separate control of active and reactive currents, among others. Such capabilities are very valuable when it comes to grid support services.

In the proposed wind turbine system, the output active and reactive current components of the grid converter are used to control the second dc-link voltage  $V_{DC2}$  (see Figure 2.3) and the reactive power being injected into the grid, respectively. The applied controller topologies are illustrated in Figure 2.7.

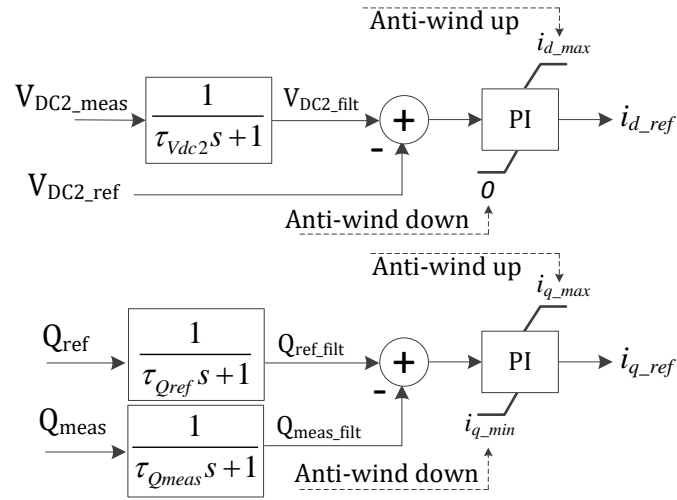


Figure 2.7 DC-link and reactive power control topologies.

The active current component is controlled by the dc-link controller, which is designed to maintain the second dc-link voltage  $V_{DC2}$  at a constant value of 1250 V. This value was chosen to meet the main performance requirements considering the chosen current control type (see further in this section) and a phase-to-phase voltage of 690 V at the ac output terminal of the turbine.

A controller of PI-type with dynamic limitations and anti-windup capabilities is used. The negative error between the reference value  $V_{DC2\_ref}$  of 1250 V and the filtered measured value of the second dc-link voltage,  $V_{DC2\_filt}$ , is used as input. During normal operation, the upper controller limit is defined by the maximal acceptable converter current,  $i_{max}$ , which is a model parameter and should take hardware constraints into account. It is noted, however, that in case of FRT operation the upper limit value can change depending on the FRT strategy in use and its settings (see subchapter 2.3.5). The lower limit is simply defined as zero, since it is assumed that the active power flow is always towards the grid.

The reactive current component is controlled to follow a reactive power reference  $Q_{ref}$ . Again, a controller of PI-type with dynamic limitations and anti-windup capability is used. Its input is the error between the filter value of  $Q_{ref}$  and the filtered measured reactive power at the turbine terminals  $Q_{meas}$ , henceforth referred to  $Q_{ref\_filt}$  and  $Q_{meas\_filt}$ , respectively. During normal operation, priority is given to the active current component and the upper and lower controller limits are

dynamically calculated under the consideration of the active current reference,  $i_{d\_ref}$  and the maximal current constraint imposed by  $i_{max}$ . Consequently, the reactive current component might be limited to meet the maximal current constraint imposed by  $i_{max}$ . Finally, it is important to note that this can, again, change during FRT operation, since, depending on the chosen FRT-strategy, priority can be given to the reactive current component. In such case, the active current component can be limited so to comply with the maximal acceptable converter current  $i_{max}$ .

### 2.3.4 Current Controller and Output Filter

A typical two-level IGBT and diode based voltage source converter has been assumed for the wind turbine system [38]. Moreover, a hysteresis-band current control (HCC) is chosen for the current control. This choice is mostly based on the robustness and high speed of response of the HCC, which also allowed for acceptable results in the comparisons against field measurements (see subchapter 2.3.7). Figure 2.8 depicts an overview of the HCC scheme for the VSC system

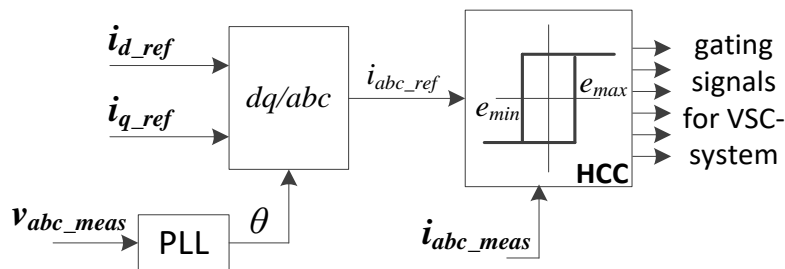


Figure 2.8 Implemented HCC scheme for two-level VSC system.

As can be extracted from Figure 2.8, the reference  $dq$ -currents sent by the grid-side converter controllers are transformed into the  $abc$ -frame by using a  $dq$ -to- $abc$ -transformation with the reference angle  $\theta$  extracted from the measured voltages  $v_{abc\_meas}$  at the turbine terminals through a phase-locked loop (PLL) system.

Furthermore, an LCL-type output filter is employed. The detailed filter topology can be extracted from Figure 2.3. It is designed to comply both with a maximum switching frequency and with some pre-defined power quality requirements. An additional RL parallel damping circuit is also considered [42]. The filter was designed to have its resonance frequency at 2 kHz, from which an attenuation rate of -60 dB/dec is expected [43], [44]. Its frequency characteristic is illustrated in the bode diagram shown in Figure 2.9.

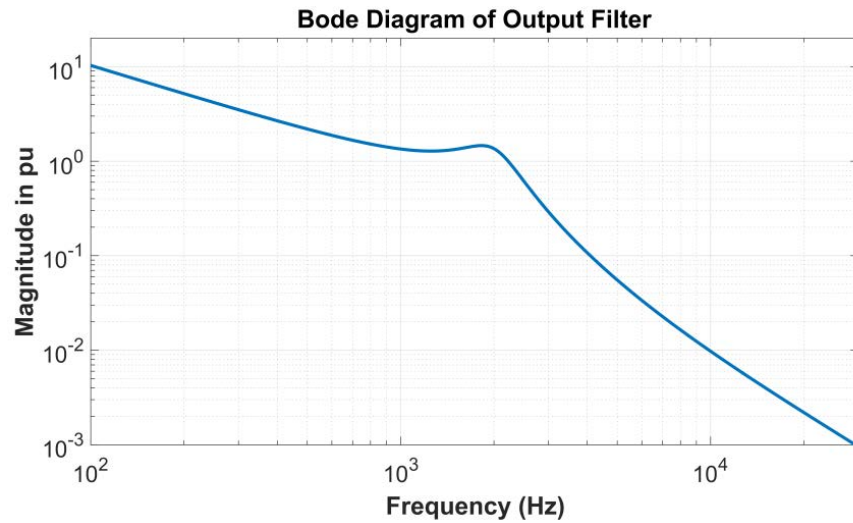


Figure 2.9 Bode diagram of grid-converter LCL-type output filter with damping circuit.

### 2.3.5 FRT Control Strategies and Protections

Two different FRT control strategies are implemented in the proposed model, which are based on existing grid-code requirements in different countries [21],[45]–[48]. They are henceforth referred to as FRT-Mode 1 and FRT-Mode 2. Their main characteristics are summarized in the diagrams illustrated in Figure 2.10.

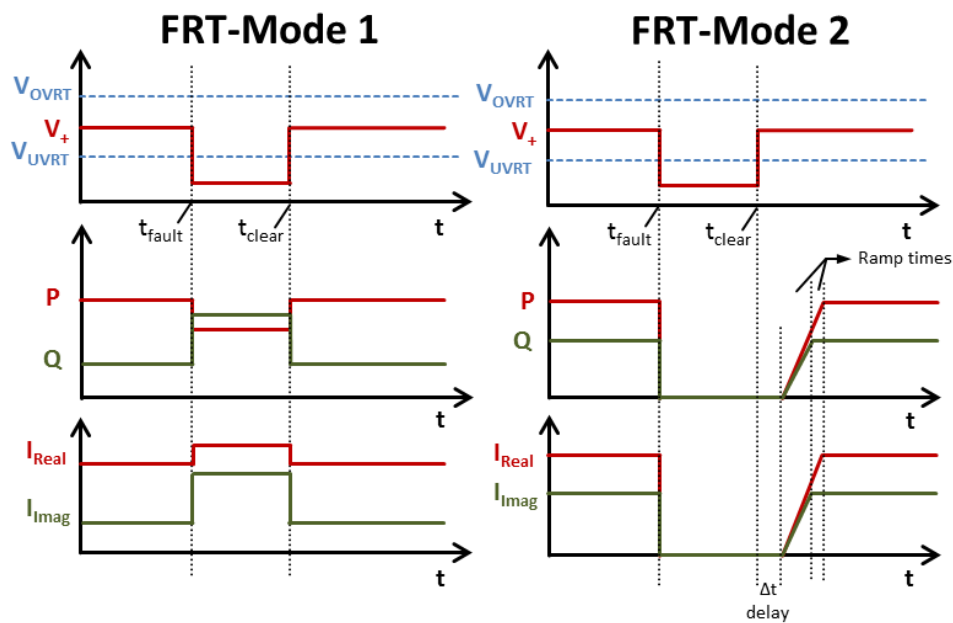


Figure 2.10 FRT-strategies implemented in the generic EMT-type wind turbine model.

FRT-Mode 1 is to be selected when grid support in form of additional reactive current injection during under-voltage ride-through (UVRT) and overvoltage ride-through (OVRT) events is required. In this case, an additional reactive current setpoint proportional to the voltage deviation is sent to the grid-side converter. More precisely, this additional current is calculated by the multiplication of the voltage deviation, in per unit, with a pre-specified proportional factor times the converter rated current. Different proportional factors  $k_{uvrt}$  and  $k_{ovrt}$  can be set for UVRT and OVRT, respectively. Moreover, FRT-Mode 1 prioritizes the reactive component so that, depending on the severity of the fault and on the values of  $k_{uvrt}$  and  $k_{ovrt}$ , the active current might be limited, or even reduced, to allow for the required reactive current injection while not exceeding the maximum current limit  $i_{max}$  provided for the VSC system. This explains the slightly reduction of active power observed for FRT-Mode 1 in Figure 2.10.

FRT-Mode 2 differs from the previous one in the sense that, once the FRT operation is triggered, the VSC stops its active and reactive power injection and remains connected to the grid. This is done by forcing the active and reactive current setpoints to zero. Once the turbine detects that the voltage has recovered, it ramps back its current reference values respecting separate pre-defined ramp rates for both active and reactive components. Furthermore, time delays can be set separately for the initialization of the ramps. Among other applications, this last feature can be used to allow for a first stabilization of the voltage after fault clearance through reactive current injection, before reinjection of active current into the grid.

A breaking-chopper system is connected in parallel to the second dc-link (see Figure 2.3) to avoid overvoltages, reduce stress on hardware components and, therefore, protect wind turbine equipment during faults. Independent of the FRT-Mode used, a maximal FRT-time is to be set in the model to account for real hardware constraints. If this time is exceeded, an opening signal is sent to the three-phase breaker connected at the turbine terminals, as also shown in Figure 2.3, consequently disconnecting the wind turbine from the grid.

A secondary protection level is also implemented in the model. It accounts for the maximum and minimal acceptable values for voltage and frequency for the hardware system. Each of these triggers is to be set with a respective action time delay to allow for the compliance of different Grid

Code requirements. Voltages and frequency are, therefore, constantly monitored by the wind turbine control system. Whenever one of the voltage or frequency protection conditions is met for its corresponding action time delay, an opening signal is sent to a three-phase breaker at the turbine terminals, consequently separating the wind turbine from the grid.

### 2.3.6 Hybrid Model Implementation

The wind turbine generic model as outlined in the previous subchapters is henceforth referred to as the detailed model (DM) representation. Due to the detailed consideration of power electronic equipment in the DM representation, it is noted that its simulation requires small numerical integration time-steps to allow for proper solution of the switching characteristics of these devices. Based on the switching characteristics resulting from the applied current control scheme, a numerical integration time-step of  $1 \mu\text{s}$  is recommended for simulating the DM.

Nevertheless, it is noted that depending on the focus of the required studies, the use of average models and switched equivalent circuits [38], based on switching functions, can be very powerful, since they allow the use of larger numerical integration time-steps, consequently improving computation times of simulations. This can be very useful, for instance, for simulation of large-scale power systems as well as for real-time applications.

As the focus of this research lies on low-frequency phenomena, the consideration of such model optimizations is useful. For this reason, this research work also set the development of a hybrid model (HM) representation (i.e., with averaged models and switched equivalent circuits) for the proposed generic wind turbine model as an objective. More specifically, it proposes an equivalent HM representation for the DM model depicted in previous subsections that aims at numerical integration time-steps as large as  $50 \mu\text{s}$ .

At this point it is reinforced that the use of an average model and switched function equivalents is based on simplified representation of power electronic equipment in conjunction with their controls [38]. More specifically, average model representations assume an averaging of power electronics' switching characteristics over one switching period and replace the switching devices by controlled voltage and current sources that impose voltage and currents mainly determined by the device duty-

cycles. By doing so, the detailed representation of device switching, which usually involve consideration of phenomena in the range of few kHz to dozens of kHz, is avoided and numerical integration time step can be increased at the cost of not having such high frequency transients being represented anymore. In the specific case of switched equivalent circuits, power electronic devices are replaced by equivalent circuit representations consisting of linear devices (resistances, capacitances and inductances) as well as controlled voltage and current sources. The difference, however, is that the detailed nonlinear characteristics of power electronics and switches are circumvented, thus improving computation times by avoiding iterations and matrix re-computations due to circuit structural changes imposed by switching devices. Additionally, the switched circuit representation of power electronics is also not limited to gating signals for power electronic devices in the form of binary values, i.e., 0 or 1. This consists of another advantage of the approach, which, if properly used, can help increase numerical integration time-step of simulation, however, still allowing for consideration of high frequency dynamics and, as it will be shown later in this chapter, discontinuity operating modes.

The wind turbine full-converter system outlined in the previous sections and illustrated in Figure 2.3 contains different power electronic stages to be separately considered in the development of the HM representation with the goal of achieving  $50 \mu\text{s}$  numerical integration time step.

From all the aforementioned power electronic stages, only the diode bridge rectifier is left in its original DM representation for the HM model. This is possible due to the expected low frequency diode transitions resulting from the low frequency ac stator voltages of the directly-coupled synchronous generator.

In contrast to the diode bridge rectifier, a switched equivalent circuit representation was preferred for the boost converter. There are two main reasons for this choice. First, high frequency current dynamics through the boost-converter reactor, which can affect the first and second dc-link voltages are considered. Secondly, the switched equivalent representation of the boost-converter also allow proper consideration of the discontinuous conduction mode, which is not the case in average models. The implementation of the switched circuit equivalent is based on [49] and is illustrated in Figure 2.11. The PWM-averaging block is explained later in this chapter.

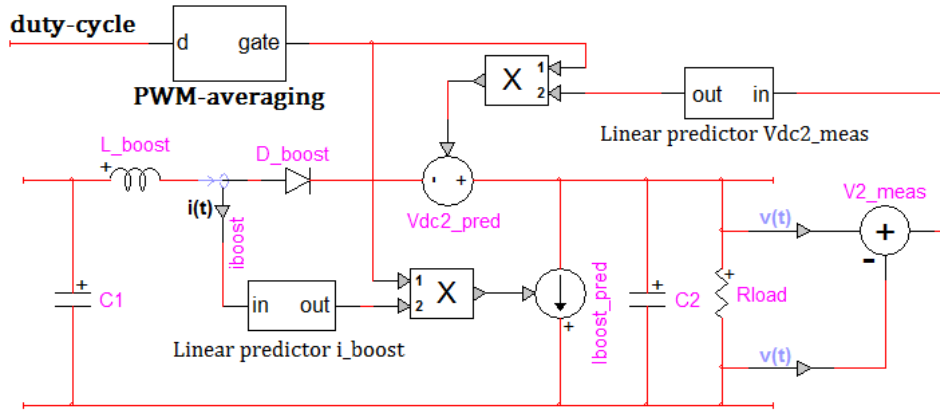


Figure 2.11 Switched equivalent representation of boost-converter circuit.

To elucidate the working principle of the switched equivalent circuit representation of the boost-converter, two cases are considered. If the received gating signal is 1 (boost-converter IGBT is in conduction mode), the measured boost reactor current  $i_{boost\_meas}$  is sent as a reference value to the controlled current source and is, therefore, completely drained by it. To guarantee a zero voltage (short-circuit) at the secondary side of the diode, the measured value of the second dc-link voltage,  $V_{DC2\_meas}$ , is sent to a controlled voltage source. If the gating signal is equal to zero (IGBT is blocked), then both controlled sources receive zero references and can be neglected in the circuit analysis.

Moreover, to avoid numeric algebraic loops in the simulation and, thus, to make the HM more suitable for real-time applications (since solver iterations can be avoided), the measured values of the boost reactor current  $i_{boost\_meas}$  and the second dc-link voltage  $V_{DC2\_meas}$  are sent to the sources through so-called linear-predictor blocks. These blocks linearly estimate the actual solution  $y_k^*$  for the measured values by considering the last two simulation solutions,  $y_{k-1}$  and  $y_{k-2}$ , respectively, and the used numerical integration time step  $T_s$  as given by

$$y_k^* = y_{k-1} + T_s \frac{(y_{k-1} - y_{k-2})}{T_s} = 2y_{k-1} - y_{k-2} \quad (2.6)$$

This assumption is acceptable, since the current through the boost reactor and the voltage over the second dc-link capacitor are expected neither to have discontinuities nor to change quickly. Thus, the use of the linear-predictor blocks results in negligible error in such cases and is, therefore, more suitable than the use of first-order delay blocks.

To exemplify the importance of this property in conjunction with large simulation time-steps, the DM representation of the boost-converter is first analyzed with a numerical integration time step  $T_s$  of  $50\ \mu\text{s}$ . Since the gating signals are converted from duty-cycle values by sawtooth or triangle function based PWM generators, the conversion precision is strongly dependent on the integration time-step used in the simulation environment. It is assumed that the PWM generators have a carrier frequency of 2 kHz. This value, combined with a simulation time-step of  $50\ \mu\text{s}$ , only allows for 10 numerical simulation results within a switching period. One direct consequence is a resulting bad resolution of the duty-cycle, as outlined next.

To overcome this issue, a special triangle function based PWM was developed. It will be further referred to as PWM-averaging. It is capable of considering the precision error resulting from the use of larger simulation time-steps and of automatically correcting it by the end of every switching period by sending a gating signal with a value between 0 and 1. This capability is illustrated in the upper diagram of Figure 2.12. In blue, the gating signal generated by a standard triangle-function based PWM-generator simulated with a time-step of  $1\ \mu\text{s}$  is shown. In dashed green, the PWM-generator simulated with a time-step of  $50\ \mu\text{s}$ ; and, in red, the resulting gating signal characteristic from the new PWM-averaging, also simulated with a time-step of  $50\ \mu\text{s}$ .

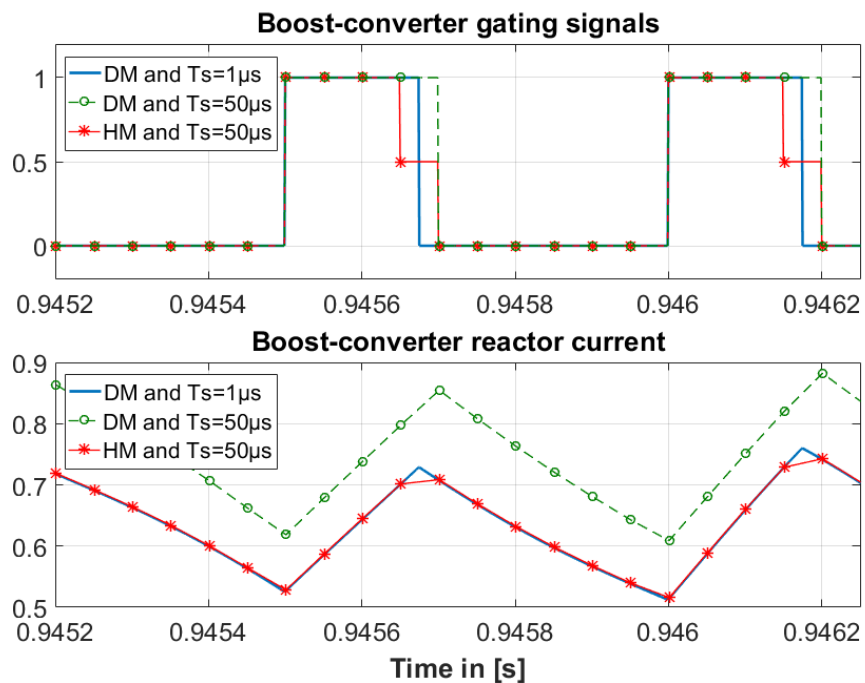


Figure 2.12 Comparison between DM and HM of boost-converter with different time steps.

As shown in Figure 2.12, a sufficiently good representation of the gating signal generator is not possible for a PWM-generator with a carrier frequency of 2 kHz and a simulation time-step of 50  $\mu\text{s}$  without the use of a more advanced technique, such as the proposed PWM-averaging. This is due to the expected 1-to-0 IGBT transitions occurring between two simulation results and the resulting poor duty-cycle resolution achieved with a 50  $\mu\text{s}$  numerical integration time-step. Consequently, the poor duty-cycle resolution affects the boost-converter reactor current, which, in turn, can become under- or over-estimated, depending on the case. This phenomenon is depicted in the lower diagram of Figure 2.12. As it can be seen, the simulation of the DM representation of the boost-circuit and a numerical integration time-step of 50  $\mu\text{s}$  leads to an over-estimated current through the boost reactor, due to the fact that the resulting duty-cycle ends up being larger due to the poor resolution. Additionally, as indicated in Figure 2.12, aside from the correction step at the end of each switching period, an almost perfect match can be obtained for the boost-reactor current between the DM simulated with a numerical integration time-step of 1  $\mu\text{s}$  and the HM representation (i.e., with the switched function equivalent circuit) simulated with a numerical integration time-step of 50  $\mu\text{s}$ .

Similarly to the boost-converter, also a switched equivalent circuit representation is chosen for the buck-converter circuit, which is responsible for the excitation of the synchronous machine. It is developed based on some similar considerations as for the boost-converter and on insights of the buck-converter from [42]. More specifically, the value of the rectified generator voltage  $V_{DC1}$  is multiplied with the gating signals from the PWM-averaging block under consideration of the buck duty-cycle  $d_{buck}$ , which results directly in the excitation voltage  $V_{SG\_field}$  as input for the synchronous machine model. Moreover, to still allow for the proper consideration of the excitation power drained from the dc-link, the primary side of the buck-converter is represented as a controlled current source connected in anti-parallel to the rectified generator voltages (i.e., to the first dc-link). Its reference value corresponds to the actual generator field current multiplied by gating signals from the PWM-averaging block. A schematic diagram of the switched equivalent circuit for the buck-converter is given in Figure 2.13.

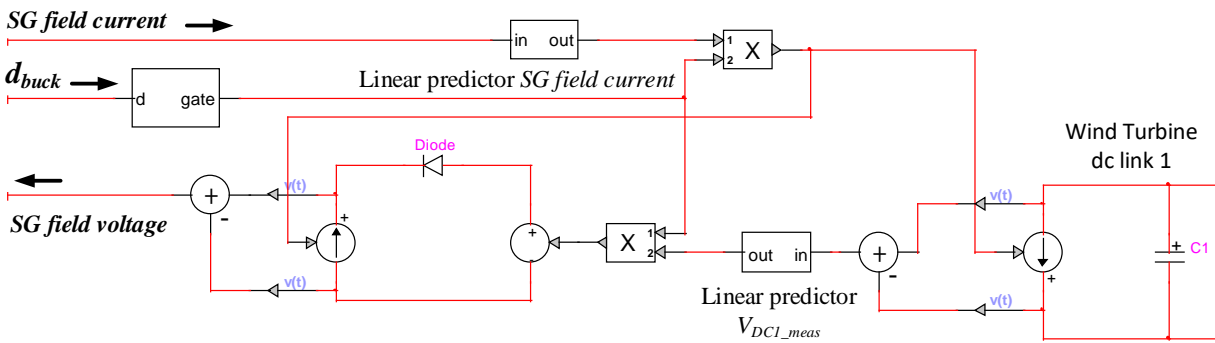


Figure 2.13 Switched equivalent circuit of buck-converter.

The afore-outlined PWM-averaging technique is also used in the HM to obtain a switched equivalent representation of the braking-chopper. Again, the switched equivalent circuit has been preferred over an averaged one due to the possibility of considering high frequency transients. In the case of the chopper, this allows to capture the high-frequency current components flowing through the braking-resistor as well as their corresponding high frequency impacts in the second dc-link voltage  $V_{DC2}$ . This is important, since a simplification at this stage could considerably affect the fast inner control loops and, thus, also the currents injected into the grid.

The implementation of the switched equivalent circuit for the chopper stage in the HM is done by considering a controlled current source connected in anti-parallel to the second dc-link capacitor, similar to previously done in the case of the buck-converter. The setpoint value of this current source is given by the multiplication of the chopper gating signal, which comes from the PWM-averaging block, with a current value, which is calculated by dividing the measured dc-link voltage by the value of the chopper resistance. The chopper IGBT conduction losses are also considered by adding its equivalent resistance to the value of the braking-chopper resistance.

Finally, an average model representation is proposed for the two-level VSC of the grid side converter. This choice is justified by the fact that the focus of this research lies at low frequency phenomena and the application of the HM for real-time simulations. In such cases, the harmonics generated by the switching of the VSC are not in focus.

Due to the main characteristics of the chosen hysteresis-band current control together with the two-level VSC system, the average model representation of the grid-side converter is proposed as two star-connected ungrounded current sources injecting the reference currents into phases  $a$  and  $b$ . A

third current source feeding into the phase  $c$  is not needed, since the VSC system is represented by a star-connected ungrounded circuit and, therefore, only the injection of two reference currents is required (the sum of the three-phase currents equals zero). The average representation of the HCC-based VSC system is given in Figure 2.14.

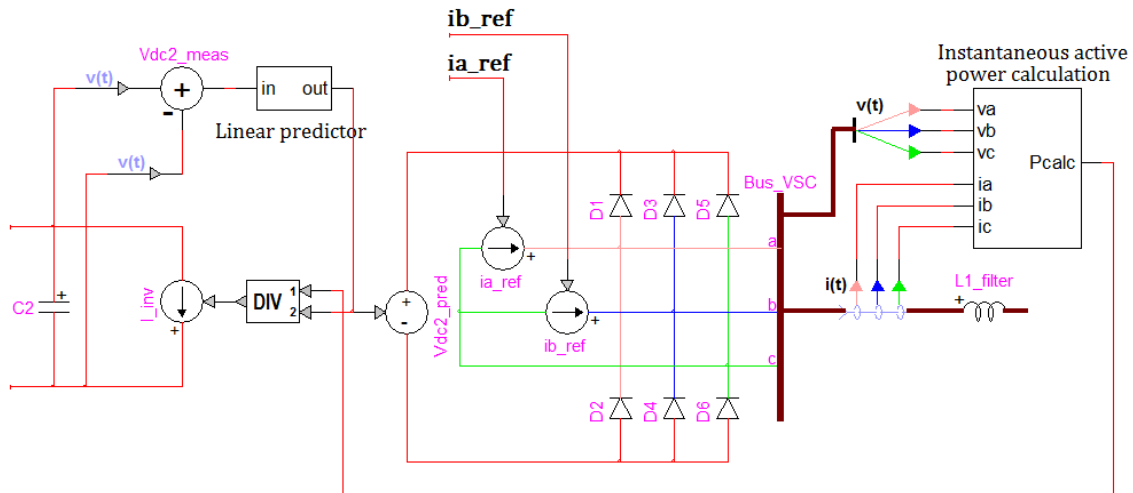


Figure 2.14 Average model representation of a two-level VSC with HCC.

Moreover, to take the effect of the anti-parallel diodes of the two-level VSC system into consideration, these are further represented as connected to the output of the controlled current sources, forming a diode-rectifier system leading to a controlled voltage source (see Figure 2.14). This source receives the linearly predicted (see equation (2.6) above) value of the second dc-link  $V_{DC2\_meas}$  as setpoint during simulation.

At this point, it is emphasized that keeping the diode representation form in the average model representation of the VSC system is important for two reasons:

- i) it avoids numerical overvoltages at the controlled current source nodes resulting from series connection of these sources to inductive elements (e.g., output filter and transformer).
- i) it can still build a path for currents back to the second dc-link capacitor in case of sustained overvoltages at the grid side.

To complete the average model representation of the VSC system, an anti-parallel current source is connected to the secondary dc-link capacitor. It allows for power balance maintenance in the HM representation of the wind turbine by considering the active power injected into the grid and

discharging the dc-link capacitor accordingly. For this, the instantaneous active power injected into the grid is measured and divided by the linearly predicted measured value of  $V_{DC2\_meas}$  to generate the current setpoint for the controlled current source. Again, the predictor block is used to avoid the creation of numeric algebraic-loops in the simulation. As explained above for the case of the switched equivalent model of the boost-converter, the use of the linear-predictor block avoids solver iterations, improving computation time and, therefore, making the model more suitable for real-time applications.

Finally, the proposed HM representation is benchmarked against its DM representation running with numerical integration time steps of  $50 \mu\text{s}$  and  $1 \mu\text{s}$ , respectively. A sudden voltage drop from 1 to 0.7 per unit applied at the voltage source of a grid Thevenin representation is simulated under FRT-Mode 2 operation. The wind turbine terminal  $abc$ -currents into the grid are compared for both model representations and are illustrated in Figure 2.15. It is possible to see a very good match between DM and HM models although a 50 times larger numerical integration time-step, i.e.,  $50 \mu\text{s}$  is used for the HM representation. It is also noted that the HM was capable of properly reproducing high frequency transients during fault application and FRT operation.

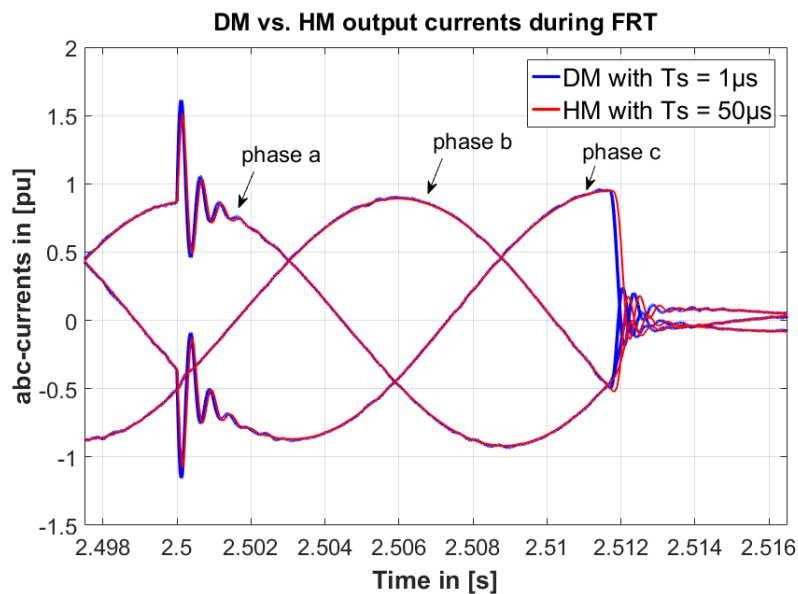


Figure 2.15 Wind turbine currents during FRT Mode 2: DM ( $T_s = 1 \mu\text{s}$ ) vs. HM ( $T_s = 50 \mu\text{s}$ ).

### 2.3.7 Model Performance Validation Against Field Tests

To benchmark the performance of the proposed generic EMT-type wind turbine representation, the model is validated against field tests performed on a turbine of similar type.

More specifically, the tests were conducted in one turbine of the 365 MW large wind farm of Seigneurie de Beaupré, in Québec, Canada. This wind farm is composed of a 34.5 kV 60 Hz underground collector system with 164 wind turbines. A so-called short circuit container, similar to the one used in [50], was connected to the middle-voltage (MV) terminals of an ENERCON E-82 2.3 MW wind turbine, i.e., at the secondary side of the wind turbine transformer. It allowed for the application of several fault types with different residual voltages directly at the wind turbine terminals. The wind turbine and the test site are shown in Figure 2.16.

To reduce the impact of the applied faults as seen from the grid, the short-circuit container makes use of a bypass-breaker that automatically opens around two seconds before fault application and, also, recloses approximately two seconds after fault application. More specifically, a high inductive element is added between the fault and the grid during the tests, thus, limiting the short-circuit contribution from the grid-side. This also allow for normal operation of other wind turbines at the same wind farm during the tests.



Figure 2.16 E-82 2.3 MW test site at Seigneurie de Beaupré, Canada (courtesy of ENERCON).

The grid representation has been developed based on its short-circuit capacity and X/R relation of 340 MVA and 3.1, respectively, provided for the wind turbine terminals with rated MV voltage of 34.5 kV, without the consideration of the short-circuit container.

To illustrate the performance of the proposed model against the field tests, four of the performed FRT tests are depicted in this work. It is emphasized that the validation is done based on the positive sequence values calculated for the terminal voltage  $V_{pos}$ , and the measured three-phase active and reactive powers for the fundamental frequency,  $P_{pos}$  and  $Q_{pos}$ , respectively.

Moreover, it is important to note that the wind turbine model proposed in the framework of this research is *generic* and does not account for real turbine parameters and controllers. For this reason, no perfect match between the measurement and simulations should be expected. The goal of this validation is to demonstrate that the overall performance of the proposed EMT-type wind turbine model is sufficiently accurate and provides adequate performance when compared to field tests of a real wind turbine of similar type and rating.

FRT Mode 1 was tested with a proportional factor  $k_{uvrt}$  equal to 3, which defines the amount of additional reactive current during FRT operation. Figure 2.17 illustrates the comparison between measurements of the real wind turbine (in blue) and the responses of the wind turbine model (in red) to a phase-to-phase to ground and a three-phase-to-ground fault, respectively.

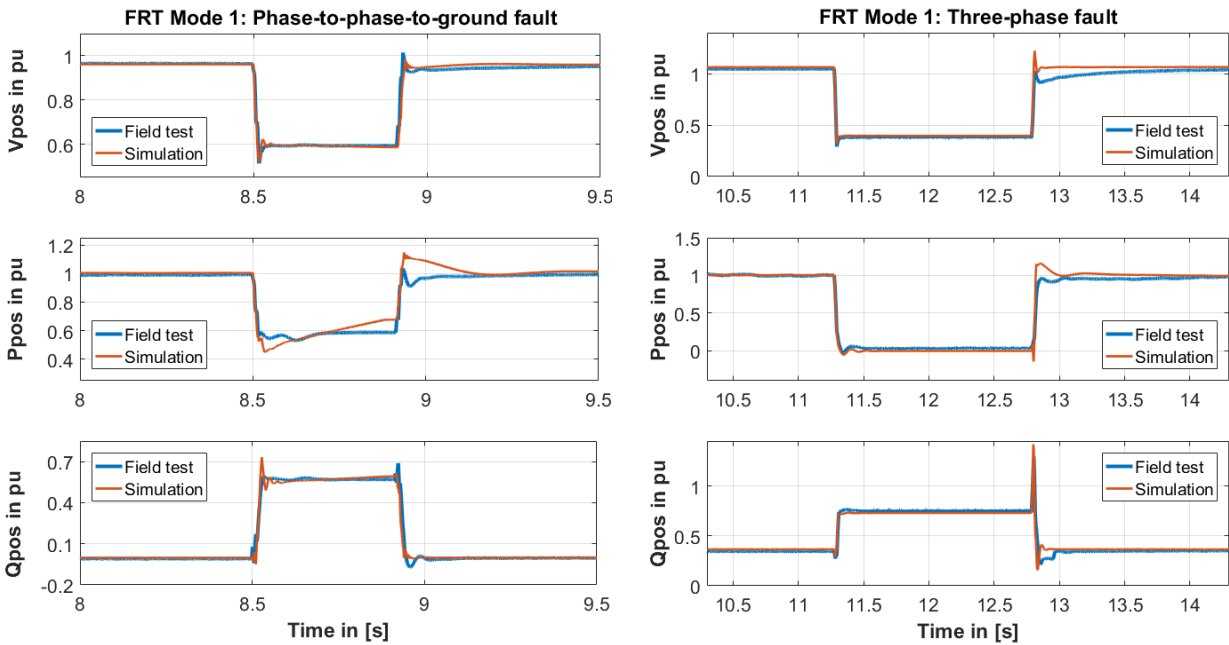


Figure 2.17 FRT-Mode 1 with  $k_{uvrt} = 3$  for phase-to-phase-to-ground and three-phase faults.

Similar tests were performed for FRT-Mode 2. The performances of real turbine and model are compared for two-phase-to-ground and three-phase-to-ground faults in Figure 2.18.

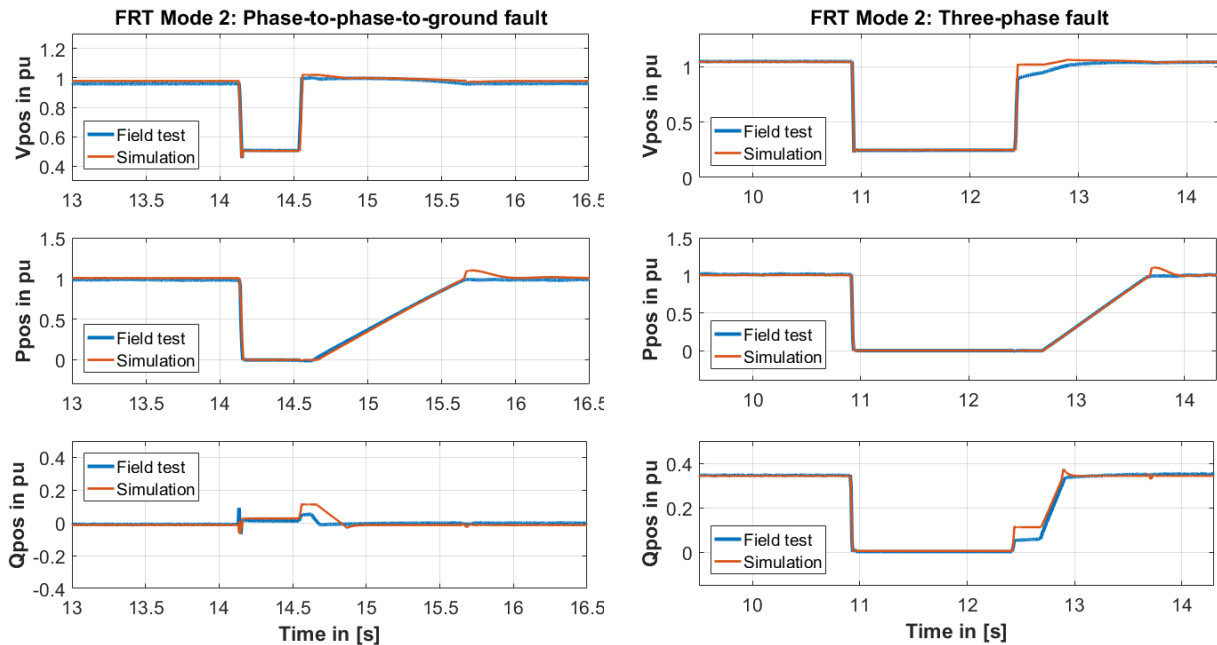


Figure 2.18 FRT-Mode 2 response for phase-to-phase-to-ground and three-phase fault.

It is also emphasized that a time delay of 100 ms was considered in the start of the active and reactive currents ramp ups after fault clearance (Figure 2.18).

As illustrated in Figure 2.17 and Figure 2.18, it is still possible to note some differences between the performances measured for the real wind turbine and the ones obtained from the proposed generic wind turbine model, for instance, at fault clearance. Part of these deviations are due to the simplified grid representation used, which, due to lack of available information, did not account for detailed collector system representation. The other part of the differences can be attributed to the proposed wind turbine model and could possibly still be reduced in a case-by-case tuning of the generic parameters and controllers. Yet, it is reinforced that the proposed model is not manufacturer-specific and, as such, does not account for the actual wind turbine parameters and controllers. Therefore, a perfect match between field tests and simulations results is not possible and should not be expected.

Nevertheless, it is emphasized that these deviations remained small and that, overall, a good match was obtained between field tests and simulated performance of the proposed wind turbine model. This confirms that the proposed generic EMT-type wind turbine model contains the required level of details to provide adequate and sufficiently accurate performance to support EMT power system studies as well as the research and investigations conducted in the next chapter.

## CHAPTER 3      LOW-FREQUENCY PHENOMENA IN WIND FARMS

This chapter focuses at the investigation of subsynchronous oscillations (SSO) in wind power systems based on electromagnetic transient (EMT) simulations. An overview of existing activities towards the understanding of SSO in power systems is provided as well as of existing benchmark models for SSO studies. A new benchmark grid for the study of low-frequency phenomena involving wind power plants in series compensated grids is proposed. This relies on realistic equipment data provided by Hydro-Québec, who also supported this research work, and serves as basis for detailed EMT studies conducted in this thesis to address low-frequency phenomena in type-III and type-IV based wind farms. Some results and contributions of this specific work package have also been published in [51].

### 3.1 Overview and Definitions

The study of low frequency oscillations in power systems and also, more specifically, in wind power systems, requires an overview and clear definition of the types of oscillations and their corresponding frequency ranges.

#### 3.1.1 Power System Oscillations

The definitions proposed in [52] are adopted in this thesis to address classical power system oscillations involving mostly conventional machines, i.e., synchronous machine based generating units. According to [52], oscillations are classified by the systems components that they effect. These are, for convenience, shortly reviewed below.

##### *Intraplant Mode Oscillations*

This category of oscillation addresses the case in which machines (usually, but not limited to, synchronous machine) oscillate against each other at the same power generation site. Such oscillations are referred to as *intraplant* because they are locally noticeable at the concerned generation plant complex; however do not affect the rest of the system. In classical power systems, intraplant oscillations happen often in the range of 2 to 3 Hz, depending on the rating of the units and on the reactance connecting them [52].

##### *Local Plant Mode Oscillations*

Local modes represent cases when a single generator unit oscillates against the rest of the system. It is noted that the impact of local modes is localized to the involved generator and the line connecting it to the grid. In studies of local modes, the rest of the system is usually modeled as a constant voltage source whose frequency is assumed to remain constant (i.e., a stiff grid). Such schema is usually referred to as a single-machine-infinite-bus connection.

Local mode oscillations are expected to take place in the range of 1 to 2 Hz. Moreover, it is emphasized that the damping and frequency of these oscillations are dependent on the machine operating condition and the impedance between the machine terminals and the infinite bus voltage.

Mitigation of local modes is often performed through the inclusion of a so-called power system stabilizer (PSS), which measure the oscillation at the generating unit and provides additional modulation to the voltage reference of the automatic voltage regulator (AVR) with adequate phase and gain compensation.

### ***Interarea Mode Oscillations***

Interarea mode involves, differently than the local plant mode, more than a generating unit and affects a larger part of the electrical grid. According to [52], it usually involves two coherent groups of generating units that oscillate against each other. Typical oscillatory frequencies are in the range of 1 Hz or less [52]. Additionally, it is noted that interarea oscillations are a complex phenomenon that involves many components of the power system and have as well nonlinear dynamic characteristics. The damping of interarea modes is usually dependent on the tie-line strength connecting the involved generator groups, load characteristics, loading condition of transmission lines and the dynamics of the generating units considering their controllers.

### ***Control Mode Oscillations***

Control modes are a different type of oscillations that typically take place as a consequence of poorly tuned AVR and PSS controllers [52]. In modern power systems, the control of inverter based devices can also influence or even start such oscillatory behaviors, as it will be shown further in this chapter, for instance, in the case of wind farms.

### ***Torsional Mode Oscillations***

These types of modes are explicitly related to the shaft systems of generating units, i.e., with their mechanical characteristics, masses and inertias. It is noted that shaft systems of conventional generating units are complex. Thermal based generating units, for instance, have separate turbine systems connected to the same shaft in order to optimize power extraction under high, medium and low pressure conditions [53]. The stiffness of such shaft systems is not infinite and, thus, it is natural that such masses may oscillate against each other if proper measures are not taken.

Torsional modes are typically associated to oscillatory frequencies in the range of 10 to 46 Hz.

Moreover, as also indicated in Chapter 1 and further elaborated in this and following chapters, mechanical torsional modes of shaft systems may interact with series compensated grids if their resonances match. More specifically, resonances are prone to appear if the natural network frequency equals the synchronous frequency minus the torsional frequency.

### **3.1.2 Subsynchronous Oscillations**

When addressing low-frequency phenomena in power systems, an overview and good understanding of one specific type of oscillations in this category is mandatory, namely, the subsynchronous oscillations (SSO). Although power system oscillations can be classified by the system components that they affect, as outlined in previous subchapter 3.1.1, SSO, which may involve one or more of the mechanisms mentioned earlier, are often seen as a topic for itself. For this reason, its definitions are also conveniently provided in this subchapter.

According to [54], SSO in power systems first appeared in the literature in 1937. However, the topic first really gained attention after the events dated from 1970 and 1971 at the Mohave power plant in the USA (see Chapter 1), resulting in two successive shaft failures [5]. Also, the investigations carried out for the Mohave Incident indicated that it was of subsynchronous resonance (SSR) type. From then on, SSO and, more specifically, SSR became an active field of research.

The incidents involving the generating units of Mohave were the result of an interaction between the power plant turbine-generators and series-compensated lines [5]. Series-compensation is an economical and efficient mean of increasing the power transfer capabilities and enhancing transient stability. For these reasons, the use of series compensation is a common practice from power systems operators when it comes to long ac transmission lines [55]. As such, the widespread use of

series compensation in long transmission lines certainly also added to the relevance of the studies in the area of SSR.

The Institute of Electrical and Electronics Engineers (IEEE) started early with some activities in this field and its Subcommittee for System Dynamic Performance created in the months to follow the publication of the Mohave Incident the Subsynchronous Resonance (SSR) Working Group. This group delivered a first report in the mid of 70's providing a first bibliography for SSR study between rotating machines and power systems [56]. In the few years that followed, the works of this working group delivered further four supplements to this first bibliography ([57]–[60]), eventually culminating at their most relevant contribution in 1985, namely, their report providing terms, definitions and symbols for SSO [61].

The work delivered by the aforementioned IEEE Working Group, summarized in [61], together with the books from Paul M. Anderson [62] and Padiyar [63], which are focused on the theoretical analysis of SSR in power systems, provide a good base for the understanding of SSR in case of conventional systems. The following definitions of SSR and its categories are mostly based on these references.

### ***Subsynchronous Oscillation (SSO)***

Before providing a definition for SSR, the IEEE Report from 1985 ([61]) first defines subsynchronous oscillation (SSO), which is given as

*“(...) an electric power system condition where the electric network exchanges energy with a turbine generator at one or more of the natural frequencies of the combined system below the synchronous frequency of the system”.*

### ***Subsynchronous Resonance (SSR)***

Under SSO, SSR is further defined as follows ([61]):

*“(...) SSR encompasses the oscillatory attributes of electrical and mechanical variables associated with turbine-generators when coupled to a series capacitor compensated transmission system where the oscillatory energy interchange is lightly damped, undamped, or even negatively damped and growing”.*

Additionally, there are two conditions (i.e., under-categories) of the SSR that are differentiated by [61]. These are: i) Self-excitation; and, ii) Transient torques. They are often denominated to as *steady-state* and *transient SSR*, respectively [63], and are defined separately in the following.

***Self-excitation (also referred to as steady-state SSR)***

The self-excitation phenomenon refers to sub-synchronous currents that enter the machine armature and produce subsynchronous terminal voltage components. Depending on the characteristics of the turbine-generator and the grid that it is connected to, these subsynchronous voltages may sustain the subsynchronous currents to produce this effect named self-excitation. Moreover, reference [61] differentiates between two types of self-excitation: a) Induction Generator Effect; and b) Torsional Interaction.

The induction generator effect (IGE) refers to the self-excitation principle caused by electrical components only. In such case, the resistance of the synchronous machine rotor, viewed from the armature terminals, is negative for a subsynchronous current. This can be explained by the induction generator principle (therefore the name), since the fact that the machine rotor turns faster than the magnetic field induced by the subsynchronous currents in the armature can be analytically represented as a negative slip at this subsynchronous frequency, as for induction machines.

The so-called subsynchronous torsional interaction (SSTI) happens when the subsynchronous torque induced in the electrical generator is close to one of the natural oscillatory modes of the turbine-generator shaft. If this condition is achieved, then oscillations build up following some initial perturbation and this motion induces armature voltage components at the subsynchronous frequency that sustain the oscillatory torque. If this torque is equal or exceeds the existing mechanical damping of the system, then the system become self-excited.

***Transient Torques (also referred to as transient SSR)***

The last SSR category defined by [61] concerns the so-called transient torques. These are the ones initiated by system disturbances, responsible for sudden changes in the network and, consequently, resulting in rapid current changes that tend to oscillate at the natural frequencies of the concerned power systems. As explained in [62], for systems without series-compensation, these transients are always dc transients that decay with a time constant depending on the X/R ratio of the system. In case of series-compensated systems, there will be one or more natural modes, depending on the

series-compensation unit. If these modes coincide with the natural oscillatory modes of the turbine-generator shaft, then this could give rise to large peak torques. Since these torques are proportional to the magnitude of the oscillatory currents following disturbances, which are generally large, the transient torques are usually very high and likely to lead to shaft damages, if no proper protection is considered.

### 3.1.3 Low-Frequency Oscillation in Power Systems

It is important to note that the definitions provided by the IEEE Working Group in [61] address SSR as a specific category of phenomena that explicitly involves the interaction of turbine-generators and series-compensated systems.

Although [61] still provides a broader category of phenomena with the definition of SSO, it has been noted throughout this research work that the phenomena related to, for instance, control interaction of inverter-based devices and power system equipment are not limited to the subsynchronous range. One example is the interconnection of the BorWin1 offshore wind farm in Germany by means of an HVDC link [15].

Since one of the objectives of this research work is to address the impacts of grid-connected inverter and their controls, whose effects are not limited to the subsynchronous range, a broader category than SSO is required. As briefly outlined in the Introduction, Chapter 1, the classification chosen in this thesis relies on the work presented in [4], which separates grid resonances that can be destabilized by inverter-based devices into two categories: i) *Harmonic Resonances*; and ii) *Near-Synchronous Resonances*. The former comprises resonances that are in the range from hundreds of Hz up to some kHz and are a consequence of the inherent impedance characteristics of transmission lines and cables in conjunction with input filters of grid-connected inverters. The latter refers to resonances in the range from few Hz up to roughly twice the system nominal frequency. The low frequency phenomena addressed in this work falls in this category.

However, as also indicated earlier in this thesis, a thorough review of recent field events as well as investigations conducted in the framework of this research indicate that interactions involving grid-connected inverters and their controls are not necessarily limited to frequency range *near* the syn-

chronous frequency and, in fact, can actually go much beyond *twice* the this frequency. For instance, the unstable oscillatory behavior observed in the interconnection of BorWin 1 in Germany, which deals with the integration of an offshore wind farm through an HVDC link (see details in Chapter 1), took place in the frequency range of 250 to 450 Hz.

Therefore, to cover these aspects, the broader term *low-frequency phenomena* is used to address resonances and instabilities in power systems whose oscillatory frequency may be as low as the interarea modes (i.e., roughly 1 Hz) up to 10 times the system nominal frequency, in order to cover cases similar to BorWin 1.

Finally, it is emphasized that this frequency range fits the bandwidth that can also be addressed by the HM wind turbine model proposed in Chapter 2, whose proposed numerical integration time-step is 50  $\mu$ s. A classical rule of thumb for choosing numerical integration time-steps in EMT software states that it has to be at least 10 times smaller than the smallest period of the phenomena to be addressed in the simulation. Thus, a numerical integration time-step of 50  $\mu$ s is more than adequate to address the low-frequency phenomena, which, as considered in this work, may go up to 500 or 600 Hz, depending on the rated frequency assumed.

## **3.2 Existing Models for the Study of Low-Frequency Phenomena**

Due to the increased relevance of understanding the phenomena and its mechanisms, the IEEE SSR Working Group of the System Dynamic Performance Subcommittee also proposed benchmark study systems. Due to their relevance, they are outlined in the next subchapters.

In addition, recent proposed benchmarks are as well outlined, which already aim at the consideration of modern power system structures involving, for instance, grid-connected inverters.

### **3.2.1 IEEE First Benchmark System for SSR Studies**

The so-called IEEE First Benchmark System (FBM) for Computer Simulation of Subsynchronous Resonance was proposed in 1977 in [64] and has since been extensively used as benchmark for research and testing of mitigation mechanisms for SSR, notably in [65]–[74].

It is also emphasized that the IEEE FBM for SSR studies is based on real values of the Navajo Project, which is in the same grid area of the Mohave power plant, in the USA. The single-line diagram representation of the IEEE FBM is given for convenience in Figure 3.1 (EMTP Model).

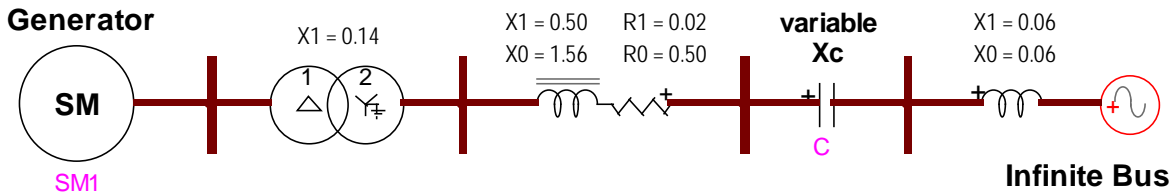


Figure 3.1 IEEE FBM for subsynchronous resonance studies [64].

It is noted that the IEEE FBM is of radial structure and is focused on providing the minimum necessary realistic system configuration to obtain a SSR for the synchronous machine SM. This is useful for analytical studies. Noticeably, following any disturbance in a radial system like the IEEE FBM, the transient current  $i_{tr}$  flowing into the generator armature and transmission line can be simply calculated as

$$i_{tr} = Ae^{-\alpha t} \sin(\omega_{er}t + \beta) \quad (3.1)$$

where the considered parameter values are given as

$$\alpha = \frac{R\omega_B}{x_s}; \quad \omega_{er} = 2\pi f_{er} = \sqrt{\omega_n^2 - \alpha^2}; \quad \omega_n = \omega_B \sqrt{\frac{x_c}{x_s}}; \quad x_s = x_E + x_t + x' \quad (3.2)$$

In the above equations,  $\omega_B$  is the rated rotational system frequency in rad/s,  $x'$ ,  $x_t$  and  $x_E$  the transient reactances of the synchronous machine, transformer reactance and transmission line, respectively. The series-capacitor reactance is represented by  $x_c$ . The electrical resonance frequency is  $f_{er}$  and  $A$  and  $\beta$  from Equation (3.1) are determined from the system initial conditions. Moreover, it is interesting to note that in case of small or negligible resistances in the radial system,  $\alpha$  is small and the approximation  $\omega_{er} \approx \omega_n$  becomes valid.

Also, it is emphasized that a mechanical system representation is proposed in [64] for the generating unit. More specifically, a turbine-generator system with several pressure stages is considered and a six-mass system representation is proposed. This consideration is important, since it makes the FBM also suitable for the investigation of SSTI (see subchapter 3.1.2).

### 3.2.2 IEEE Second Benchmark System for SSR Studies

The study of simple systems, such as the radial system configuration of the IEEE FBM, is useful, especially for analytical investigations. Nevertheless, it is noted that radial configurations do not always correspond to the normal operating conditions of power generating units. In fact, such conditions are rarely expected, mostly only after disturbances. For this reason, the IEEE SSR Working Group also provided in 1985 an additional benchmark model for SSR studies [75]. More specifically, [75] proposed two new benchmark systems with a more common configuration to deal with the so-called parallel resonance cases and interaction between turbine-generators with a common mode, respectively. These are, for convenience, illustrated in Figure 3.2.

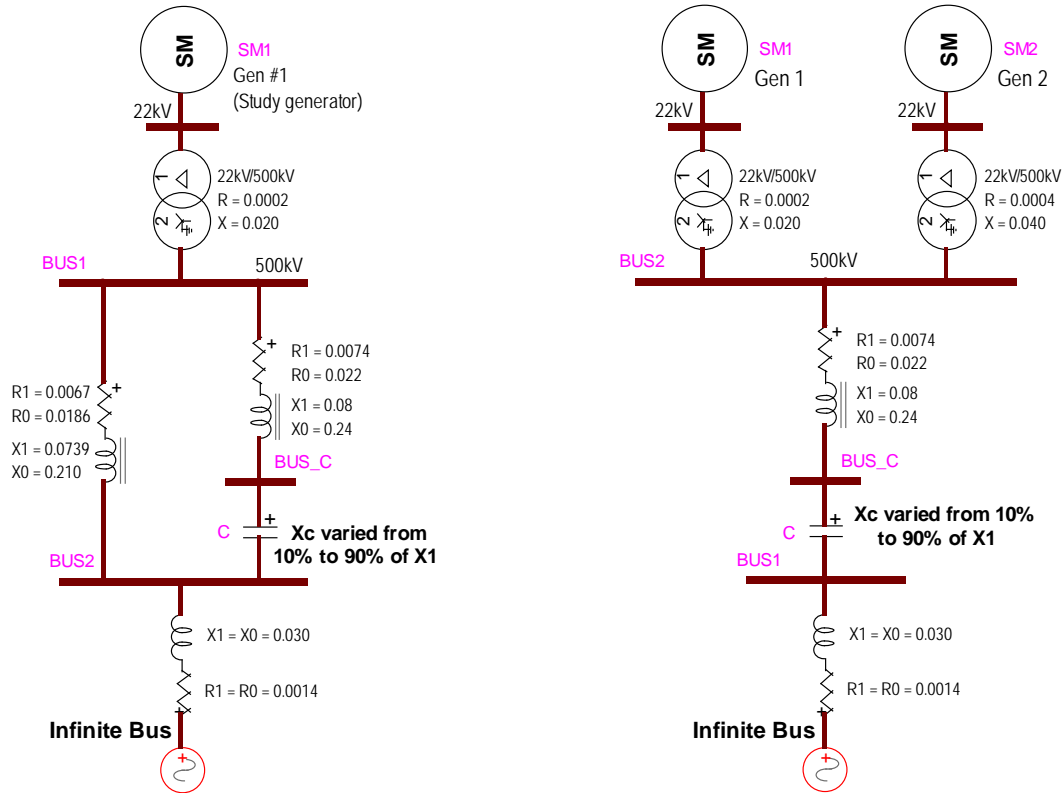


Figure 3.2 Sys-1 (left) and Sys-2 (right) of the IEEE second benchmark for SSR studies [75].

Finally, it is noted that the systems proposed by the IEEE Working Group in [75] have also found widespread use in research works since, notably in [55], [76]–[78].

### 3.2.3 Review of Benchmark System for SSO involving Wind Generation

The benchmark systems proposed by the IEEE SSR Working Group are intended to illustrate the SSR phenomena and to provide a common base for testing different mitigation approaches. It is noted, however, that these benchmarks address only conventional generating units. Although recent publications have based SSO studies with inverter-based generation on these benchmarks, the industry has also identified the need for improvements in these benchmarks to take new generating units into account.

Notably, recent working groups and task forces have been created to address these needs. For instance, [79] reviewed existing benchmarks and added modeling details required for them to be adequate for high precision EMT-type studies as well as proposed EMT-type representations for new equipment and new benchmark systems. Also, the CIGRE WG C4.56 entitled “Electromagnetic Transient Simulation Model for Large-Scale System Impact Studies in Power Systems Having High Penetration of Inverter-Connected Generation” has been recently created to address similar needs, reinforcing the importance of detailed models for the studies of large-scale issues in power systems.

In the framework of this thesis, models provided by the recent IEEE Task Force on Modeling Subsynchronous Oscillations in Wind Energy Interconnected Systems and presented in [37] are used. Details of the type-III and type-IV wind turbines used in these models can be extracted from [27] and [30], respectively.

Additionally, a benchmark grid model of a multi-converter system provided by the aforementioned IEEE Task Force will also be investigated. More specifically, the large-scale generic grid benchmark model presented under the name “SSCI Benchmark-I” will be used [37]. This benchmark system is illustrated in Figure 3.3 (EMTP model).

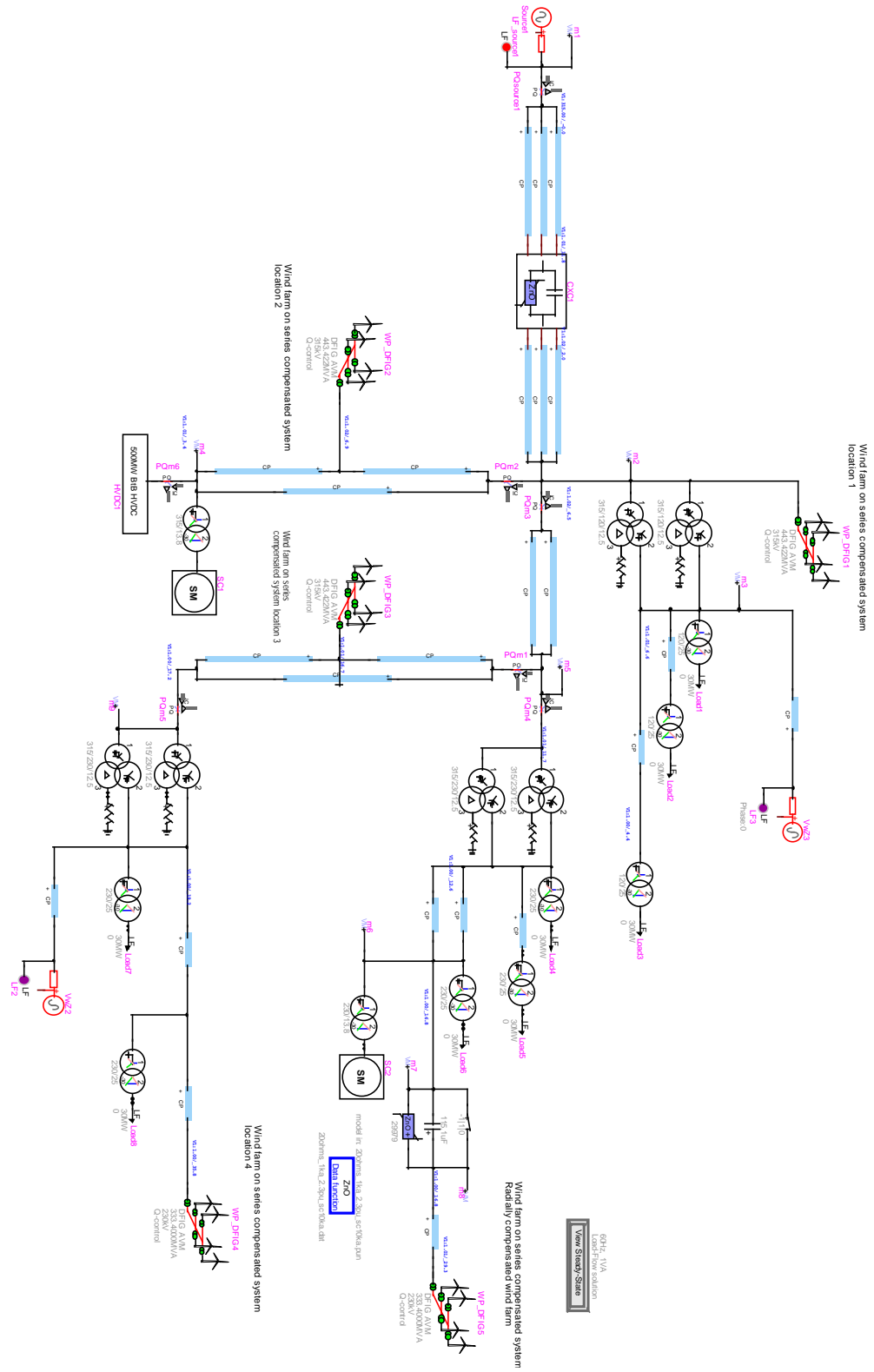


Figure 3.3 SSCI-Benchmark-I – Large-scale system [37].

It is noted here that the network topology and parameters of the SSCI Benchmark-I (Figure 3.3) are inspired by an actual system. Distributed parameter line models are used to represent transmission lines, transformers contain the detailed representation of magnetizing branches including saturation characteristics, synchronous condensers are considered to support system voltage, and additional nonlinear equipment such as surge arresters and varistors are as well taken into account. As it will be also shown later in this thesis, this benchmark system allows the representation of several phenomena, including SSR, SSCI, problems related to low short-circuit ratio (SCR), ferroresonance, and voltage control interaction with synchronous condensers [37].

### **3.3 Benchmark for Low-Frequency Studies involving Wind Farms**

An in-depth literature research in the area of SSO studies involving grid-connected inverters in power systems indicates that the IEEE FBM and SBM proposed in [64] and [75], respectively, have served as well to for studies addressing other technologies other than conventional generating units based on synchronous generators.

It is noted, however, that the IEEE FBM and SBM for SSR studies are of very simple structures and do not account for very detailed representation of power system components other than the considered generating units. This is understandable, since these systems were originally created to address the SSR phenomena for such units. Additionally, these systems were created decades ago in times which the low-frequency dynamics of power systems were mostly influenced by synchronous machine based turbine-generator systems only. It is known that such systems have torsional frequencies limited to the low (and very low) frequency range [52]. In fact, oscillations that involve both electrical system and rotating machines are usually in the range of 0.1 to several Hz only and are well understood. Notably, [80] presented a study on the influence of generator-to-turbine inertia ratio on damping subsynchronous oscillations and provided typical values for the torsional frequencies of conventional power plant units. It was shown that hydro-generators typically have their torsional frequencies in the range of a few Hz up to 24 Hz, whereas turbo generators have a large range, normally providing some torsional frequencies from 5 to 45 Hz.

Under this perspective of conventional generating units, it can be therefore stated that the IEEE FBM and SBM have acceptable assumptions and represent a reasonable compromise between complexity and what is really needed to represent the SSR issue.

When it comes to grid-connected inverters, however, it is known that these devices introduce different dynamics than those of conventional units. The controls of grid-connect inverters act in different bandwidths going up to some kHz [4]. For this reason, detailed EMT studies involving grid-connect inverters require models that are capable of properly representing the dynamics of power systems components at least up to these frequencies.

Additionally, inverter based generating units have also other characteristics if compared to conventional ones. One of them is the fact that, for instance, wind and solar plants consists of several (dozens to hundreds) of single generating units that are interconnected. So, generating units, i.e., the wind or solar parks, have also their own electrical grid. The impact of such grids, usually referred to as collector systems, is not negligible ([81]) and, therefore, should be taken into account in detailed EMT studies.

It is noted that such considerations are existent in recent benchmark systems proposed by the IEEE Task Force on Modeling Subsynchronous Oscillations in Wind Energy Interconnected Systems and presented in [37]. Nevertheless, these systems are intended mostly for EMT simulation studies and not for analytical analyses due to their size.

Having identified the aforementioned needs and aiming at a system that is still capable to be used in analytical studies, a new benchmark system for SSO studies involving wind generation is proposed in this work. As the IEEE FBM, it guards the radial structure, which is known to date to be the most critical one for SSR studies, however considers more detailed power system equipment representation, for instance, with distributed parameter line model, relevant nonlinear equipment (e.g. arresters and transformer saturation characteristics) as well as collector system equivalent.

The proposed system is based on a wind integration project that Hydro-Québec had a few years ago, which was never realized for technical and economic reasons. It assumes, therefore, realistic components and parameters and serves already for testing wind turbines to be connected to series-compensated grid areas of Hydro-Québec.

It consists of a wind farm connected to an equivalent grid through a series-compensated transmission line. The planned system was supposed to accommodate three different wind farms, however just the closest one to the series-capacitor is considered, to reduce complexity. The transmission line is modelled as a distributed parameter line model. A typical wind farm collector system, based

on the findings and data from [81], is considered. A grounding transformer is also included in the collector system. The proposed benchmark system is illustrated in Figure 3.4.

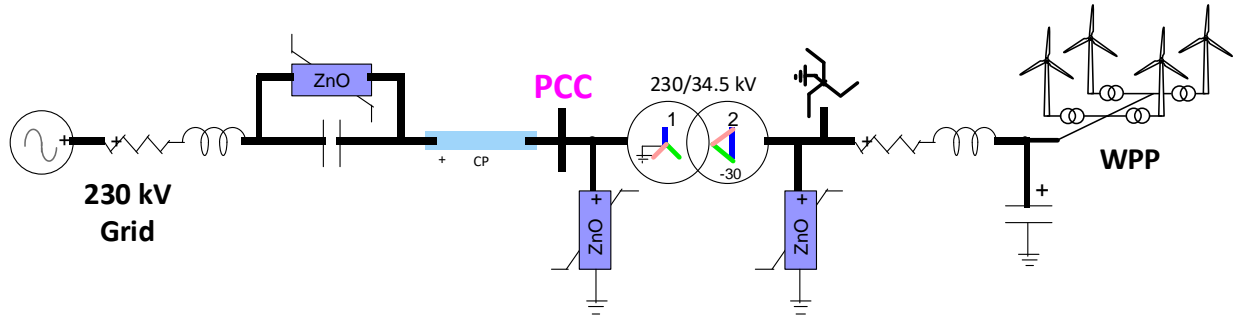


Figure 3.4 Benchmark for studies involving wind farms and series-compensated grids.

The system is designed to accommodate a wind farm of approximately 100 MW. The point of common coupling (PCC) is assumed at the 230 kV side of the substation transformer (indicated in Figure 3.4). The proposed parameters for the benchmark are given in Table 3.1.

Table 3.1 Electrical Parameters of the Proposed Benchmark Grid for SSO Studies

<b>Benchmark grid parameters</b>
Grid equivalent : 230kV, $2 + j25 \Omega$ , 60 Hz
Series compensation : $30 \Omega$ , 1 kA, 2.3pu protection level
Line data : $R1=5.96\Omega$ , $X1=50.9\Omega$ , $B1=324\mu S$ , $R0=2.74 \Omega$ , $X0=120.75 \Omega$ , $B0=220.14\mu S$ , length=100km, continuously transposed
Main transformer data : 230/34.5kV, 115MVA, 11.5%, X/R=45
Grounding transformer: $R0 = 0.28\Omega$ , $X0 = 7.5\Omega$
Collector system data : $R1=0.22\Omega$ , $X1=0.147\Omega$ , $C1=7.17\mu F$
Turbine (lumped) transformer: 34.5/0.575kV, 115MVA, 5.7%, X/R=15.2
Saturation characteristic for transformers [current magnitude (pu), Flux(pu)]: [0.002;1], [0.01;1.075], [0.025;1.15], [0.05;1.2], [0.1;1.23], [2;1.72]

Moreover, the nonlinear characteristics of the varistor connected across the series-capacitor, surge arresters and transformer saturation are considered. Surge arresters are used to limit transient over-voltages following grid events. Varistors are used to protect series-capacitors during transient limiting voltage across terminals between 2.1 and 2.6 pu, depending on the design. In the proposed benchmark, the protection level has been set at 2.3 pu. Varistors also limit the voltage that can be trapped on the line side of series compensation following a grid event. Such trapped voltages could contribute to transformer saturation leading, for instance, to ferroresonance. In reality, varistors

and surge arresters are typically composed of several ZnO (zinc oxide) discs. For the EMT modeling, just one is considered based on fitting. The proposed values for the considered varistor and surge arresters are provided in Table 3.2.

Table 3.2 Electrical Parameters of the Proposed Benchmark Grid for SSO Studies

Series Compensation		230 kV Substation		35 kV Substation	
I(A)	V(kV)	I(A)	V(kV)	I(A)	V(kV)
0.045	76.9	0.03	280.8	0.004	38.4
15	81.5	4	321.4	5	46.9
150	86	300	363.2	200	52
2250	93.6	2000	396.6	2000	57.2
15000	101.5				

### 3.3.1 Impacts of Nonlinear Components in Low-Frequency Phenomena

This subchapter highlights the importance of considering nonlinear equipment in low-frequency studies. It is noted that, for instance, the IEEE FBM and SBM (see subchapters 3.2.1 and 3.2.2, respectively) do not consider any nonlinear component. Moreover, it has also been noted throughout this research that several works aiming at explaining and mitigating SSO phenomena, also in conjunction with grid-connected inverters, often neglect these aspects. It is demonstrated here, however, that the non-consideration of nonlinearities may lead to inaccurate results.

To prove this point, the effects of transformer saturation in low-frequency studies are investigated in the benchmark proposed in previous subsection 3.3. The dynamics of the grid are investigated after a fault at the terminals of the series compensation unit. The exact fault location and the transformer saturation characteristics (based on Table 3.1) are illustrated in Figure 3.5

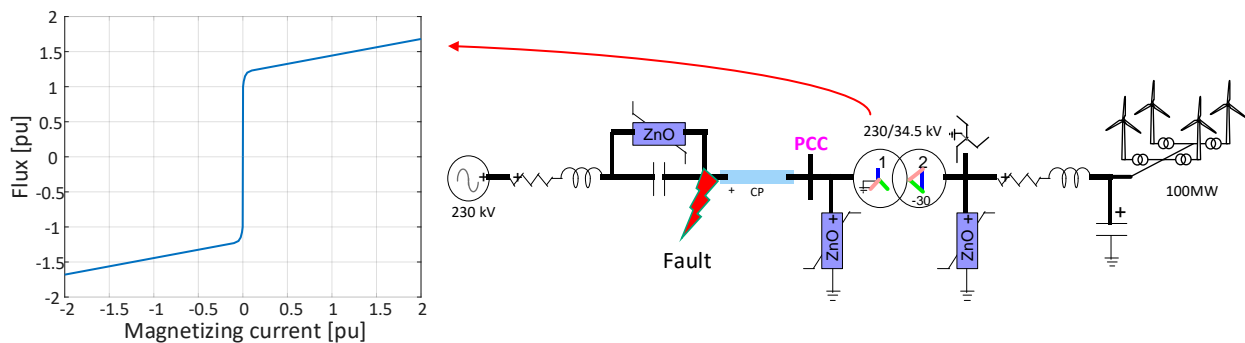


Figure 3.5 Fault location and considered transformer saturation characteristic in EMT.

Three different simulations were performed in EMTP for the subsystem shown in Figure 3.5. The wind farm is based on the type-III wind turbine model introduced in subchapter 2.2 and the same considered in [51].

The first EMTP simulation is done neglecting completely the transformer saturation and the representation of a transformer core, similar to the IEEE FBM. In such case, the transformer model is based only on its short-circuit voltage and its X/R ratio. Then, in a second simulation, a magnetizing branch of the transformer is considered, however a linear one approximated to match the linear part of the transformer saturation characteristic illustrated in Figure 3.5. And, finally, in a third simulation, the saturation characteristic (Table 3.1) is fully considered. During the three different simulations, the voltage across the series capacitor was monitored and a comparison is illustrated for phase  $a$  in Figure 3.6.

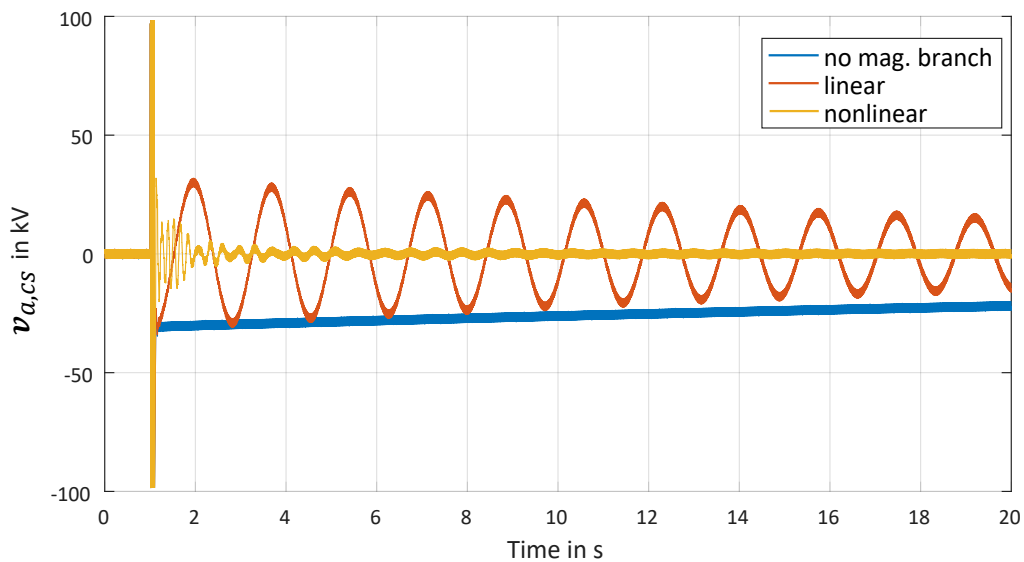


Figure 3.6 Comparison of voltages across the series capacitance for the investigated cases.

It is evident from Figure 3.6 that the consideration or not of the transformer saturation has a significant qualitative impact in the simulation results and these can be explained. First, it is noted that the fault current charges the series capacitor, which remains charged after fault clearance.

In the first case, in which the magnetizing branch is completely neglected, the trapped charges in the series capacitance have almost no path to discharge, since no loads are considered in the benchmark system and discharging happens mostly through the line and components resistances, which are typically very low. This is evident through the small slope of the blue curve Figure 3.6.

In the second case, which considers a linear representation (i.e., more precisely, a high linear inductance in parallel with a high resistance) for the transformer magnetizing branch, oscillations are observed. These oscillations correspond to the natural frequency of the resulting LC circuits. They are mostly dictated by the magnetizing inductance  $L_{mag}$  and the series capacitance  $C_s$  and can be approximatively estimated by

$$f_{res} \approx \frac{1}{2\pi\sqrt{L_{mag}C_s}} \quad (3.3)$$

Applying the benchmark parameters provided in Table 3.1 to equation (3.3) and considering a 50 % line series compensation gives an estimated oscillatory frequency of approximately 0.6 Hz, which matches well the frequency observed for the case of the consideration of a linear inductance to represent the magnetizing core of the transformer, illustrated in red in Figure 3.6.

Moreover, it is also noted that these oscillations damp out slowly. This is due to the fact that, as for the first case, the oscillatory energy can only be discharged through the system resistances, which are very low.

Finally, in the third case, in which the saturation of the magnetizing branch is considered, an interesting effect takes place. As for the second case, an oscillatory behavior is observed during the first milliseconds after fault clearance; however these oscillations are damped out quickly. This phenomenon can be explained by the fact that the inductance of the magnetizing branch now behaves in a nonlinear manner. The trapped voltages across the series capacitances result in dc (or very low-frequency) currents that flow through the magnetizing inductance of the transformer. In the linear case, these currents would require a very long time to build up through the magnetizing inductance, due to its large value, however, once saturation is considered, this happens in a much fast manner. This is due to the fact that the saturation changes the current-flux characteristic of the magnetizing branch and the magnetizing inductance  $L_{mag}$  appears smaller in saturated conditions. As a result, the dc and low-frequency components are capable of building up faster and find a shunt path to

dissipate much faster the trapped charges across the series capacitance. The whole phenomenon takes no more than a few seconds and the system is capable of quickly going back to a steady-state condition as prior to the fault application.

These cases highlight the importance of considering the detailed representation including nonlinearities of components in EMT studies. It is emphasized that neglecting such device characteristics may lead to qualitatively incorrect results. As seen above, even resulting almost sustained low-frequency oscillatory could appear from such simplified considerations, which could lead to misleading interpretation especially in cases of low-frequency studies.

Finally, as it will be seen in Chapter 4, it is noted that in certain cases the consideration of linearized representations is still possible to address low-frequency phenomena. Nevertheless, based on the results presented in this subchapter, it is strongly recommended, if not mandatory, that any results based on the consideration of linear or linearized components only be validated against their corresponding detailed consideration, for instance, in EMT software packages.

### **3.4 Type-IV Wind Farm Behavior in Series-Compensated Grids**

The performance of the proposed type-IV wind turbine system from Chapter 2 is now tested against small perturbations in the proposed benchmark system (see subchapter 3.3). To obtain a wind farm representation, an aggregated model of 50 wind turbines (each of 2 MW) is assumed.

The wind speed was set to the nominal value of the wind turbines (i.e., 11 m/s) so that the wind farm injects 100 MW at the point of common coupling (PCC), which is in accordance with the equipment rating considered in the design of the benchmark system.

The small perturbation is generated with a three-phase high-impedance fault (1.35 k $\Omega$ ) applied at the PCC at time  $t = 1$  s for 100 ms. Such high-impedance fault leads to a voltage drop of around 5% at the PCC, which can still be regarded as a small perturbation. It is noted that such perturbation is not expected to trigger the FRT-response of the wind turbines (set to +/- 10% of the rated voltage) and the turbines should be capable of riding-through this small perturbation in normal operation mode. Different line series compensation levels were tested, varying from 10 to 80% in steps of 10%. It is emphasized, however, that, in reality, compensation levels are usually set in the range

of 30 to 70 %. All results indicated a stable behavior of the type-IV wind farm. In the interest of readability, only the result for the case of 50 % line series compensation is illustrated in Figure 3.7.

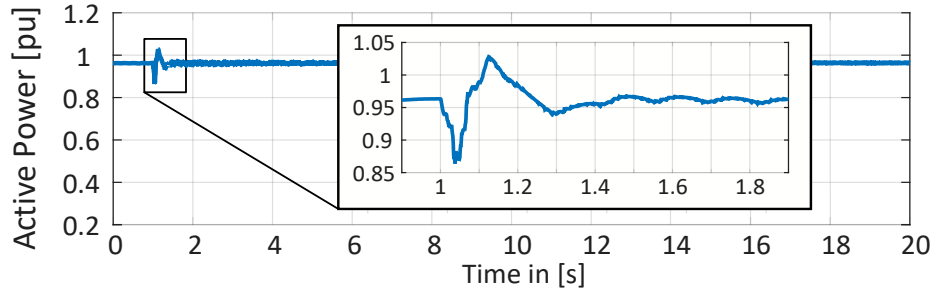


Figure 3.7 Type-IV wind farm: active power at the PCC (base power: 100 MVA).

It is evident from Figure 3.7 that the considered type-IV wind farm is capable of riding-through the perturbation and no instability was triggered. For academic purposes, series compensation levels higher than 80 % were also tested, going up to 300 %. The results are not illustrated here due to the lack of practical relevance, but it has been observed that the type-IV response to the small perturbation did not change qualitatively from the behavior seen in Figure 3.7. Although no general statement is possible for all type-IV converters, these results indicate that stability is not affected by the series compensation for the case of the considered type-IV wind turbine system.

### 3.5 Type-III Wind Farm Behavior in Series-Compensated Grids

Similarly to the analysis applied in subchapter 3.4 to the type-IV wind farm, the performance of a type-III wind farm is now investigated. For this, an aggregated model of 66 wind turbines (each of 1.7 MW) is assumed. The type-III wind turbine model is the same as introduced in subchapter 2.2 and accounts for detailed system representation.

For the sake of comparison, the wind speed has been adjusted so to have the wind farm injecting 100 MW. The wind farm small-signal response is evaluated for the same high-impedance fault (1.35 k $\Omega$ ) as for the type-IV investigations with fault duration of 100 ms.

Several series compensation levels have been tested in conjunction with the type-III wind farm, however it has been observed that the type-III wind farm in question was not capable of withstanding small-signal perturbations in a system with more than 10 % series compensation level. To illustrate it, Figure 3.8 shows the EMTP simulation results for 1, 9 and 10 % series compensation,

respectively, for the active power measured at the PCC. It is emphasized that, in order to guarantee an initial stable steady-state condition in all cases, the series compensation was initialized at a very slow level and was increased slowly. Figure 3.8 illustrate the simulation results after a steady-state condition was achieved.

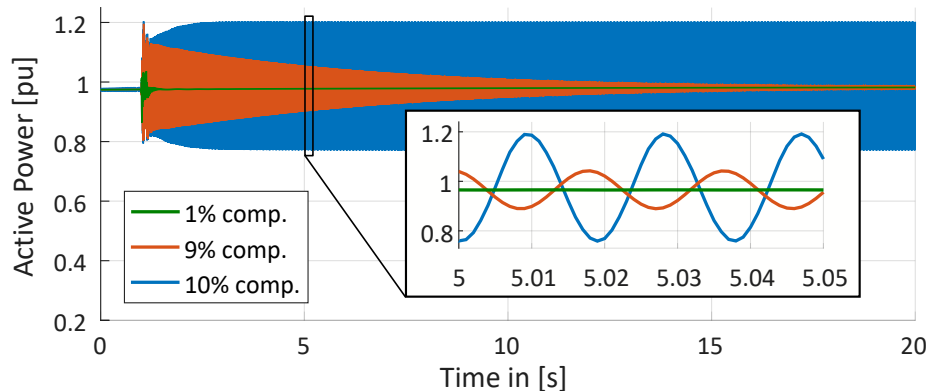


Figure 3.8 Type-III wind farm: active power at the PCC (base power: 100 MVA).

It is evident from Figure 3.8 that, differently than the case of a type-IV wind farm, the type-III wind farm is sensitive to the series compensation. Not only the wind farm became unstable after the small-signal perturbation, but it is also noted that only no practical values of series compensation (i.e., very low values) were possible for a stable operation.

The results of this subchapter and the previous one are in-line with what is expected from the literature, namely, the type-IV wind turbines are apparently less susceptible to interact with series compensation and result in SSO issues, whereas this is not the case for type-III machines [78], [82], [83]. It is emphasized that this is not a general statement, however it is noted that also most of the SSO field events reported in the literature concern type-III wind turbines [19].

The next chapter provides an in-depth analytical assessment of the scenarios investigated for the type-III and type-IV wind turbines based on the application of modal analysis. They provide not only a more profound insight into the issue, but also orientation for possible mitigation.

## CHAPTER 4      MODAL ANALYSIS APPLIED TO GRID-CONNECTED CONVERTERS

This chapter deals with modal analysis of grid-connected converters as means of better understanding and assessing the dynamics of low-frequency phenomena, especially those concerning the type-III and type-IV based wind farm scenarios addressed in earlier chapter. Moreover, differently than in existing literature, detailed representation of grid equipment and wind turbine systems are considered, i.e., not only electrical, but also mechanical and control systems are taken into account. Two methodologies are outlined to address how separately developed analytical systems can be combined to form a complete linearized state-space representation for modal analysis. This is done based on a simplified example of a voltage-source converter. Some results and contributions coming out of this work package were also published in [51], [84].

### 4.1 Review of Modal Analysis Applied to Low-Frequency Phenomena

Modal analysis is one area of the linear control theory that has long been regarded as a powerful technique for addressing power system stability. It has the advantage of providing good insight into systems dynamics through the analysis of eigenvalues and their respective frequencies and damping characteristics. As it will be shown later in this chapter, this is particularly useful for identification of mitigation measures. Nevertheless, the widespread use of modal analysis for power system studies in industrial applications is hindered by its intrinsic requirement for rigorously developed analytical system equations, which is not always possible. For instance, as already stated in subchapter 2.3 as a motivation for the development of the generic type-IV wind turbine in this thesis, interconnection studies are usually carried out with protected (i.e., black-box) models due to confidentiality issues.

In cases where the rigorous analytical development of a system of equation is possible, however, a broad range of powerful mathematical tools can be used. Sensitivity analysis to changes in system parameters and control gains, calculation of participation factors, application of robust control theory to assess stability margins, are all examples of techniques that can be applied to the resulting system, which still justify in certain cases the effort-intensive way to obtain an analytical representation for the system under study.

Due to the aforementioned wide range of powerful tools, it is understandable that, although resource-intensive, modal analysis has found large deployment for power system stability and low-frequency interaction studies. Already in 1976, Nolan et al. ([85]) proposed the combined use of eigenvalue and sensitivity analysis to address network stability and turbine-generator shaft dynamic issues. In the same year, Dandeno and Kundur ([86]) proposed a computer program for small signal dynamic stability characteristics of power systems. In 1978, Fouad et al. applied eigenvalue analysis to assess both IGE and SSTI in studies based on the IEEE FBM and proposed damping mitigations [87], [88].

Successful application of modal analysis has as well been reported as a fundamental tool for the development and analysis of power electronics and FACTS controllers with different applications. For instance, eigenvalue analysis appears in [89] and in [90] to address the use of imbalanced series compensation and TCSC control schemes to mitigate SSR, respectively. Also, in [74] eigenvalue theory is used to base development of a damping control for a SSSC system.

Jovcic et. al developed in [91] an analytical model for a HVDC-HVAC system, already including PLL dynamics. This analytical representation was then used for stability analysis of control loops in [92] and small-signal analysis of interactions of HVDC systems in weak ac grids in [93]. More recently, a similar work was conducted by Saad et. al in [94] for an MMC-HVDC system.

The use of modal analysis is not less important when it comes to integration and stability assessment of wind farms in power systems. Ostadi et al. developed in [95] an analytical representation for a type-III wind turbine in a series-compensated grid to investigate low-frequency issues. Similar work was conducted by Fan et al. in [72] and also by Varma et al. in [96]. The later outlines an interesting result towards the consideration of different operating conditions: a test case is shown for which a 200 MW wind farm injecting rated power is stable, however unstable behavior is observed for a 500 MW wind farm injecting the same 200 MW into the same system. Also, mitigation based on modal analysis has been proposed both for the type-III system, for instance, in [97] with focus on type-III machine controllers and in [98] with focus on coordinated use of gate-controller series capacitor (GCSC) controller capabilities.

Type-IV wind turbine systems were as well subject of modal analysis investigations. Huang et al. developed in [99] a small-signal representation for a direct-drive permanent magnet synchronous

machine based system and applied participation factor analysis to reveal origins of system modes. In [100], Strachan et al. used eigenvalue analysis to investigate stability issues in similar type-IV wind turbines when connected to weak ac grids. And, recently, modal analysis was also applied to assess SSR in type-IV systems when connected to series-compensated grids in [78].

Therefore, due to the importance of modal analysis in the field of power system stability, its theory and application is applied and investigated in this thesis with focus on the type-III and type-IV wind farm scenarios introduced in Chapter 3. However, due to the amount and complexity of equations and their linearization required for the development of a complete state-space representation of these systems, the methodology used in this work is first outlined for a simpler system before being applied to the aforementioned scenarios.

## 4.2 Modal Analysis of a Simple VSC System

To better outline the approach applied in this thesis to obtain an analytical linearized state-space form representation for modal analysis, a simplified grid-connected inverter is investigated. It consists of a two-level VSC connected to a Thevenin circuit equivalent of a grid. The VSC system is assumed to be supplied by an ideal dc voltage source, and outer loops are neglected. In the interest of simplicity, its controls are limited to the synchronization controller and current regulator. The considered system is illustrated in Figure 4.1.

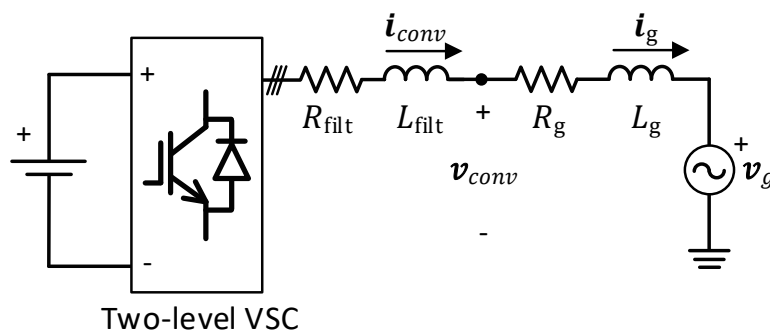


Figure 4.1 Simple VSC system used in investigation studies.

A  $dq$ -vector current control is proposed for the system above. It consists basically of PI-controllers with feedforward, whose aim is to reduce the error between the reference currents  $i_{d\_ref}$  and  $i_{q\_ref}$  and the measured output converter currents  $i_{conv}$  in the  $dq$ -frame,  $i_{d\_meas}$  and  $i_{q\_meas}$ , respectively.

For the sake of simplicity, the dynamics of measurement sensor is neglected. The current control scheme is illustrated in Figure 4.2.

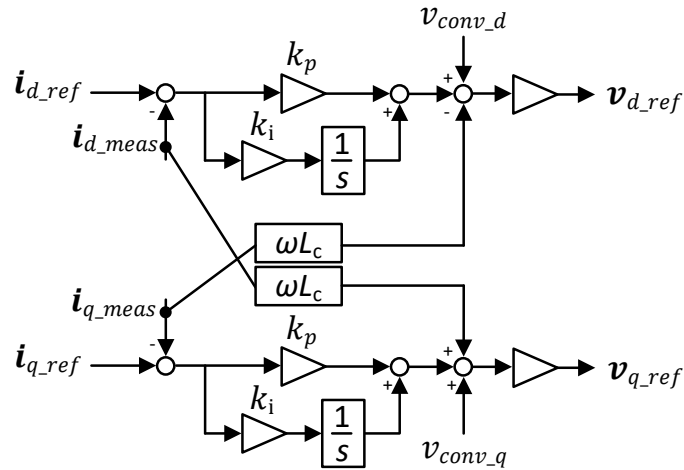


Figure 4.2 Current regulator schematic diagram in  $dq$ -frame.

The applied  $dq$ -vector current control requires the measured output converter currents  $i_{conv}$  to be transformed into the  $dq$ -frame. This requires a synchronization unit that is capable of extracting a reference angle from the measured voltages at the VSC terminals  $v_{conv}$ . This is typically done by a so-called phase-locked-loop (PLL) unit. There are different PLL variants, however a synchronous rotating frame PLL (SRF-PLL) is assumed. It basically tracks the system phase by using a PI-controller to eliminate the  $q$ -component of the measured  $abc$ -voltage. The applied PLL control scheme is illustrated in Figure 4.3.

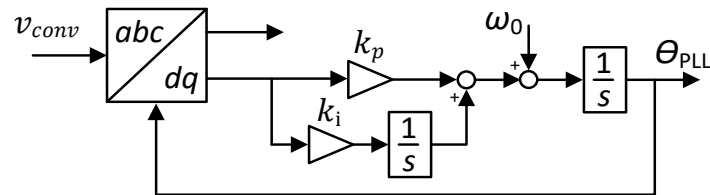


Figure 4.3 Synchronous rotating frame PLL control scheme.

It is noted that the reference angle extracted by the PLL is used twice in the simplified VSC system outlined above. First, it is applied to transform the measured converter currents  $i_{conv}$  into its  $dq$ -components  $i_{d\_meas}$  and  $i_{q\_meas}$ , respectively. Second, it transforms the reference voltages  $v_{d\_ref}$

and  $v_{q\_ref}$  coming out of the current controller into their  $abc$ -equivalents that are then sent as reference voltages to the PWM gating control of the VSC system. Although a transport time-delay is considered between the outputs of the current regulator and the inputs of the VSC system, it is assumed that the PWM gating control and the VSC system itself are ideal.

The design of the VSC hardware and control system depicted in Figure 4.1 is made following considerations outlined in [38]. Its rated power is 1 MVA and a phase-to-phase voltage of 690 V is assumed at the PCC. The VSC hardware and control parameters are provided in Table 4.1.

Table 4.1 Electrical and Control Parameters of simple VSC system.

Parameters	Value	Description
$v_{rated}$	690 V	Rated voltage (phase-to-phase)
$f_{rated}$	60 Hz	Rated frequency
$S_{rated}$	1 MVA	Rated apparent power
$R_{filt}$	4.761 m $\Omega$	Output filter resistance
$L_{filt}$	416 $\mu$ H	Output filter inductance
$k_{p\_PLL}$	163.254	PLL proportional gain
$k_{i\_PLL}$	30767 1/s	PLL integral gain
$k_{p\_CC}$	0.9	Current controller proportional gain
$k_{i\_CC}$	12 1/s	Current controller integral gain

The grid is represented by its short-circuit level and X/R ratio resulting in a simple Thevenin RL-circuit representation. Its parameters are given in Table 4.2.

Table 4.2 Thevenin grid parameters.

Parameters	Value	Description
$v_g$	690 V	Rated voltage (phase-to-phase)
$f_{rated}$	60 Hz	Rated frequency
X/R	5	X/R ratio seen at the PCC
$S_{SC}$	10 MVA	Grid short-circuit power

A complete system representation of the VSC system above is required for modal analysis. One possible dynamic system representation can be generally given as

$$\begin{cases} \dot{x}_i = f_i(x_i, u_i) \\ y_i = g_i(x_i, u_i) \end{cases} \quad (4.1)$$

where  $x_i$ ,  $u_i$  and  $y_i$  denote the vectors of states, inputs and outputs for the  $i$ -th component, respectively.

Such representation as given in equation (4.1) is capable of accounting for both linear and nonlinear functions. It is noted at this point that the simple VSC system introduced above falls in the latter category, due to the nonlinearities introduced by the the  $dq$ -transformations existent in the PLL and current regulator.

To conduct modal analysis, a linear representation of the system of equations in (4.1) is required. For this, linearization is applied by means of a Taylor series truncated at the first term. By doing so, it is assumed that a function can be approximated at a given operating point by

$$f(x) \approx f(a) + \frac{df(a)}{dx}(x - a) \quad (4.2)$$

where  $f(x)$  denotes any differentiable function and  $a$  the point where the function is evaluated.

The linearization suggested by equation (4.2) is only valid for the small region around the point  $a$  for which the function  $f(x)$  is evaluated. Moreover, generally only the variation of the function  $f(x)$  as a result of a small perturbation of  $x$  around the operating point  $a$  is of interest. For this reason, the formulation found in (4.2) is often replaced by

$$\Delta f(x) \approx \frac{df(a)}{dx} \Delta x \quad (4.3)$$

where  $\Delta f(x)$  and  $\Delta x$  denotes a small variation of  $f(x)$  and  $x$ , respectively.

The formulation shown in (4.3) is the base for the small-signal analysis. Its application on the formulation shown in equation (4.1) results in a linearized system representation to which tools of the linear control theory can be applied to. In other words, the system in (4.1) can be linearized by a Taylor series with truncation in the first term to provide a multivariable linear system as in

$$\begin{cases} \Delta \dot{x} = \mathbf{A} \Delta x + \mathbf{B} \Delta u \\ \Delta y = \mathbf{C} \Delta x + \mathbf{D} \Delta u \end{cases} \quad (4.4)$$

where  $\mathbf{A}$ ,  $\mathbf{B}$ ,  $\mathbf{C}$  and  $\mathbf{D}$  are real-valued time-invariant matrices.

The system representation based on (4.4) is a linearized small-signal representation of (4.1) for a chosen operating point  $a$ . Although (4.4) has a limited validity region around  $a$ , it has the advantage of being a linear representation of the complete system. Thus, well-known tools from the linear control theory can be applied.

It is emphasized at this point that nonlinear techniques could also be applied to allow for the direct use of the formulations given in equation (4.1), and also to avoid the steps required to obtain a linearized state-space for representation for small-signal analysis as given in (4.4). However, it is noted that linear analysis is often preferred due to the broader range of available techniques whose results are easier to grasp if compared to nonlinear ones. For instance, identifying root causes of oscillations is much simplified when based on the application of classic linear control techniques.

There exist different methods for obtaining a complete system representation based on the connection of several dynamic systems as given by (4.4). The advantage of such techniques consists of allowing the development of a system of equations for smaller subsystems separately. As a result, each subsystem can be analytically developed and validated separately, which reduce the chances of incorrect analytical formulations in the complete system. For instance, in the case of the VSC outlined above, such techniques allow for the development of a subsystem containing only the PLL. Only after having developed, linearized and validated the small-signal formulation of the PLL the subsystem is then connected to the rest of the system. In the next subchapters, the analytical equations for the simple VSC system are developed. Then, two of such techniques to connect separate subsystems to obtain a complete state-space representation, which have been used in the framework of this thesis, are outlined in the next subchapters.

#### **4.2.1 Obtaining a Linear Time-Invariant Representation for Equations**

In order to apply the modal analysis, a complete linearized time-invariant representation is required. The studied simple VSC system is three-phase ac and, under ideal steady-state conditions, the system states are expected to oscillate at the system rated frequency. Therefore, additional mathematical manipulations are required on the equations in order for them to respect the requirements of the small-signal modal analysis.

To obtain constant values for the system states in steady-state, the VSC system equations are transformed into the  $dq$ -frame. All details to the applied  $dq$ -transformation in this thesis are provided in Appendix B. By choosing the rotational speed of the  $dq$ -transformation to be equal the system frequency, the system states can be calculated as constants in steady-state. This allows then the application of the linearization and of the small-signal theory. This is done in the next subsections for each of the VSC subsystems.

## 4.2.2 RL-Grid

One subsystem of the complete system depicted in Figure 4.1 is the three-phase RL-grid corresponding to a system Thevenin representation of a more complex system. It is noted that the state variables of an RL-circuit correspond to the currents through the inductance. Typically, voltages are assumed as inputs to such systems (see example in Appendix B).

In the case of the simple VSC circuit, it is emphasized that the output currents of the VSC are controlled and, therefore, the VSC can be seen behaving similarly to current sources. Thus, it is expected that the interface of the VSC and the RL-grid is done through currents and not voltages.

For this reason, a small modification is proposed in the RL-grid circuit to allow the converter currents  $i_{conv}$  (see Figure 4.1) to be system inputs and not states of the RL-grid system. More specifically, a shunt resistance with a high value is considered at the PCC (as part of the grid). Such resistance, whose magnitude is assumed equal to 1 M $\Omega$ , is not expected to impact qualitatively the results. Its consideration in the RL-circuit is illustrated in Figure 4.4.

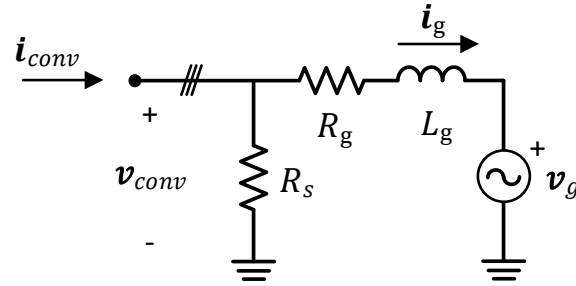


Figure 4.4 Thevenin grid equivalent with consideration of a shunt resistance.

In the  $abc$ -frame, it can be written for one single phase that

$$v_{conv} = (i_{conv} - i_g)R_s = R_g i_g + L_g \frac{di_g}{dt} + v_g \quad (4.5)$$

Considering equation (4.5) for the three-phase system and transforming it into the  $dq$ -frame (see Appendix B) gives

$$\begin{cases} (i_{d,conv} - i_{d,g})R_s = R_g i_{d,g} + L_g \frac{di_{d,g}}{dt} - \omega_0 L_g i_{q,g} + v_{d,g} \\ (i_{q,conv} - i_{q,g})R_s = R_g i_{q,g} + L_g \frac{di_{q,g}}{dt} + \omega_0 L_g i_{d,g} + v_{q,g} \end{cases} \quad (4.6)$$

Solving the equation (4.6) to the derivative terms gives

$$\begin{cases} \frac{di_{d,g}}{dt} = -\frac{(R_g + R_s)}{L_g} i_{d,g} + \omega_0 i_{q,g} + \frac{R_s}{L_g} i_{d,conv} - \frac{1}{L_g} v_{d,g} \\ \frac{di_{q,g}}{dt} = -\frac{(R_g + R_s)}{L_g} i_{q,g} - \omega_0 i_{d,g} + \frac{R_s}{L_g} i_{q,conv} - \frac{1}{L_g} v_{q,g} \end{cases} \quad (4.7)$$

Equation (4.7) can be written in matrix form to obtain a standard state-space representation as in

$$\begin{aligned} \begin{bmatrix} \frac{di_{d,g}}{dt} \\ \frac{di_{q,g}}{dt} \end{bmatrix} &= \begin{bmatrix} -\frac{(R_g + R_s)}{L_g} & \omega_0 \\ -\omega_0 & -\frac{(R_g + R_s)}{L_g} \end{bmatrix} \begin{bmatrix} i_{d,g} \\ i_{q,g} \end{bmatrix} \\ &+ \begin{bmatrix} \frac{R_s}{L_g} & 0 & -\frac{1}{L_g} & 0 \\ 0 & \frac{R_s}{L_g} & 0 & -\frac{1}{L_g} \end{bmatrix} \begin{bmatrix} i_{d,conv} \\ i_{q,conv} \\ v_{d,g} \\ v_{q,g} \end{bmatrix} \end{aligned} \quad (4.8)$$

Additionally, the  $dq$ -voltages over the shunt resistance  $R_s$  are assumed as subsystem outputs. As such, the subsystem output equations can be derived from (4.5) in state-space form as in

$$\begin{bmatrix} v_{d,conv} \\ v_{q,conv} \end{bmatrix} = \begin{bmatrix} -R_s & 0 \\ 0 & -R_s \end{bmatrix} \begin{bmatrix} i_{d,g} \\ i_{q,g} \end{bmatrix} + \begin{bmatrix} R_s & 0 & 0 & 0 \\ 0 & R_s & 0 & 0 \end{bmatrix} \begin{bmatrix} i_{d,conv} \\ i_{q,conv} \\ v_{g,d} \\ v_{g,q} \end{bmatrix} \quad (4.9)$$

### 4.2.3 Phase-locked-loop (PLL)

As indicated earlier in this chapter, the considered synchronous rotating frame PLL is of nonlinear nature due to the  $abc$ -to- $dq$ -transformation applied. Thus, a linearized representation of the PLL is required for its state-space development. Moreover, it is also noted that the PLL as given in Figure 4.3 has the measured voltages as inputs, however in the  $abc$ -frame. For modal analysis, inputs and outputs need to be in  $dq$ -frame in order to obtain an LTI system representation.

For this, the PLL is further interpreted as an interface between two different  $dq$ -reference frames [101]. The first is the one where the measured grid voltages are and is henceforth referred to as the global reference frame. The other is what is called the internal  $dq$ -reference of the VSC itself, where

the controls are done. Following this idea, it is possible to redraw the PLL representation in Figure 4.3 completely with  $dq$ -variables as in Figure 4.5.

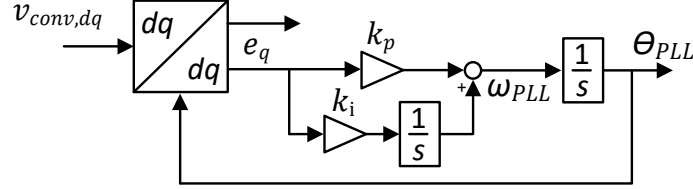


Figure 4.5 PLL in  $dq$ -frame.

It is noted that, differently than for the PLL structure illustrated earlier in Figure 4.3, the voltage angle used for synchronization,  $\theta_{PLL}$ , is constant in steady-state since the integration of the system rated rotational frequency  $\omega_0$  is not required in the  $dq$ -frame. The  $dq$ -to- $dq$  transformation in Figure 4.5 is a frame rotation also known from the field of electrical machines [102]. The derivation of the transformation matrix is provided in Appendix C. It is conveniently repeated here as its linearization is required next.

$$\begin{bmatrix} \cos(\theta_y - \theta_x) & \sin(\theta_y - \theta_x) \\ -\sin(\theta_y - \theta_x) & \cos(\theta_y - \theta_x) \end{bmatrix} = \begin{bmatrix} \cos(\theta_{PLL}) & \sin(\theta_{PLL}) \\ -\sin(\theta_{PLL}) & \cos(\theta_{PLL}) \end{bmatrix} \quad (4.10)$$

It is evident from equation (4.10) that  $\theta_{PLL}$  should be understood as an angle difference between the global reference frame and the VSC internal frame. For instance, any phase shifts occurring at system level and captured by the measured voltages  $v_{dq,conv}$  are passed internally to the VSC through the dynamics of the PLL PI-controller. Due to its development in the  $dq$ -frame, equation (4.10) has constant terms in steady-state ( $\theta_{PLL}$  is constant), however is not yet linear time-invariant, as required for small-signal analysis.

Therefore, the PLL has to be linearized for a given steady-state operating condition  $\theta_{PLL}^0$ . By considering such operating condition, denoted by superscript 0, the PLL controller equations can be developed and linearized. From Figure 4.5, it is straightforward to derive for small-signals perturbations that

$$\theta_{PLL} = \int \omega_{PLL} \rightarrow \frac{d\theta_{PLL}}{dt} = \omega_{PLL} \rightarrow \frac{d\Delta\theta_{PLL}}{dt} = \Delta\omega_{PLL} \quad (4.11)$$

Moreover, by defining

$$\gamma_q = \int e_q \rightarrow \frac{d\gamma_q}{dt} = e_q \rightarrow \frac{d\Delta\gamma_q}{dt} = \Delta e_q \quad (4.12)$$

it is also possible to write from Figure 4.5 that

$$\Delta\omega_{PLL} = k_p\Delta e_q + k_i\Delta\gamma_q \quad (4.13)$$

Equations (4.11), together with (4.13), and (4.12) form the set of state-space equations required to represent the linearized PLL. Variable  $e_q$  represented the input error of the PI-controller and is given in per unit by

$$e_q = -\sin\theta_{PLL} \frac{v_{d,conv}}{v_{base}} + \cos\theta_{PLL} \frac{v_{q,conv}}{v_{base}} \quad (4.14)$$

where  $v_{base}$  is the amplitude of the phase-to-ground base voltage.

Equation (4.14) is clearly nonlinear. Linearizing it for a steady-state operating point gives

$$\begin{aligned} \Delta e_q &= \left[ -\cos\theta_{PLL}^0 \frac{v_{d,conv}^0}{v_{base}} - \sin\theta_{PLL}^0 \frac{v_{q,conv}^0}{v_{base}} \right] \Delta\theta_{PLL} - \frac{\sin\theta_{PLL}^0}{v_{base}} \Delta v_{d,conv} + \frac{\cos\theta_{PLL}^0}{v_{base}} \Delta v_{q,conv} \\ &= K_\theta \Delta\theta_{PLL} + K_{vd} \Delta v_{d,conv} + K_{vq} \Delta v_{q,conv} \end{aligned} \quad (4.15)$$

where  $K_\theta$ ,  $K_{vd}$  and  $K_{vq}$  are constants defined to simplify equation (4.15). Then, substituting equation (4.15) in (4.13) gives

$$\Delta\omega_{PLL} = k_p K_\theta \Delta\theta_{PLL} + k_p K_{vd} \Delta v_{d,conv} + k_p K_{vq} \Delta v_{q,conv} + k_i \Delta\gamma_q \quad (4.16)$$

By replacing equation (4.16) in (4.11) it is possible to write a state-space representation for the linearized PLL as

$$\begin{bmatrix} \frac{d\Delta\theta_{PLL}}{dt} \\ \frac{d\Delta\gamma_q}{dt} \end{bmatrix} = \begin{bmatrix} K_p K_\theta & K_i \\ K_\theta & 0 \end{bmatrix} \begin{bmatrix} \Delta\theta_{PLL} \\ \Delta\gamma_q \end{bmatrix} + \begin{bmatrix} K_p K_{vd} & K_p K_{vq} \\ K_{vd} & K_{vq} \end{bmatrix} \begin{bmatrix} \Delta v_{d,conv} \\ \Delta v_{q,conv} \end{bmatrix} \quad (4.17)$$

and, finally, by defining the small-signal variations of the PLL angle  $\Delta\theta_{PLL}$  as system outputs, it is possible to writing following output equation for the state-space representation of the PLL

$$[\Delta\theta_{PLL}] = [1 \quad 0] \begin{bmatrix} \Delta\theta_{PLL} \\ \Delta\gamma_q \end{bmatrix} + [0 \quad 0] \begin{bmatrix} \Delta v_{d,conv} \\ \Delta v_{q,conv} \end{bmatrix} \quad (4.18)$$

Equations (4.17) and (4.18) form together the linearized state-space representation of a synchronous rotating frame PLL in  $dq$ -frame.

#### 4.2.4 VSC Output Filter

The output filter of the VSC system is also considered as a separate subsystem for the analytical equation development. It is represented simply by an RL-circuit whose inputs are the VSC voltages  $v_{dq,VSC}$  and the voltages at the terminals of the VSC system  $v_{dq,conv}$ . The circuit is illustrated in Figure 4.6.

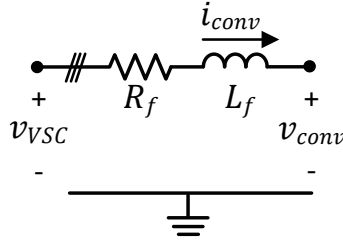


Figure 4.6 VSC output filter.

It is straightforward to demonstrate that the circuit shown in Figure 4.6 can be analytically developed to have a state-space representation as shown in

$$\begin{bmatrix} \frac{di_{d,conv}}{dt} \\ \frac{di_{q,conv}}{dt} \end{bmatrix} = \begin{bmatrix} -\frac{R_f}{L_f} & \omega_0 \\ -\omega_0 & -\frac{R_f}{L_f} \end{bmatrix} \begin{bmatrix} i_{d,conv} \\ i_{q,conv} \end{bmatrix} + \begin{bmatrix} \frac{1}{L_f} & 0 & -\frac{1}{L_f} & 0 \\ 0 & \frac{1}{L_f} & 0 & -\frac{1}{L_f} \end{bmatrix} \begin{bmatrix} v_{d,VSC} \\ v_{q,VSC} \\ v_{d,conv} \\ v_{q,conv} \end{bmatrix} \quad (4.19)$$

And, finally, by defining the converter currents  $i_{dq,conv}$  as system outputs, the output equation can be written as

$$\begin{bmatrix} i_{d,conv} \\ i_{q,conv} \end{bmatrix} = \begin{bmatrix} 1 & 0 \\ 0 & 1 \end{bmatrix} \begin{bmatrix} i_{conv,d} \\ i_{conv,q} \end{bmatrix} + \begin{bmatrix} 0 & 0 & 0 & 0 \\ 0 & 0 & 0 & 0 \end{bmatrix} \begin{bmatrix} v_{VSC,d} \\ v_{VSC,q} \\ v_{d,conv} \\ v_{q,conv} \end{bmatrix} \quad (4.20)$$

### 4.2.5 Current Controller

The current controller depicted in Figure 4.2 is of linear nature and, as such, does not required linearization. Following its control structure, it is straightforward to demonstrate that the outputs of the applied PI-controllers, here referred to as  $i_{d,PI}$  and  $i_{q,PI}$ , are given by

$$\begin{cases} i_{d,PI} = k_p(i_{d,ref} - i_{d,meas}) + k_i \int (i_{d,ref} - i_{d,meas}) \\ i_{q,PI} = k_p(i_{q,ref} - i_{q,meas}) + k_i \int (i_{q,ref} - i_{q,meas}) \end{cases} \quad (4.21)$$

Following definitions are introduced for the development of the state-space representation

$$\begin{aligned} \gamma_{d,ref} &= \int i_{d,ref} \rightarrow \frac{d\gamma_{d,ref}}{dt} = i_{d,ref} \\ \gamma_{q,ref} &= \int i_{q,ref} \rightarrow \frac{d\gamma_{q,ref}}{dt} = i_{q,ref} \\ \gamma_{d,meas} &= \int i_{d,meas} \rightarrow \frac{d\gamma_{d,meas}}{dt} = i_{d,meas} \\ \gamma_{q,meas} &= \int i_{q,meas} \rightarrow \frac{d\gamma_{q,meas}}{dt} = i_{q,meas} \end{aligned} \quad (4.22)$$

By considering the variables introduced in (4.22), the states of the current controller subsystem have been defined. As such, it is now possible to write its state-space representation as

$$\begin{bmatrix} \frac{d\gamma_{d,ref}}{dt} \\ \frac{d\gamma_{d,meas}}{dt} \\ \frac{d\gamma_{q,ref}}{dt} \\ \frac{d\gamma_{q,meas}}{dt} \end{bmatrix} = \begin{bmatrix} 0 & 0 & 0 & 0 \\ 0 & 0 & 0 & 0 \\ 0 & 0 & 0 & 0 \\ 0 & 0 & 0 & 0 \end{bmatrix} \begin{bmatrix} \gamma_{d,ref} \\ \gamma_{d,meas} \\ \gamma_{q,ref} \\ \gamma_{q,meas} \end{bmatrix} + \begin{bmatrix} 1 & 0 & 0 & 0 & 0 & 0 \\ 0 & 0 & 1 & 0 & 0 & 0 \\ 0 & 1 & 0 & 0 & 0 & 0 \\ 0 & 0 & 0 & 1 & 0 & 0 \end{bmatrix} \begin{bmatrix} i_{d,ref} \\ i_{q,ref} \\ i_{d,meas} \\ i_{q,meas} \\ v_{d,meas} \\ v_{q,meas} \end{bmatrix} \quad (4.23)$$

Moreover, using (4.22), it is possible to rewrite (4.21) as function of the system states as in

$$\begin{cases} i_{d,PI} = k_p(i_{d,ref} - i_{d,meas}) + k_i(\gamma_{d,ref} - \gamma_{d,meas}) \\ i_{q,PI} = k_p(i_{q,ref} - i_{q,meas}) + k_i(\gamma_{q,ref} - \gamma_{q,meas}) \end{cases} \quad (4.24)$$

It is evident from Figure 4.2 that the  $dq$ -voltage reference values  $v_{dq,ref\_cc}$  for the VSC are the system outputs of the current controller. Using (4.24), the output equations can be given as

$$\begin{cases} v_{d,ref\_cc} = k_p(i_{d,ref} - i_{d,meas}) + k_i(\gamma_{d,ref} - \gamma_{d,meas}) + v_{d,meas} - X_{f,pu}i_{q,meas} \\ v_{q,ref\_cc} = k_p(i_{q,ref} - i_{q,meas}) + k_i(\gamma_{q,ref} - \gamma_{q,meas}) + v_{q,meas} + X_{f,pu}i_{d,meas} \end{cases} \quad (4.25)$$

where  $X_{f,pu}$  is the output filter reactance in per unit.

Finally, equation (4.25) can be written in matrix form to conclude the state-space development for the current controller as given in

$$\begin{aligned} \begin{bmatrix} v_{d,ref\_cc} \\ v_{q,ref\_cc} \end{bmatrix} &= \begin{bmatrix} k_i & 0 & -k_i & 0 \\ 0 & k_i & 0 & -k_i \end{bmatrix} \begin{bmatrix} \gamma_{d,ref} \\ \gamma_{d,meas} \\ \gamma_{q,ref} \\ \gamma_{q,meas} \end{bmatrix} \\ &+ \begin{bmatrix} k_p & 0 & -k_p & -X_{f,pu} & 1 & 0 \\ 0 & k_p & X_{f,pu} & -k_p & 0 & 1 \end{bmatrix} \begin{bmatrix} i_{d,ref} \\ i_{q,ref} \\ i_{d,meas} \\ i_{q,meas} \\ v_{d,meas} \\ v_{q,meas} \end{bmatrix} \end{aligned} \quad (4.26)$$

#### 4.2.6 Transport Time-Delay

A transport time-delay is considered between the output of the current regulator and input of the VSC system. The delay is assumed as large as the numerical integration time-step  $T_s$ .

For its consideration, the time delay must first be approximated as a rational transfer function. A second order Padé approximation is considered here and is given as

$$H_{delay}(s) = \frac{s^2 - \frac{6}{T_s}s + \frac{12}{T_s^2}}{s^2 + \frac{6}{T_s}s + \frac{12}{T_s^2}} \quad (4.27)$$

The transfer function in (4.27) can be also represented in state-space form. For this, a controllable canonical form is assumed, which results in the  $A$ ,  $B$ ,  $C$  and  $D$  matrices given by

$$A = \begin{bmatrix} 0 & 1 \\ -\frac{12}{T_s^2} & -\frac{6}{T_s} \end{bmatrix}; B = \begin{bmatrix} 0 \\ 1 \end{bmatrix}; C = \begin{bmatrix} 0 & -\frac{12}{T_s} \end{bmatrix}; D = [1] \quad (4.28)$$

Using the second order Padé approximation given in (4.28) and assuming that a time-delay exists in both  $dq$ -channels of  $v_{dq,ref\_cc}$ , the state-space representation of the time-delay in the VSC system can be given as

$$\begin{bmatrix} \frac{dY_{d,delay}}{dt} \\ \frac{d\xi_{d,delay}}{dt} \\ \frac{dY_{q,delay}}{dt} \\ \frac{d\xi_{q,delay}}{dt} \end{bmatrix} = \begin{bmatrix} 0 & 1 & 0 & 0 \\ \frac{-12}{T_s^2} & \frac{-6}{T_s} & 0 & 0 \\ 0 & 0 & 0 & 1 \\ 0 & 0 & \frac{-12}{T_s^2} & \frac{-6}{T_s} \end{bmatrix} \begin{bmatrix} Y_{d,delay} \\ \xi_{d,delay} \\ Y_{q,delay} \\ \xi_{q,delay} \end{bmatrix} + \begin{bmatrix} 0 & 0 \\ 1 & 0 \\ 0 & 0 \\ 0 & 1 \end{bmatrix} \begin{bmatrix} v_{d,ref\_cc} \\ v_{q,ref\_cc} \end{bmatrix} \quad (4.29)$$

where  $Y_{dq,delay}$  are generic names given to system states. The output equation is given as

$$\begin{bmatrix} v_{d,ref} \\ v_{q,ref} \end{bmatrix} = \begin{bmatrix} 0 & \frac{-12}{T_s} & 0 & 0 \\ 0 & 0 & 0 & \frac{-12}{T_s} \end{bmatrix} \begin{bmatrix} Y_{d,delay} \\ \xi_{d,delay} \\ Y_{q,delay} \\ \xi_{q,delay} \end{bmatrix} + \begin{bmatrix} 1 & 0 \\ 0 & 1 \end{bmatrix} \begin{bmatrix} v_{d,ref\_cc} \\ v_{q,ref\_cc} \end{bmatrix} \quad (4.30)$$

It is finally noted here that any other time-delay value can be considered in equations (4.29) and (4.30) by just replacing  $T_s$  by the corresponding new time-delay value.

#### 4.2.7 Current Measurement and Frame Rotation

The current controller of the simple VSC system, which is depicted in Figure 4.2, requires the measured currents through the output filter in the  $dq$ -frame. This subsystem is illustrated in Figure 4.7 and indicates the current sensors as dynamic systems with characteristic  $H(s)$  at each phase and the  $dq$ -transformation based on the PLL angle  $\theta_{PLL}$ .

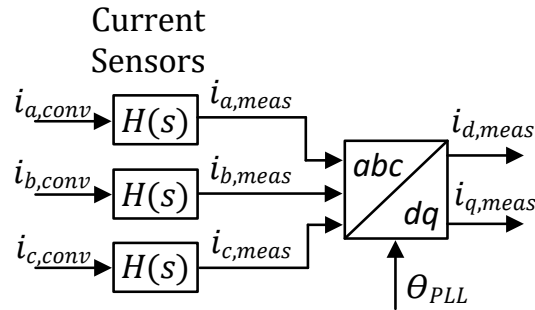


Figure 4.7 Current measurements and  $dq$ -transformation.

For simplicity, the dynamics of the current sensors are neglected. Since the measured currents are required in per unit values,  $H(s)$  can be considered as a gain as given in

$$H(s) = \frac{1}{i_{base}} \quad (4.31)$$

Since for the small-signal development the equations need to be written in the  $dq$ -frame in order to allow for an LTI system representation, the  $dq$ -transformation of Figure 4.7 is replaced by a  $dq$ -rotation transformation that converts the output filter currents  $i_{dq,conv}$  from the global reference frame to the internal VSC reference frame defined by the PLL angle  $\theta_{PLL}$ . This is illustrated in Figure 4.8.

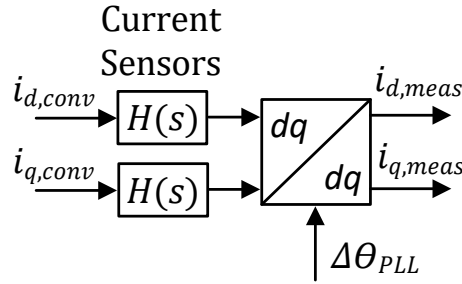


Figure 4.8 Current measurement subsystem in  $dq$ -frame.

From Figure 4.8 it is evident that, besides the per unit scaling, the current measurement subsystem is nothing else than a frame rotation of the output filter currents  $i_{dq,conv}$ . This frame rotation is governed by the dynamics of PLL and is given by (see Appendix C for details)

$$\begin{bmatrix} i_{d,meas} \\ i_{q,meas} \end{bmatrix} = \frac{1}{i_{base}} \begin{bmatrix} \cos(\theta_{PLL}) & \sin(\theta_{PLL}) \\ -\sin(\theta_{PLL}) & \cos(\theta_{PLL}) \end{bmatrix} \begin{bmatrix} i_{d,conv} \\ i_{q,conv} \end{bmatrix} \quad (4.32)$$

Equations in (4.32) are nonlinear and need to be linearized to allow for the state-space representation of the current measurement subsystem. Their linearization for a given operating point gives

$$\begin{aligned} \Delta i_{d,meas} &= \frac{1}{i_{base}} \{ [-\sin \theta_{PLL}^0 i_{d,conv}^0 + \cos \theta_{PLL}^0 i_{q,conv}^0] \Delta \theta_{PLL} + \cos \theta_{PLL}^0 \Delta i_{d,conv} + \sin \theta_{PLL}^0 \Delta i_{q,conv} \} \\ \Delta i_{q,meas} &= \frac{1}{i_{base}} \{ [-\cos \theta_{PLL}^0 i_{d,conv}^0 - \sin \theta_{PLL}^0 i_{q,conv}^0] \Delta \theta_{PLL} - \sin \theta_{PLL}^0 \Delta i_{d,conv} + \cos \theta_{PLL}^0 \Delta i_{q,conv} \} \end{aligned} \quad (4.33)$$

Comparing the coefficients of  $\Delta \theta_{PLL}$  in (4.33) with equation (4.32) it is possible to see that they correspond to the steady-state values of  $i_{q,meas}^0$  and  $-i_{d,meas}^0$ , respectively. It is noted that  $i_{q,meas}^0$

and  $-i_{d,meas}^0$  are already given in per unit. Therefore, equation (4.33) can be further written in matrix form for a state-space development as

$$\begin{bmatrix} \Delta i_{d,meas} \\ \Delta i_{q,meas} \end{bmatrix} = \frac{1}{i_{base}} \begin{bmatrix} i_{q,meas}^0 i_{base} & \cos(\theta_{PLL}^0) & \sin(\theta_{PLL}^0) \\ -i_{d,meas}^0 i_{base} & -\sin(\theta_{PLL}^0) & \cos(\theta_{PLL}^0) \end{bmatrix} \begin{bmatrix} \Delta \theta_{PLL} \\ \Delta i_{d,conv} \\ \Delta i_{q,conv} \end{bmatrix} \quad (4.34)$$

Finally, it is noted that equation (4.34) corresponds to the output equation of the current measurement subsystem. Since the relations are all algebraic, this subsystem has no states. Nevertheless, as it will be shown in the next subchapters, a state-space equation is still required for the subsystem. This is done here with a dummy variable  $\xi_{i,meas}$  with no physical sense, just to allow for the consideration of a state-space matrix, which is zeroed, as given in

$$\left[ \frac{d\xi_{i,meas}}{dt} \right] = [0] [\xi_{i,meas}] + [0 \quad 0 \quad 0] \begin{bmatrix} \Delta \theta_{PLL} \\ \Delta i_{d,conv} \\ \Delta i_{q,conv} \end{bmatrix} \quad (4.35)$$

Equations given in (4.34) and (4.35) form the linearized state-space representation of the current measurement system and frame rotation.

## 4.2.8 Voltage Measurement

The current controller depicted in Figure 4.2 requires the measured voltages at the terminals of the VSC system  $v_{dq,meas}$  in per unit as well. The considerations and assumptions required for the development of a linearized representation of this subsystem are similar to those for the current measurement subsystem depicted in previous subchapter 4.2.7. For this reason, only the results are presented here. The state-space equation is given by

$$\left[ \frac{d\xi_{v,meas}}{dt} \right] = [0] [\xi_{v,meas}] + [0 \quad 0 \quad 0] \begin{bmatrix} \Delta \theta_{PLL} \\ \Delta v_{d,conv} \\ \Delta v_{q,conv} \end{bmatrix} \quad (4.36)$$

and the output equation can be developed as

$$\begin{bmatrix} \Delta v_{d,meas} \\ \Delta v_{q,meas} \end{bmatrix} = \frac{1}{v_{base}} \begin{bmatrix} v_{q,meas}^0 v_{base} & \cos(\theta_{PLL}^0) & \sin(\theta_{PLL}^0) \\ -v_{d,meas}^0 v_{base} & -\sin(\theta_{PLL}^0) & \cos(\theta_{PLL}^0) \end{bmatrix} \begin{bmatrix} \Delta \theta_{PLL} \\ \Delta v_{d,conv} \\ \Delta v_{q,conv} \end{bmatrix} \quad (4.37)$$

### 4.2.9 Reference frame conversion: from internal to global frame

The VSC system is assumed ideal, i.e., the dynamics of sensor, PWM and power electronics are neglected. In other words, it is assumed that the VSC is capable of directly implementing at its terminals the voltage references that it receives.

Under these assumptions, the VSC can be further understood as the subsystem that interfaces the internal  $dq$ -reference frame and the global  $dq$ -frame. More specifically, it receives the reference voltages  $v_{dq,ref}$  from the current controller, which are in the internal  $dq$ -frame defined by the PLL reference angle, and implements these voltages as  $v_{dq,VSC}$ , which are in the global  $dq$ -frame and are directly applied to the output filter subsystem. This is analytically calculated as

$$\begin{bmatrix} v_{d,VSC} \\ v_{q,VSC} \end{bmatrix} = \begin{bmatrix} \cos(-\theta_{PLL}) & \sin(-\theta_{PLL}) \\ -\sin(-\theta_{PLL}) & \cos(-\theta_{PLL}) \end{bmatrix} \begin{bmatrix} v_{d,ref} \\ v_{q,ref} \end{bmatrix} \quad (4.38)$$

It is emphasized in (4.38) that the reference frame conversion applied by the VSC system is the opposite as the one done by the PLL system, therefore the consideration of  $-\theta_{PLL}$ . More precisely, the PLL system is responsible for converting the equations from the global to the internal  $dq$ -frame of the VSC system, whereas the VSC itself is considered as the subsystem that converts the internal variables back to the global frame.

Moreover, equation (4.38) is clearly nonlinear. For this reason, a linearization for a given operating point is required for the linear state-space development. The process here is similar to the one already conducted for the PLL and the linearized version of (4.38) is given as

$$\begin{aligned} \Delta v_{d,VSC} &= -\left[-\sin \theta_{PLL}^0 v_{d,ref}^0 + \cos \theta_{PLL}^0 v_{q,ref}^0\right] \Delta \theta_{PLL} + \cos(-\theta_{PLL}^0) \Delta v_{d,ref} + \sin(-\theta_{PLL}^0) \Delta v_{q,ref} \\ \Delta v_{q,VSC} &= -\left[-\cos \theta_{PLL}^0 v_{d,ref}^0 - \sin \theta_{PLL}^0 v_{q,ref}^0\right] \Delta \theta_{PLL} - \sin(-\theta_{PLL}^0) \Delta v_{d,ref} + \cos(-\theta_{PLL}^0) \Delta v_{q,ref} \end{aligned} \quad (4.39)$$

Comparing the coefficients of  $\Delta \theta_{PLL}$  in (4.39) with equation (4.38) it is possible to see that they correspond to the steady-state values of  $-v_{q,VSC}^0$  and  $v_{d,VSC}^0$ , respectively. It is noted that  $v_{dq,VSC}^0$  is given in V. Moreover, it is also noted that the current controller was designed and developed in per unit, whereas the grid equations not. Therefore, equation (4.39) has also to be multiplied with the voltage base value  $v_{base}$ . With these considerations, equation (4.39) can be further developed in matrix form to

$$\begin{bmatrix} \Delta v_{d,VSC} \\ \Delta v_{q,VSC} \end{bmatrix} = v_{base} \begin{bmatrix} \frac{-v_{q,VSC}^0}{v_{base}} & \cos(-\theta_{PLL}^0) & \sin(-\theta_{PLL}^0) \\ \frac{v_{d,VSC}^0}{v_{base}} & -\sin(-\theta_{PLL}^0) & \cos(-\theta_{PLL}^0) \end{bmatrix} \begin{bmatrix} \Delta \theta_{PLL} \\ \Delta v_{d,ref} \\ \Delta v_{q,ref} \end{bmatrix} \quad (4.40)$$

Finally, it is noted that equation (4.40) corresponds to the output equation of the VSC representation. In fact, the VSC system has no states under the assumptions taken. Nevertheless, as it will be shown in the next subchapters, a state-space equation is still required for the VSC system. This is done here by including a variable  $\xi_{VSC}$  with no physical sense, just to allow for the consideration of a state-space matrix, which is zeroed, for the VSC system. This is illustrated next as

$$\begin{bmatrix} \frac{d\xi_{VSC}}{dt} \end{bmatrix} = [0][\xi_{VSC}] + [0 \quad 0 \quad 0] \begin{bmatrix} \Delta \theta_{PLL} \\ \Delta v_{d,ref} \\ \Delta v_{q,ref} \end{bmatrix} \quad (4.41)$$

Equations (4.40) and (4.41) form, thus, together the linearized state-space representation of the converter system and conclude the analytical development of separate subsystems for the VSC.

### 4.3 Complete State-Space Representation of the VSC System

In previous subchapters, the VSC system has been divided in several subsystems, for which analytical equations were developed and linearized. Each of this subsystem is, thus, represented by a linearized state-space system of equations, which has the advantage of allowing for separate validation of the analytical formulations. This is particularly useful when systems, from which the analytical representations are derived and linearized, are large, since errors in the formulations can be easier tracked.

Nevertheless, at the end of the process, when all analytical subsystems are developed and validated, their interconnection still allow for a complete state-space representation. Two methodologies emerge to address this task and are outlined in this subchapter.

The Component Connection Method, henceforth referred to as CCM, is one approach that can be used to aggregate several dynamic systems to obtain a complete system representation. Its application has as well already been reported for power systems [103].

In the CCM, the aggregation of subsystems is based on a so-called interconnection diagram, which identifies inputs and outputs of each subsystem and their interdependencies in view of the complete system. For the simple VSC system outlined in previous subchapters, for instance, such diagram can as well be developed and is illustrated in Figure 4.9.

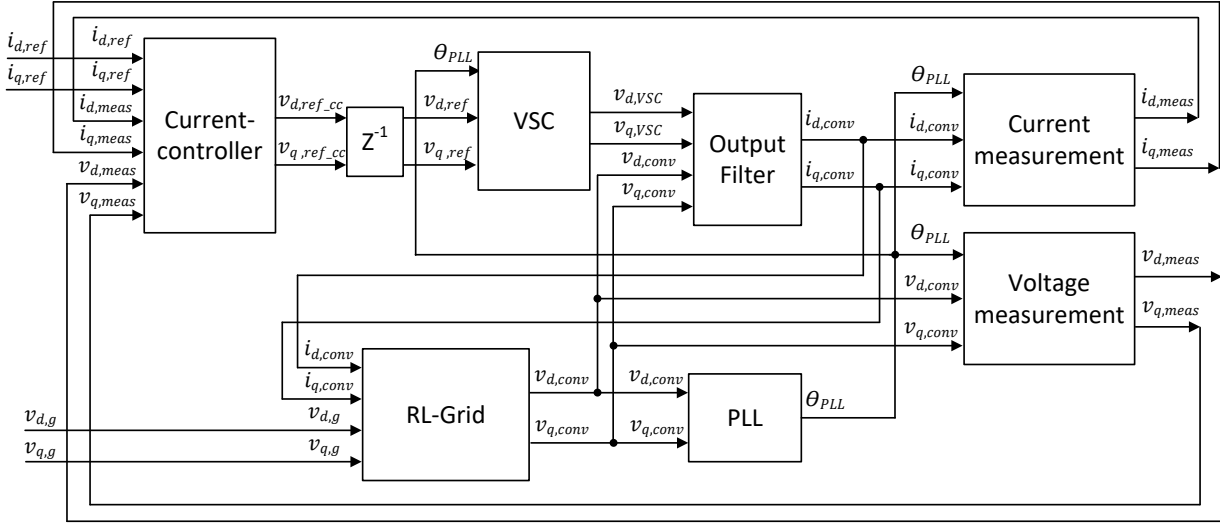


Figure 4.9 Interconnection diagram of subsystems from the simple VSC system.

For the aggregation of subsystem into a complete system representation, the CCM requires a composite component state model in the following form

$$\begin{bmatrix} \dot{x} \\ b \end{bmatrix} = \begin{bmatrix} A_{diag} & B_{diag} \\ C_{diag} & D_{diag} \end{bmatrix} \begin{bmatrix} x \\ a \end{bmatrix} \quad (4.42)$$

where  $A_{diag} = \text{diag}(A_1, A_2, \dots, A_n)$ ,  $B_{diag} = \text{diag}(B_1, B_2, \dots, B_n)$ ,  $C_{diag} = \text{diag}(C_1, C_2, \dots, C_n)$  and  $D_{diag} = \text{diag}(D_1, D_2, \dots, D_n)$  are diagonal matrices containing the individual subsystem matrices and  $a$  and  $b$  are the subsystems input and output vectors, respectively.

Then, the CCM requires the development of a so-called interconnection matrix  $L$ , which is formed by four submatrices  $L_{11}$ ,  $L_{12}$ ,  $L_{21}$  and  $L_{22}$ . These matrices consists of only zeros and ones to indicate incidences and relates subsystems input and output vectors  $a$  and  $b$  with the complete system inputs  $u$  and outputs  $y$ . These relations are given by

$$\begin{bmatrix} a \\ y \end{bmatrix} = \begin{bmatrix} L_{11} & L_{12} \\ L_{21} & L_{22} \end{bmatrix} \begin{bmatrix} b \\ u \end{bmatrix} \quad (4.43)$$

Using the relations from equations (4.42) and (4.43), it is possible to develop following equations

$$\begin{aligned}
a &= L_{11}b + L_{12}u = L_{11}(C_{diag}x + D_{diag}a) + L_{12}u \\
a - L_{11}D_{diag}a &= L_{11}C_{diag}x + L_{12}u \\
(I - L_{11}D_{diag})a &= L_{11}C_{diag}x + L_{12}u \\
a &= (I - L_{11}D_{diag})^{-1}L_{11}C_{diag}x + (I - L_{11}D_{diag})^{-1}L_{12}u
\end{aligned} \tag{4.44}$$

By replacing the expression obtained for  $a$  in the first equation of (4.42) gives

$$\begin{aligned}
\dot{x} &= A_{diag}x + B_{diag} \left[ (I - L_{11}D_{diag})^{-1}L_{11}C_{diag}x + (I - L_{11}D_{diag})^{-1}L_{12}u \right] \\
\dot{x} &= \left[ A_{diag}x + B_{diag}(I - L_{11}D_{diag})^{-1}L_{11}C_{diag} \right] x + \left[ B_{diag}(I - L_{11}D_{diag})^{-1}L_{12} \right] u
\end{aligned} \tag{4.45}$$

Similar analysis can be developed for the output equation. From (4.42) and (4.43) we have

$$\begin{aligned}
b &= C_{diag}x + D_{diag}a = C_{diag}x + D_{diag}(L_{11}b + L_{12}u) \\
b - D_{diag}L_{11}b &= C_{diag}x + D_{diag}L_{12}u \\
(I - D_{diag}L_{11})b &= C_{diag}x + D_{diag}L_{12}u \\
b &= (I - D_{diag}L_{11})^{-1}C_{diag}x + (I - D_{diag}L_{11})^{-1}D_{diag}L_{12}u
\end{aligned} \tag{4.46}$$

Applying equation (4.46) to the second line equation of (4.43) gives

$$\begin{aligned}
y &= L_{21} \left[ (I - D_{diag}L_{11})^{-1}C_{diag}x + (I - D_{diag}L_{11})^{-1}D_{diag}L_{12}u \right] + L_{22}u \\
y &= \left[ L_{21}(I - D_{diag}L_{11})^{-1}C_{diag} \right] x + \left[ L_{21}(I - D_{diag}L_{11})^{-1}D_{diag}L_{12} + L_{22} \right] u
\end{aligned} \tag{4.47}$$

Finally, by comparing equations (4.45) and (4.47) with the standard linear state-space representation provided in (4.4), it is straightforward to derive the relations of the CCM as

$$\begin{aligned}
A &= A_{diag}x + B_{diag}(I - L_{11}D_{diag})^{-1}L_{11}C_{diag} \\
B &= B_{diag}(I - L_{11}D_{diag})^{-1}L_{12} \\
C &= L_{21}(I - D_{diag}L_{11})^{-1}C_{diag} \\
D &= L_{21}(I - D_{diag}L_{11})^{-1}D_{diag}L_{12} + L_{22}
\end{aligned} \tag{4.48}$$

The relations in (4.48) set the basis of the CCM. It is evident that the interconnection matrices  $L_{11}$ ,  $L_{12}$ ,  $L_{21}$  and  $L_{22}$  play a major role in the aggregation process. Their derivation can be done based on the interconnection diagram and, although straightforward, can become resource intensive, and also prone to errors, in case of large systems.

The process of developing the interconnection matrices, however, can be replaced by automated and, thus, less resource intensive software based solutions. In the framework of this thesis, a Matlab solution has been used. More specifically, the function *connect* has been used [104]. To circumvent the need of requiring the user to provide the interconnection information, this function simply requires consistent naming of system inputs and outputs and connect the subsystems accordingly. It is noted that matrices  $L_{11}$ ,  $L_{12}$ ,  $L_{21}$  and  $L_{22}$  are sparse, which also makes them suitable for software application. Although it is not evident from [104] that the complete state-space development follow the exact relations outlined in (4.48), the effectiveness of function *connect* and its results have been compared to those of (4.48).

Details of the Matlab programming for the development of a complete state-space representation for the VSC system outlined in previous subsections can be extracted from Appendix D and are as well available in file *VSC\_Analytical\_AramisST.m* in [105].

#### 4.4 Validation of Complete VSC State-Space Representation

The complete small-signal representation for the VSC system has been validated against its non-linear representation simulated in Matlab/Simulink with the toolbox Simscape Power Systems [106]. A series of small perturbations in the form of steps were applied to both the detailed representation and the linearized one.

More specifically, at time  $t = 0.1s$ , a step of 0.01 per unit is applied at the  $d$ -axis of the grid voltage  $v_{d,g}$ . A step down of the same amplitude is applied half of a second later at  $t = 0.6s$ . Similar perturbation is applied at the grid voltage  $q$ -axis  $v_{q,g}$  at  $t = 1.1s$ , with the corresponding step down at  $t = 1.6s$ . Then, the reference value for the VSC currents are changed; at  $t = 2.1s$ ,  $i_{d,ref}$  is increased stepwise by 0.05 per unit and at  $t = 2.6s$  the corresponding step down is applied to eliminate the change. Finally, at  $t = 3.1s$  and  $t = 3.6s$  a step up and step down of 0.05 per unit, respectively, are applied to  $i_{q,ref}$ .

Some comparison plots were selected to illustrate the validation procedure. Figure 4.10 focuses on the PLL behavior, whereas Figure 4.11 and Figure 4.12 show a comparison of the converter currents  $i_{dq,conv}$  and measured voltages  $v_{dq,meas}$  at the terminals of the VSC.

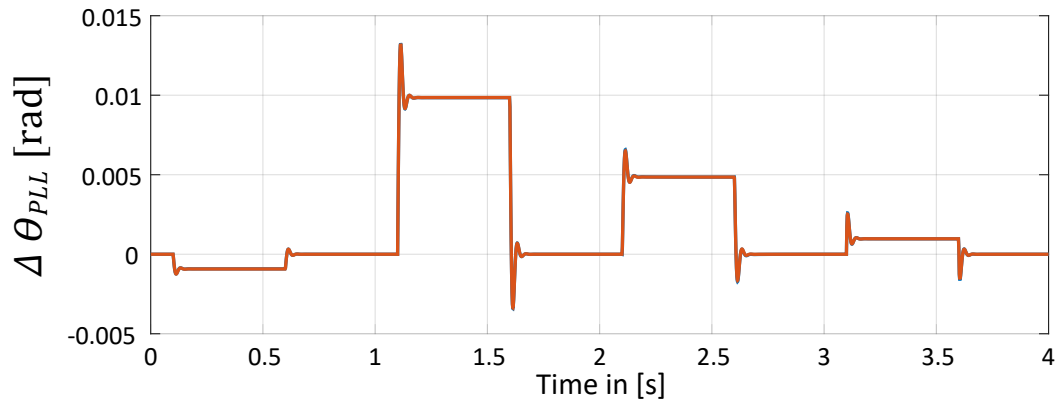


Figure 4.10 PLL validation: nonlinear model (blue) vs. linearized model (red).

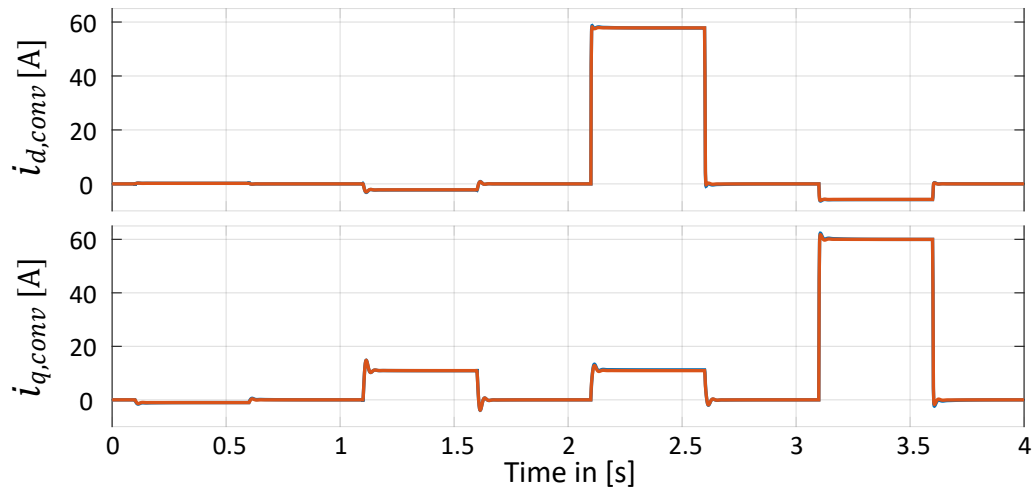


Figure 4.11 Comparison:  $i_{dq}$ , from nonlinear (blue) vs. linearized model (red).

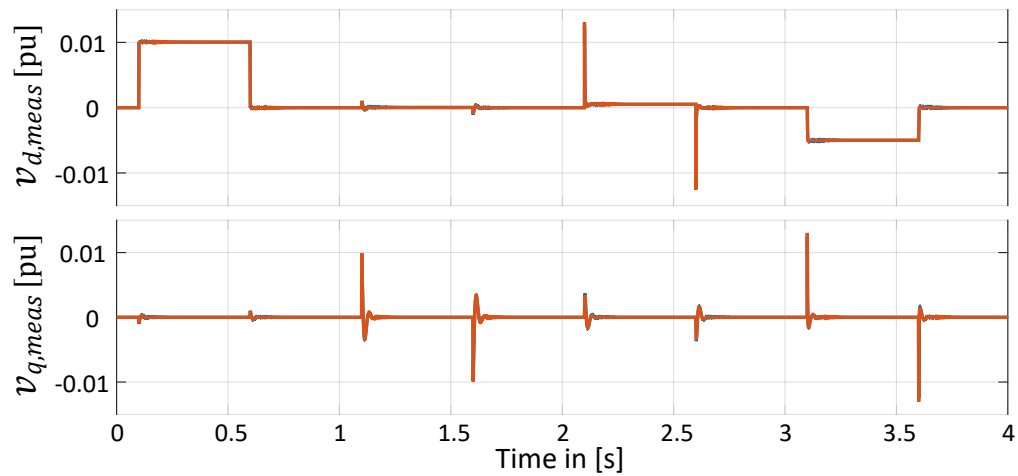


Figure 4.12 Comparison:  $v_{dq,meas}$  from nonlinear (blue) vs. linearized model (red).

As can be observed in the validation figures above, a good match was obtained between the non-linear and the linearized representations of the VSC system. For instance, in the case of the PLL (Figure 4.10), it can be seen that its dynamics are well captured and also that oscillations following perturbations are well-damped, indicating a stable system. More specifically, it is noted that when stepwise variations of  $v_{q,g}$  were applied, these were well tracked so that  $v_{q,meas}$ , which is the in the internal converter frame, was capable of going back to zero after each perturbation.

## 4.5 Eigenvalue Analysis Applied to VSC System

As observed in the simulation results obtained in previous subchapter, the simple VSC system presents a stable behavior against small-signal perturbations. It is, thus, expected that such behavior is also reflected in the eigenvalues of its linearized small-signal representation. More specifically, it is expected that all system eigenvalues have negative real parts, thus, indicating exponential stability [107].

To verify this hypothesis, the complete small-signal representation of the VSC system (as shown in Figure 4.9) is analyzed and its eigenvalues calculated. Figure 4.13 illustrate the eigenvalue plot calculated for the steady-state condition assumed for the plots from previous subchapter. In the interest of figure readability, two stable modes with very large negative real parts are not shown in Figure 4.13, since they do not change the interpretation of the figure.

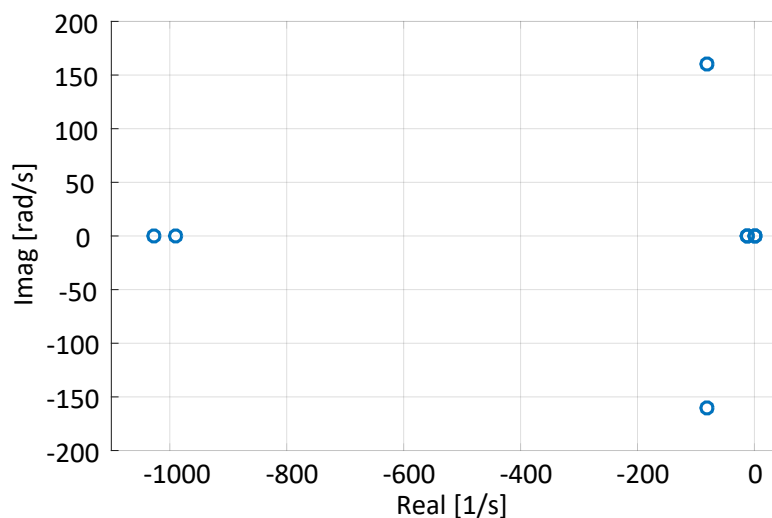


Figure 4.13 Eigenvalues of linearized VSC system representation.

It can be seen in Figure 4.13 that the eigenvalues are not in the right-half-plane indicating, thus, a stable system. This result confirms the expectation of a stable system and also supports the results seen in previous subchapter.

## 4.6 Modal Analysis Applied to the Type-IV Wind Farm Scenario

Previous subchapters focused on highlighting the methodology applied in this thesis to obtain a linearized state-space representation of a nonlinear system consisting of several subsystems to allow for the application of modal analysis. These techniques have been applied to the scenario investigated in subchapter 3.4 involving a type-IV wind farm connected to the series-compensated benchmark grid proposed in subchapter 3.3. Due to space constraints, the equation development and linearization procure are omitted here, however it is emphasized that all equations as well as their interconnection are included in the file *typeIV\_Analytical\_AramisST.m*, which has been made available together with this thesis [105].

In comparison with the simple VSC scenario investigated extensively in previous subchapters, however, some additional considerations were necessary to allow a linearized small-signal representation for the scenario involving the type-IV based wind farm connected to the benchmark grid. More specifically, in the proposed benchmark grid a distributed parameter line model was adopted for the transmission line. This representation was replaced by a pi-line in order to allow for state-space equation representation. Additionally, average model representations were assumed for power electronic stages of the type-IV wind turbine and the specific nature of its turbine-generator system also allowed for an ideal power source representation. It is emphasized, however, that these considerations are not expected to have significant impacts in the low-frequency region being addressed by the investigations throughout this thesis.

To validate the aforementioned assumptions, small-signal perturbations were applied to the systems inputs and the system behavior was compared against its detailed model responses in EMTP. Figure 4.14, Figure 4.15 and Figure 4.16 show, for instance, the comparison for the PLL angle, PCC  $dq$ -voltages and transmission line  $dq$ -currents, respectively.

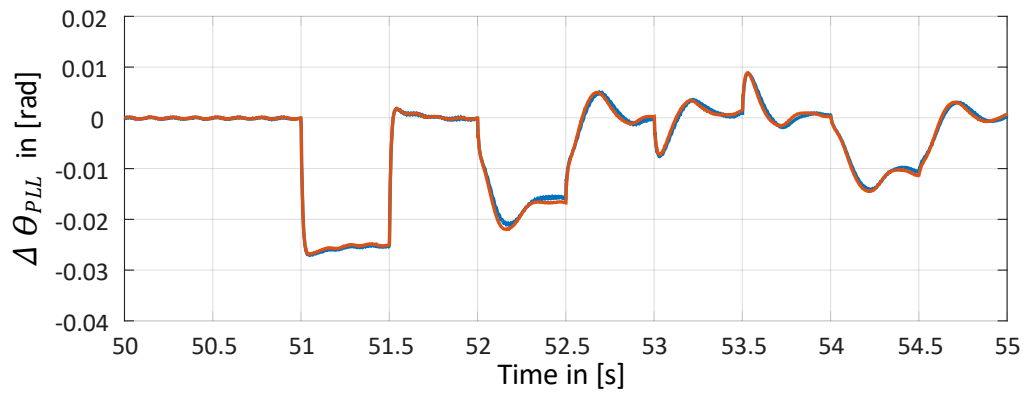


Figure 4.14 Comparison of PLL angle: detailed (blue) vs. linearized (red) models.

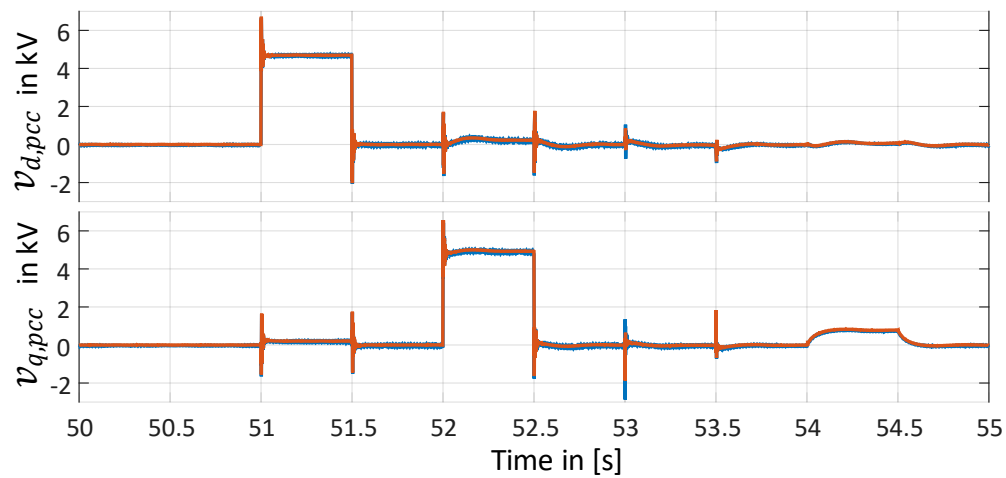


Figure 4.15 PCC voltages: detailed (blue) vs. linearized (red) models

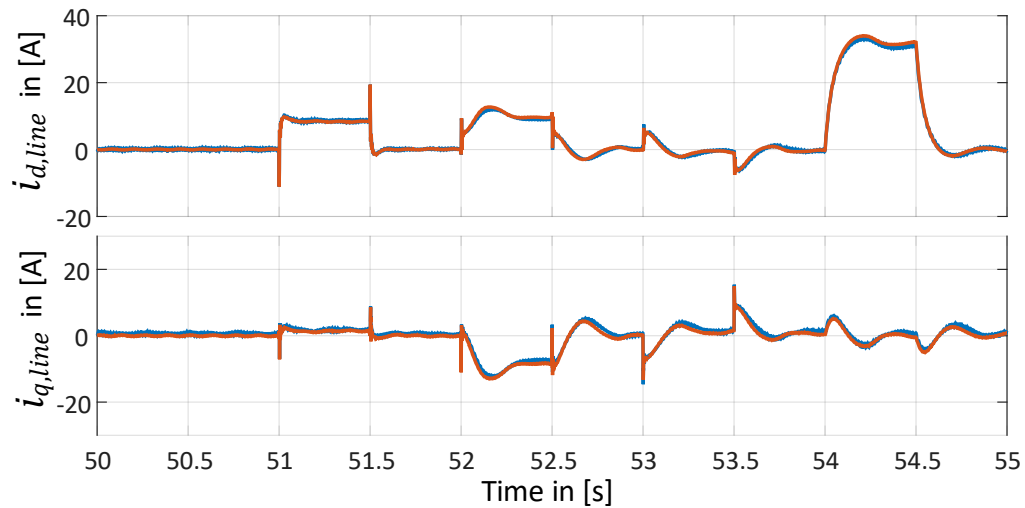


Figure 4.16 Transmission line currents: detailed (blue) vs. linearized (red) models.

It is seen in Figure 4.14, Figure 4.15 and Figure 4.16 that, although some small deviations are visible, overall, a good match between the linearized model and its corresponding detailed nonlinear representation has been achieved.

To conclude the investigations, the eigenvalues of the linearized system above were calculated and the results are shown in Figure 4.17. As can be observed, no eigenvalues resulted with positive real parts (i.e., in the right-half-plane side), thus, corroborating the EMTP results obtained earlier in subchapter 3.4 and illustrated in Figure 3.7.

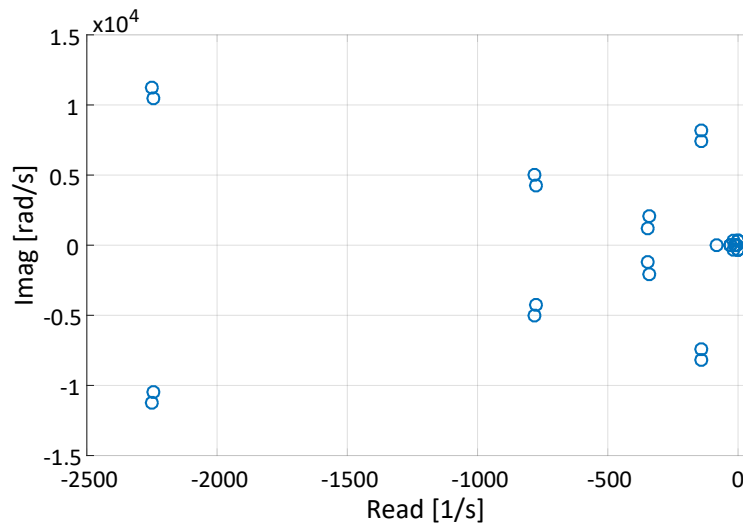


Figure 4.17 Eigenvalue plot for type-IV wind farm in series-compensated benchmark grid.

## 4.7 Modal Analysis Applied to the Type-III Wind Farm Scenario

It is known from the EMTP detailed simulations conducted in subchapter 3.5 that the type-III based wind farm becomes unstable when connected to the series-compensated benchmark grid. Moreover, these results also indicated that the series-compensation level plays an important role in the oscillatory and damping characteristics of the complete system (see Figure 3.8).

This subchapter aims at verifying these results by means of modal analysis. As previously done for the simple VSC system and for the type-IV wind farm, a small-signal representation is developed for the type-III wind farm in the series-compensated benchmark grid. The procedure applied is the same as used for the VSC and type-IV wind farm and the resulting equations for the small-signal representation are included in *TypeIII\_Analytical\_AramisST.m* [105].

Similarly as done for the type-IV wind farm case, certain assumptions were necessary for establishing a linearized state-space representation for the type-III wind farm scenario. These include, for instance, average consideration for power electronic stages and pi-representation of the transmission lines. It is emphasized, however, that all mechanical, electrical and control structures have been considered. This is important, since, for instance, in case of SSTI, which have been reported for type-III systems, the influence of mechanical components can be investigated.

The resulting complete linearized state-space form representation for the type-III scenario has been as well validated against its detailed nonlinear representation simulated in EMTP. Figure 4.18 to Figure 4.20 were selected to illustrate the comparison. All other system states and outputs can be compared in the files available in [105].

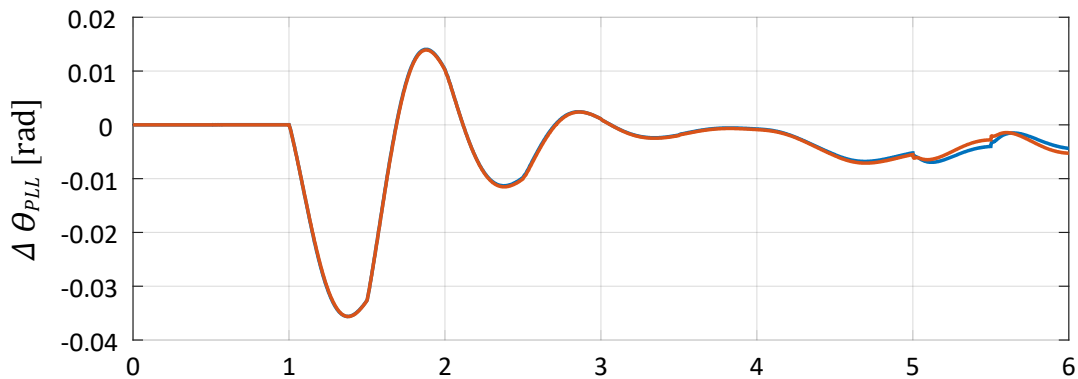


Figure 4.18 Comparison of PLL angle: EMTP detailed (blue) vs. linearized (red) models.

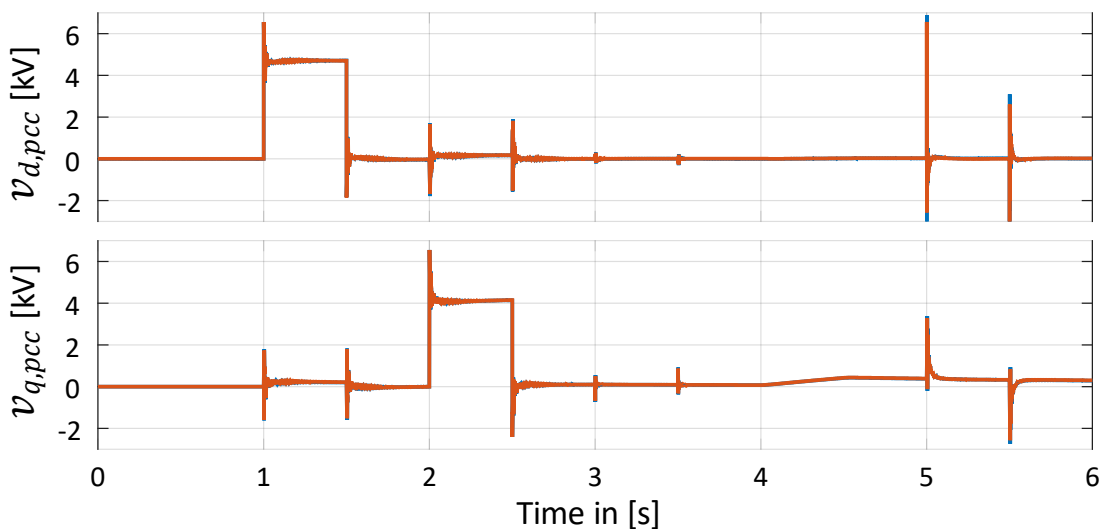


Figure 4.19 PCC voltages: detailed (blue) vs. linearized (red) models.

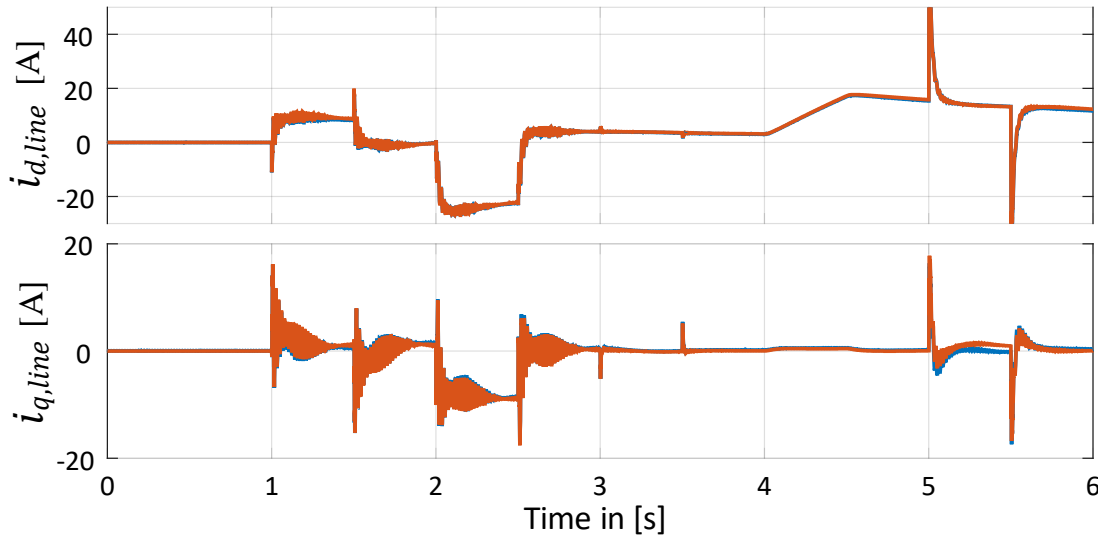


Figure 4.20 Transmission line currents: detailed (blue) vs. linearized (red) models.

It is evident from Figure 4.18 to Figure 4.20 that a good match was possible between the small-signal dynamics of the detailed system simulated in EMTP and those of the linearized one. This corroborates to the premise that the linearized small-signal representation can be used to investigate the instabilities found for type-III wind farm case. Both the impact of the series compensation as well as of control parameters are assessed through modal analysis in the next subchapters.

#### 4.7.1 Impact of Series Compensation

To investigate the impact of the series compensation level in the stability of the type-III wind farm connected to the benchmark grid for SSO studies, eigenvalue traces were plotted for small increments in the series compensation level. More specifically, since it is known from detailed EMTP simulations that the system becomes unstable for series compensation levels equal or higher than 10%, the system eigenvalues were evaluated for series compensation levels varying from 1% to 15% in steps of 1%. The results are illustrated in Figure 4.21, which focus in the region of the low-frequency modes, which are more affected by the variations.

It is observed in Figure 4.21 that the series compensation level indeed affects significantly the system behavior. It is seen that, as the series compensation level increases, a mode is strongly affected and shifts to the right-half-plane, eventually crossing the boundary for a series compensation level between 9% and 10%. It is interesting to note that these results correspond accurately to

the expectations obtained from detailed EMTP simulations illustrated in Figure 3.8, in subchapter 3.5, and, thus, reinforces the validity of the small-signal representation.

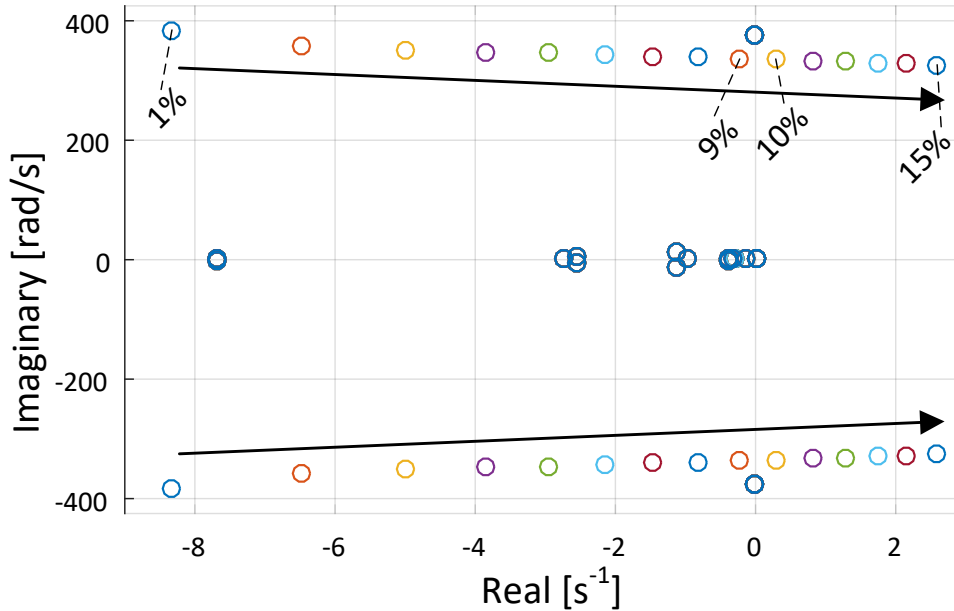


Figure 4.21 Eigenvalue traces for varying series compensation level.

Moreover, it is also highlighted that, as can be seen in Figure 4.21, as the critical mode moves to the right-half-plane, its damping characteristic decreases. This behavior is as well confirmed by the EMTP detailed simulations conducted in subchapter 3.5 and illustrated in Figure 3.8. Finally, it is also noted that the frequency of the unstable modes is approximately 53 Hz and matches well the frequency estimated from the EMTP results in Figure 3.8.

## 4.7.2 Participation Factor Analysis

To better understand the interaction phenomenon between the type-III wind farm and the series compensated benchmark grid, participation factor analysis was conducted in the system small-signal representation considering the unstable condition seen for a series compensation of 10%.

Participation factors provide a measure of the contribution that a  $k$ -th state has to a specific  $i$ -th mode of the system and, thus, help highlight whose elements are participating in the oscillations. Participation factors are defined as in [53], [108], [109]:

$$p_{ki} = u_{ik} w_{ki} \quad (4.49)$$

where  $u_{ik}$  and  $w_{ki}$  are the  $k$ -th elements of the  $i$ -th left and right eigenvectors, respectively.

Table 4.3 summarizes the participation factors calculated for the critical mode of the analyzed system in descending order of magnitude  $|p|$ . For convenience, participation factors were normalized so that their sum adds to unity.

Table 4.3 Participation factors for critical model of type-III wind farm case.

State	$ p $
$I_{d,s}$ (d-axis stator current of IG)	0.2383
$I_{q,s}$ (q-axis stator current of IG)	0.2014
$I_{d,r}$ (d-axis rotor current of IG)	0.2087
$I_{q,r}$ (q-axis rotor current of IG)	0.1766
$v_{d,cs}$ (d-axis voltage of series capacitor)	0.0623
$v_{q,cs}$ (q-axis voltage of series capacitor)	0.0604
All other system states	0.0523

The results in Table 4.3 allow the verification that the states that mostly participate in the critical mode are of electrical nature (current and voltages). More specifically, they are related to states from the induction generator and series capacitor and account for approximately 95 % of the oscillatory behavior. It is important to note that, although the complete system was considered in the development of a small-signal representation for the investigated scenario, no states associated with mechanical or control systems appear listed among the most contributing states (all remaining states participate only around 5 % to the oscillation).

These results indicate that the type of instability seen in the type-III wind farm case is of electrical nature. As such, it could be categorized as of a classical SSR type [61]. It is noted that the term subsynchronous control interaction (SSCI) appears in previous works when SSO is seen in conjunction with wind turbines, for instance in [11]. However, for the specific case investigated above, it is emphasized that the use of such terminology may be misleading, since control states are not actually participating in the unstable oscillatory behavior.

### 4.7.3 Impact of RSC Current Regulator Gains

Additional investigations are conducted in this subchapter to assess the impact of control parameters in the instabilities seen for the type-III wind farm in conjunction with the series-compensated

benchmark grid. Since it has been observed in subchapter 4.7.2 that states related to the induction generator rotor and stator belong to the group of states most participating in the oscillatory behavior of the critical mode and, given the fact that only the rotor currents are controlled in a type-III wind turbine generator (i.e., a doubly-fed induction generator), mitigation attempts were oriented towards the rotor-side current regulator. More specifically, following analyses focus on the assessment of impact of varying current regulator gains in the complete system stability.

To assess their impact, eigenvalue traces were investigated. For simplicity, it has been assumed that both proportional and integral gains of the rotor-side converter current regulator were varied simultaneously and proportionally to their original values. These gains were decreased to 30 % of their original values in steps of 10 %. Additionally, a line series compensation level of 20 % was assumed, which, as demonstrated in previous subchapters, leads to an unstable condition for the original rotor-side converter current regulator gains. The resulting eigenvalue traces are illustrated in Figure 4.22.

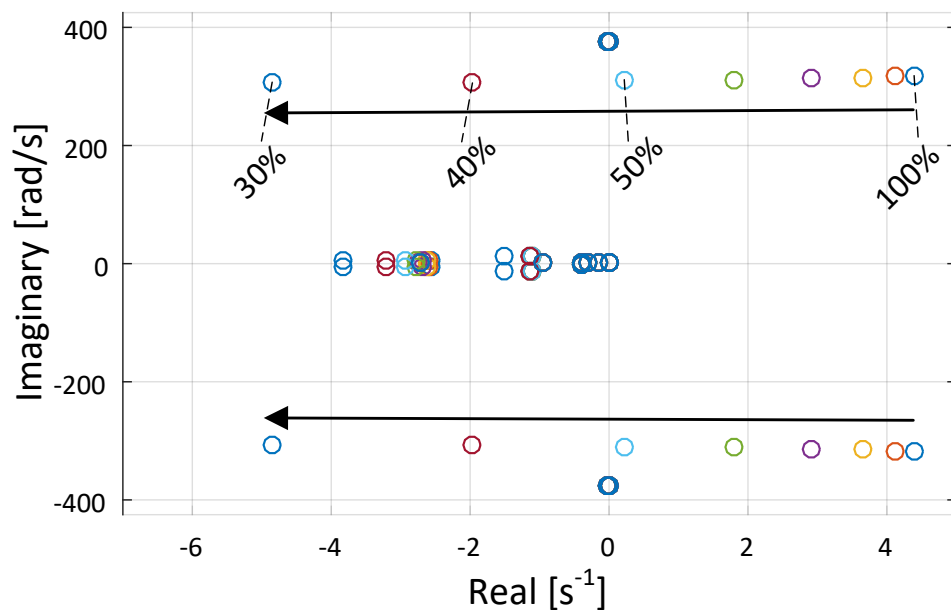


Figure 4.22 Eigenvalue traces for varying RSC current regulator gains (20% compensation).

It is readily visible from Figure 4.22 that the rotor-side current regulator gains have significant impact in the critical mode and, therefore, can affect the stability of the complete system in the same manner. Results of Figure 4.22 also indicate that reducing the current regulator gains to

around 48 % (or less) of their original value leads to having all modes in the left-half-plane and, thus, should help stabilize the system.

To validate these conclusions, the detailed representation of the system in EMTP was used. A line series-compensation level of 20 % was assumed in the EMTP simulation accordingly. The rotor-side converter current controller were reduced to 40 % of their original value. The system was perturbed with the same high impedance fault considered in the EMTP analyses conducted in sub-chapter 3.5 that result in a small voltage drop at the wind farm PCC. The results are illustrated in Figure 4.23 for the active power measured at the PCC and the dc-link voltage of the type-III wind turbine system.

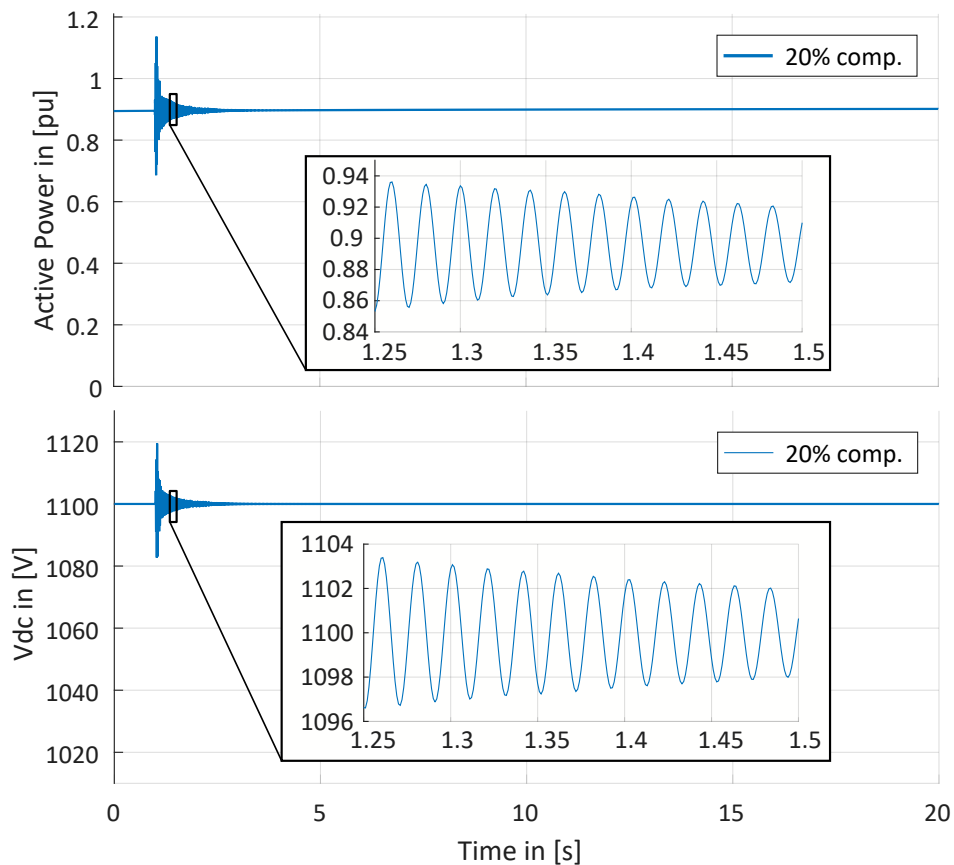


Figure 4.23 EMTP results for reduced current regulator gains and 20 % series compensation.

The EMTP results shown in Figure 4.23 confirm that reducing the rotor-side current regulator gains indeed has a positive effect in the overall system stability, as predicted by the eigenvalue traces illustrated in Figure 4.22. It is emphasized, however, that these conclusions are applicable to the

specific scenario investigated. Other type-III controller structures in different grids may require different considerations. Moreover, in practical interconnection projects, such tuning requires as well the subsequent verification that other performance requirements are still met.

Finally, it has been observed that modal analysis, although resource-intensive, was capable of precisely predicting instabilities as well as of providing guidance to mitigation by means of participation factor analysis and eigenvalue traces.

## **CHAPTER 5 STABILITY ASSESSMENT BASED ON BLACK-BOXES**

This chapter starts by reviewing existing techniques proposed for the assessment of low-frequency stability of power systems. Then, it focuses its investigations on the capabilities of a specific screening technique that is currently used by the industry, namely, the combined scan technique. It is shown that this technique is capable of properly addressing the stability for the scenario involving a type-III based wind farm, however it fails to accurately predict stability for the type-IV wind farm scenario. Detailed investigation is conducted to identify fundamental limitations of this approach and orient research to better address them. Some research results obtained in this work package were also published in [110].

### **5.1 Motivation**

Chapter 4 of this thesis indicated that modal analysis is a powerful technique for addressing power system small-signal stability, notably with regards to low-frequency phenomena. Not only it allows for a good insight into system dynamics through eigenvalue analysis and their damping characteristics, but it also provides a good indication for mitigation, as seen in subchapter 4.7.2 and 4.7.3 for the scenario involving a type-III wind farm.

The widespread use of modal analysis, however, is hindered by its requirement for rigorously developed analytical system equations. In Chapter 4, it has been seen that the process for obtaining and validating small-signal representations for realistic systems is laborious and resource-intensive, which make it not always practicable for the industry. Additionally, it is noted that, even if resources in such dimension were available, the application of modal analysis is not always possible. For instance, as highlighted in earlier chapters in this thesis, due mostly to intellectual property concerns, interconnection studies are usually conducted with protected (i.e., black-box) simulation models of manufacturer specific equipment, such as wind turbines or photovoltaic inverters.

Hence, integration of new generating units and grid-connected inverters require other techniques other than the modal analysis to efficiently support interconnection studies. Certainly, EMT-studies play an important role in such studies ([34], [111]), however the consideration of large-scale sys-

tems together with the range of possible operating conditions imposed by contingencies and intermittency of renewable generation reveals the need for more efficient screening techniques for fast identification of potentially critical scenarios.

Next subchapter reviews proposed screening techniques that could be used for assessing low-frequency instabilities in power systems.

## 5.2 Review of Screening Techniques

The term *screening technique* is used in this thesis to address any technique aiming at efficiently identifying potentially critical scenarios related to power system stability, notably with focus in the low-frequency range. In that sense, it is noted that modal analysis and EMT simulations are purposely not considered in this thesis as screening techniques. This is due to the fact that the former, although powerful, is resource-intensive and, thus, arguably not efficient. The latter is understood as the ultimate tool validating results obtained from screening techniques and, therefore, per se not a screening technique.

Initially, it is emphasized that, to the author's knowledge, the first screening techniques addressing specifically low-frequency phenomena have been proposed in the framework of the assessment of SSR risks. Notably, already in 1979, Agrawal et al. proposed in [112] the use of the so-called frequency scanning technique to address SSR in conventional systems involving synchronous machine. In this approach, the system impedance is analyzed over frequency as seen from the neutral bus of the synchronous generator under study. It was introduced as a very cost effective method to screen out system conditions that are potentially critical from a SSR perspective.

It is emphasized that different types of SSR were addressed in [112] with different corresponding criteria. For instance, a critical induction generator effect condition is found, if inspection of frequency scanning results indicates any frequency for which the reactance is zero (or close to it) and resistance is negative. These results are based on the induction generator equivalent representation of synchronous generators for the subsynchronous range as illustrated in Figure 5.1.

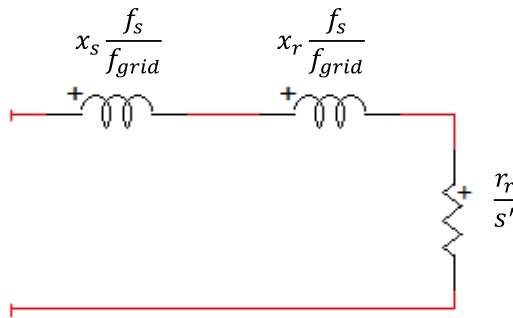


Figure 5.1 Synchronous machine equivalent for SSO studies.

In Figure 5.1,  $x_s$  and  $x_r$  represent the rotor and stator reactance, respectively,  $r_r$  the rotor resistance, all in per unit.  $s'$  is defined as the machine slip and is calculated as

$$s' = \frac{\omega_s - \omega_r}{\omega_s} \quad (5.1)$$

where  $\omega_s$  and  $\omega_r$  are the electrical stator and rotor rotational speeds, respectively. It is noted that for subsynchronous frequencies at the stator,  $\omega_s$  is smaller than the rated rotational frequency  $\omega_{rated}$  and also  $\omega_r$  resulting in negative slip  $s'$ .

Agrawal et al. also proposed criteria for SSTI and transient torque amplification in [112]. For the first, additional information on the mechanical system, such as the mechanical damping, is required. For the latter, reactance dips in the system impedance are used as indicators if their minimum is close to rated frequency complements of modal frequencies.

In the beginning of the 80's, Canay proposed an alternative technique to address SSR in conventional systems [113], [114]. More specifically, in [113] the *complex torque technique* was proposed, which is based on so-called complex torque coefficients  $k_e$  and  $k_m$ . The electrical complex torque coefficient  $k_e$  was introduced as

$$k_e(j\lambda) = K_e + j\lambda D_e \quad (5.2)$$

and is used to characterize the electrical damping of a system. An additional coefficient  $k_m$  is used to characterize the mechanical damping of the same system. In equation (5.2),  $\lambda$  represents the relative system frequency (i.e., rotor frequency divided by rated system frequency),  $K_e$  the electrical spring constant and  $D_e$  the electrical damping constant. It is emphasized that these parameters depends on: i) power system configuration; ii) operating point; iii) type of existing controllers; and

iv) number of machines connected in parallel. Corresponding real and imaginary parts are also derived for the mechanical system in [113], however, are omitted here, since these depend mostly on the design and physical characteristics of the concerned turbine-generator unit.

With the help of the complex torque coefficients  $k_e$  and  $k_m$ , Canay then proposed a sufficient condition of the decaying (i.e., asymptotic stability) of subsynchronous oscillations after a system disturbance. More specifically, Canay stated in [113] that for oscillatory frequencies for which the sum of electrical and mechanical damping are zero (or very close to zero), i.e.,

$$k_m(j\lambda) + k_e(j\lambda) \cong 0 \quad (5.3)$$

Then, following condition is to be met in order to avoid growing oscillations

$$(D_m + D_e) > 0 \quad (5.4)$$

meaning that the sum of electrical and mechanical damping needs to be positive. Moreover, if the condition in (5.4) is not met, then it is noted from equations (5.2) and (5.3) that factors  $K_e$  and  $K_m$  help determine the interaction frequency, which is then directly given by  $\lambda$ .

Canay also outlines in [113] that the basic idea underlying his approach is that it should be possible to describe the interaction effect of a conventional synchronous machined based turbine-generator system by its equation of motion, which he assumes as a two-mass system. This idea allows for the representation of the system as a classical spring-mass one, as shown in Figure 5.2.

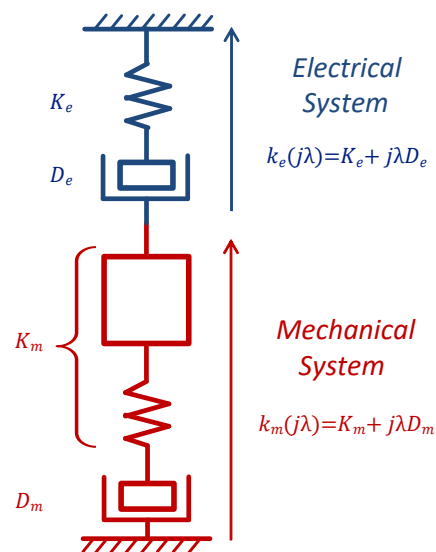


Figure 5.2 Representation used by Canay for conventional generator shaft systems.

In his first publication on the complex torque technique [113], Canay considered simple circuit representations for the grid. More specifically, his technique was demonstrated analytically for a radial RLC and a parallel RLC/RL system. In his second publication [114], however, Canay addressed the specific issue of analytical development for more complex system structures and proposed the use of a frequency scan technique to circumvent it.

A major limitation of the complex torque technique proposed by Canay in [113] and [114] was highlighted years later by Tabesh et al. in [67], which pointed out that the technique can only be applied to one turbine-generator system at a time and that it is only applicable in case of synchronous machines. To fulfil this gap, [67] then proposed the analytical development of an open-loop transfer function and analysis of its frequency-response combined with some performance indicators. Although with these considerations the approach as in [67] is capable of addressing other types of generators and multi-machine power systems, its main drawback is its requirement of rigorous analytical development, which, as stated earlier, remains resource-intensive and not always practicable.

At this point it is noted that the frequency scanning proposed both by Agrawal et al. in [112] and by Canay in [114] consider only network passive components and correspond, therefore, to those obtained by a passive frequency scanning available in EMT software packages [106], [115]. Such assumption is strong and, therefore, also limiting. However, it is emphasized that it still holds for systems with simple structures in specific conditions where the main system dynamics agree with those of the passive components only. The frequency scanning in such form has also found use in other works, notably in [76], [116], [117].

When it comes to modern power system structures, however, controllers are expected to assume a significant role in defining system behavior. It is, therefore, important to capture their dynamics in the frequency scan. To deal with this need, Jiang et al. suggested in [118] the use of current sources to inject a spectrum of frequency components into a system to obtain its small-signal frequency response. This method includes the response of control systems and is readily expandable to any network size. Its applicability has been demonstrated on the First CIGRE HVDC Benchmark Model in the same work [118].

Since [118], several publications followed focusing on applying the frequency scanning technique based on small-signal perturbations, here henceforth referred to as *active* frequency scanning, to assess low-frequency stability issues in power systems, mostly with focus on SSR issues, notably in [119], [120]. Also interesting to note, not necessarily currents or voltages are subjected to small-signal perturbation in active frequency scans. In fact, reference [121], for instance, proposed small-signal perturbations in generator speeds for calculation of torque coefficients.

Badrzadeh et al. presented the active frequency scanning as an important tool for the assessment of subsynchronous interactions in wind power plant systems in [122] and following works applied it to investigate real field events in [123]. The technique is also outlined with more details by Sahni et al. in [124]. It is demonstrated in [122]–[124] that it can be used in conjunction with detailed manufacturer models for grid-connected equipment as well as more complex system structures. Moreover, references [122]–[124] also proposed some criteria for potentially critical conditions based on the active frequency scanning results of grid and wind farms. According to them, such conditions are indicated if

- i) Any reactance crossover on the turbine (i.e., wind farm) side coincides with resonant conditions on the system side, even if the turbine resistance is positive.*
- ii) Any resonant condition on the system side if the turbine resistance is negative for the same frequency.*

If any of the above conditions is met, detailed EMT simulations are then suggested for validation of results and verification of risks. It is highlighted at this point, however, that references [122]–[124] do not provide any analytical explanation for the criteria stipulated.

Although several works have been dealing with active frequency scanning techniques, care must be taken when it comes to perturbation signals. It is emphasized that power systems are nonlinear systems and such nonlinear characteristics are expected to be more pronounced in modern power system structures. As such, systems are likely to respond adversely to different magnitudes and types of perturbations, as correctly pointed out by Wrate et al. in 1997 in [125].

More recently, another category of frequency-response based approaches, denominated impedance-based stability criterion, has been gaining popularity in screening and stability assessment of grid-connected inverters and inverter-based systems, thus, modern power systems.

The impedance-based theory has its roots in a work published by Middelbrook in 1976 ([126]) that aimed at assessing stability and proposing constraints on the design of input filters for dc-regulators. According to it, a sufficient condition for the stability of dc-regulators is possible based on the impedance ratio of the input filter and dc-regulator. It is interesting to note that Middelbrook already considered in [126] the possibility of using measurements to circumvent the need of analytical developments and to deal with black-box devices. The aforementioned approach proposed by Middelbrook was then extended to address three-phase systems.

In [127] Belkhaty used the impedance-based theory to address the stability of inverter-based devices, especially those with constant power characteristics. Harnefors outlined in [128] considerations on the design of inverter-based devices to guarantee stability based on the input admittance characteristics of these equipment and in [129] he demonstrated how it can be used in the assessment of SSTI. Sun presented in [130] an overview of small-signal methods for power systems with large integration of inverter-based devices. Among the outlined techniques, the impedance-based technique was highlighted as a promising tool for stability analysis of modern power systems. Two years later, in [131], Sun dedicated a whole work to outline the impedance-based technique and its fundamentals.

It is noted, however, that in the above works on impedance-based theory, there are some nuances in how they are applied. Independent on these details, the essence of the impedance-based technique is the division of the system under study in two parts: a source subsystem and a load subsystem. It is noted that different representation forms are found in the literature (e.g., with the source subsystem modeled as Thevenin equivalent or as a Norton-equivalent and the load subsystem as an impedance or admittance). Figure 5.3 illustrates the most recurrent of these possibilities, namely, the one based on a Thevenin equivalent representation for the grid.

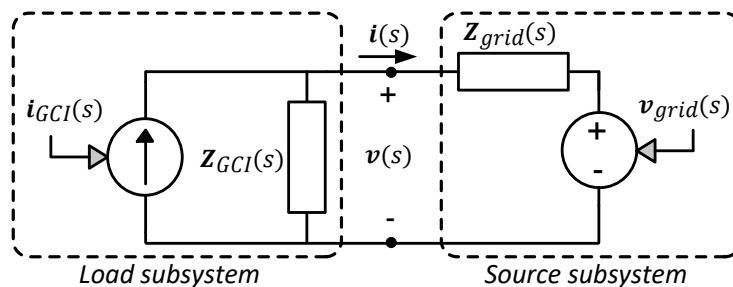


Figure 5.3 Impedance-based small signal representation of a grid-connected inverter.

It is straightforward to demonstrate for the system in Figure 5.3 that the current  $i(s)$  flowing at the point of connection can be given by

$$i(s) = \frac{i_{GCI}(s)Z_{GCI}(s)}{Z_{GCI}(s) + Z_{grid}(s)} - \frac{v_{grid}(s)}{Z_{GCI}(s) + Z_{grid}(s)} \quad (5.5)$$

where  $i_{GCI}(s)$  is the source current of the grid-connected inverter,  $v_{grid}(s)$  the grid voltage and  $Z_{GCI}(s)$  and  $Z_{grid}(s)$  the inverter and grid input impedances, respectively. Moreover, it is noted that equation (5.5) can be rearranged to

$$i(s) = \left( i_{GCI}(s) - \frac{v_{grid}(s)}{Z_{GCI}(s)} \right) \frac{1}{1 + \left( \frac{Z_{grid}(s)}{Z_{GCI}(s)} \right)} \quad (5.6)$$

For system stability analysis, Sun suggests in [131] that the source subsystem can be assumed stable when unloaded and the load subsystem can be assumed stable when powered from an ideal voltage source. Under these considerations, the first term of equation (5.6) is stable and system stability depends on the second term on the right hand side, given by

$$H(s) = \frac{1}{1 + \left( \frac{Z_{grid}(s)}{Z_{GCI}(s)} \right)} \quad (5.7)$$

The impedance-based theory relies on the observation that  $H(s)$  resembles the resulting closed-loop transfer function of a negative feedback loop with unity forward gain and feedback gain equal the impedance ratio of grid and grid-connected inverter impedances. As such, stability can be assessed by well-proven criteria, among which the Nyquist stability criterion [107].

As also outlined by Sun in [130], one of the advantages of the impedance-based theory is the fact that, when analytical impedance models are not available or not possible to develop, input impedances can be obtained by numerical simulations or even experimentally, if the unit is built. Due mostly to this aspect, the impedance-based approach has found recently large industry acceptance. Details to the impedance-based theory are further provided in Chapter 6.

Finally, another approach that merits attention as a screening technique for low-frequency stability assessment of power systems is the *combined scan technique* [132]. This technique is currently one of the most used techniques by system operators and project developers especially in conjunction

with grid-connected inverters ([19], [133], [134]) and, for this reason, is investigated in this thesis in detail.

The approach is based on active frequency scanning, however, differently than aforementioned techniques, these are performed in a combined manner to consider simultaneously both grid and grid-connected inverters [132]. More specifically, small current disturbances are injected at the PCC at different frequencies and the positive sequence frequency-dependent impedances of grid and grid-connected inverters (i.e., wind farm, solar park, HVDC, among others) are extracted from the measured voltages and currents through Discrete Fourier Transform (DFT). The total frequency-dependent impedance is then calculated by adding both impedances as

$$Z_{comb}(s) = Z_{grid}(s) + Z_{GCI}(s) \quad (5.8)$$

The procedure is illustrated in Figure 5.4. It is emphasized that the approach is oriented to numerical simulations in EMT software packages, where such small-signal perturbations with fictive current sources are possible.

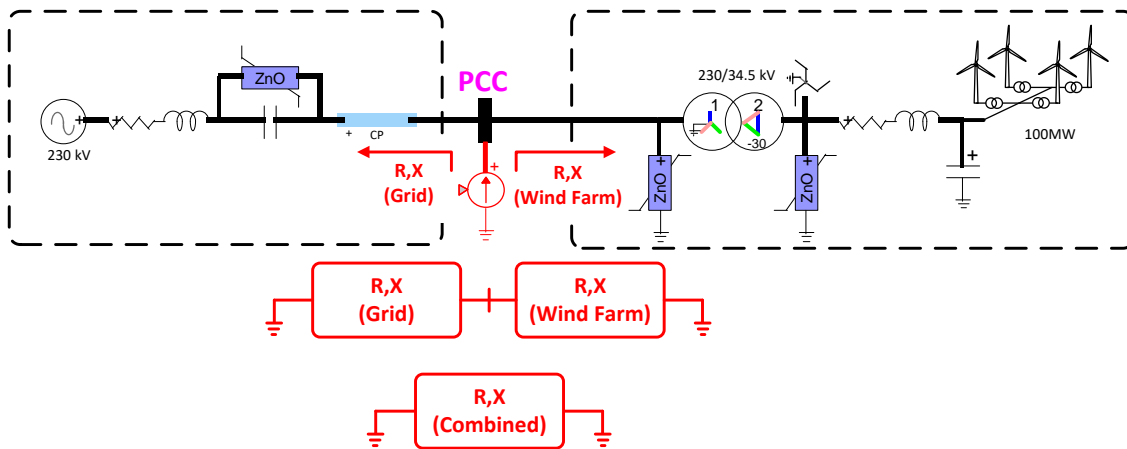


Figure 5.4 Combined scan technique applied to a wind farm interconnection [132].

According to [132], critical operating conditions are indicated for cases in which the combined resistance is negative whenever the combined reactance crosses zero. It is noted, however, that although the criteria may make heuristic sense, especially if compared to very simple cases, for instance, RLC circuits, no mathematical base has been provided to justify them.

In the framework of this thesis it has been verified that the combined scan technique has its roots in the SSR analysis for synchronous machines and its use has been proposed for grid-connected

converters. Moreover, analysis conducted in this thesis also indicated that, although the applied scanning approach applied in [132] differs from the one published by Sun in [131], the combined scan technique still relies on the impedance-based theory (as outlined above for Figure 5.3).

To justify this point, it is noted, first, that both approaches rely on frequency-dependent positive sequence impedance representation for grid and grid-connected inverter input impedances. Second, the stability condition of the impedance-based approach presented by Sun in [131] relies on the observation that the interconnection stability is dictated by equation (5.7), where  $H(s)$  resembles a transfer function of a closed-loop with negative feedback. Sun suggests in [131] the use of the Nyquist criterion to assess the stability of  $H(s)$ , but it is noted that  $H(s)$  becomes unstable when its denominator is equal zero, as given in

$$1 + \left( \frac{Z_{grid}(s)}{Z_{GCI}(s)} \right) = 0 \quad (5.9)$$

Finally, multiplying both sides of equation (5.9) with  $Z_{GCI}(s)$  gives

$$Z_{grid}(s) + Z_{GCI}(s) = 0 \quad (5.10)$$

It can be observed from equation (5.10) that, although indirectly, the impedance-based theory looks at the sum of grid and grid-connected inverter impedances as well. Nevertheless, it is emphasized at this point that, although the fundamentals of both approaches are the same, their stability criteria of differ.

Additionally, another important nuance between the approaches concerns the extracted input impedances of grid and grid-connected inverters,  $Z_{GCI}(s)$  and  $Z_{grid}(s)$ , respectively. It is noted that while Sun insists in [131] that these can be obtained separately, in the combined scan technique [132] the operating condition of the interconnection is inherently considered. Since realistic grid and grid-connected inverters representations contain nonlinear equipment and controllers, the consideration of the operating condition in their input impedances is essential for proper small-signal stability analysis. Although possible in the impedance-based theory with additional efforts, this aspect is directly taken care of by the combined scan technique.

Due to its relevance for industry applications [19], the capabilities of the combined scan technique is next evaluated for the type-III and type-IV wind farms scenarios in conjunction with the proposed series-compensated benchmark grid previously investigated in this thesis by means of detailed EMTP simulations and modal analysis (see Chapter 3 and Chapter 4, respectively).

### 5.3 Combined Scan Technique Applied to Type-III Wind Farm

The combined scan technique is now applied to the scenario involving a type-III wind farm connected to the series-compensated benchmark grid, which has been investigated by means of detailed EMTP simulations in subchapter 3.5 and subjected to modal analysis in subchapter 4.7.

The combined scan has been applied to the case considering the type-III wind turbines injecting approximately 100 MW at their terminals. It is known from aforementioned investigations that interconnection becomes unstable for series-compensation levels of 10 % or higher. The results of the combined scan analysis are summarized in Figure 5.5. In the interest of figure readability, only four series-compensation levels are illustrated.

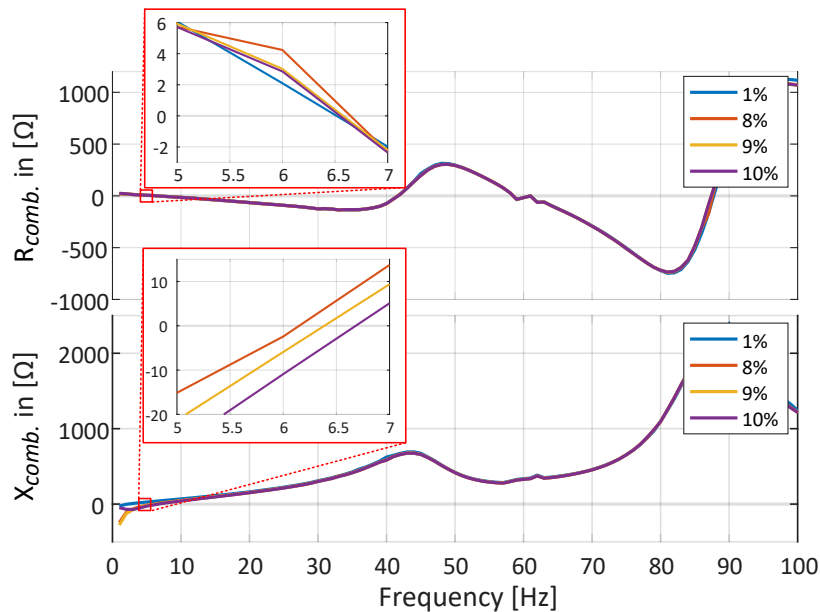


Figure 5.5 Combined scan results for type-III wind farm connected to benchmark grid.

It is emphasized here that some assumptions are necessary to generate the results illustrated in Figure 5.5. First, when applying the combined scan technique aiming at extracting the frequency dependent positive sequence impedance of the wind farm, i.e.,  $Z_{GCI}(s)$ , the grid representation is

replaced by a Thevenin equivalent. Such consideration is necessary; otherwise, for instance, a stable EMT simulation would not be possible for all considered series-compensation levels. Second, similar as for the wind farm and due to the same reason, for 10 % series compensation, the wind farm is replaced by a three-phase current source initialized so to inject the 100 MW expected from the corresponding wind farm.

It is evident from Figure 5.5 that the combined resistance is positive at the reactance crossover for a 9 % series-compensation level, however becomes negative for 10 % series compensation, thus, indicating a critical operating condition for this level. These results are, thus, in accordance with those obtained by modal analysis in subchapter 4.7 and are verified by the detailed EMTP simulations in subchapter 3.5. Therefore, they indicate that the combined scan technique was capable of accurately predicting stability in these cases.

## **5.4 Combined Scan Technique Applied to Type-IV Wind Farm**

This subchapter deals with the application of the combined scan technique to the scenario investigated in subchapter 3.4 involving the type-IV based wind farm connected to the proposed series-compensated benchmark systems.

Similar as done for the type-III wind farm, the wind speed was adjusted to obtain an active power of approximately 100 MW at the terminals of the type-IV wind turbines. Reactive power was set to zero. Different series-compensation levels have been tested. The combined scan results are illustrated in Figure 5.6.

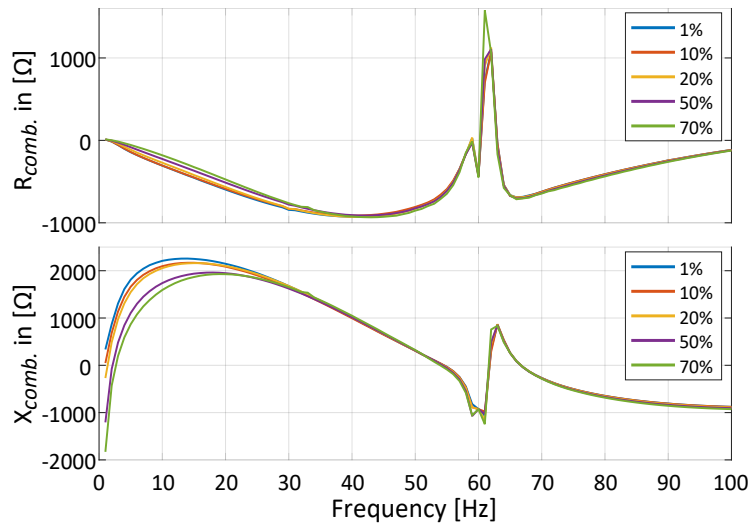


Figure 5.6 Combined scan results for type-IV wind farm connected to benchmark grid.

It can be seen in Figure 5.6 that reactance crossovers with negative resistance exist for different frequencies for the type-IV wind farm case. More specifically, such conditions are seen for frequencies around 3 Hz, 55 Hz and 65 Hz. Therefore, according to the combined scan stability criteria, unstable conditions should be expected.

It is noted, however, that no instabilities were expected for the type-IV wind farm case connected to the series-compensated benchmark grid. Modal analysis applied in subchapter 4.6 pointed out to eigenvalues on the left-half-plane for the small-signal characteristics of the investigated scenario. Moreover, these results are in fact confirmed by detailed EMTP simulations conducted in subchapter 3.4 (see, for instance, simulation results illustrated in Figure 3.7).

Based on these results, it is evident that the combined scan methodology has some limitations. Although its predictions were precise for the type-III case in previous subchapter 5.3, those for the type-IV case are inaccurate. The next subchapters deal with possible reasons for these discrepancies.

## 5.5 Combined Scan Predictions for Simple VSC System

Initially, it is emphasized that, based on the results outlined in subchapters 5.3 and 5.4 for the type-III and type-IV scenarios, it could be argued that the combined scan technique is not necessarily inadequate for stability assessment, but just overly conservative. This is due to the fact that the

technique aims at screening out potentially critical scenarios, which, in turn, should be validated by means of detailed EMT simulations. In that sense, in a practical case, for instance, the inaccurate predictions for the type-IV wind farm would result in additional investigations, namely, the detailed EMT studies, which, finally, would allow the verification that no risk is expected for this case. Nevertheless, it is noted that no real critical case would remain unseen by the technique, thus, corroborating the premise that it may just be too conservative.

This subchapter deals with the investigation of this premise. Goal is to verify the possibility of the combined scan technique missing a potentially critical condition and, thus, provide counter-examples to the premise of it being too conservative.

For this, the simple VSC system introduced in Chapter 4 is used. More specifically, the combined scan technique is applied to the system consisting of the VSC connected to a simple grid representation with different parametrization. Due to the reduced complexity of this system when compared to the realistic wind farm representations investigated earlier, the search for relevant conditions is accelerated and results become easier to grasp.

Several cases were simulated with varying PLL controller gains and, finally, a set of controller gains was found for which the above condition was found, namely, the combined scan technique predicts stability, but the detailed simulation shows the opposite.

The modified controller gains for the VSC are given in Table 5.1. The variations to the original controller gains proposed in subchapter 4.2 are also indicated.

Table 5.1 Modified controller gains of simple VSC system.

<b>Parameters</b>	<b>Value</b>	<b>Variation in %</b>	<b>Description</b>
$k_{p\_PLL}$	81.6270	-50%	PLL proportional gain
$k_{i\_PLL}$	92301 1/s	300%	PLL integral gain

Several grid strengths were analyzed, varying from 10 MVA to 3 MVA short-circuit power. In other words, different short-circuit ratios (SCR), which indicates the ratio between grid short-circuit power and the rated power of the simple VSC system (assumed 1 MVA), were taken into consideration. A constant X/R ratio of 5 is assumed in all cases. Finally, it is assumed that the simple VSC system receives current setpoints of  $i_{d,ref} = 0,95$  pu and  $i_{q,ref} = 0,1$  pu.

Initially, detailed EMT simulations were conducted to investigate the VSC performance under different grid strengths. Figure 5.7 illustrates the measured  $dq$ -currents for varying SCRs. The system is initialized with SCR of 10 (i.e., for grid strength of 10 MVA) and then the grid strength is gradually reduced until a SCR level of 3. It can be seen from Figure 5.7 that the smaller the SCR, the less damping the system has, i.e., the longer it takes to regain a steady-state condition, and, also, that the VSC system is not capable of withstanding a SCR of 3.

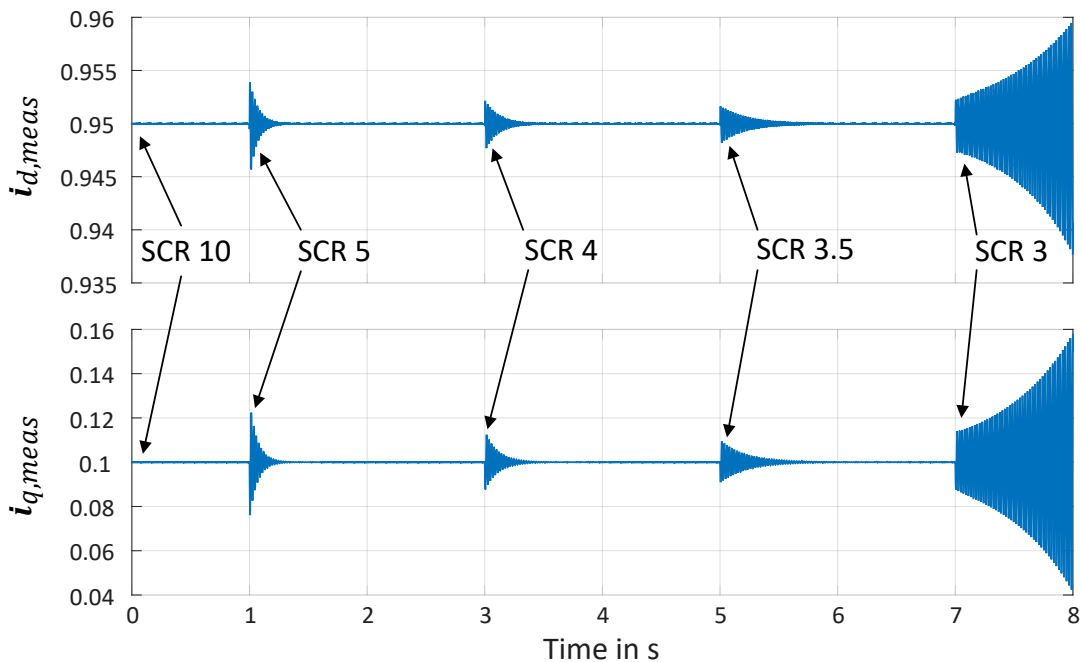


Figure 5.7 Detailed EMT simulation of simple VSC system under different SCR levels.

The combined scan technique is now applied to investigate these cases. It is noted, however, that the application of the technique is not possible for SCR of 3, since no steady-state condition is possible at this grid strength. Therefore, in the following, the VSC input impedances calculated for a SCR of 3.5 will be considered in the combined scans for a SCR 3. It is emphasized that this assumption is not expected to impact much the results, since it has been previously verified that the VSC input impedance do not vary significantly under different grid strengths. This assessment is illustrated in Figure 5.8.

As can be seen in Figure 5.8, the VSC input resistance is not affected by the different operating conditions imposed by the different grid strengths, whereas small variations are observed for the

input reactances. These variations remain, however, in the range of approximately  $0.2 \Omega$  for extreme cases of 10 MVA and 3.5 MVA grid strengths. The maximal difference, for instance, between SCR of 4 and 3.5 is less than  $0.04 \Omega$ .

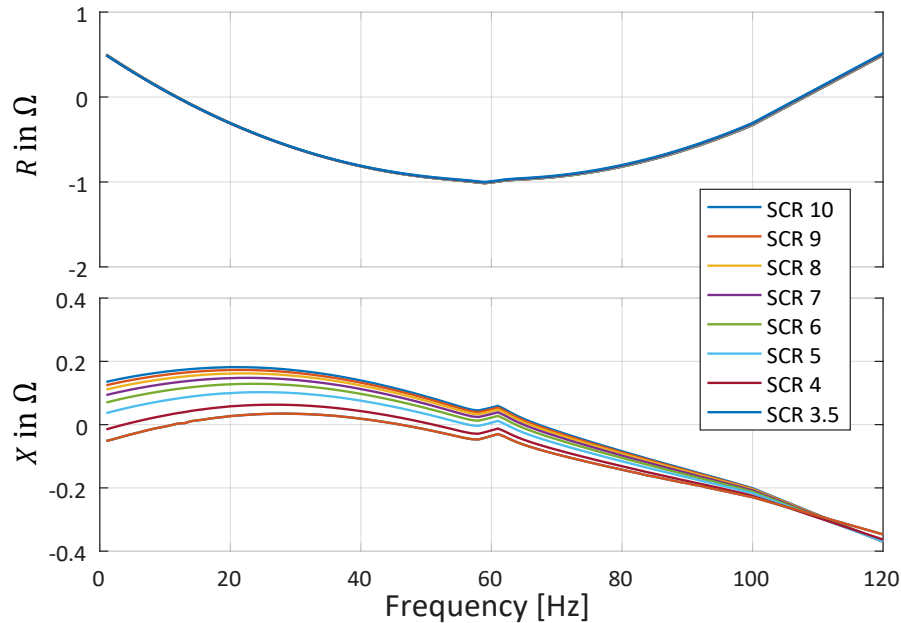


Figure 5.8 Input impedances of simple VSC system for different grid strengths.

The combined scan technique was applied for two of the cases investigated above, namely, the cases of a SCR of 10 and a SCR of 3. In other words, a case of a strong grid condition is now compared with a case of a weak grid condition. The results are illustrated in Figure 5.9.

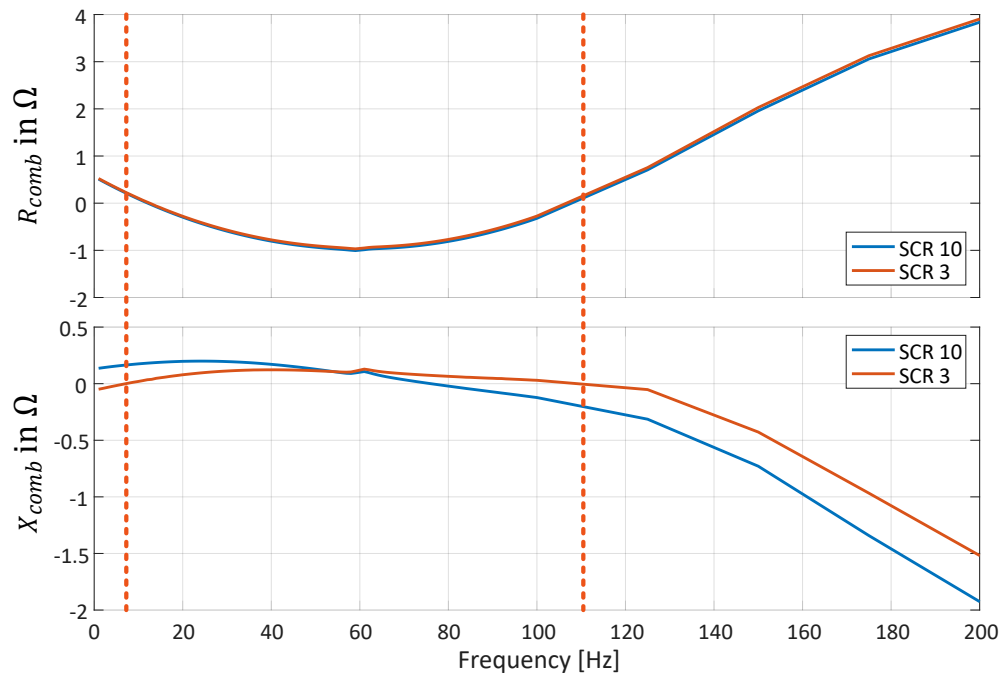


Figure 5.9 Combined scan results for simple VSC system for SCR of 10 and 3.

It is evident from Figure 5.9 that the combined scan technique failed to address the stability in both investigated cases. First, for a known unstable case of SCR of 3 (see the EMT simulation results in Figure 5.7), it can be seen that the combined resistance is positive for the reactance crossovers (indicated by the red dashed lines), thus indicating no potential issues, which is not correct. Second, for the stable case of SCR of 10, the combined resistance is clearly negative at the reactance crossover. Such conditions should indicate a potential issue, which is not seen (and also not expected for such a strong grid condition).

Additionally, it could be argued that the resistances illustrated in Figure 5.9 at the reactance crossovers for the case of a SCR of 3 are just “marginally” positive. Model or even numerical uncertainties, for instance, could be evoked to help explaining the misleading results. To address this hypothesis, the combined scan results for even lower SCR levels, for which obviously no stable operation of the VSC is possible, were calculated. They are illustrated in Figure 5.10.

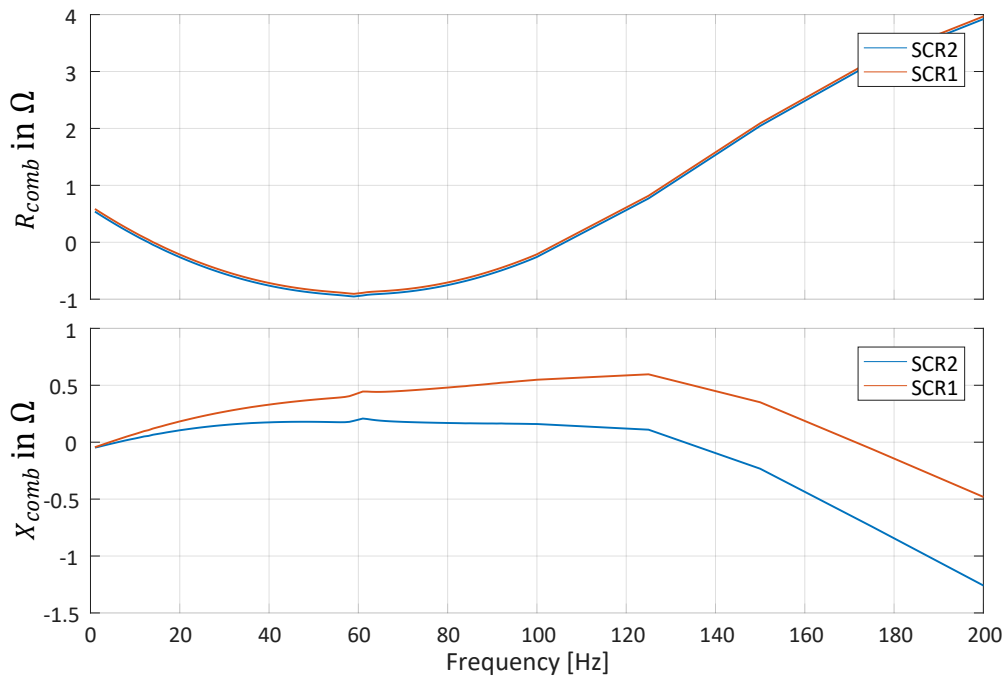


Figure 5.10 Combined scan results for simple VSC system for SCR of 2 and 1.

It can be observed in Figure 5.10 that reducing the SCR at the point of connection has, in fact, the effect of increasing the combined scan resistance at the reactance crossover frequencies. It is evident that the resulting stability predictions are contradictory to those expected for the system under extremely weak grid conditions and seen in the EMT simulation results.

Therefore, these results confirm that the inaccurate combined scan technique predictions for the type-IV wind farm were not a consequence of overly conservative assumptions. Other than that, they indicate as well inherent risks of the combined scan technique application, since wrong stability predictions are, indeed, possible.

## 5.6 Combined Scan Technique Limitations

Additional research was conducted to understand the limitations found for the combined scan technique for the investigated scenarios. In this context, it has been observed that the combined scan technique has similar roots to assessment techniques for subsynchronous oscillations in case of conventional synchronous generators. More specifically, similar stability criteria, i.e., based on a

negative resistance at reactance crossover frequencies, were as well proposed to address the induction generator effect as well as subsynchronous torsional oscillations in the context of synchronous generator based power plants, notably in [62], [63], [112], [135].

Although this stability criterion has been reported to perform well when applied to conventional synchronous generator based power plants, the question is raised if additional considerations are necessary to address modern power system structures with grid-connected inverters, such as the ones investigated in previous subchapters.

Recently, this approach relying on the value of the frequency dependent resistance at the reactance crossover frequency has been further extended to include the information of the slope of resistance and reactance curves in [136]. Its application has been reported to address subsynchronous oscillation analysis for direct-drive wind turbines with type-IV characteristic in [137] and for STATCOMs connected to weak and series-compensated grids in [138].

According to this methodology, a negative value for the resistance at the reactance crossover frequency is not enough to indicate a potential unstable condition. The stability of the system is proposed to be determined by the following criteria (see additional explanations in [136] and [138]):

- i) In case the investigated system has a reactance crossover at frequency  $f_r$ , the system is stable if the product of the system's resistance  $R_{sys}(f_r)$  and the slope of the system's reactance evaluated at the same frequency  $\left. \frac{d[X_{sys}(f_r)]}{df} \right|_{f_r}$  is positive. Otherwise, the system is predicted to be unstable. This condition summarized in

$$R_{sys}(f_r) \cdot \left. \frac{d[X_{sys}(f_r)]}{df} \right|_{f_r} > 0, \text{ otherwise system is unstable} \quad (5.11)$$

- ii) In case the investigated system has a resistance crossover at a given frequency  $f_r$ , the system is stable in case the product of the system's reactance  $X_{sys}(f_r)$  and the slope of the frequency dependent system resistance  $\left. \frac{d[R_{sys}(f_r)]}{df} \right|_{f_r}$ , both evaluated at  $f_r$ , is positive, otherwise the system is predicted to be unstable. This condition is summarized in

$$X_{sys}(f_r) \cdot \left. \frac{d[R_{sys}(f_r)]}{df} \right|_{f_r} > 0, \text{ otherwise system is unstable} \quad (5.12)$$

At this point it is noted that in [136]–[138], multivariable impedance representations in the  $dq$ -frame and in the augmented sequence domain (contrary to [132], where only positive sequence scan is applied) are used to address system stability. In such cases, the determinants of these multivariable representations are calculated to obtain an equivalent system impedance. The resulting equivalent resistance and reactance correspond to the real and imaginary parts of this determinant. The reasoning behind this approach is outlined in [136] and [138].

The application of the methodology proposed in [136]–[138] may change the conclusions derived for the combined scan results presented, for instance, in Figure 5.9 and Figure 5.10. It remains, however, to be verified if augmented sequence domain conclusions are also valid for the positive sequence scan only [132].

Recent works indicated that a single-input single-output representation for grid-connected inverters, for instance, the positive sequence representation, may have restrictions, as explained in [139]–[142]. Their results point to the need for the verification of the existence of asymmetric input impedances in considered wind farm models either in  $\alpha\beta$ - or in the  $dq$ -frames as well as for a consequent multivariable framework for the representation of these devices.

To investigate these aspects in depth, the analytical representations developed for the type-III and type-IV wind farms in Chapter 4 are used. These analytical representations consider the exact same operating conditions evaluated in subchapters 5.3 and 5.4 for which the combined scan technique has been applied.

The relations between  $dq$ -voltages at the PCC  $v_{dq,PCC}$  (system inputs) and  $dq$ -currents flowing into the wind farm from the grid  $i_{dq,GCI}$  (system outputs) were extracted. In other words, the transfer function between these input and output signals has been developed based on their state-space representations. Such relations (i.e., transfer functions) can be analytically calculated by applying the Laplace transformation to equation (4.4) and then solving it to the system outputs  $\mathbf{Y}(s)$ . The resulting formulation is provided as

$$\mathbf{Y}(s) = [\mathbf{C}(s\mathbf{I} - \mathbf{A})^{-1}\mathbf{B} + \mathbf{D}]\mathbf{U}(s) \quad (5.13)$$

where  $s$  is the Laplace operator.

The resulting transfer-functions expressing the relations between  $v_{dq,PCC}$  and  $i_{dq,GCI}$  can then be further understood as the input admittances of the wind farms in the  $dq$ -frame,  $\mathbf{Y}_{dq}(s)$ , given as

$$\begin{bmatrix} i_{d,GCI}(s) \\ i_{q,GCI}(s) \end{bmatrix} = \mathbf{Y}_{dq}(s) \begin{bmatrix} v_{d,PCC}(s) \\ v_{q,PCC}(s) \end{bmatrix} = \begin{bmatrix} Y_{dd}(s) & Y_{dq}(s) \\ Y_{qd}(s) & Y_{qq}(s) \end{bmatrix} \begin{bmatrix} v_{d,PCC}(s) \\ v_{q,PCC}(s) \end{bmatrix} \quad (5.14)$$

Following the procedure above indicated through equations (5.13) and (5.14), the frequency response of all four elements of the transfer-matrix  $\mathbf{Y}_{dq}(s)$  were calculated for the interval of 1 to 100 Hz and the results are illustrated in Figure 5.11.

The input  $dq$ -admittances were also calculated for the type-III wind farm following the same procedure. These are shown in Figure 5.12.

It is clear from Figure 5.11 that the input  $dq$ -admittances of the type-IV wind farm are asymmetric, i.e., conditions  $Y_{dd} = Y_{qq}$  and  $Y_{dq} = -Y_{qd}$  do not hold [63]. Interestingly, for the type-III wind farm case in Figure 5.12 the input  $dq$ -admittances are much closer to be balanced, since conditions  $Y_{dd} = Y_{qq}$  and  $Y_{dq} = -Y_{qd}$  hold almost precisely.

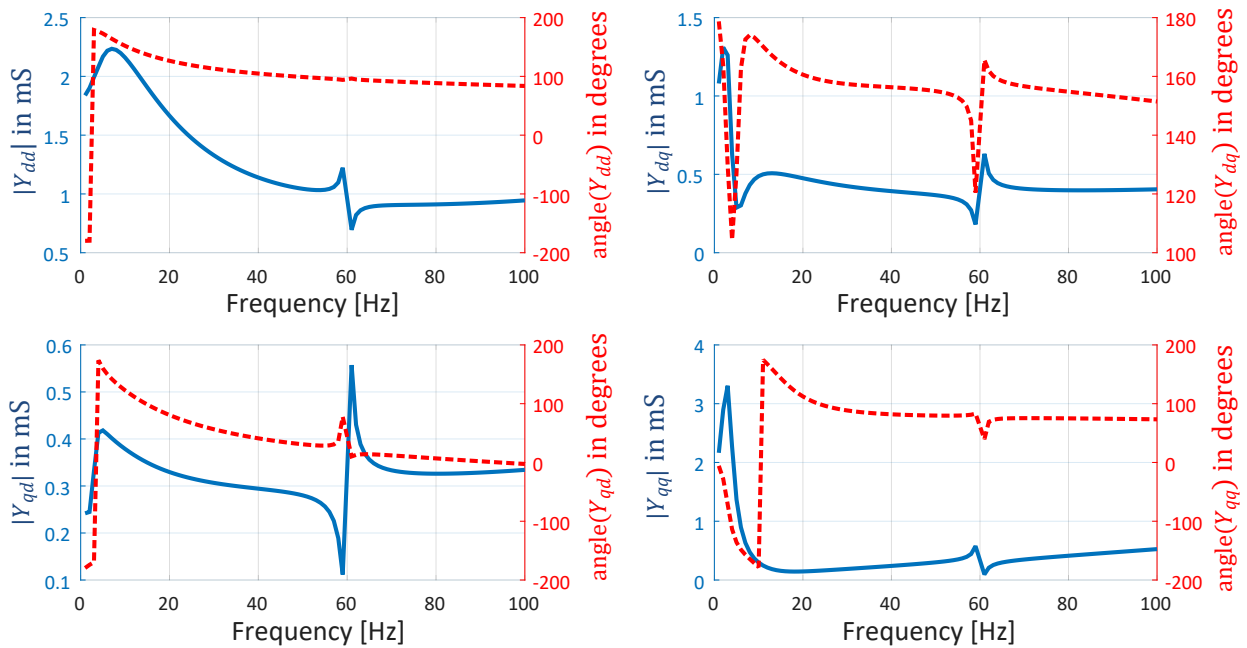


Figure 5.11 Analytical input  $dq$ -admittances of type-IV wind farm.

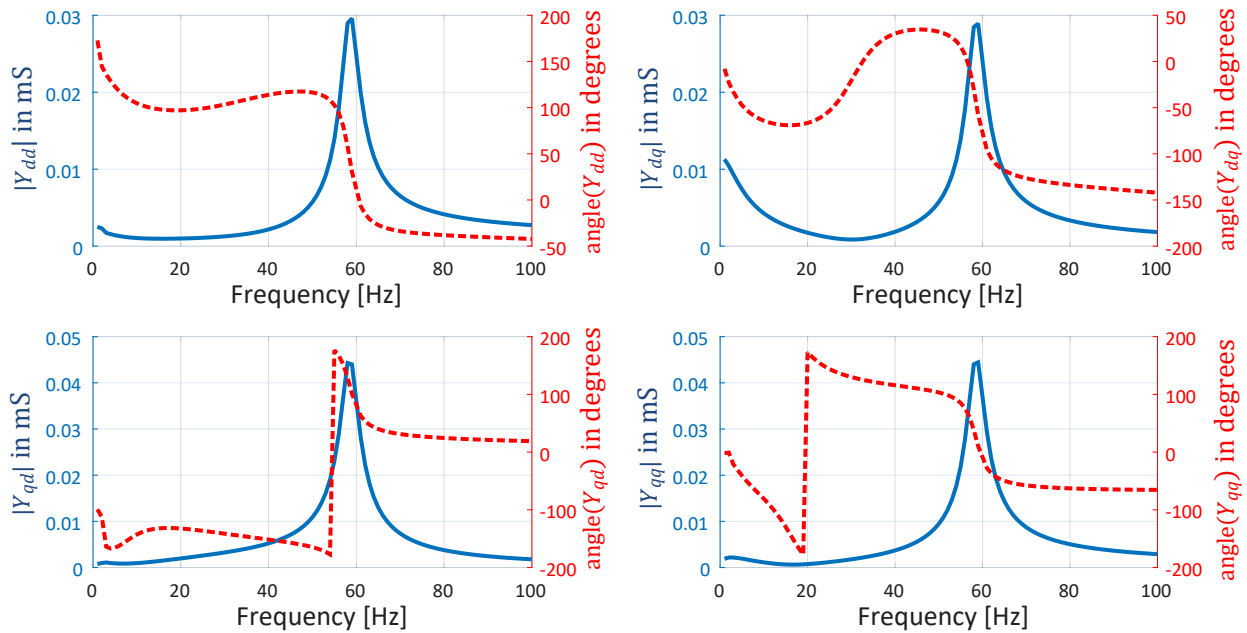


Figure 5.12 Analytical input  $dq$ -admittances of type-III wind farm.

The results illustrated in Figure 5.11 and Figure 5.12 corroborate the aforementioned discussions of previous works [139]–[142]. In other words, it is evident that a precise representation of the type-IV wind farm input admittances require a multivariable (i.e., multi-input multi-output) representation. The consideration of a single-input single-output frequency-dependent positive sequence impedance is not capable of capturing system couplings observed, for instance, in the  $dq$ -frame. For this reason, it is expected that this fundamental limitation of system representation poses an issue during stability assessment based on the combined scan technique. It is emphasized that the combined scan results were inaccurate for the type-IV case (see subchapter 5.4), which is the one with the most pronounced asymmetric admittance structures.

On the other hand, it is noted that the asymmetry is much less pronounced for the type-III wind farm in Figure 5.12. In fact, the system is close to balanced, i.e., the conditions  $Y_{dd} = Y_{qq}$  and  $Y_{dq} = -Y_{qd}$  are roughly respected. In such condition, it is expected that a positive sequence impedance representation may suffice and, thus, led to precise results in the stability assessment based on the combined scan technique as observed in subchapter 5.3.

Additionally, it is also highlighted at this point that modal analysis of the type-III wind farm scenario in subchapter 4.7 indicated that the system states mostly contributing to the oscillatory behavior of the critical mode are of electrical nature and attributed to the induction machine and series capacitance. These findings indicate not only a clear case of a typical SSR between electrical machine and series-capacitance, but also that the components involved in the unstable phenomena are of symmetric nature and have also been modeled accordingly.

As a consequence, these results also indicate that, in case the instabilities observed for the type-III wind farm scenario were attributed to asymmetric structures and components, the combined scan would possibly fail. This topic is covered in greater detail in next subchapter.

## **5.7 Asymmetric Input Admittance Characteristics**

Besides classical asymmetries of unbalanced systems and the ones known in the  $dq$ -frame, for instance, in the case of electrical machines with pole saliency [102], it has been observed in the framework of this thesis that controllers of grid-connected converters can significantly contribute to asymmetric input  $dq$ -admittances (or impedances) characteristics. This is demonstrated in this subchapter with focus on the simple VSC system introduced in subchapter 4.2.

It is emphasized that the concerned VSC electrical components are all of symmetrical nature, i.e., resistances and inductances of the output filter, for instance, are all modeled as three-phase symmetric devices, and are not expected to introduce asymmetries. Moreover, it is noted that only two control structures were assumed in the VSC system, namely, the PLL and the current regulator. Their controller schemes are, for convenience, shown again here in Figure 5.13.

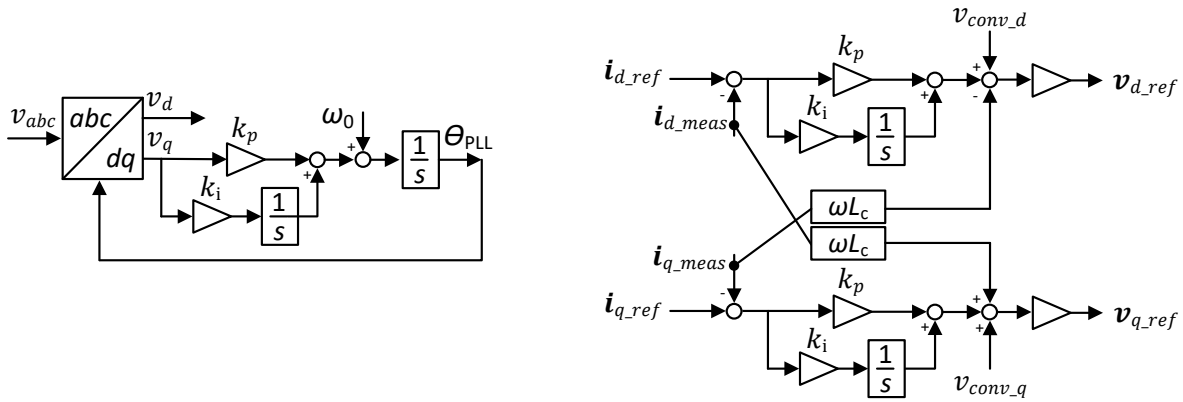


Figure 5.13 PLL and current regulator control schemes of simple VSC system.

By examining the control schemes illustrated in Figure 5.13, it is evident that the PLL has an asymmetric control structure. This is due to the fact that only the  $q$ -component of the voltage is controlled while the  $d$ -component is ignored. Differently than the PLL, however, it can be observed that the current regular scheme is of symmetrical nature, if assumed that its proportional and integrator gains,  $k_p$  and  $k_i$ , are equal, which is typically the case.

In order to evaluate the impact of the asymmetric control structure of the PLL in the overall VSC system, the analytical formulation of this system, extensively derived in subchapter 4.2, is used. Then, the input admittances of the VSC systems are extracted following the same procedure outlined and applied for the type-III and type-IV wind farms in previous subchapter 5.6. The resulting input  $dq$ -admittances calculated for the simple VSC system are shown in Figure 5.14.

It is readily visible from Figure 5.14 that the simple VSC system has an asymmetric input admittance characteristic. In other words, conditions  $Y_{dd} = Y_{qq}$  and  $Y_{dq} = -Y_{qd}$  do not hold. This can be explained by the asymmetric control structure imposed by the PLL.

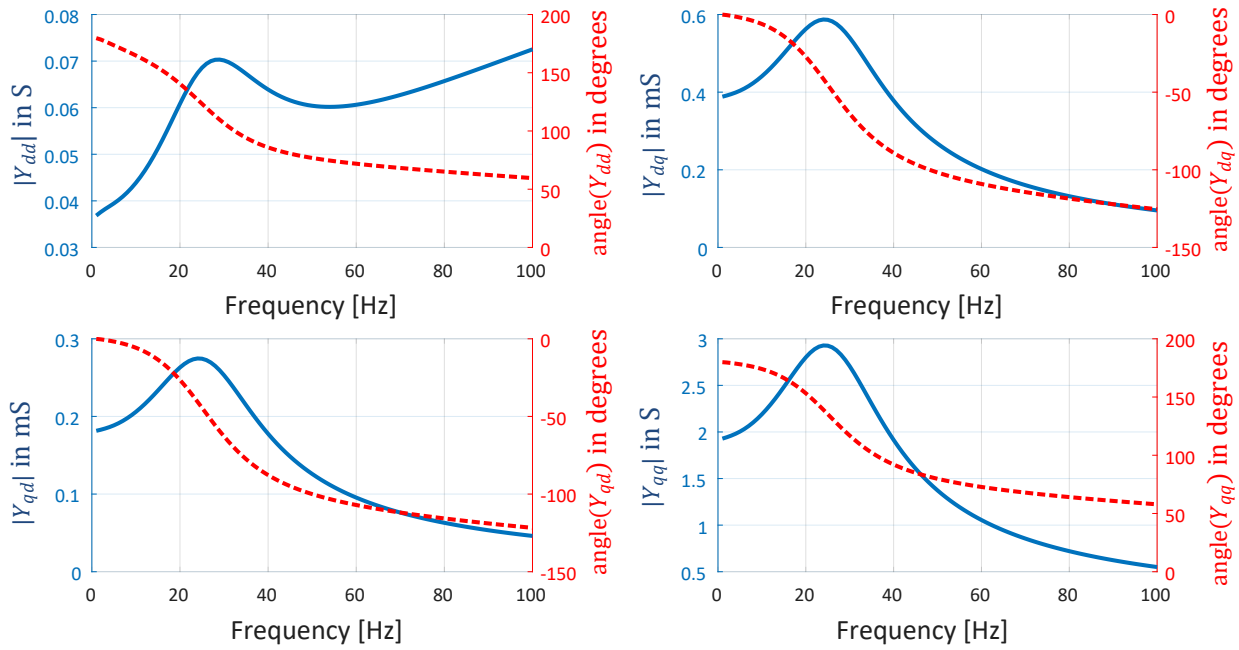


Figure 5.14 Input  $dq$ -admittances of simple VSC system.

To prove this point, a separate analysis is conducted. For this, the VSC system has been modified. The PLL control scheme has been bypassed in order to measure its impact in the overall input  $dq$ -admittances. More specifically, the PLL control structure has been replaced by a fictive block that generates an ideal reference angle for the VSC controllers. This is possible, since the steady-state condition can be calculated for the imposed VSC operating condition and, therefore, the steady-state PLL angle  $\theta_0$  can be computed. Moreover, since the grid frequency is constant (imposed by the grid voltage source), the angle  $\theta_0$  can be added to another angle resulting from the rated system rotation speed integration. This scheme is illustrated in Figure 5.15.

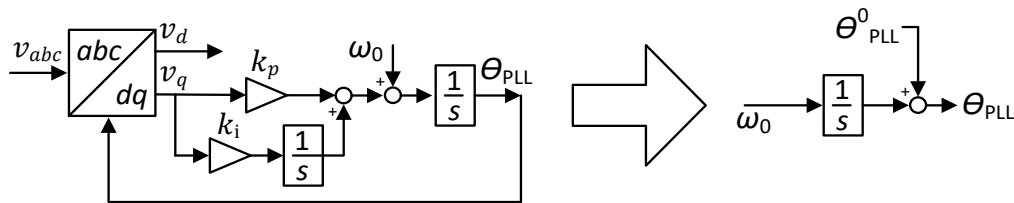


Figure 5.15 Reference angle calculation without PLL dynamics.

The corresponding analytical representation of the scheme illustrated on the right side of Figure 5.15 is simply done by directly considering the PLL angle  $\theta_{PLL}$  as a system input of the complete

system representation, thus, *bypassing* any dynamics. A final modal representation can be derived for the modified VSC system, as done in subchapter 4.2.

From the resulting simple VSC system analytical representation without PLL, it is possible to calculate the input  $dq$ -admittances as done above. The results are illustrated in Figure 5.16.

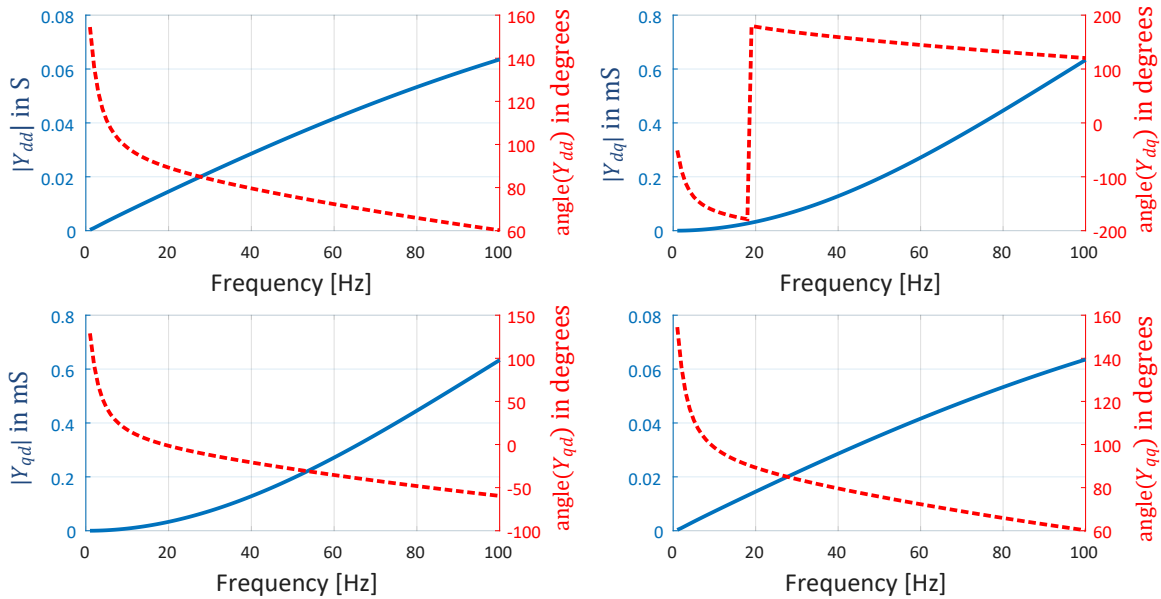


Figure 5.16 Input  $dq$ -admittances of simple VSC system without PLL dynamics.

It can be seen from Figure 5.16 that the exclusion of the PLL leads to symmetric input  $dq$ -admittances for the simple VSC system and, thus, confirms the expectations that, in this simple VSC case, the asymmetric input admittance characteristics are caused by the PLL.

It is important to note that these results indicate that typical grid-connected structures, especially those based on full-converter systems, are likely to have small-signal input  $dq$ -admittances (or impedances) of asymmetrical nature, since most of them rely on PLL schemes for reference angle extraction. Moreover, it is also to expect that additional typical controller add to these asymmetries. For instance, in the case of the type-IV wind turbine system outlined earlier in this theses, the  $d$ -channel of the outer-loop control is used to control the dc-link voltage and the  $q$ -channel the reactive power. They both are not only based on different PI-controller gains, but also control variables governed by different system dynamics.

Finally, it is emphasized that these findings and demonstrations, therefore, corroborate the argumentation that, under the perspective of small-signal impedance-based theory, typical grid-connected structures require a multivariable framework for their proper representation. Consequently, modern power systems, which are likely to consist of several of such systems with asymmetrical nature, as well.

## CHAPTER 6 DQ-SCANNING TECHNIQUE

This chapter proposes a methodology for the small-signal stability assessment of power systems, capable of addressing asymmetrical admittance or impedance characteristics and, thus, applicable to modern power systems structures. It is shown that the methodology is capable of properly extracting the required information from grids and grid-connected inverters, even in cases where these models are protected. This is demonstrated by comparing the results of the proposed technique with those obtained by rigorously analytical development of the corresponding systems. Finally, to test the capabilities of the new technique, it is applied to the same systems investigated earlier in this thesis as well as to additional scenarios. The proposed technique as well as specific investigations carried out in this work package are also subject of following publication [110].

### 6.1 Multivariable Impedance-based Stability Assessment

It has been demonstrated in Chapter 5 that grid-connected inverters and, thus, modern power system require a multivariable, i.e., multi-input multi-output, framework to allow for proper small-signal impedance-based representation.

To the author's knowledge, multivariable impedance-based stability assessment of grid-connected inverters was first rigorously conducted in [127]. Moreover, studies presented in [128], [129], [143]–[145] further paved the way for a multivariable impedance-based stability assessment in the  $dq$ -frame.

It is noted here, however, that multivariable impedance-based stability assessment is not necessarily done in the  $dq$ -frame. As outlined in [128] and extensively demonstrated in [146], analysis can equivalently be conducted, for instance, in the  $\alpha\beta$ -frame.

Additionally, other works aimed at expanding the positive sequence impedance representation suggested in [131] to account for the negative sequence impedance. Notably, [147] and [148] demonstrated how a converter can be modelled by a positive and a negative sequence impedance directly in the phase domain. However, it is noted that impedance couplings between positive and negative sequence impedances were not identified in these works.

Positive and negative sequence domain couplings were subject of study in [139] and [149], which proposed a so-called modified sequence-domain impedance definition. According to these works,

the modified sequence domain can be further interpreted as positive and negative sequence impedance representations together with their couplings. Moreover, systems with positive-negative sequence impedance couplings are classified as mirror frequency coupled according to these works and it is shown that these couplings are present when  $dq$ -impedances are asymmetric.

More recently, however, it has been analytically demonstrated in [150] that the modified sequence-domain proposed in [139] and [149] are actually merely a transformation of the  $dq$ -frame transfer matrix representation with real space vectors into a matrix based on complex space vectors. In other words, the modified sequence-domain remains a  $dq$ -domain impedance-based representation, however complex. Furthermore, it is shown that the positive and negative sequence components correspond to those space vectors in  $\alpha\beta$ -frame, however evaluated at their positive and negative frequencies given by  $\pm\omega_0$ , where  $\omega_0$  is the system rated rotational speed.

The above works provide theoretical basis for the multivariable impedance-based stability assessment of grid-connected inverters. However, due to their theoretical and analytical nature, the considered grid-connected inverters and systems used in their studies and demonstrations remained oversimplified. For instance, the voltage-source converters schemes used focused mostly solely on inner control loops and PLL. Moreover, these studies also assumed constant dc-link voltage and neglected outer loop controls. These considerations are similar to the simple VSC representation analytically developed in subchapter 4.2.

It remains, therefore, of great importance to investigate the application of multivariable impedance-based stability assessment in conjunction with more realistic considerations of grid-connected inverters and power system representations.

Additionally, with the perspective of power system industry, it remains to be determined whether the effects of outer control loops can be properly captured by means of appropriate techniques, thus, avoiding the need for rigorously analytical development.

To address these points, the next subchapters of this thesis propose, in a first step, a new methodology for extracting  $dq$ -impedances and  $dq$ -admittances of grid and grid-connected inverters, respectively, and, in a second step, validate the effectiveness of the proposed technique against theoretical values extracted from their rigorously developed analytical representations.

## 6.2 Application of the DQ-Scanning Technique

A methodology, henceforth named DQ-Scanning, is proposed to extract input  $dq$ -impedances and  $dq$ -admittances of grid and grid-connected inverters, respectively, through an enhanced frequency scanning technique in an EMT software package.

More specifically, the DQ-Scanning aims at the extraction of small-signal relations (transfer functions) between input currents and voltages, and vice-versa, which are then further interpreted as input impedances and admittances, respectively, for the impedance-based stability assessment.

As the impedance-based stability assessment suggests, the DQ-Scanning technique relies on the separation of the system to be analyzed into two subsystems. Typically, the point-of-common-coupling (PCC) is suggested as the partition point, but in case voltage control is applied at the PCC, another partition point should be taken to avoid controller saturation resulting from the application of ideal voltage sources by the DQ-Scanning. In such cases, a busbar one node away from the PCC, typically after a transmission line, can be adopted as a partition point.

Figure 6.1 illustrates the DQ-Scanning application to a wind farm system from which the input  $dq$ -admittances are to be extracted.

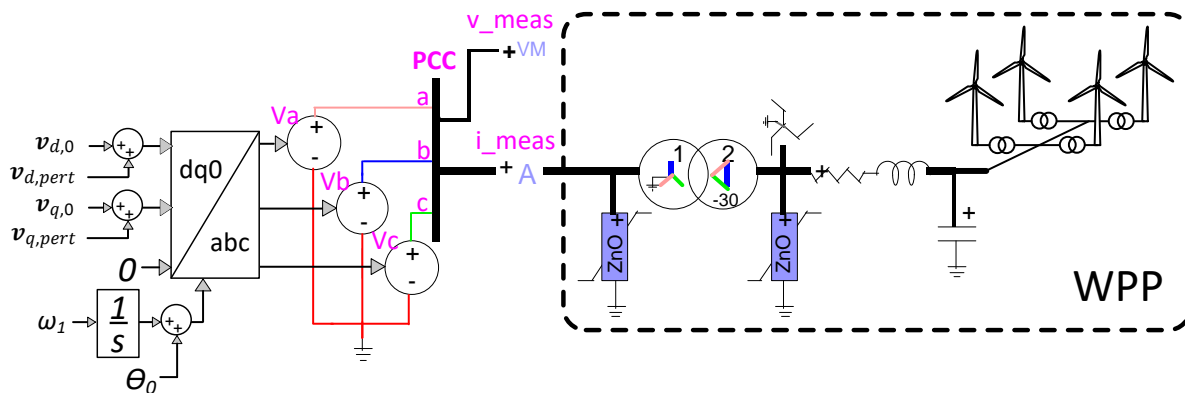


Figure 6.1 DQ-Scanning application to a wind power plant (WPP).

The procedure for the input  $dq$ -admittances extraction of grid-connected inverters is summarized in the following steps:

- i) Controlled voltage sources are connected to the PCC of the analyzed grid-connected inverter subsystem.

- ii) Appropriate single-tone perturbations  $v_{d,pert}$  and  $v_{q,pert}$  are applied separately on top of  $v_{d,0}$  and  $v_{q,0}$  in the  $dq$ -axes.
- iii) A  $dq$ -to- $abc$  transformation is used to convert the generated input  $dq$ -signals into  $abc$ -values for the EMTP simulation.
- iv) Three-phase voltages and currents are monitored at the PCC and back-transformed into the  $dq$ -frame.
- v) Spectral analysis is performed on the monitored  $v_{dq,meas}$  and  $i_{dq,meas}$  signals and input  $dq$ -admittances  $Y_{dd}$ ,  $Y_{dq}$ ,  $Y_{qd}$  and  $Y_{qq}$  are calculated

$$\begin{aligned} Y_{dd}(f_i) &= i_d^d(f_i)/v_d^d(f_i) & Y_{dq}(f_i) &= i_d^q(f_i)/v_q^q(f_i) \\ Y_{qd}(f_i) &= i_q^d(f_i)/v_d^d(f_i) & Y_{qq}(f_i) &= i_q^q(f_i)/v_q^q(f_i) \end{aligned} \quad (6.1)$$

where superscripts  $d$  and  $q$  indicate in which of the  $dq$ -axes the perturbation was applied and  $f_i$  is the perturbation frequency.

A similar procedure is applied for the extraction of the input  $dq$ -impedances of the grid, however it is based on current perturbations. Figure 6.2 illustrates the DQ-Scanning for the grid subsystem of the proposed benchmark as seen from the PCC.

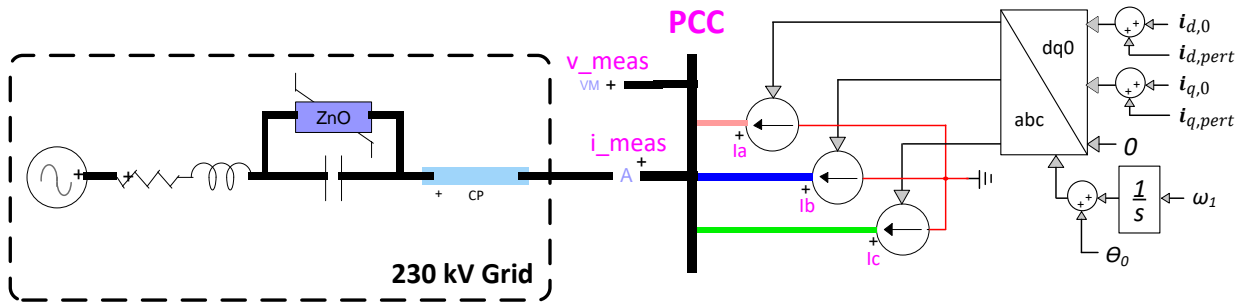


Figure 6.2 DQ-Scanning application to grid subsystem in EMTP.

At this point, it is emphasized that, although in most cases it would be possible to apply the exact same steps outlined above to extract the input  $dq$ -admittances, this is not recommended. Reason is the fact that the input admittances may contain right-half-plane zeros that, when inverted, become unstable poles in the input impedance representations [151]. As it will be shown further in this chapter, such condition (i.e., with unstable poles), if not properly addressed, may lead to incorrect stability assessments.

The procedure for the grid subsystem is summarized as follows:

- i) Controlled current sources are connected to the PCC.
- ii) Appropriate single-tone perturbations  $i_{d,pert}$  and  $i_{q,pert}$  are applied separately on top of  $i_{d,0}$  and  $i_{q,0}$  in the  $dq$ -axes.
- iii) A  $dq$ -to- $abc$  transformation is used to convert the generated input  $dq$ -signals into  $abc$ -values for the EMTP simulation.
- iv) Three-phase voltages and currents are monitored at the PCC and back-transformed into the  $dq$ -frame.
- v) Spectral analysis is performed on the monitored  $v_{dq,meas}$  and  $i_{dq,meas}$  signals and input  $dq$ -admittances  $Z_{dd}$ ,  $Z_{dq}$ ,  $Z_{qd}$  and  $Z_{qq}$  are calculated as

$$\begin{aligned} Z_{dd}(f_i) &= v_d^d(f_i)/i_d^d(f_i) & Z_{dq}(f_i) &= v_d^q(f_i)/i_q^q(f_i) \\ Z_{qd}(f_i) &= v_q^d(f_i)/i_d^d(f_i) & Z_{qq}(f_i) &= v_q^q(f_i)/i_q^q(f_i) \end{aligned} \quad (6.2)$$

where superscripts  $d$  and  $q$ , again, indicate in which of the  $dq$ -axes the perturbation was applied and  $f_i$  is the perturbation frequency.

It is emphasized that the steady-state voltages in the  $dq$ -frame,  $v_{d,0}$  and  $v_{q,0}$ , in the case of the grid-connected inverters, as well as the corresponding steady-state currents,  $i_{d,0}$  and  $i_{q,0}$ , in the case of the grid, are required and play an important role in the DQ-Scanning application. These are ideally obtained from a steady-state solution in EMTP for the chosen operating condition. If that is not possible, for instance, in cases where the complete model is not available, their values can be estimated from a load-flow calculation considering the available grid model. It is emphasized, however, that their consideration is important, since they guarantee that the small-signal input admittances and impedances are extracted for an operating condition considering interconnected grid and grid-connected inverters.

Moreover, it is also highlighted that, contrary to other existing methodologies, notably the combined scan technique [132] and the methodologies outlined in [143] and in [136], the DQ-Scanning technique is based on a separate analysis of grid and grid-connected inverters. This establishes an advantage of the proposed methodology, since DQ-Scanning of grid and grid-connected inverters can be assigned to different stakeholders during interconnection projects. It is, therefore, possible

that extraction of grid input  $dq$ -impedances remain the responsibility of system operators while grid-connected inverters input  $dq$ -admittances are calculated by equipment manufacturers (or project developers). This may allow for stability assessments in very early stages of interconnection projects, since  $dq$ -impedances and  $dq$ -admittances could be exchanged without raising much concerns on intellectual property and further assessment and verification of results is possible based on black-boxes.

Additionally, it is also noted that the DQ-Scanning technique aims at the direct extraction of the two-port (i.e., the  $dq$ -channels) input impedance and admittance representation of grid and grid-connected inverters, no matter their size and complexity. This avoids, for instance, concerns related to the required order for proper system representation. This constitutes a clear distinction to previous works, whose approaches are based on matrix-fitting for the extraction of state-space matrices for the investigated systems [152], [153].

Another important aspect of the DQ-Scanning concerns the applied perturbation signals in the  $dq$ -channels, i.e.,  $v_{dq,pert}$  and  $i_{dq,pert}$ . It is noted that these signals need to be small enough to satisfy the small-signal assumptions and high enough to allow for proper signal processing. Several signal shapes and characteristics could be considered for the perturbation signals [143], [148], [152]–[154]. Notably, reference [155] also reviews implications of multi-tone injections; however results recently published in [156] indicate that simple single-tone sinusoidal perturbations are more suitable when addressing manufacturer specific models.

Finally, still with regards to perturbation signals, investigations carried out in the framework of this thesis indicated that faithful consideration of power system equipment, which has been overlooked in previous works, requires that special attention be paid to the definition of the perturbation signals. This is demonstrated in the next subchapter.

### **6.3 Impact of Realistic Equipment Modeling**

Subchapter 3.3.1 provided insights of the impact of realistic equipment modeling in detailed EMT studies focusing on the analysis of low-frequency phenomena. This subchapter deals with their consideration in the DQ-Scanning technique. For this, the DQ-Scanning has been applied to the same detailed representations of the type-III wind farm previously investigated in this thesis by

means of detailed EMT simulations in subchapter 3.5, modal analysis in subchapter 4.7 and combined scan technique in subchapter 5.3.

For the application of the DQ-technique, however, simple sinusoidal perturbations with constant amplitudes of 0.01 and 0.02 per unit of the nominal voltage at the PCC were applied. Moreover, to reduce impacts of spectral analysis, long perturbation times were assumed, allowing therefore small frequency bin and, thus, a higher precision in the evaluation. The resulting input  $dq$ -admittances extracted for the two cases with different perturbation amplitudes are illustrated in Figure 6.3 for the frequency range from 50 to 70 Hz.

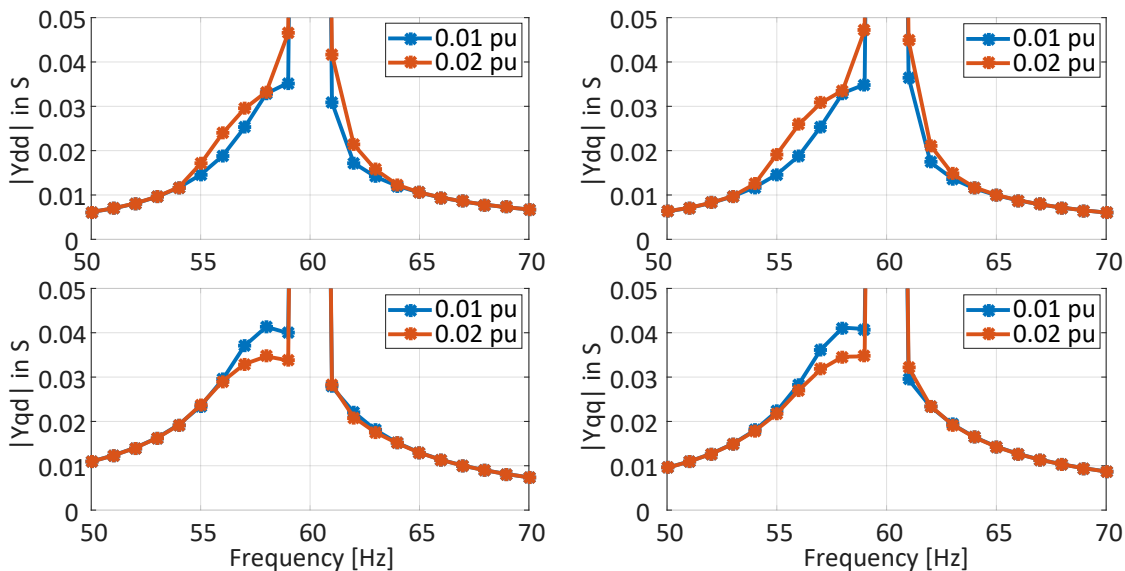


Figure 6.3 Input  $dq$ -admittances for type-III wind farm.

It is evident from Figure 6.3 that the assessed input  $dq$ -admittances differ depending on the perturbation amplitude, although the system investigated remained the same in both cases. Moreover, it has been observed that such discrepancies are mostly concentrated in the 60 Hz region (in  $dq$ -frame), which corresponds to the low-frequency range in the stationary  $abc$ -frame.

Detailed investigation for root-cause of these differences revealed that these are mostly due to the consideration of realistic representation of transformer and type-III wind turbines models.

More specifically, in the case of transformers, their core saturated due to the low-frequency voltage perturbations, i.e., the voltage perturbations applied by the DQ-Scanning in the region of 60 Hz in

the rotation  $dq$ -frame. This is understandable, since the flux in the magnetizing branch of the transformer is inversely proportional to the frequency of the applied voltages. It is emphasized, however, that such phenomenon is only possible when the magnetizing branch is modeled with saturation, which has been overlooked by previous works.

In the case of type-III wind turbines, the low frequency voltages resulting from the DQ-Scanning perturbations in the range of 60 Hz in the  $dq$ -frame give rise to low-frequency stator currents. It is important to note that these resulting stator currents can have relatively large amplitudes, since, at these low frequencies, they are mainly limited by the winding resistances, which are generally low. The air gap flux created by the low-frequency stator currents also rotates at low speed. As the machine rotor speed is much higher than that of the air gap flux, the induced voltages in the rotor winding can have relatively large magnitudes, and their frequency is higher than the nominal slip frequency. These induced voltages result in rotor currents that are then added to those of the machine unperturbed condition. Consequently, the resulting rotor currents can get significantly distorted and considerably impact the operation of the rotor-side converter current regulator. In the framework of these investigations, it has been observed that even small voltage perturbations were enough to push the operating condition of the rotor-side converter current regulator far from the unperturbed one, even leading to regulator reaching its saturation zone.

Finally, it is noted that such conditions in which transformers are saturated and the rotor-side converter of type-III wind turbines is pushed to operate far from its steady-state operating point without perturbation are not representative of the normal operation of the interconnection. In fact, they are a consequence of the perturbations applied. Moreover, it has been seen that even voltages perturbations in the order of 0.02 per unit of the rated voltage were enough to impact the DQ-Scanning results qualitatively, especially in these low-frequency ranges, eventually resulting in incorrect small-signal input  $dq$ -admittance assessments.

To overcome these issues and still allow for faithful consideration and modeling of components, modifications and improvements are suggested in the following subchapter for the perturbations signals applied in the DQ-Scanning technique.

## 6.4 Enhanced Perturbation Signals for Realistic Systems

To deal with detailed and realistic modeling of power system equipment and grid-connected inverters, a different perturbation signal is proposed in this thesis.

Separate sinusoidal perturbations of the  $dq$ -axes are still assumed (as in previous subchapter), however with variable amplitude and perturbation times to take into account the experienced constraints of faithful modeling representations.

More specifically, to avoid issues encountered with the applied low-frequency perturbations, perturbations amplitudes  $a_w$  are suggested to become smaller and perturbations times larger the closer the perturbation frequency (in the  $dq$ -frame) is to the system rated frequency. This reduces the risks, for instance, of triggering transformer saturation and of reaching controller limits in type-III wind turbine systems due to low-frequency voltage perturbations applied to the investigated system. The typical perturbation signal used in the DQ-Scanning technique to extract input  $dq$ -admittances is illustrated in Figure 6.4.

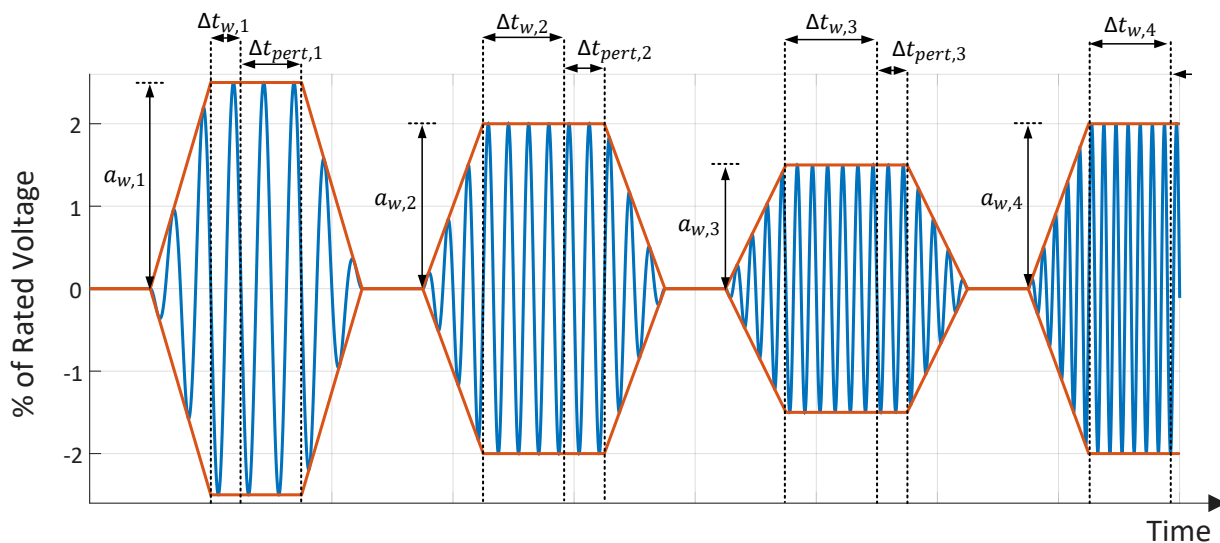


Figure 6.4 Perturbation signal characteristics applied by the DQ-Scanning technique.

As can be seen in Figure 6.4, sinusoidal perturbations are applied sequentially and waiting times between perturbations are introduced to guarantee a steady-state condition of the investigated subsystem prior to application of a new perturbation with another frequency.

Additionally, perturbation signals are ramped up and down instead of being applied stepwise. Stepwise perturbations (or simply frequency changes resulting in stepwise phase jumps) were found to trigger nonlinearities in specific cases. For instance, in case of series-compensated transmission lines, a stepwise voltage perturbation may result in currents with dc-components that, depending on line resistances and system loading conditions, decay slowly. These components, if not avoided or properly considered in the spectral analysis, could lead to incorrect small-signal input impedance (or admittance) assessments.

It is noted at this point that the perturbation signal illustrated in Figure 6.4 assumes one single simulation in an EMT software package. In other words, in one single EMT simulation, the small-signal system characteristics are assessed for different frequencies. Another possible implementation could rely on using snapshots of time-domain simulation, as available in EMTP [115]. In this case, a snapshot of the investigated system is taken for the considered steady-state condition. Then, separate simulations are performed for each perturbation frequency, which start from the steady-state operating condition imposed by the snapshot, thus avoiding the need of ramp downs and waiting times between perturbations.

Based on the fact that flux in the magnetizing branch of transformers is inversely proportional to the frequency of the applied voltage, good results were obtained by defining the perturbation amplitudes according to following relation

$$a_{w,i} = \frac{|f_{rated} - f_i|}{f_{rated}} a_{w,max} \quad (6.3)$$

where  $a_{w,max}$  is the maximal perturbation amplitude,  $a_{w,i}$  the perturbation amplitude to be applied,  $f_{rated}$  the system nominal frequency and  $f_i$  the perturbation frequency. To avoid large perturbation amplitudes in cases the numerator becomes large and to still allow for small-signal characteristics assessment at rated frequency,  $a_{w,i}$  can be limited after application of (6.3) as

$$a_{w,i} = \begin{cases} a_{w,i} = a_{w,max}, & \text{if } a_{w,i} > a_{w,max} \\ a_{w,i} = a_{w,min}, & \text{if } a_{w,i} < a_{w,min} \end{cases} \quad (6.4)$$

where  $a_{w,min}$  is defined as the minimal perturbation amplitude.

Moreover, waiting times and perturbation times were also defined as function of each applied perturbation frequency. In the case of waiting times  $\Delta t_{w,i}$  (i.e., the time given to investigated systems

to reach steady-state prior the evaluating time window), these are calculated for each perturbation frequency as a function of the difference between rated and perturbation frequency as

$$\Delta t_{w,i} = \frac{n_{wait}}{|f_{rated} - f_i|} \quad (6.5)$$

where  $n_{wait}$  is a factor (user input) used to increase the waiting time as a function of the inverse of the absolute difference between rated and perturbation frequencies and is the same for all perturbation frequencies. It avoids very small waiting times in case the difference between  $f_{rated}$  and  $f_i$  gets relatively large. Also, to avoid very large waiting times when  $f_i$  approaches  $f_{rated}$ , the waiting time is limited by a user defined maximal waiting time  $\Delta t_{w,max}$ , as follows

$$\Delta t_{w,i} = \Delta t_{w,max}, \text{ if } \Delta t_{w,i} > \Delta t_{w,max} \quad (6.6)$$

In the case of perturbation times  $\Delta t_{pert,i}$ , these are calculated as a function of a user defined number of perturbation periods  $n_{pert}$  as given in

$$\Delta t_{pert,i} = \frac{n_{pert}}{f_i} \quad (6.7)$$

As can be seen in (6.7), perturbation times are not dependent on the difference between rated and perturbation frequencies. This is not necessary, since the waiting times already take this difference into account and, thus, the system is given enough time to reach steady-state condition after perturbation ramp up. It suffices then to analyze  $n_{pert}$  numbers of the perturbation period.

At this point, it is emphasized that spectral analysis is applied to the time windows defined by  $\Delta t_{pert,i}$  of the monitored signals. More specifically, Discrete Fourier Transform (DFT) is applied to the  $dq$ -components of the measured voltages and currents,  $v_{dq,meas}$  and  $i_{dq,meas}$  respectively. Nevertheless, certain aspects of the spectral analysis should not be overlooked when applying the DFT, as they could eventually lead to misleading results.

For instance, it is noted that equation (6.7) can lead to irrational numbers of perturbation times (e.g., assuming  $f_i$  equal 3 Hz). Especially in cases when numerical simulation time steps  $T_s$  are relatively large, for example, considering the  $T_s = 50 \mu s$  suggested for hybrid model of the wind turbine in Chapter 2, it is not possible to capture an exact integer number of perturbation periods assuming  $f_i$  equal 3 Hz. As a consequence, spectral leakage results from the DFT analysis.

Additionally, it is also emphasized that, when performing EMT simulation based on faithful and realistic equipment modeling, consideration of non-transposed transmission lines, asymmetric loads and harmonics result in small oscillations in the measured signals  $v_{dq,meas}$  and  $i_{dq,meas}$ .

Luckily, in most cases, these oscillations are a function of the rated system frequency  $f_{rated}$ . For this reason, it is suggested that the perturbation times  $\Delta t_{pert,i}$  be not only an integer number of the perturbation period, but also an integer number of periods defined by the fundamental frequency and by the numerical integration time step  $T_s$ .

For instance, taking the aforementioned example assuming  $f_i$  equal 3 Hz into account, a  $T_s$  of 50  $\mu$ s and a rated frequency of 60 Hz, instead of taking the irrational number defined by  $\Delta t_{pert,i} = 1/3$  s, the applied perturbation time is recalculated to be  $\Delta t_{pert,i} = 1$  s. As such, it considers exact 3 periods of the perturbation period, 60 periods of the fundamental frequency and 20000 periods of the applied numerical integration time step.

It has been observed that such considerations reduce the possibility of having spectral leakage when applying the DFT in the monitored signals and, thus, reduce risks of incorrect assessments. This is especially important in cases when the DQ-Scanning is automated in EMT software packages, since such details are likely to be overlooked.

The implementation of the above considerations to take an integer number of periods of the rated, perturbation and numerical integration frequency (i.e., the inverse of  $T_s$ ) at the same time into account is based on a least common number of numerical integration time steps  $T_s$  logic. Its exact implementation can be found, for instance, in file *run\_DQscan\_voltage\_WPP.m* in [105].

Finally, it is emphasized that the exact definition of maximal and minimal perturbation amplitudes, ramp rates and number of waiting and perturbation periods is left to the engineering judgement based on the available knowledge of the investigated system. This is because, in practical cases, typical considerations from the field of system identification, such as compromises between precision and computation times, can be applied on a project specific basis. For instance, rapid impedance or admittance assessments are possible, however usually at the cost of precision. In this work, perturbation amplitudes varying between 0.002 and 0.025 per unit of the rated voltage at the partition point were applied together with perturbation times that varied from 0.1 to 10 s, depending on

the applied perturbation frequency. Ramp times were set fixed for all perturbation frequencies as 1 s and also 1 s was considered between ramp down and another ramp up of the perturbation signals.

## 6.5 Analytical Validation of the DQ-Scanning Technique

To validate the capability of the DQ-Scanning technique to correctly extract  $dq$ -admittances given faithful and realistic modeling of investigation systems, its results are compared with those obtained through rigorous analytical development in this subchapter. For this, the analytical representations developed for the type-III and type-IV wind farms in Chapter 4 are used.

It is emphasized that such validation is relevant, especially when considering the application of the DQ-Scanning technique in practical cases, since it allows a comparison from the results one would obtain from black-box models, typically the case in industry, to the ones one would obtain in the ideal case of having access to all components and controllers detailed models.

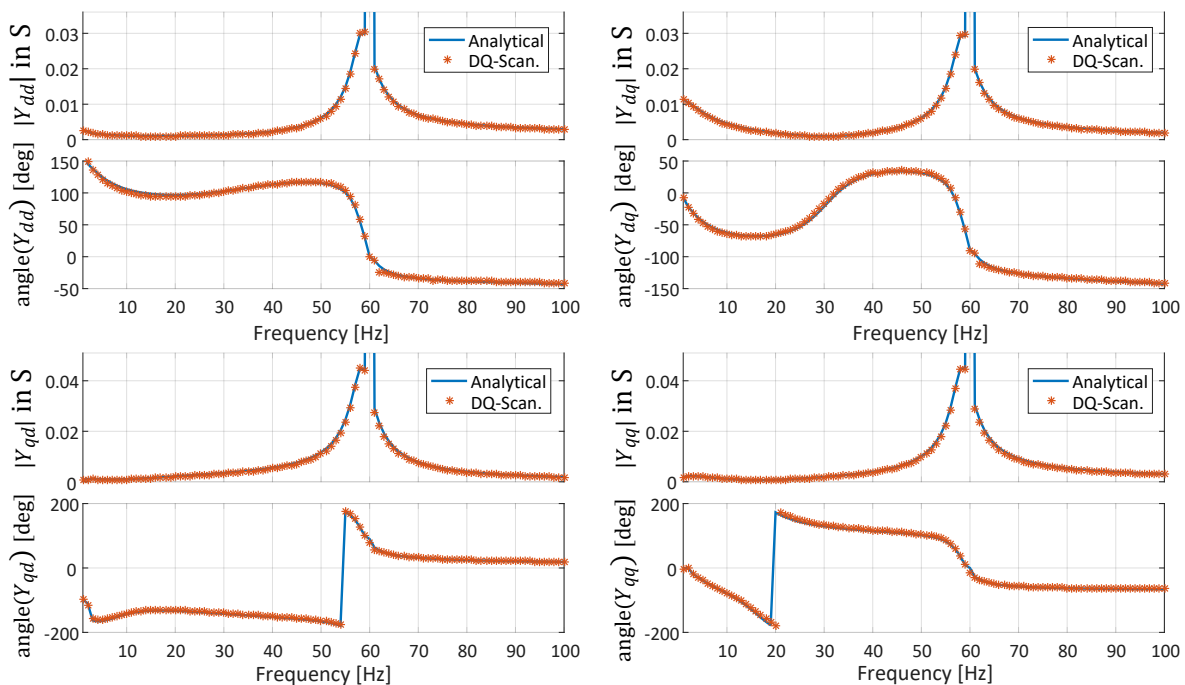


Figure 6.5 Input  $dq$ -admittances of type-III wind farm: DQ-Scanning vs. analytical.

Figure 6.5 illustrates this comparison for the input  $dq$ -admittances in the case of the type-III wind farm. The DQ-Scanning was performed for all integer frequencies ranging from 1 to 100 Hz.

Additionally, the same analysis has also been conducted for the type-IV wind farm. The results are shown in Figure 6.6. Again, in the interest of figure readability, the results are shown only for the range from 1 to 100 Hz.

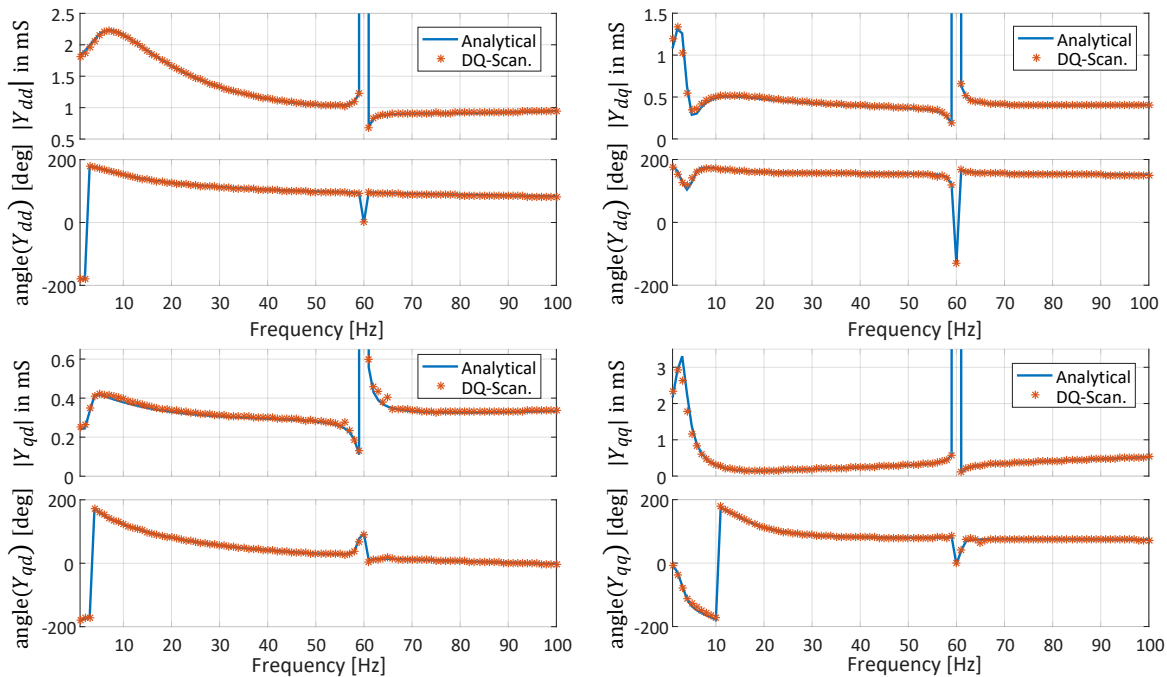


Figure 6.6 Input  $dq$ -admittances of type-IV wind farm: DQ-Scanning vs. analytical.

It is evident from Figure 6.5 and Figure 6.6 that the DQ-Scanning technique was capable of properly assessing the input  $dq$ -admittances of both wind farms, even with detailed consideration of their power equipment.

Additionally, following the methodology outlined in subchapter 6.2, the current perturbation based DQ-Scanning is also applied to the benchmark grid to extract its small-signal input  $dq$ -impedances as seen from the PCC of the interconnection. The comparison between the DQ-Scanning results and the analytical ones are shown in Figure 6.7.

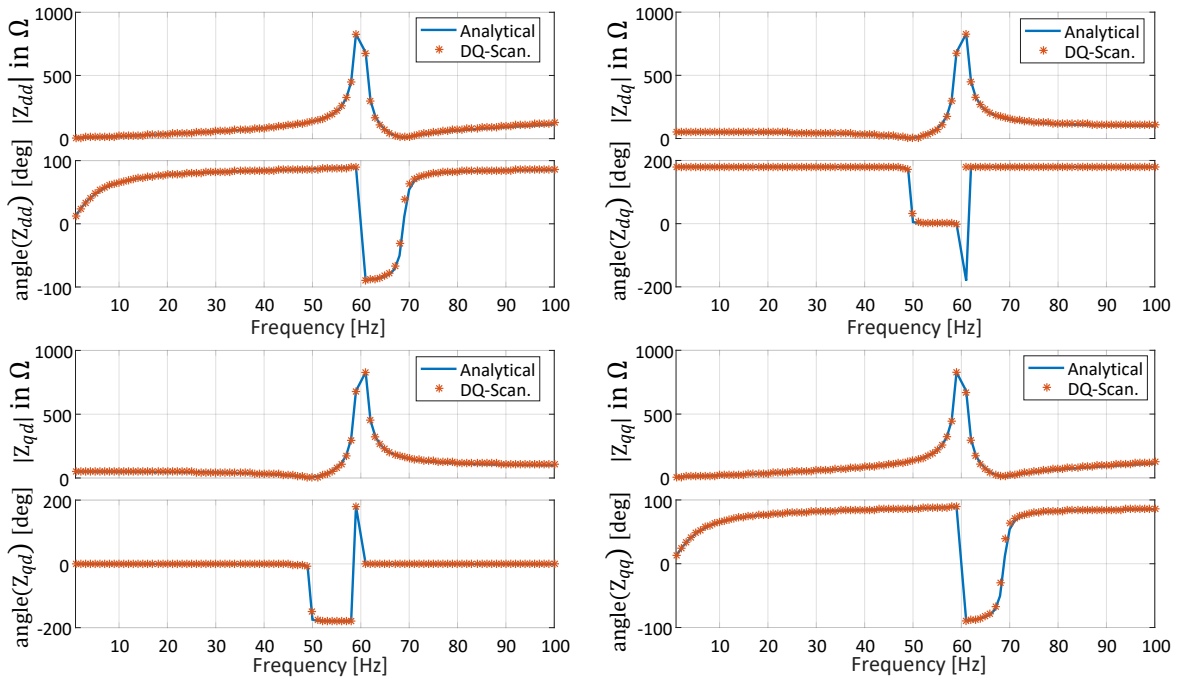


Figure 6.7 Input  $dq$ -impedances of benchmark grid: DQ-Scanning vs. analytical formulation

These results confirm the ability of the DQ-Scanning technique to replace resource-intensive analytical developments to obtain input  $dq$ -impedances and admittances of investigated systems, even under consideration of realistic and faithful equipment representation.

Finally, it is also emphasized that good matches were also obtained even for the frequency region around the rated frequency (60 Hz in this case), thus demonstrating the effectiveness of the applied perturbation method, which did not unnecessarily trigger nonlinearities, and, therefore, helped respecting required small-signal assumptions.

## 6.6 Stability Assessment based on DQ-Scanning Results

As demonstrated in previous subchapters, the DQ-Scanning technique results in frequency-dependent characteristics of input  $dq$ -impedances  $\mathbf{Z}_{dq,grid}$  and admittances  $\mathbf{Y}_{dq,GCI}$  for grid and grid-connected inverter, respectively. They contain the small-signal characteristics of the investigated subsystems.

To address the stability of the interconnection, the impedance-based stability assessment theory is used. As addressed earlier in subchapter 5.2, it relies on the separation of the investigated system into source- and load-subsystems [127], [128], [131], [150]. This is illustrated in Figure 6.8.

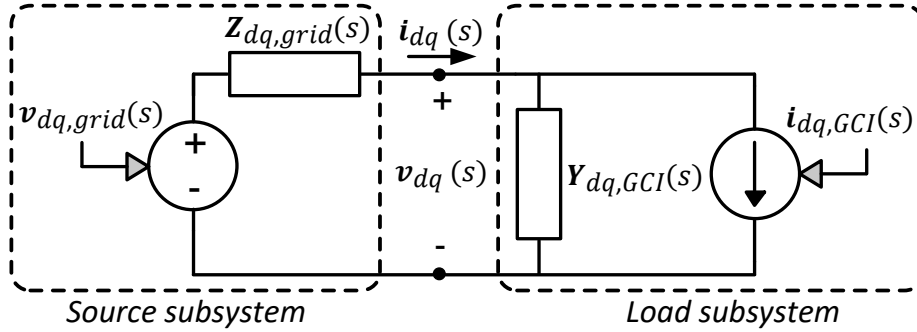


Figure 6.8 Impedance-based circuit interpretation in the  $dq$ -frame.

Starting with the  $dq$ -circuit diagram from Figure 6.8, it is then straightforward to demonstrate that the  $dq$ -voltage and current relations can also be represented in an equivalent block diagram form as given in Figure 6.9.

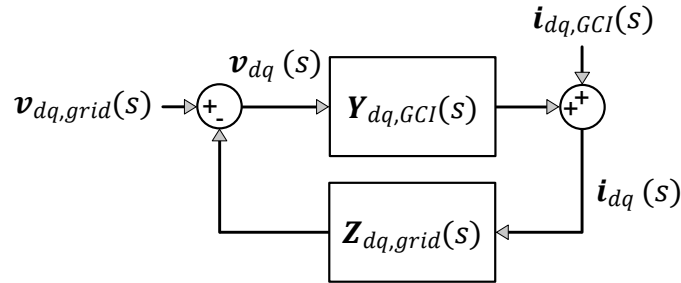


Figure 6.9 Block diagram representation of impedance-based source- and load-subsystems.

The advantage of having the impedance-based subsystems represented as the block diagram given in Figure 6.9 is that it allows the observation that the stability of the interconnection can be assessed as a system given by closed-loop transfer function with negative feedback.

In other words, the stability of the control loop illustrated in Figure 6.9 can be assessed by means of the Generalized Nyquist Criterion [157]. For this purpose, the system return ratio is first defined as

$$\mathbf{L}(s) = \mathbf{Z}_{dq,grid}(s)\mathbf{Y}_{dq,GCI}(s) \quad (6.8)$$

Given that  $\mathbf{Z}_{dq,grid}(s)$  and  $\mathbf{Y}_{dq,GCI}(s)$  have no open-loop uncontrollable and unobservable modes in the right-half-plane, the system is stable if and only if the net sum of counter-clockwise encirclements of the critical point  $(-1,0)$  by the set of characteristics loci of  $\mathbf{L}(s)$  is equal to the total number of right-half-plane poles of  $\mathbf{Z}_{dq,grid}(s)$  and  $\mathbf{Y}_{dq,GCI}(s)$  [127], [157].

It is noted that the Generalized Nyquist Criterion relies on the knowledge of total number of right-half-plane poles of  $\mathbf{Z}_{dq,grid}(s)$  and  $\mathbf{Y}_{dq,GCI}(s)$  individually in order to make a statement on the amount of closed-loop right-half-plane poles and, thus, on the stability of the closed-loop system illustrated in Figure 6.9.

To deal with this requirement, the stand-alone stability of each subsystem needs to be verified. Reference [131] suggests the application of two conditions:

- i) The grid is stable prior to the connection of the GCI.
- ii) The GCI is stable when powered from an ideal source.

According to [131], if both conditions are met, then it can be assumed that  $\mathbf{Z}_{dq,grid}(s)$  and  $\mathbf{Y}_{dq,GCI}(s)$  are individually stable and, thus, have no right-half-plane poles.

In the present work, however, the application of the DQ-Scanning is proposed as a condition to verify the stand-alone stability of the investigated subsystems  $\mathbf{Z}_{dq,grid}(s)$  and  $\mathbf{Y}_{dq,GCI}(s)$ . This is due to the fact that the DQ-Scanning technique is based on assessing the individual response of both subsystems to small-signal perturbations for the chosen operating point (imposed by the pairs  $v_{d,0}$  and  $v_{q,0}$  or  $i_{d,0}$  and  $i_{q,0}$ ).

Moreover, it is noted that if, for instance,  $\mathbf{Z}_{dq,grid}(s)$  and  $\mathbf{Y}_{dq,GCI}(s)$  have right-half-plane poles, the corresponding stand-alone instabilities are expected to be captured by the DQ-Scanning application. In other words, subsystems containing right-half-plane poles are expected to behave unstably during DQ-Scanning application, not being able to maintain their operating condition. In this sense, its application can also be understood as a more complete and strict condition than the ones proposed in [131].

Nevertheless, it is emphasized that the aforementioned condition for stand-alone stability assessment of the interconnection subsystems and their link to the right-half-plane poles of  $\mathbf{Z}_{dq,grid}(s)$  and  $\mathbf{Y}_{dq,GCI}(s)$  are based on the practical engineering sense.

From linear system theory perspective, the above conditions may only address the so-called bounded-input bounded-output stability type [107], [127]. However, it is emphasized that, in the framework of this thesis, no practical case was found for which the above conditions have failed. The assessment and consideration of subsystems with right-half-plane poles is, in fact, subject of ongoing research [158], [159].

Another aspect of the DQ-Scanning that merits attention is the consideration of a common reference frame for both subsystems  $\mathbf{Z}_{dq,grid}(s)$  and  $\mathbf{Y}_{dq,GCI}(s)$ . For proper stability assessment it is mandatory that  $\mathbf{Z}_{dq,grid}(s)$  and  $\mathbf{Y}_{dq,GCI}(s)$  refer to the same  $dq$ -frame, henceforth referred to as the common reference frame. The one defined by the PCC voltages (or other partition point) is a suitable one.

In cases, however, in which the DQ-Scanning is performed for  $\mathbf{Z}_{dq,grid}$  in a different  $dq$ -frame than  $\mathbf{Y}_{dq,GCI}$ , then the application of methodology outlined in [158] is recommended for the purpose of referencing both subsystems to the same global reference frame prior to assessing the interconnection stability.

Such conditions resulting  $\mathbf{Z}_{dq,grid}$  and  $\mathbf{Y}_{dq,GCI}$  in different  $dq$ -frames may arise, for instance, in cases the input  $dq$ -impedances of grid and  $dq$ -admittances of the connecting units are extracted by different stakeholders, which work with different  $dq$ -transformation matrices.

It may also arise in very early project stages, when the steady-state conditions, i.e., the information on the pairs  $v_{d,0}$  and  $v_{q,0}$  or  $i_{d,0}$  and  $i_{q,0}$ , may still not be available for the manufacturer or project developer. In such case, the manufacturer may assume arbitrary values for  $v_{d,0}$  and  $v_{q,0}$  (e.g. choosing  $v_{d,0}$  equal to the nominal PCC voltage and setting  $v_{q,0}$  to zero) and still apply the DQ-Scanning for admittance extraction to obtain  $\mathbf{Y}_{dq,GCI}$ . Later, however, when assessing the interconnection stability based on  $\mathbf{Z}_{dq,grid}$  and  $\mathbf{Y}_{dq,GCI}$ , the extracted input  $dq$ -admittances  $\mathbf{Y}_{dq,GCI}$  need to be rotated to fit the operating condition imposed by the values of  $v_{d,0}$  and  $v_{q,0}$ , which result from the consideration of the interconnection.

For convenience, the required equation to transform a general set of  $dq$ -impedances or admittances, next simply referred to as  $\mathbf{X}_{dq}$ , from an arbitrary  $dq$ -frame to a common reference frame (CRF) is given by

$$\mathbf{X}_{dq}^{CRF} = \begin{bmatrix} \cos(\Delta\theta) & \sin(\Delta\theta) \\ -\sin(\Delta\theta) & \cos(\Delta\theta) \end{bmatrix} \mathbf{X}_{dq} \begin{bmatrix} \cos(\Delta\theta) & -\sin(\Delta\theta) \\ \sin(\Delta\theta) & \cos(\Delta\theta) \end{bmatrix} \quad (6.9)$$

where  $\mathbf{X}_{dq}^{CRF}$  corresponds to  $\mathbf{X}_{dq}$  as seen from the common reference frame and  $\Delta\theta$  corresponds to the angle rotation needed for the arbitrary  $dq$ -frame to align with the common reference frame, for instance, the one imposed by the voltages at the PCC.

Following proper consideration of a common reference frame for both subsystems  $\mathbf{Z}_{dq,grid}$  and  $\mathbf{Y}_{dq,GCI}$ , the interconnection stability can be assessed by applying the Generalized Nyquist Criterion to the system return ratio defined as

$$\mathbf{L}^{CRF}(s) = \mathbf{Z}_{dq,grid}^{CRF}(s) \mathbf{Y}_{dq,GCI}^{CRF}(s) \quad (6.10)$$

Finally, it is noted that equation (6.10) is generally written in the Laplace domain considering the Laplace operator  $s$ , although  $\mathbf{Z}_{dq,grid}$  and  $\mathbf{Y}_{dq,GCI}$  obtained by applying the DQ-Scanning technique are numerical matrices. This, however, does not pose a problem for the technique, since the eigenvalue loci resulting from the Generalized Nyquist Criterion can also be obtained by numerically calculating  $\mathbf{L}^{CRF}$  for each perturbation frequency and plotting the eigenvalue graphs (i.e., plotting the contours defined by both eigenvalues of  $\mathbf{L}^{CRF}$  evaluated for each perturbation frequency  $f_i$ ). Moreover, it is also emphasized that, it is not necessary to evaluate the eigenvalue graphs ranging from minus infinity to plus infinity, as ideally suggested by the Nyquist Criterion to encircle the whole right-half plane. Since the focus lies on low-frequency stability assessment, unstable oscillatory behaviors lying inside the assessed frequencies should reflect in eigenvalue loci, i.e., Generalized Nyquist contours, that encircle the critical point for cases where  $\mathbf{Z}_{dq,grid}$  and  $\mathbf{Y}_{dq,GCI}$  are stand-alone stables [160]. On the other hand, high-frequency instabilities of the interconnection, are not expected to result in encirclements of the critical point (-1,0) if they were not in the range of the assessed perturbation frequencies.

Finally, it is highlighted that if the subsystems  $\mathbf{Z}_{dq,grid}(s)$  and  $\mathbf{Y}_{dq,GCI}(s)$  are stand-alone stable and, thus, have no right-half plane poles, the Generalized Nyquist Criterion on the stability of the

feedback system (i.e., the interconnection) can be simplified to the verification that the resulting eigenvalue loci does not have any encirclement of the critical point  $(-1,0)$ .

## 6.7 DQ-Scanning based Stability Assessment of Simple VSC System

To demonstrate the effectiveness of the proposed stability assessment technique, the cases investigated in subchapter 5.5 through application of the combined scan technique are now assessed by means of the DQ-Scanning technique.

It has been observed in subchapter 5.5 that the simple VSC system is susceptible to instabilities in systems with low short-circuit ratio (SCR). More specifically, as the detailed EMT simulation results shown in Figure 5.7 demonstrate, the smaller the SCR, the less damping there is in the system until the system becomes unstable for a SCR level of approximately 3.

According to the DQ-Scanning technique, the steady-state  $dq$ -voltages and  $dq$ -currents measured at the point-of-common-coupling (PCC),  $v_{dq,0}$  and  $i_{dq,0}$ , respectively, are required for the extraction of the input  $dq$ -admittances and  $dq$ -impedances of both grid-connected inverter and grid. These values are obtained through a time-domain EMT simulation, as indicated in Figure 6.10.

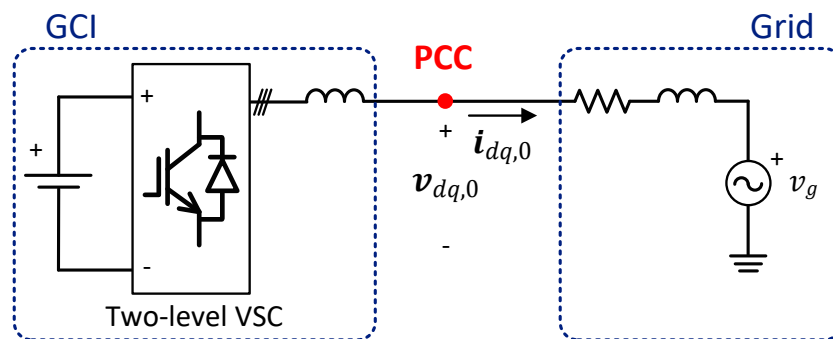


Figure 6.10 Steady-state condition obtained from a time-domain EMT simulation.

At this point, it is emphasized that, for the following evaluation of different SCR values, the above procedure has been repeated for each new operating condition, with the exception of a SCR value of 3, for which a steady-state condition is not possible due to instabilities. For this case, the steady-state values obtained for a SCR of 3.5 were used.

The DQ-Scanning has been used for the extraction of input  $dq$ -admittances and  $dq$ -impedances, as outlined in subchapter 6.2, and the resulting Generalized Nyquist diagrams were plotted for four different SCR levels going from 10 down to 3. These are illustrated in Figure 6.11.

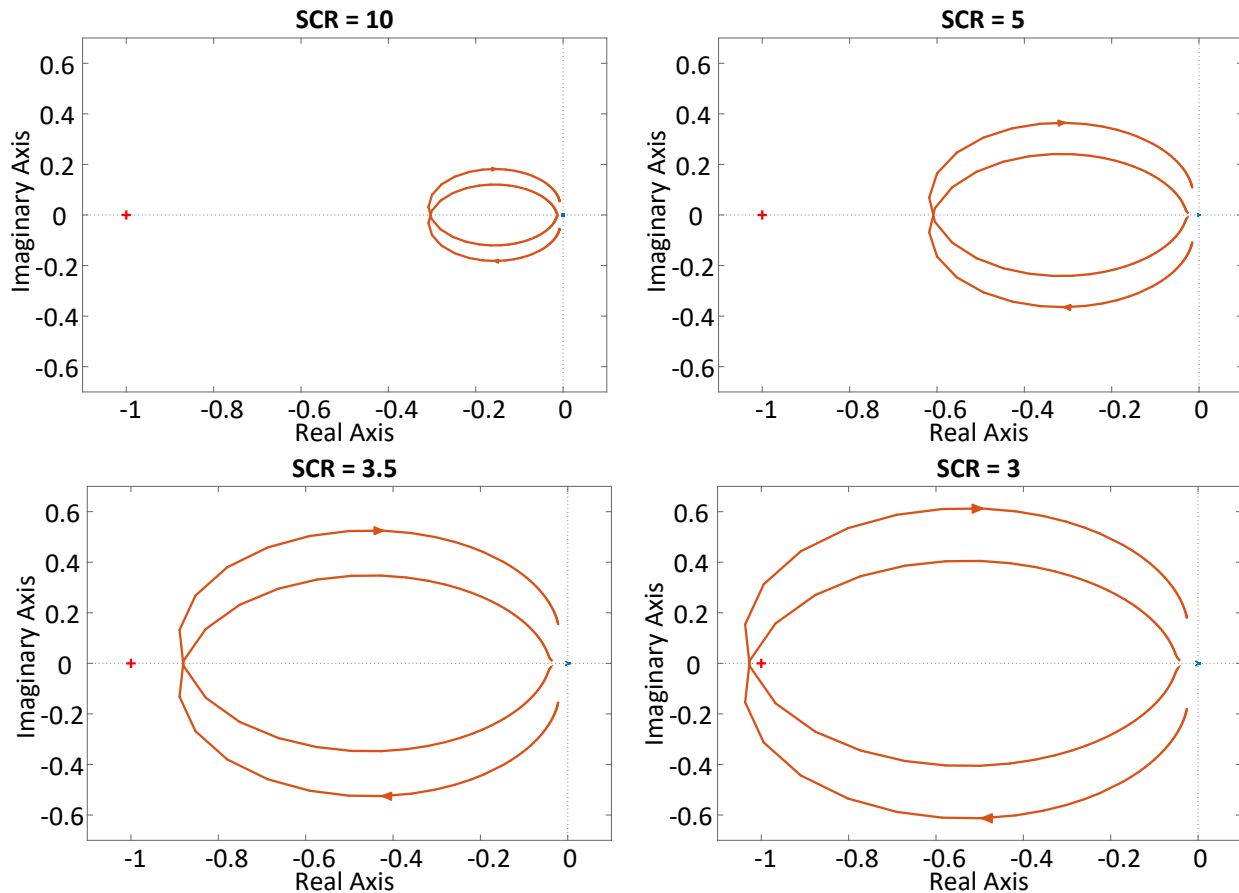


Figure 6.11 GNC diagrams for the VSC system in grids for different SCR levels.

It can be observed in Figure 6.11 that the Nyquist contours do not encircle the critical point  $(-1,0)$  in three of the four cases, more specifically, for SCR values from 10 down to 3.5. However, for a SCR level of 3, it can be observed that the Nyquist contour encircles the critical point, thus, indicating instabilities for this case.

It is noted that these results are in perfect accordance with those obtained through detailed EMT simulation of the corresponding scenarios shown in Figure 5.7 (subchapter 5.5). Additionally, it is also emphasized that a clear tendency towards a critical condition can be observed through in the Nyquist contours illustrated in Figure 6.11 for the different grid strengths. With the decrease of the

SCR, less “margin” is seen between the Nyquist contour and the critical point, therefore, demonstrating that the VSC system is susceptible to varying SCR ratios and that less stability margin is expected the lower the SCR values.

## 6.8 Stability Assessment of Type-III and Type-IV Wind Farms

To verify the effectiveness of the proposed approach when applied to realistic cases, the interconnection stability investigated earlier in this thesis for type-III and type-IV based wind farms connected to the proposed series-compensated benchmark grid is assessed.

The input  $dq$ -impedances of the grid and  $dq$ -admittances were extracted for the frequency range from 1 to 100 Hz in steps of 1 Hz. A dedicated code was written to automate the procedure of plotting the Generalized Nyquist contour (*GNC\_FRDbased\_blackBox.m* in [105]).

Figure 6.12, Figure 6.13 and Figure 6.14 illustrate the results for the type-III wind farm interconnected to the benchmark grid with line series-compensation levels of 8%, 9% and 10%, respectively.

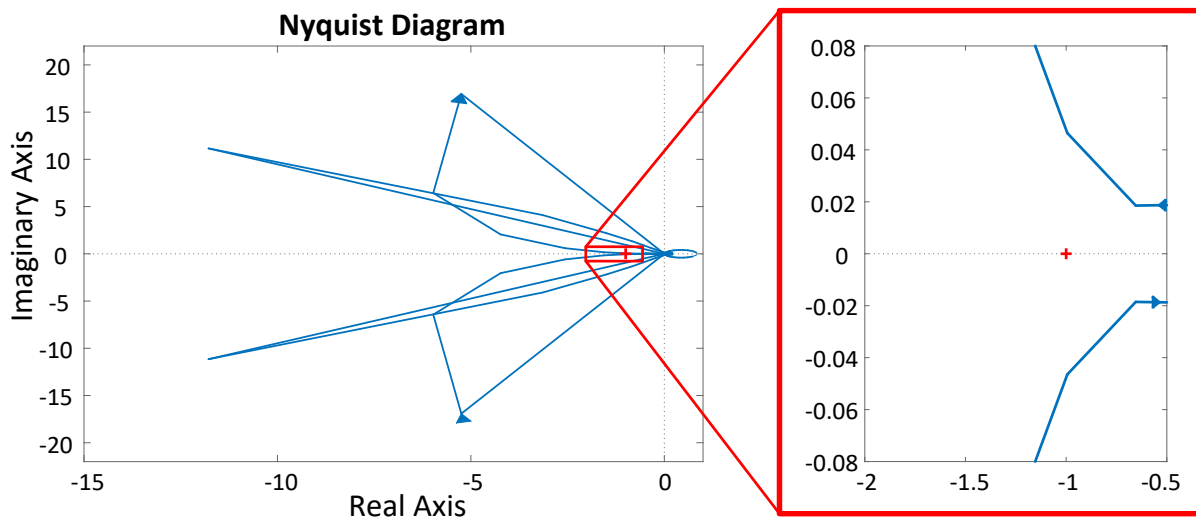


Figure 6.12 GNC based on DQ-Scanning for type-III WF and 8% series compensation.

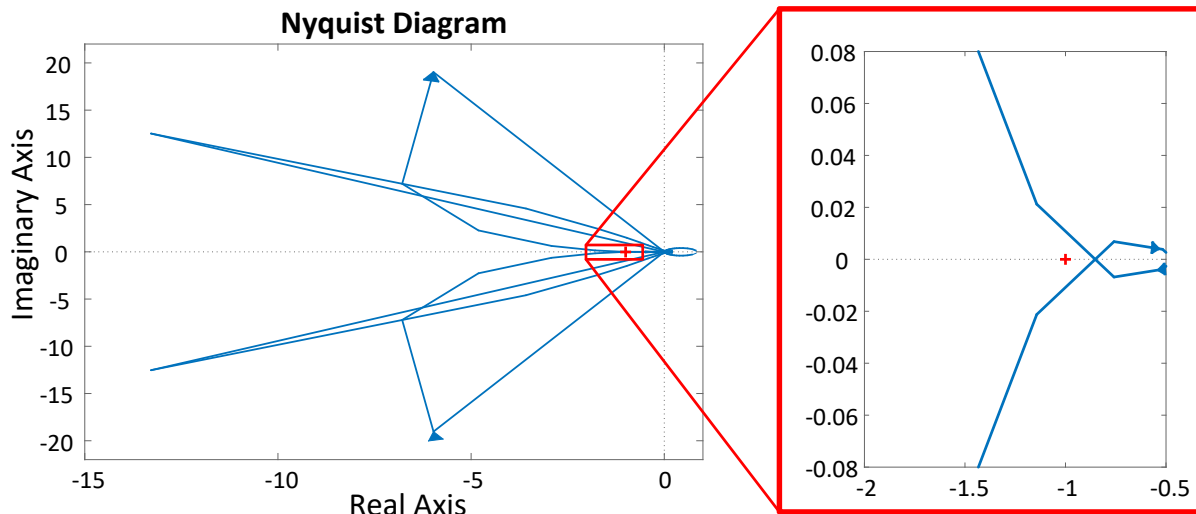


Figure 6.13 GNC based on DQ-Scanning for type-III WF and 9% series compensation.

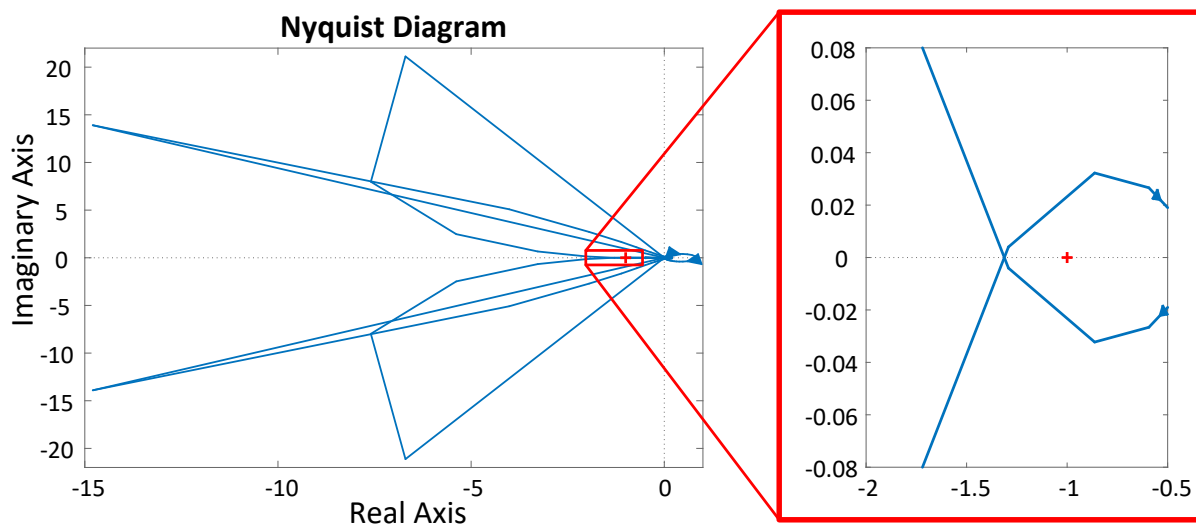


Figure 6.14 GNC based on DQ-Scanning for type-III WF and 10% series compensation.

It is evident from Figure 6.12, Figure 6.13 and Figure 6.14 that the proposed approach was capable of properly capturing the stability in all investigated scenarios for the type-III wind farm case. It is seen that no encirclement of the critical point happens for the cases of 8% and 9% series-compensation levels. However, two encirclements are seen for the scenario with 10% series compensation, indicating therefore an unstable operating condition.

It is also interesting to observe how, as the series compensation was increased, the generalized Nyquist contour kept approaching the critical point  $(-1,0)$ , until, for a 10 % series-compensation level, it got encircled.

It is noted that this prediction is in exact accordance with the modal analysis results performed in subchapter 4.7, whose results are shown in Figure 4.21, and are as well confirmed by the EMTP simulation of the detailed system representation, which are illustrated in Figure 3.8.

Another interesting property of the generalized Nyquist contour is the fact that the unstable oscillatory behavior can also be extracted from the resulting diagram [161]. The expected oscillatory frequency of the unstable system is expected to be the one closest to the critical point from the contour. As illustrated in Figure 6.15, the unstable oscillatory frequency is, in the case of 10 % series compensation, estimated to be between 53 and 54 Hz and, again, is in perfect accordance with the results from modal analysis (see Figure 4.21) and EMTP simulation results carried out for this case (see subchapter 3.5).

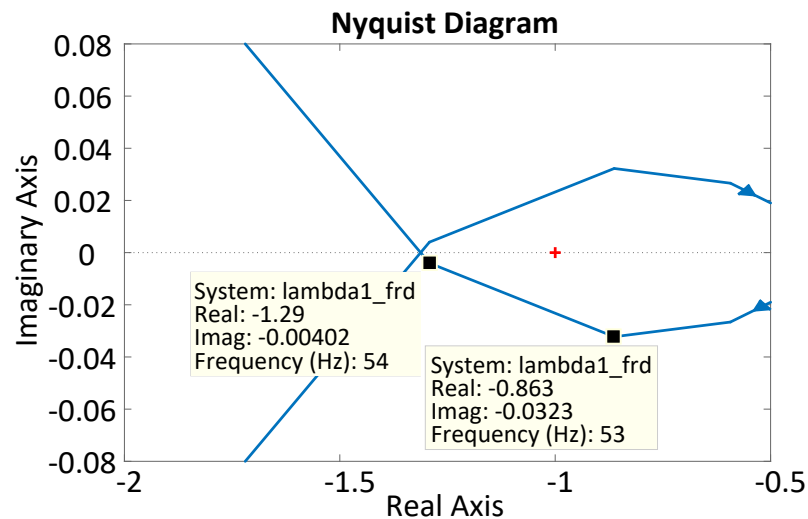


Figure 6.15 Unstable oscillatory frequencies estimated from GNC for type-III WF.

Finally, the case of the type-IV wind farm connected to the series-compensated benchmark grid is also investigated. At this point, however, it is reinforced that the consideration of the magnetizing characteristics of transformers played an important role during the investigation of the type-IV wind farm scenario as well as in the application of the DQ-Scanning technique.

More specifically, it has been observed for the case involving a type-IV wind farm that the detailed model representation in EMTP was not capable of achieving a steady-state condition if the saturation characteristic of the 230/34.5 kV substation transformer (see Figure 3.4) was not considered. Reason for it are low-frequency oscillations resulting from LC resonances involving the series compensation capacitors and the linear representation of the magnetizing branch of the substation transformer, in case the saturation is not included, as discussed in Section 3.3.1.

It is emphasized here that, as long as a steady-state operating condition is not achieved for the interconnection, the application of the DQ-Scanning technique is not possible, as it relies on the use of steady-state values of the voltages at the PCC and the currents flowing into the grid (see Section 6.2). Furthermore, it is noted that its non-consideration may lead to results that are qualitatively incorrect, as outlined in Section 3.3.1. Therefore, further investigation on oscillatory conditions observed for the type-IV wind farm without the consideration of transformer saturation characteristics was not pursued in this work.

Finally, with the proper consideration of all nonlinear equipment characteristics, thus, including the transformer saturation, the DQ-Scanning was applied to the type-IV wind farm scenario. The resulting generalized Nyquist contours are illustrated in Figure 6.16 and Figure 6.17 for the cases of a line series-compensation level of 50 % and 70 %, respectively.

As can be seen from Figure 6.16 and Figure 6.17, no encirclements of the critical point is seen for both 50 % and 70 % line series-compensation levels, thus indicating no critical condition for the type-IV wind farm case. These predictions are also in alignment with those obtained by means of the modal analysis in subchapter 4.6 and with the EMTP detailed simulations performed in subchapter 3.4 (illustrated in Figure 3.7). Interestingly, it is also noted that the distance to the critical point is just slightly changed from a 50 % to 70 % line series-compensation level increase, what justify no major behavior difference in the EMTP results, as indicated in subchapter 3.4.

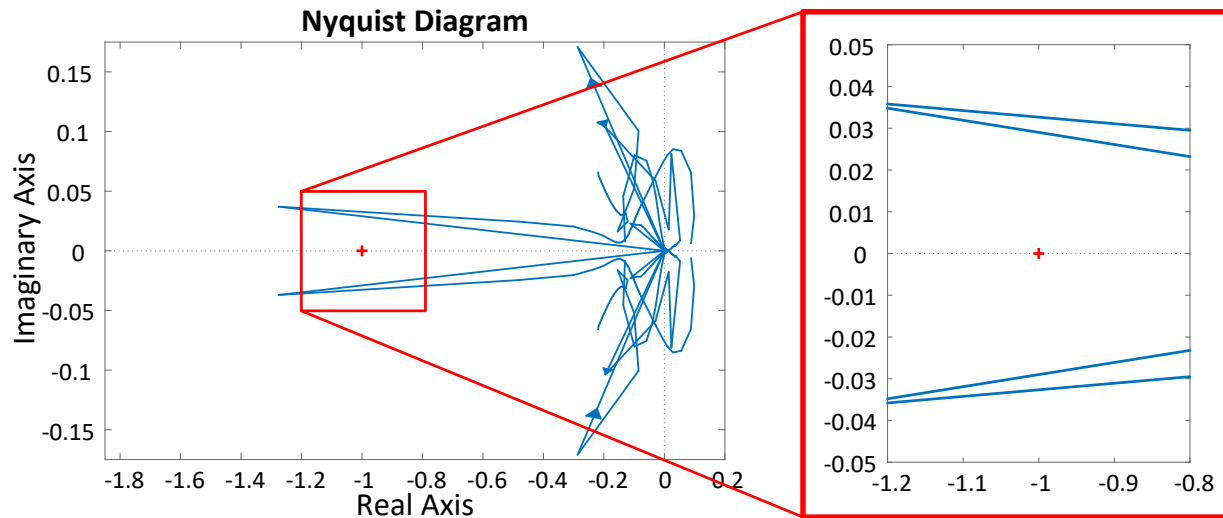


Figure 6.16 GNC based on DQ-Scanning for type-IV WF and 50% series compensation.

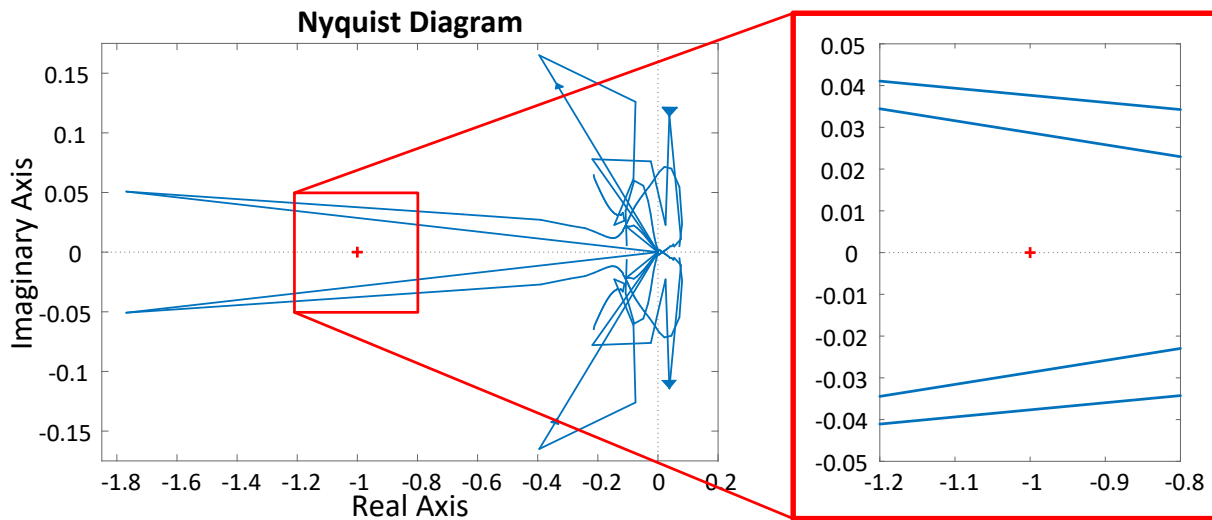


Figure 6.17 GNC based on DQ-Scanning for type-IV WF and 70% series compensation.

## 6.9 Effects of Right-Half-Plane Poles

This subchapter deals with the effects of right-half-plane poles in the impedance and admittance characteristics of grid impedances, and the subsequent importance of applying a current perturbation based DQ-Scanning at the grid-side subcomponent.

Two different three-phase grid structures are considered in the following. To reduce complexity, these structures are exceptionally assumed simple to allow for straightforward analytical demonstrations. Nevertheless, their results can be translated to larger realistic systems.

### 6.9.1 Right-Half-Plane Poles in the Admittance Representation

A simple 230 kV three-phase grid structure consisting of two Thevenin grid representations is considered. The system is illustrated in Figure 6.18. Additionally, it is assumed that a new interconnection is planned, whose point-of-common-coupling (PCC) is also indicated Figure 6.18.

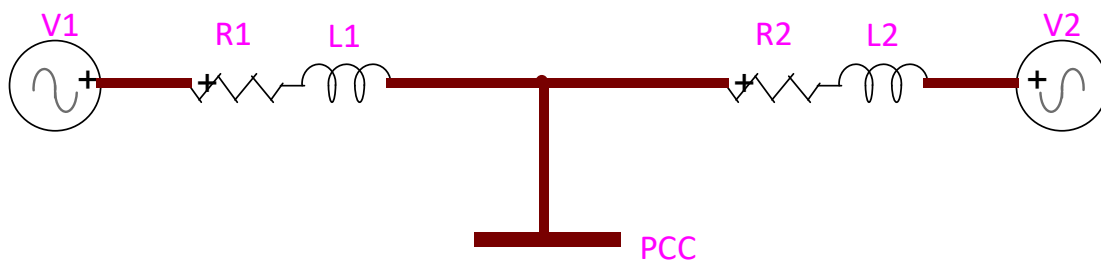


Figure 6.18 Simple grid structure to investigate effects of RHP poles in grid  $dq$ -admittances.

Assuming all components to be symmetric, it is evident that the system in Figure 6.18 is stable (without the new interconnection) if, and only if, the sum of the resistances per phase is positive, i.e.,  $R_1 + R_2 > 0$ , where  $R_1$  and  $R_2$  are the positive sequence resistances of the inductive-resistive elements R1, L1 and R2, L2 in Figure 6.18. Otherwise, following well-known dynamics of RL-circuits, an exponential increase of currents should be expected.

In the interest of simplicity and regardless of physical interpretations, the parameters in Table 6.1 are proposed for the system in Figure 6.18.  $L_1$  and  $L_2$  correspond to the positive sequence inductances of the inductive-resistive elements R1, L1 and R2, L2 in Figure 6.18. It is noted that the stability condition  $R_1 + R_2 > 0$  is respected, although the value of  $R_1$  is negative. Additionally, it is emphasized that in realistic system representations, frequency regions characterized by negative resistances may arise as the result of, for instance, induction generator effect (in the case of synchronous generators) or controllers of grid-connected inverters.

Table 6.1 Grid parameters.

Parameters	Value	Unit	Description
------------	-------	------	-------------

$R_1$	-4	$\Omega$	Positive sequence impedance
$L_1$	66	mH	Positive sequence inductance
$R_2$	5	$\Omega$	Positive sequence impedance
$L_2$	66	mH	Positive sequence inductance

Supposing that the stability of a new interconnection at the PCC indicated in Figure 6.18 with the parameters of Table 6.1 is to be investigated, it can be demonstrated that the grid input  $dq$ -impedances can only be assessed from the PCC by the current perturbation based DQ-Scanning technique (see subchapter 6.2). This is illustrated in Figure 6.19 in which the results of (a) a voltage perturbation based DQ-Scanning (perturbation is ramped up in  $v_d$ ) is compared with (b) a current based perturbation DQ-Scanning (perturbation is ramped up in  $i_d$ ). It can be seen that in the case of the application of voltage perturbations, the measured  $i_{dq}$  currents tend to infinity.

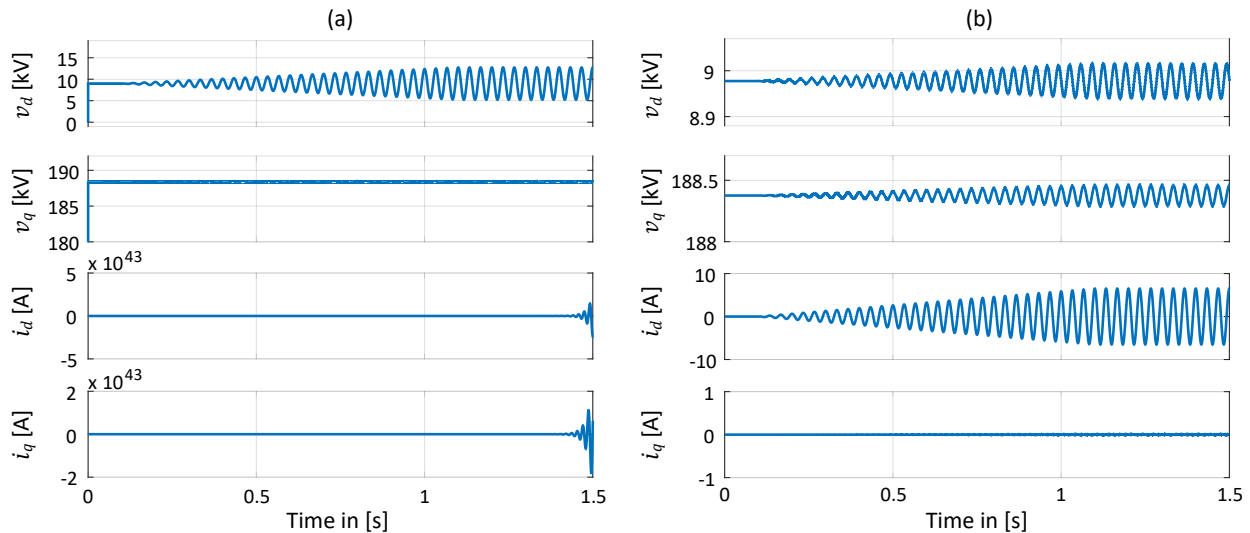


Figure 6.19 (a) voltage perturbation based vs. (b) current perturbation based DQ-Scanning.

Intuitively, the instabilities for the voltage perturbation based DQ-Scanning can be easily explained. It is emphasized that once a voltage perturbation based DQ-Scanning is considered, an ideal voltage source is connected to the PCC (with the corresponding steady-state values  $v_{dq,0}$ ) and, consequently, the grid is separated into two smaller subsystems. This is indicated in Figure 6.20, in which the smaller subsystems are framed with dashed lines.

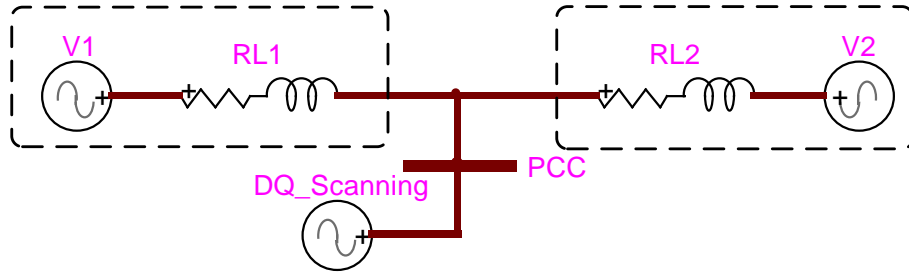


Figure 6.20 Voltage perturbation based DQ-Scanning application.

Since the smaller subsystems of Figure 6.20 can be evaluated separately, the fact that  $R_1$  is negative becomes now evident. Any perturbation applied by the DQ-Scanning voltage source shown in Figure 6.20 results in exponentially increasing currents through the  $L_1$  inductance.

These results can also be confirmed analytically. For this, the state-space representation of the grid for voltage perturbations (inputs) is developed.

It is straightforward to demonstrate that for the small system on the left side of Figure 6.20 equations are valid in the  $dq$ -domain

$$\begin{aligned} \begin{bmatrix} \frac{di_{1,d}}{dt} \\ \frac{di_{1,q}}{dt} \end{bmatrix} &= \begin{bmatrix} -R_1/L_1 & \omega_0 \\ -\omega_0 & -R_1/L_1 \end{bmatrix} \begin{bmatrix} i_{1,d} \\ i_{1,q} \end{bmatrix} + \begin{bmatrix} 1/L_1 & 0 & -1/L_1 & 0 \\ 0 & 1/L_1 & 0 & -1/L_1 \end{bmatrix} \begin{bmatrix} v_{1,d} \\ v_{1,q} \\ v_{PCC,d} \\ v_{PCC,q} \end{bmatrix} \\ \begin{bmatrix} i_{1,d} \\ i_{1,q} \end{bmatrix} &= \begin{bmatrix} 1 & 0 \\ 0 & 1 \end{bmatrix} \begin{bmatrix} i_{1,d} \\ i_{1,q} \end{bmatrix} + \begin{bmatrix} 0 & 0 & 0 & 0 \\ 0 & 0 & 0 & 0 \end{bmatrix} \begin{bmatrix} v_{1,d} \\ v_{1,q} \\ v_{PCC,d} \\ v_{PCC,q} \end{bmatrix} \end{aligned} \quad (6.11)$$

where  $v_{1,dq}$  represent the grid  $dq$ -voltages,  $i_{1,dq}$  the  $dq$ -currents through inductances  $L_1$  and  $v_{PCC,dq}$  the PCC voltages resulting from the application of the DQ-Scanning.

Similarly, a state-space representation can also be developed for the right-side system of Figure 6.20 in the  $dq$ -domain, as given in

$$\begin{bmatrix} \frac{di_{2,d}}{dt} \\ \frac{di_{2,q}}{dt} \end{bmatrix} = \begin{bmatrix} -R_2/L_2 & \omega_0 \\ -\omega_0 & -R_2/L_2 \end{bmatrix} \begin{bmatrix} i_{2,d} \\ i_{2,q} \end{bmatrix} + \begin{bmatrix} 1/L_2 & 0 & -1/L_2 & 0 \\ 0 & 1/L_2 & 0 & -1/L_2 \end{bmatrix} \begin{bmatrix} v_{PCC,d} \\ v_{PCC,q} \\ v_{2,d} \\ v_{2,q} \end{bmatrix} \quad (6.12)$$

$$\begin{bmatrix} i_{2,d} \\ i_{2,q} \end{bmatrix} = \begin{bmatrix} 1 & 0 \\ 0 & 1 \end{bmatrix} \begin{bmatrix} i_{2,d} \\ i_{2,q} \end{bmatrix} + \begin{bmatrix} 0 & 0 & 0 & 0 \\ 0 & 0 & 0 & 0 \end{bmatrix} \begin{bmatrix} v_{PCC,d} \\ v_{PCC,q} \\ v_{2,d} \\ v_{2,q} \end{bmatrix}$$

where  $i_{2,dq}$  represent the  $dq$ -currents through the inductance  $L_2$ .

It is noted that the calculation of input  $dq$ -admittances required the relation between the measured  $dq$ -voltages at the PCC as well as the total  $dq$ -currents flowing into the grid  $i_{grid,dq}$ . For this reason, a third state-space system is required to perform the needed algebraic calculations as in

$$[Y] = [0][Y] + [0 \ 0 \ 0 \ 0] \begin{bmatrix} i_{1,d} \\ i_{1,q} \\ i_{2,d} \\ i_{2,q} \end{bmatrix} \quad (6.13)$$

$$\begin{bmatrix} i_{grid,d} \\ i_{grid,q} \end{bmatrix} = [0] [Y] + \begin{bmatrix} -1 & 0 & 1 & 0 \\ 0 & -1 & 0 & 1 \end{bmatrix} \begin{bmatrix} i_{1,d} \\ i_{1,q} \\ i_{2,d} \\ i_{2,q} \end{bmatrix}$$

With the state-space representations in (6.11), (6.12) and (6.13) it is now possible to develop a complete state-space representation for the grid. For this, the same methodology applied in subchapter 4.3 is used. The interconnection diagram is given in Figure 6.21. Details concerning the development of the complete equations can be extracted from *originalGrid\_V\_v1.m* [105].

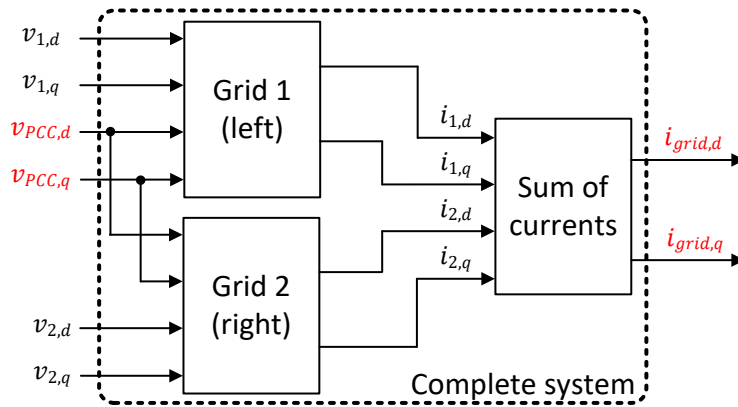


Figure 6.21 Interconnection diagram for grid (with voltage as input and current as output).

Once a complete system state-space representation is obtained, it is possible to apply modal analysis to identify the system eigenvalues. The resulting eigenvalues are given in Table 6.2.

Table 6.2 Eigenvalues of 230 kV grid (with PCC voltages as input).

Eigenvalue	Value
$\lambda_1$	$60.60 + j377$
$\lambda_2$	$60.60 - j377$
$\lambda_3$	$-75.75 + j377$
$\lambda_4$	$-75.75 - j377$

Since the complete system representation contains four state variables ( $dq$ -currents through inductances  $L_1$  and  $L_2$ ), it can be observed in Table 6.2 that system dynamics are dictated by four eigenvalues, from which two have positive real parts. Thus, these results confirm that a complete system consideration considering the PCC voltages  $v_{PCC,dq}$  is unstable and indicate that the input  $dq$ -admittance characteristics of the grid contain two right-half-plane poles.

Interestingly, it has been observed in Figure 6.19 that a current perturbation based DQ-Scanning is possible, which indicate no right-half-plane poles in the grid input  $dq$ -impedance characteristics, although their existence has been demonstrated for the input  $dq$ -admittances.

To verify this hypothesis, a state-space representation is developed for the same system, however considering PCC currents as system inputs, i.e., corresponding to a current perturbation DQ-Scanning application as illustrated in Figure 6.22.

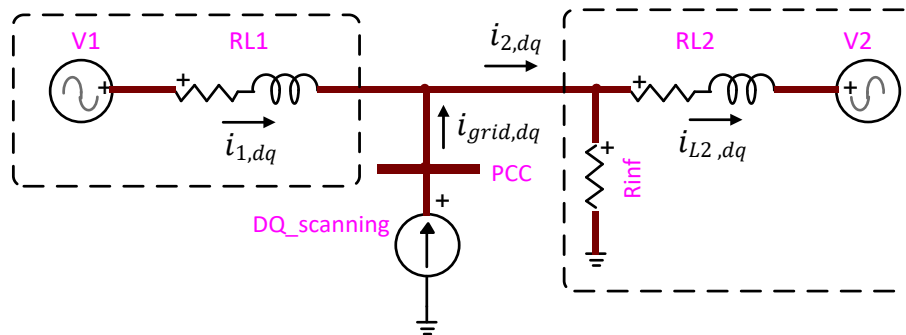


Figure 6.22 Current perturbation based DQ-Scanning application.

The state-space representation developed for the subsystem indicated by dashed lines on the left side of Figure 6.22 is exactly the same as given in (6.11), however the state-space equations for the subsystem on the right side required a small modification to allow for currents as inputs. For this, a resistance  $R_{inf}$  with high value of  $1 \text{ M}\Omega$  is introduced. It is noted that due to its high value, its effect are negligible in the system. Nevertheless, with its consideration it is possible to write

$$\begin{cases} v_{PCC,d} = R_{inf}(i_{1,d} + i_{grid,d} - i_{2,d}) \\ v_{PCC,q} = R_{inf}(i_{1,q} + i_{grid,q} - i_{2,q}) \end{cases} \quad (6.14)$$

where it is noted that  $i_{2,dq}$  now correspond to the total input  $dq$ -currents of the subsystem on the right side, whereas  $i_{L2,dq}$  indicate the  $dq$ -currents through the inductance  $L_2$ . Using the relations given in (6.14), it is possible to write

$$\begin{cases} v_{PCC,d} - v_{2,d} = R_2 i_{L2,d} + L_2 \frac{di_{L2,d}}{dt} - \omega_0 L_2 i_{L2,q} \\ v_{PCC,q} - v_{2,q} = R_2 i_{L2,q} + L_2 \frac{di_{L2,q}}{dt} + \omega_0 L_2 i_{L2,d} \end{cases} \quad (6.15)$$

Considering equations (6.14) and (6.15) and assuming the PCC voltages  $v_{PCC,dq}$  as system outputs, it is possible to write a state-space representation for the subsystem on the right side of Figure 6.22 as given in

$$\begin{aligned} \begin{bmatrix} \frac{di_{L2,d}}{dt} \\ \frac{di_{L2,q}}{dt} \end{bmatrix} &= \begin{bmatrix} \frac{-(R_2 + R_{inf})}{L_2} & \omega_0 \\ -\omega_0 & \frac{-(R_2 + R_{inf})}{L_2} \end{bmatrix} \begin{bmatrix} i_{L2,d} \\ i_{L2,q} \end{bmatrix} \\ &+ \begin{bmatrix} \frac{R_{inf}}{L_2} & 0 & \frac{-R_{inf}}{L_2} & 0 & \frac{-1}{L_2} & 0 \\ 0 & \frac{R_{inf}}{L_2} & 0 & \frac{-R_{inf}}{L_2} & 0 & \frac{-1}{L_2} \end{bmatrix} \begin{bmatrix} i_{1,d} \\ i_{1,q} \\ i_{grid,d} \\ i_{grid,q} \\ v_{2,d} \\ v_{2,q} \end{bmatrix} \\ v_{PCC,d} \\ v_{PCC,q} \end{bmatrix} &= \begin{bmatrix} -R_{inf} & 0 \\ 0 & -R_{inf} \end{bmatrix} \begin{bmatrix} i_{L2,d} \\ i_{L2,q} \end{bmatrix} + \begin{bmatrix} R_{inf} & 0 & -R_{inf} & 0 & 0 & 0 \\ 0 & R_{inf} & 0 & -R_{inf} & 0 & 0 \end{bmatrix} \begin{bmatrix} i_{1,d} \\ i_{1,q} \\ i_{grid,d} \\ i_{grid,q} \\ v_{2,d} \\ v_{2,q} \end{bmatrix} \end{aligned} \quad (6.16)$$

Differently than observed for the case of considering PCC voltages  $v_{PCC,dq}$  as system inputs, once these are considered as system outputs, the subsystems on the left and right sides of Figure 6.22 can be directly connected to each other as indicated by the interconnection diagram illustrated in Figure 6.23.

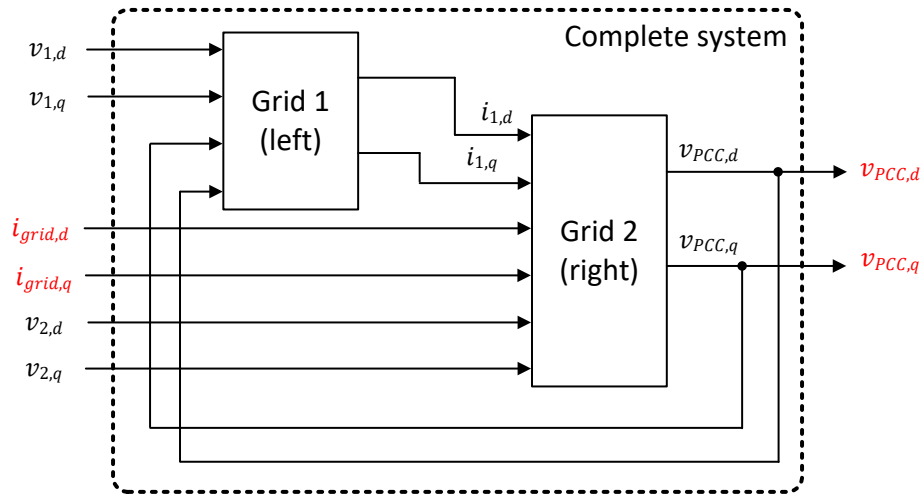


Figure 6.23 Interconnection diagram for grid (with current as input and voltage as output).

A complete state-space form can as well be obtained for the complete system representation as illustrated in Figure 6.23, from which the eigenvalues can be calculated. These are provided in Table 6.3. Detailed calculations are included in *original Grid\_I\_v1.m* in [105].

Table 6.3 Eigenvalues of 230 kV grid (with grid currents as input).

Eigenvalue	Value
$\lambda_1$	$-7.58 + j377$
$\lambda_2$	$-7.58 - j377$
$\lambda_3$	$-3.03e7 + j377$
$\lambda_4$	$-3.03e7 - j377$

It can be seen in Table 6.3 that all four eigenvalues have negative real parts indicating, thus, a stable system representation. These results therefore corroborate the simulation results illustrated in Figure 6.19 and confirm that a system representation for which currents are seen as inputs and voltage as output, i.e., an impedance representation, is stable.

The above demonstration consolidates the DQ-Scanning methodology proposed in subchapter 6.2, which relies on the use of a current perturbation based DQ-Scanning to extract directly the grid subsystem input  $dq$ -impedances, as required for stability analysis (see Figure 6.9). It is noted that, by doing so, issues involving right-half-plane poles in the grid small-signal input  $dq$ -admittances are circumvented. Finally, it is also emphasized that a stable current perturbation based DQ-Scanning application, i.e., without measuring unstable exponential increasing PCC voltages  $v_{PCC,dq}$ ,

serves as a good indicator for the absence of right-half-plane poles in the grid small-signal input  $dq$ -impedance characteristics.

## 6.9.2 Right-Half-Plane Poles in the Impedance Representation

This subchapter deals with the investigation of right-half-plane poles in grid  $dq$ -impedances. In the interest of simplicity for mathematical demonstrations, a 100 V grid system is assumed consisting only of resistances and an inductance as illustrated in Figure 6.24.

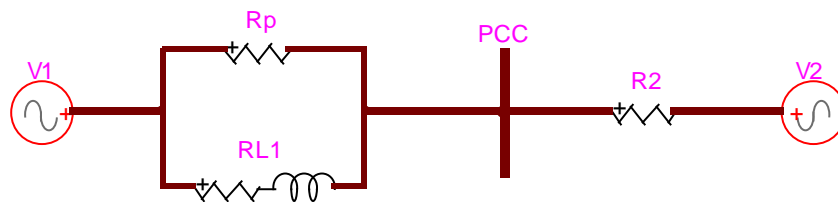


Figure 6.24 Simple three-phase 100 V grid structure.

As shown in Figure 6.24, the considered grid structure assumes the connection of two smaller grids, one (on the left) consisting of a parallel connection of a resistance and a RL-branch and a second one (on the right) just resistive. In the following studies, the parameters shown in Table 6.4 are applied. All electrical elements and sources are assumed symmetrical.

Table 6.4 Grid parameters.

Parameters	Value	Unit	Description
$R_p$	-2	$\Omega$	Positive sequence resistance
$R_1$	1	$\Omega$	Positive sequence resistance
$L_1$	2.7	mH	Positive sequence inductance
$R_2$	2.1	$\Omega$	Positive sequence resistance

It is supposed that the interconnection of both grids in Figure 6.24 is to be assessed by means of the DQ-Scanning application at their point-of-common-coupling (PCC). Furthermore, regardless of physical interpretations, it is assumed that the system on the left side corresponds to a grid subsystems, whereas the system on the right side to the grid-connected inverter subsystem.

According to the DQ-Scanning methodology (see subchapter 6.2), a current perturbation based DQ-Scanning should be applied to the grid subsystem, i.e., to the system on the left side of the

PCC in Figure 6.24. However, when applying it, unstable results are observed (measured  $dq$ -voltages tend to infinity). On the other hand, when applying a voltage perturbation based DQ-Scanning, it is noted that responses are stable. This is illustrated in Figure 6.25.

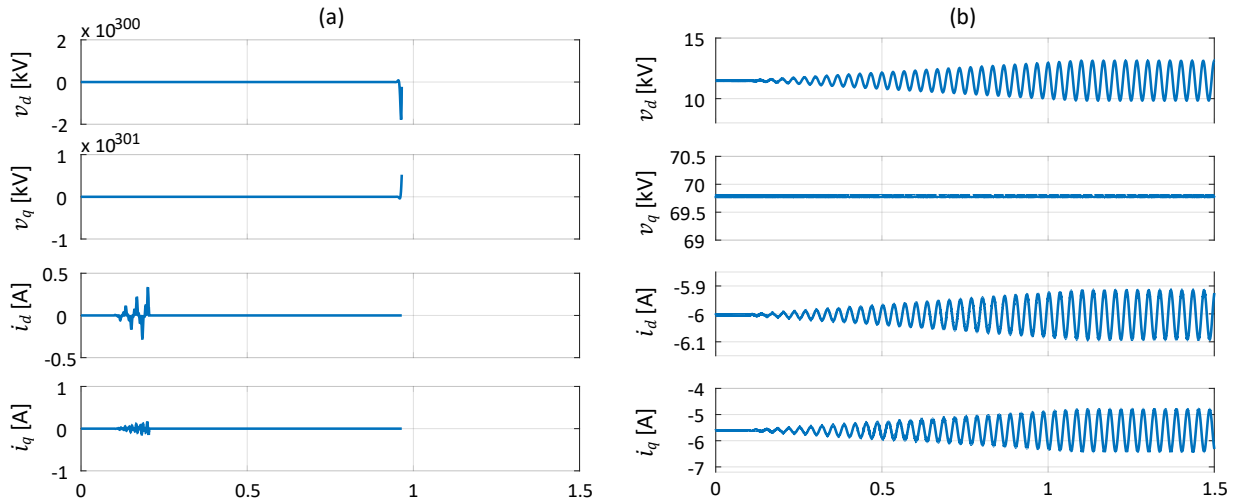


Figure 6.25 (a) current perturbation based vs. (b) voltage perturbation based DQ-Scanning.

The unstable results illustrated in Figure 6.25 (a) for a current perturbation based DQ-Scanning are an indicator for right-half-plane poles in the grid impedance characteristics (see subchapter 6.2), whereas the stable results for voltage perturbation DQ-Scanning indicate stable small-signal  $dq$ -admittances, i.e., without right-half-plane poles.

To demonstrate the presence of right-half-plane poles in the input  $dq$ -impedances, a state-space representation is developed for the grid subsystem (shown in Figure 6.26), considering  $dq$ -currents as system inputs and the measured voltages at the PCC as outputs  $v_{PCC,dq}$ .

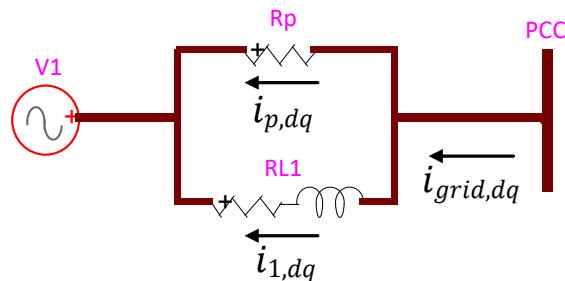


Figure 6.26 Grid subsystem with used current notations.

From Figure 6.26 it is possible to write following relations for the grid input currents  $i_{grid,dq}$

$$\begin{cases} i_{grid,d} = i_{p,d} + i_{1,d} = \frac{-v_{RL,d}}{R_p} + i_{1,d} \\ i_{grid,q} = i_{p,q} + i_{1,q} = \frac{-v_{RL,q}}{R_p} + i_{1,q} \end{cases} \quad (6.17)$$

where the voltages over the RL-branch  $v_{RL,dq}$  are further calculated as

$$\begin{aligned} v_{RL,d} &= R_1 i_{1,d} + L_1 \frac{di_{1,d}}{dt} - \omega_0 L_1 i_{1,q} \\ v_{RL,q} &= R_1 i_{1,q} + L_1 \frac{di_{1,q}}{dt} + \omega_0 L_1 i_{1,d} \end{aligned} \quad (6.18)$$

Replacing equations in (6.17) in those of (6.18), and considering the PCC  $dq$ -voltages,  $v_{PCC,dq}$ , as system outputs, it is possible to develop the following state-space equations for the grid subsystem

$$\begin{aligned} \begin{bmatrix} \frac{di_{1,d}}{dt} \\ \frac{di_{1,q}}{dt} \end{bmatrix} &= \begin{bmatrix} \frac{-(R_1 + R_p)}{L_1} & \omega_0 \\ -\omega_0 & \frac{-(R_1 + R_p)}{L_1} \end{bmatrix} \begin{bmatrix} i_{1,d} \\ i_{1,q} \end{bmatrix} + \begin{bmatrix} 0 & 0 & R_p & 0 \\ 0 & 0 & 0 & R_p \end{bmatrix} \begin{bmatrix} v_{1,d} \\ v_{1,q} \\ i_{grid,d} \\ i_{grid,q} \end{bmatrix} \\ \begin{bmatrix} v_{PCC,d} \\ v_{PCC,q} \end{bmatrix} &= \begin{bmatrix} -R_p & 0 \\ 0 & -R_p \end{bmatrix} \begin{bmatrix} i_{1,d} \\ i_{1,q} \end{bmatrix} + \begin{bmatrix} 1 & 0 & R_p & 0 \\ 0 & 1 & 0 & R_p \end{bmatrix} \begin{bmatrix} v_{1,d} \\ v_{1,q} \\ i_{grid,d} \\ i_{grid,q} \end{bmatrix} \end{aligned} \quad (6.19)$$

Using the state-space representation in (6.19) it is now possible to calculate the eigenvalues of the grid subsystem using the data in Table 6.4. These are given in Table 6.5.

Table 6.5 Eigenvalues of 100 V grid subsystem (with grid currents as system input).

Eigenvalue	Value
$\lambda_1$	<b>370.37 + j377</b>
$\lambda_2$	<b>370.37 - j377</b>

It can be seen in Table 6.5 that both system eigenvalues have positive real parts, thus explaining the instabilities observed in the application of current perturbation based DQ-Scanning illustrated in Figure 6.25.

As a matter of comparison, a state-space representation with the consideration of the PCC  $dq$ -voltages as inputs and the grid  $dq$ -currents as outputs, i.e., an admittance, is also developed for the

grid subsystem. Using Figure 6.26, it is possible to write for the currents through the inductances  $L_1$

$$\begin{aligned} v_{PCC,d} - v_{1,d} &= R_1 i_{1,d} + L_1 \frac{di_{1,d}}{dt} - \omega_0 L_1 i_{1,q} \\ v_{PCC,q} - v_{1,q} &= R_1 i_{1,q} + L_1 \frac{di_{1,q}}{dt} + \omega_0 L_1 i_{1,d} \end{aligned} \quad (6.20)$$

Solving equations in (6.20) to their derivative terms and considering the relations already provided in (6.17) for the grid  $dq$ -currents, following state-space representation it is possible to write

$$\begin{aligned} \begin{bmatrix} \frac{di_{1,d}}{dt} \\ \frac{di_{1,q}}{dt} \end{bmatrix} &= \begin{bmatrix} \frac{-R_1}{L_1} & \omega_0 \\ -\omega_0 & \frac{-R_1}{L_1} \end{bmatrix} \begin{bmatrix} i_{1,d} \\ i_{1,q} \end{bmatrix} + \begin{bmatrix} \frac{1}{L_1} & 0 & \frac{-1}{L_1} & 0 \\ 0 & \frac{1}{L_1} & 0 & \frac{-1}{L_1} \end{bmatrix} \begin{bmatrix} v_{PCC,d} \\ v_{PCC,q} \\ v_{1,d} \\ v_{1,q} \end{bmatrix} \\ \begin{bmatrix} i_{grid,d} \\ i_{grid,q} \end{bmatrix} &= \begin{bmatrix} 1 & 0 \\ 0 & 1 \end{bmatrix} \begin{bmatrix} i_{1,d} \\ i_{1,q} \end{bmatrix} + \begin{bmatrix} \frac{1}{R_p} & 0 & \frac{-1}{R_p} & 0 \\ 0 & \frac{1}{R_p} & 0 & \frac{-1}{R_p} \end{bmatrix} \begin{bmatrix} v_{PCC,d} \\ v_{PCC,q} \\ v_{1,d} \\ v_{1,q} \end{bmatrix} \end{aligned} \quad (6.21)$$

Considering the grid parameters provided in Table 6.4, it is possible to calculate the eigenvalues for the system in (6.21). These are given in Table 6.6.

Table 6.6 Eigenvalues of 100 V grid subsystem (with grid voltages as system input).

Eigenvalue	Value
$\lambda_1$	$-370.37 + j377$
$\lambda_2$	$-370.37 - j377$

It can be observed in Table 6.6 that all eigenvalues have negative real parts indicating, thus, a stable system. These results explain, therefore, why voltage perturbation based DQ-Scanning was possible for the considered grid subsystem.

At this point it is emphasized that, although the application of DQ-Scanning methodology as proposed in subchapter 6.2 for extraction of the grid input  $dq$ -impedances is not possible due to the existence of right-half-plane poles, the possibility of using the  $dq$ -admittances extracted from a voltage perturbation based DQ-Scanning could still be considered in order to assess the interconnection stability. However, their use requires additional considerations before stability assessment by means of the Generalized Nyquist Criterion.

More specifically, it is possible to invert the  $dq$ -admittances obtained from a voltage perturbation based DQ-Scanning and use the resulting  $dq$ -impedances in the stability assessment, however the exact number of right-half-plane poles in  $dq$ -impedances is required. In the aforementioned example, this number has been obtained by analytical development and is known, namely, there are two right-half-plane poles (see Table 6.5).

It is noted, for instance, that in practical cases this analytical procedure may not be possible due to the use of protected models. Other techniques may be considered to estimate the number of right-half-plane poles from the frequency characteristics of the  $dq$ -impedances ([152], [159], [162]), however the verification of the assessment of their applicability and effectiveness is outside the scope of this thesis and has not been investigated.

Assuming that the information on right-half-planes poles for the grid  $dq$ -impedances is available, it suffices to consider their number in the evaluation of the Generalized Nyquist. For this, it is reminded that the Nyquist condition for the stability of closed-loop system consisting of the grid impedances and grid-connected inverter admittances (subchapter 6.6) requires one counter-clockwise encirclement of the critical point for each open-loop right-half-plane pole in the grid and grid-connected inverter representations.

In the considered example of interconnection (see Figure 6.24), it is evident that the simplified consideration of grid-connected inverter does not contain right-half-plane in its input  $dq$ -admittance representation, since it consists of only three-phase resistances with positive values (see Table 6.4). Therefore, in total only two open-loop right-half-plane poles need to be considered in the analysis of the Nyquist diagram for the interconnection.

The resulting Generalized Nyquist diagram for the interconnection considering the parameters given in Table 6.4 is illustrated in Figure 6.27.

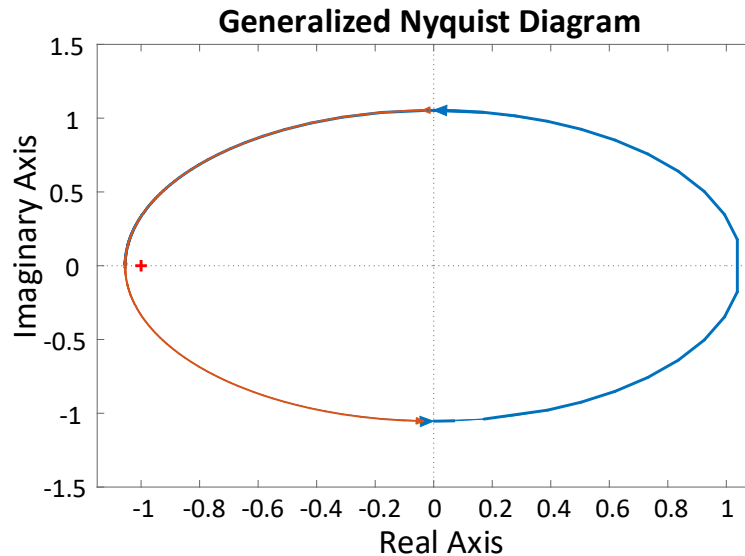


Figure 6.27 Nyquist diagram for stability assessment of the 100 V grid interconnection.

It can be seen in Figure 6.27 that the critical point  $(-1,0)$  is encircled twice (indicated by the blue and red colors). With the prior knowledge of two open-loop right-half-plane poles, these results thus indicate a stable interconnection with the consideration of parameters given in Table 6.4. At this point, it is emphasized that without the information on the open-loop right-half-plane poles, correct stability assessment based on the Nyquist diagram would not have been possible. For instance, the direct application of the criteria proposed in subchapter 6.2 without proper consideration of the right-plane-poles would have led to wrong stability predictions.

To verify the Generalized Nyquist results, the detailed EMT representation of the interconnection shown in Figure 6.24 is simulated. Small-signal perturbations are applied to the voltage sources  $V_1$  and  $V_2$  and the currents through inductance  $L_1$  (system states) are monitored. More specifically, the  $dq$ -components of both sources are sequentially stepped up and down by a factor of 2.5% of the system rated voltage (100 V) every half of a second. The results are shown in Figure 6.28.

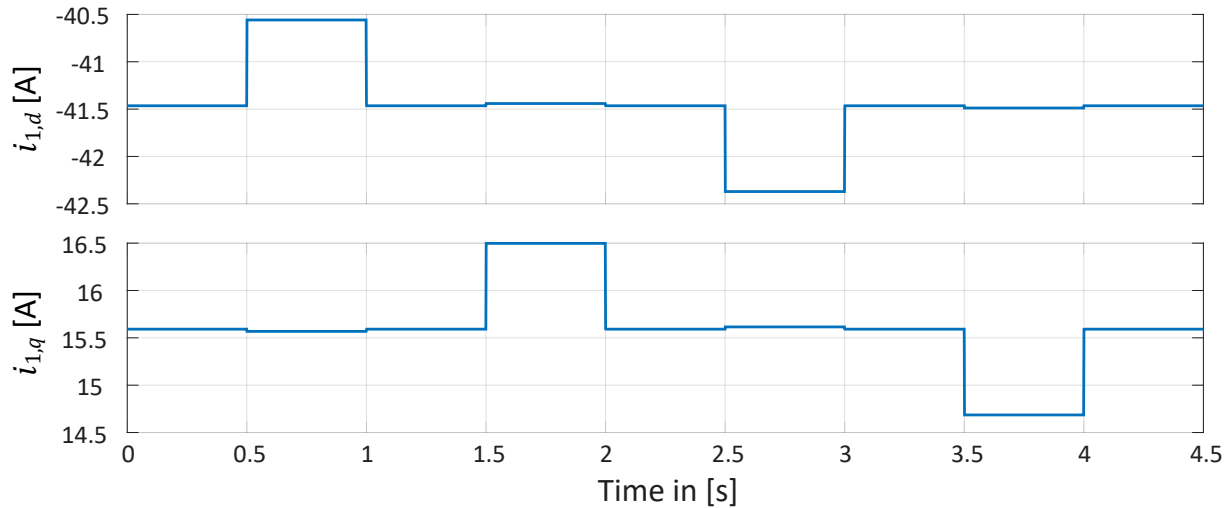


Figure 6.28 Measured  $dq$ -currents through inductance  $L_1$  for small voltage perturbations.

The results illustrated in Figure 6.28 confirm the predictions obtained by means of the Generalized Nyquist criterion application with consideration of right-half-plane poles in the open-loop subsystems. It is observed that the state-variable, i.e., the currents through inductance  $L_1$ , are capable of riding through the perturbations and of regaining a new steady-state conditions after each voltage step.

To further consolidate these analyses involving right-half-plane poles in the open-loop subsystems, a variation of the parameters given in Table 6.4 is proposed. More specifically, a change in the resistance values for the simplified grid-connected inverter representation from  $2.1 \Omega$  to  $1.9 \Omega$  is assumed. The grid subsystem remains unchanged.

The stability of the “new” interconnection is now evaluated. The DQ-Scanning technique is reapplied to extract the new input  $dq$ -admittance values of the simplified grid-connected inverter subsystem. Finally, a new Generalized Nyquist diagram is generated and is illustrated in Figure 6.29.

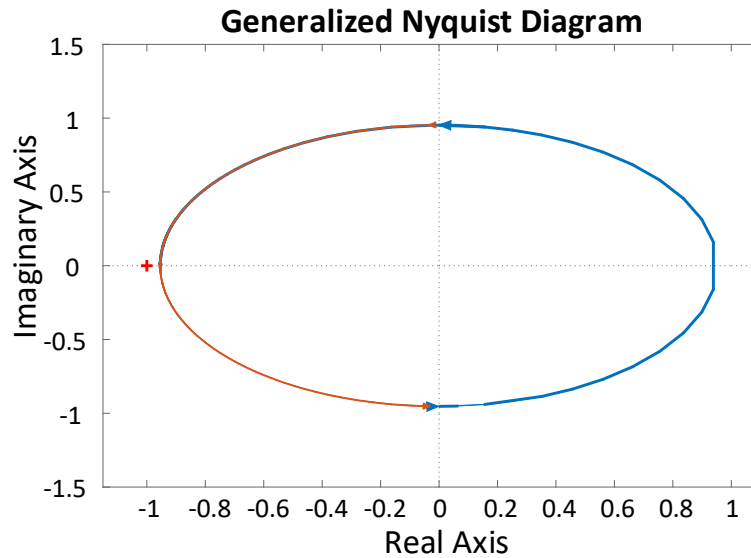


Figure 6.29 GNC diagram for stability assessment of the new interconnection.

It is seen in Figure 6.29 that the Generalized Nyquist diagram does not encircle the critical point  $(-1, 0)$ . It is emphasized, however, that the grid subsystem parameters have not been changed and, thus, still contain two open-loop right-half-plane poles, whereas the new assumed resistance values for the grid-connected inverter subsystem representation do not introduce any further right-half-plane poles to this count. Based on this information, the Generalized Nyquist contour should still encircle the critical point twice counter-clockwise to ensure the interconnection stability. Since this is not the case observed in Figure 6.29, the stability assessment indicates an unstable interconnection.

To verify these results, the detailed representation of the interconnection has been simulated in EMT. The simulation is initialized with the parameters given in Table 6.4 and at time  $t = 1\text{ s}$  the resistance values of the grid-connected inverter subsystem is changed to the new value from  $2.1\ \Omega$  to  $1.9\ \Omega$ . The currents through inductance  $L_1$  (system states) are monitored and the results are illustrated in Figure 6.30.

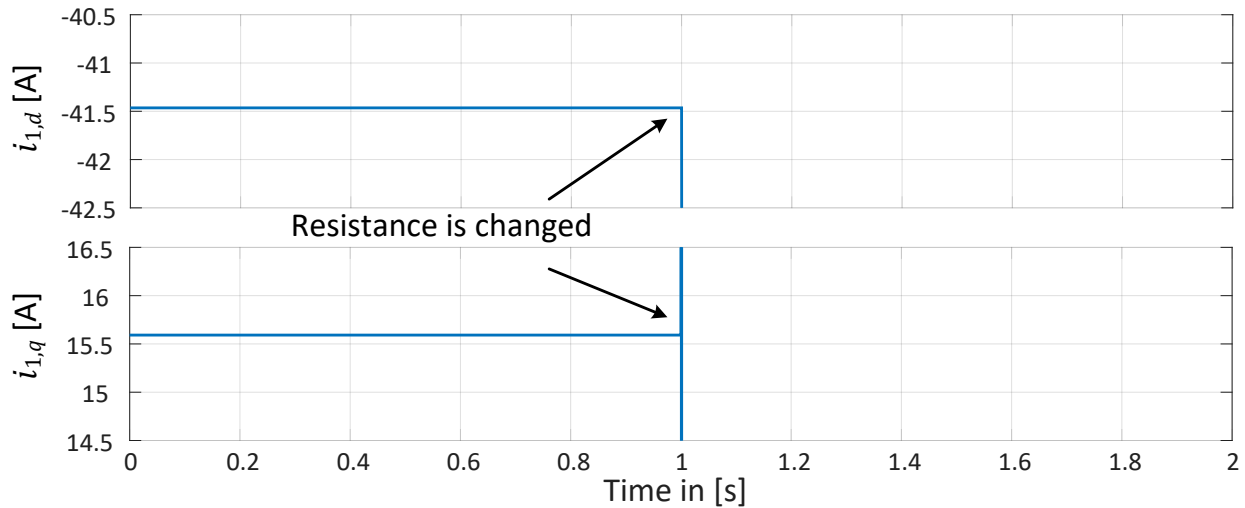


Figure 6.30 Measured  $dq$ -currents through inductance  $L_1$  for GCI resistance change.

It is observed in Figure 6.30 that once the resistance value of the simplified representation of the grid-connected inverter (GCI) is changed to  $2.1 \Omega$ , the measured  $dq$ -currents through the inductances  $L_1$  tends to infinity and no numerical solution is possible anymore. These results, thus, confirm the DQ-Scanning based Generalized Nyquist stability predictions.

Finally, it is highlighted that these results reinforce the generality of the proposed DQ-Scanning methodology when properly used in conjunction with the generalized Nyquist stability assessment. Nevertheless, it is emphasized that, in the interest of simplicity and mathematical demonstrations, the examples used in this subchapter are oversimplified and parameters have been chosen regardless of physical interpretations.

It is yet to be demonstrated if the consideration of right-half-plane poles in the impedance representation of grids, or in the admittance representation of grid-connected inverters, is of practical relevance. To date, the author is not aware of a practical case for which the above considerations have been necessary. Further research for this purpose is outside the scope of this thesis and is recommended for future works.

## 6.10 Application Cases: DQ-Scanning for Stability Assessment

In previous subchapters, the DQ-Scanning technique has been outlined and its effectiveness demonstrated for the scenarios investigated throughout this thesis by means of other techniques as well, notably, modal analysis, the combined scan technique and EMT simulations.

To allow for its application in practical cases, it is therefore essential to further demonstrate its applicability in cases involving more grid-connected inverters as well as larger and more complex grid structures. This is done in the next subchapters.

### 6.10.1 Unstable Type-IV based Wind Farm in Weak Grid System

It has been observed for the scenarios investigated in this thesis that type-IV wind farms are less susceptible to interact with series compensation than type-III wind farm systems. On the other hand, it has also been demonstrated by means of a simplified VSC system that grid-connected converters can also interact with a grid, even in cases of no series compensation. It has been seen in subchapters 5.5 and 6.7, for instance, that the simplified (full-converter) VSC system adversely interacted with a simple grid structure in case of low SCR ratios.

A similar case has been also found for the type-IV system considered in this thesis. More specifically, the benchmark system proposed in subchapter 3.3 has been slightly modified to account for a longer transmission line between the PCC of the wind farm and the rest of the system. Additionally, enhanced transmission line models were considered, more specifically, transmission line models with frequency dependent (FD) parameters (assumed continuously transposed) were used. The WPP has not been changed, i.e., a type-IV based wind farm of 100 MW installed capacity is still assumed, however the wind speed has been reduced in this case to 9.91 m/s, so that the wind farm operating condition considers an active power injection of approximately 75 MW. The reactive power setpoint has been adjusted so to have a voltage of approximately 0.98 per unit at the PCC in steady-state condition. The system is illustrated in Figure 6.31 and further details are available and can be extracted from *case3\_thesis\_AramisST.ecf* [105].

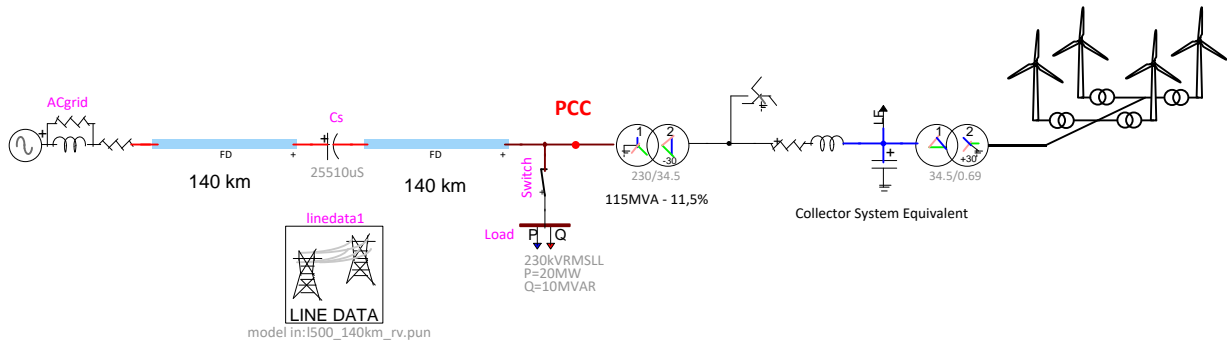


Figure 6.31 Modified benchmark system: case with unstable type-IV wind farm.

In the system illustrated in Figure 6.31 it is noted that a load is considered at the PCC. This is a 20 MW, 10 MVAR load. Initially, this load is considered connected (switch is closed), but at time  $t = 30\text{s}$  the load is disconnected by opening the three-phase switch. The resulting active and reactive powers measured at the PCC (flowing into the grid) are illustrated in Figure 6.32.

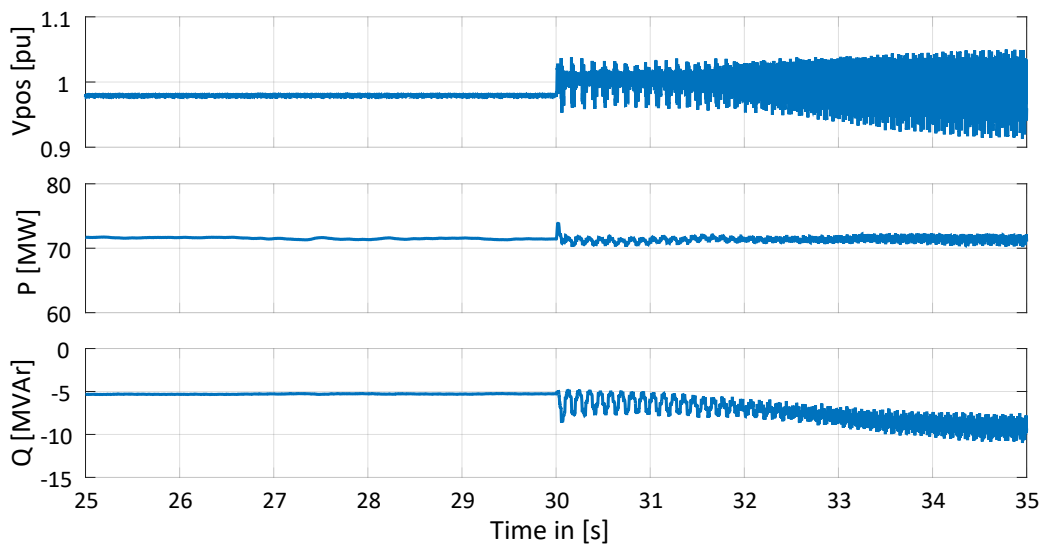


Figure 6.32 Positive sequence voltage, active and reactive powers measured at the PCC.

It is observed in Figure 6.32 that the disconnection of the load at the PCC leads to an unstable condition. Oscillations are measured at the PCC and it is also noted that the reactive power starts drifting from its reference value.

This scenario is now to be investigated by means of the DQ-Scanning technique to verify if the instability could be captured by the technique. For this, the steady-state conditions, i.e., the  $dq$ -voltages and currents,  $v_{dq,0}$  and  $i_{dq,0}$ , respectively, are obtained for the base case (considering the

load at the PCC) and the input  $dq$ -admittances and impedances are extracted for both wind farm and grid as seen from the PCC. Another DQ-Scanning is applied for the grid to extract its input  $dq$ -impedances for a case without the load at the PCC. Finally, stability is assessed by means of the Generalized Nyquist criterion. The corresponding Nyquist contours are shown in Figure 6.33 and Figure 6.34 for the cases of a grid with and without load considered at the PCC.

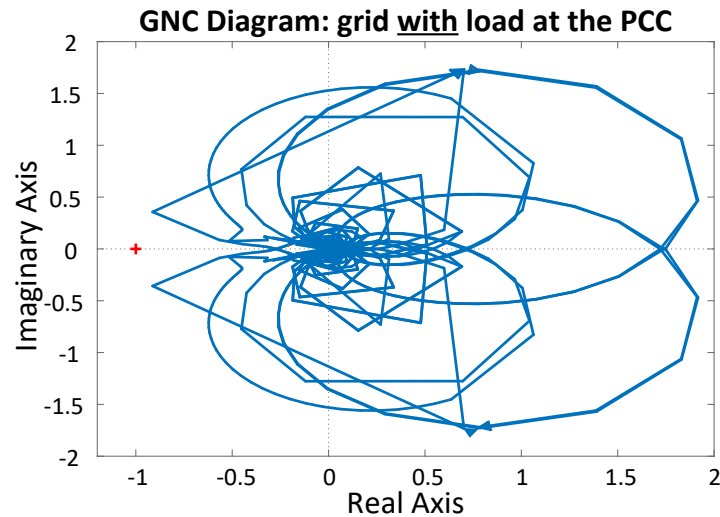


Figure 6.33 Generalized Nyquist contour for scenario with load at the PCC.

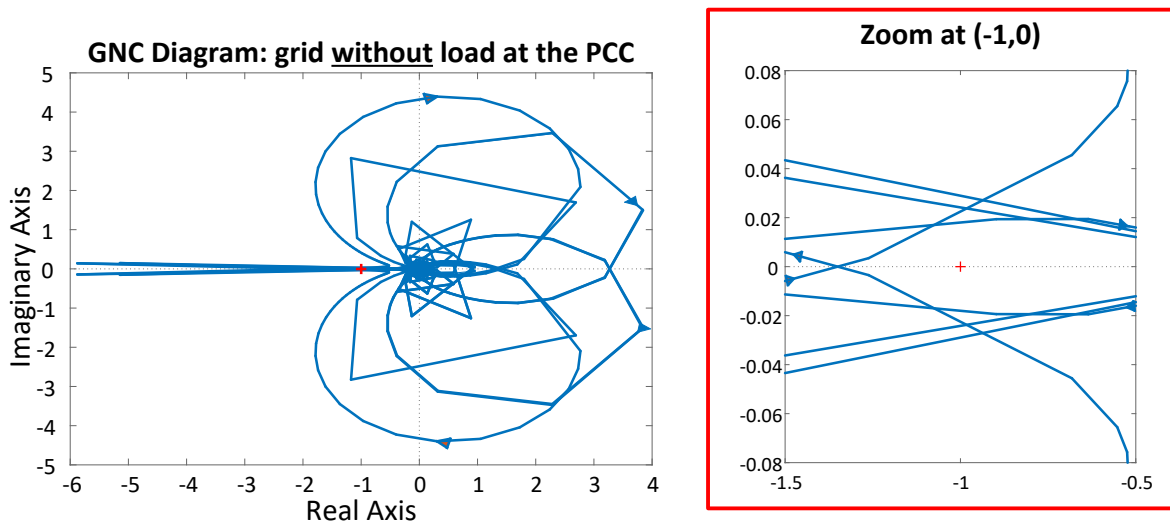


Figure 6.34 Generalized Nyquist contour for scenario without load at the PCC.

It is evident from Figure 6.33 and Figure 6.34 that the Nyquist contour does not encircle the critical point  $(-1,0)$  for the case the load is considered connected at the PCC, whereas the contour does

encircle the critical point several times for the case the load is considered disconnected. Therefore, the stability assessment based on the DQ-Scanning technique does predict instability for the grid scenario without load and, thus, these results are in accordance with those obtained through detailed EMTP simulation shown in Figure 6.32.

### 6.10.2 Offshore Type-III Wind Farm connection through an HVDC Link

This subchapter investigates a case of an offshore type-III wind farm interconnection to the shore through an MMC-HVDC link presented in [163]. The original case has been slightly modified for these investigations in order to give a more realistic and practical consideration to the scenario, since it has been verified that for the case presented in [163], the voltage measured at the ac-side of the offshore HVDC converter station was low (approximately 0.85 per unit). For this, a higher voltage setpoint is used at the offshore station. Additionally, the ac transmission line model connecting the wind farm to the converter station is now considered as a distributed parameters line model instead of simple resistances and reactances. It is noted, however, that these modifications do not change the qualitative nature of the instabilities observed for this scenario. Details and parameters can be extracted from *case4\_thesis\_AramisST.ecf* [105]. The scenario is illustrated in Figure 6.35.

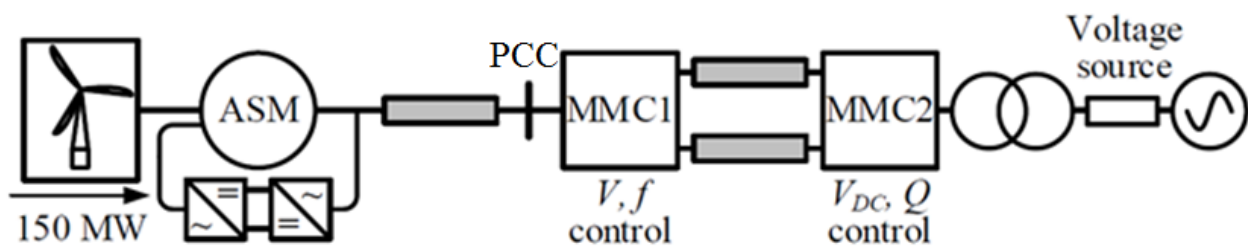


Figure 6.35 Type-III wind farm offshore interconnection through HVDC link [163].

This scenario investigates the impact of the so-called circulating current control (CCC), which is a controller existent in the MMC-HVDC link to reduce circulating currents in the HVDC arms. It has been observed for the particular case illustrated in Figure 6.35 that the deactivation of the CCC leads to subsynchronous oscillations involving the offshore wind farm and the HVDC link. This is illustrated in Figure 6.36, in which the CCC is deactivated at time  $t = 20s$ .

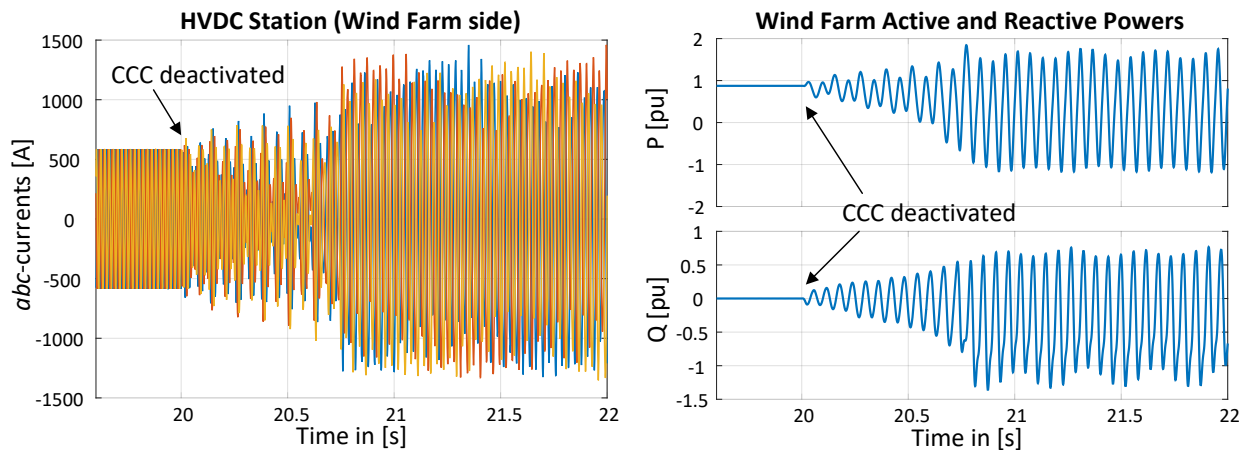


Figure 6.36 Left: HVDC MMC  $abc$ -currents; Right: Wind farm active and reactive powers.

It is evident from Figure 6.36 that the deactivation of the CCC takes the system, which was prior in steady-state, to an oscillatory condition. This is clear both in the currents measured at the ac-side of the MMC-HVDC link as well as in the active and reactive powers measured at the type-III based wind farm terminals.

The DQ-Scanning is applied to this case to investigate its capability of identifying the potential risk of deactivating the CCC in the HVDC station. More specifically, the interconnection stability is assessed at the point-of-common-coupling (PCC), indicated in Figure 6.35. The input  $dq$ -admittances of the wind farm as well as the input  $dq$ -impedances of the HVDC link were extracted. In the case of the HVDC link, this is done twice: i) one for a case considering the CCC activated, and ii) a second time with the CCC deactivated. The results are illustrated in Figure 6.37 and Figure 6.38 for the cases with and without CCC, respectively.

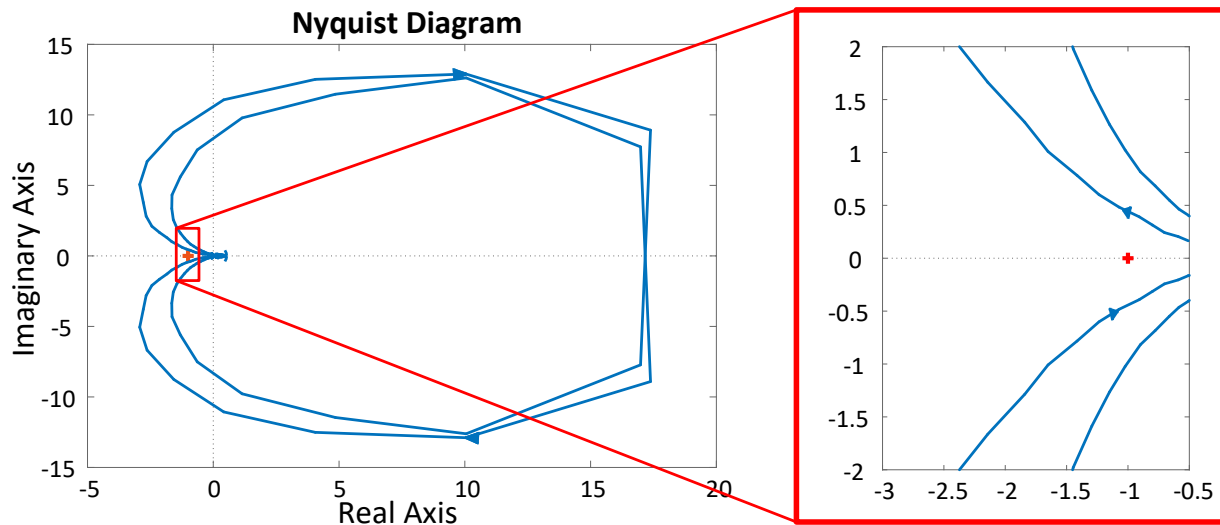


Figure 6.37 GNC contour for the wind farm – HVDC interconnection with CCC active.

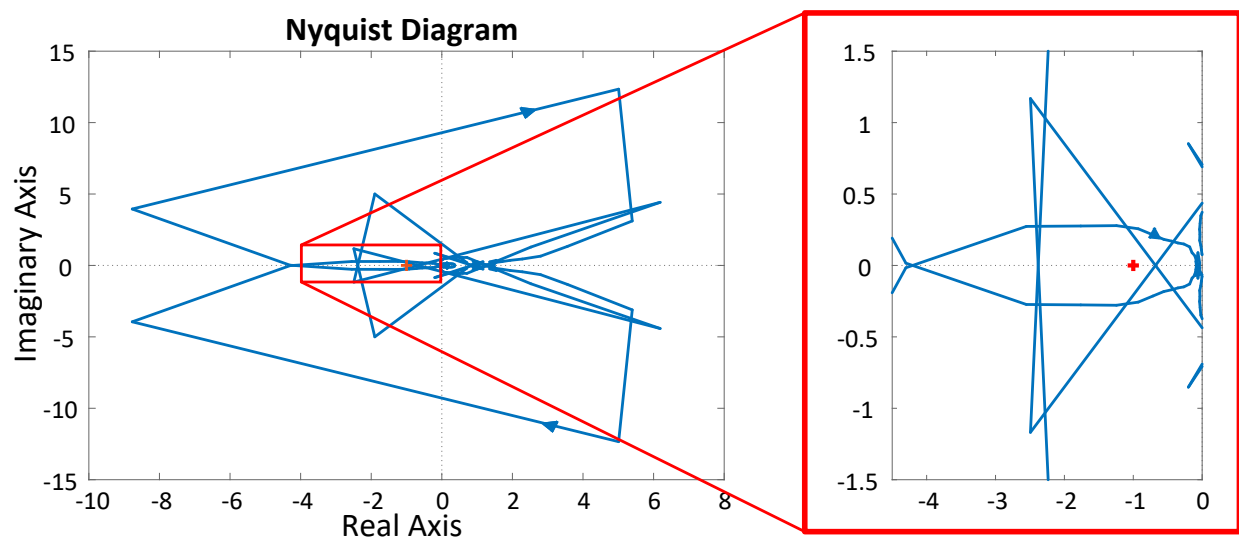


Figure 6.38 GNC contour for the wind farm – HVDC interconnection with CCC deactivated.

It can be observed in Figure 6.37 and Figure 6.38 that the DQ-Scanning based stability assessment of the interconnection was capable of properly predicting the risks related to the deactivation of the CCC in the HVDC station. While the Nyquist contour for the case with CCC did not encircle the critical point, more than one encirclement is seen in the case without CCC, thus, indicating instability for the latter.

Finally, it is emphasized that in this scenario, the HVDC connector has been assessed as being the “grid subsystem”. In other words, differently than the previous cases investigated in this thesis, it

is noted that more than one grid-connected inverter system has been considered, namely, the DFIG based wind farm and the HVDC system. This is another indication of the generality of the DQ-Scanning approach.

Nevertheless, to help consolidating the DQ-Scanning application in multi-converter system, other scenarios involving multi-converters in larger systems are assessed in the next subchapters.

### 6.10.3 Large-Scale Grid under n-1 Contingency Condition

In this subchapter, the DQ-Scanning methodology is applied to a larger power system. More specifically, SSCI-Benchmark I system, introduced in [37], is used. As previously briefly outlined in subchapter 3.2 (see Figure 3.3), this system allows the representation of several phenomena, including SSR, SSCI, problems related to low short-circuit ratio (SCR), ferroresonance and voltage control interaction with synchronous condenser.

Some modifications have been, however, applied to the system to create the scenario investigated in this subchapter, which focus on the “new” interconnection of a WPP 1. For this, WPPs 2, 3 and 5 are assumed disconnected and only WPP 1 and WPP 4 were left in the system. It is also considered in this analysis that, due to the low level of wind generation, the HVDC link (in the “south” of the system), is also disconnected. The Thevenin grid representation introduced close to the HVDC system, to represent an interconnector to another grid, is as well excluded. Finally, the WPP 1, original from the SSCI-Benchmark I grid, has been replaced by a type-III based wind farm with the DFIG technology and parameters introduced in subchapter 2.2. A collector system representation for the WPP 1 has been considered, with an upscaling of the collector system parameters proposed in this thesis in subchapter 3.3, to accommodate an aggregated representation of 295 DFIG wind turbines, i.e., a wind farm of approximately 500 MW installed capacity. Wind speed is assumed at 10.45 m/s at WPP 1 and 11.24 m/s (nominal wind) at WPP 4. All other details and parameters can be directly extracted from *case5\_thesis\_AramisST.ecf* [105]. The final system is illustrated in Figure 6.39, where exclusions are also indicated (in red).

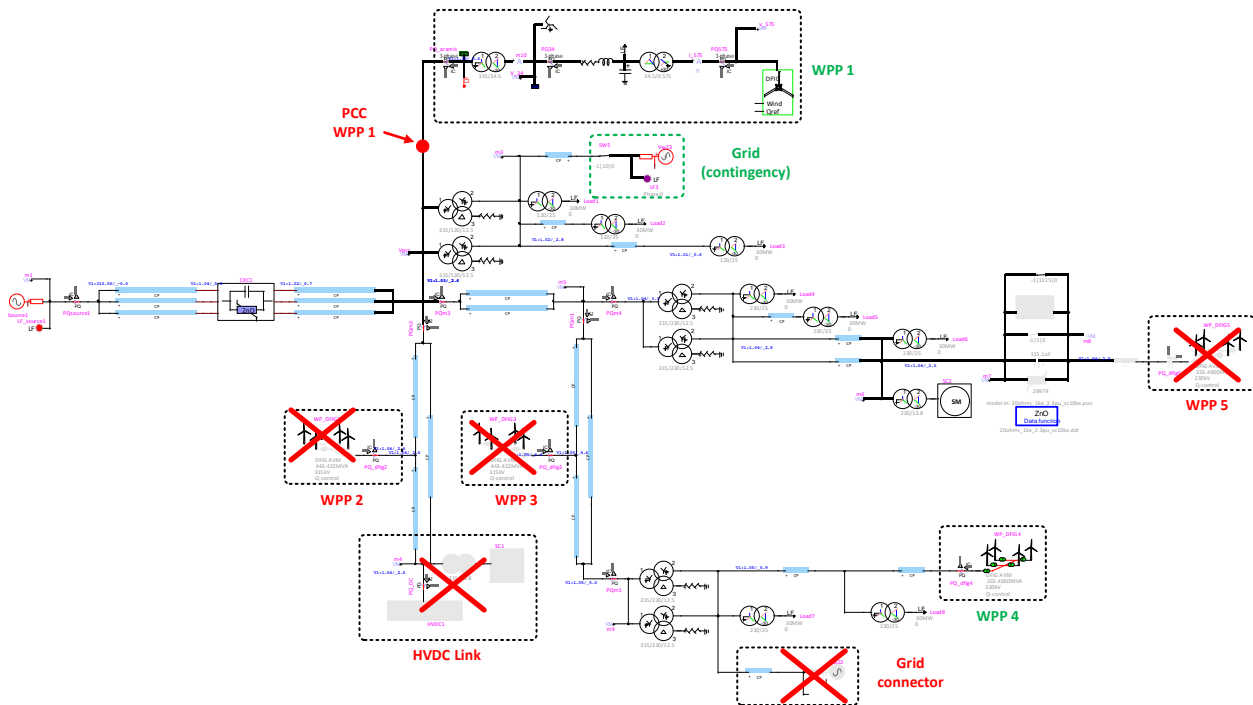


Figure 6.39 Large scale grid – investigation of new WF (WPP 1) under n-1 contingency.

The interconnection of WPP 1 is studied in conjunction with a possible n-1 contingency in the grid. More specifically, it is assumed that the interconnection leading to another grid may be lost (indicated by the Thevenin grid in the area covered by the green dashed line in Figure 6.39).

To assess the impact of having the “new” WPP 1 interconnection to the grid while such a condition (losing the ac interconnector) arises, the DQ-Scanning is applied. For this, the input  $dq$ -admittances as seen from their point-of-common-coupling (PCC) of WPP 1 are extracted. Similarly, the grid input  $dq$ -impedances are extracted for both cases, namely, considering the normal and the contingency condition (without the ac interconnector).

Finally, the Generalized Nyquist criterion is applied to the resulting DQ-Scanning  $dq$ -impedances and admittances. The results are illustrated in Figure 6.40 and Figure 6.41 for the cases of a normal and contingency grid operating modes, respectively.

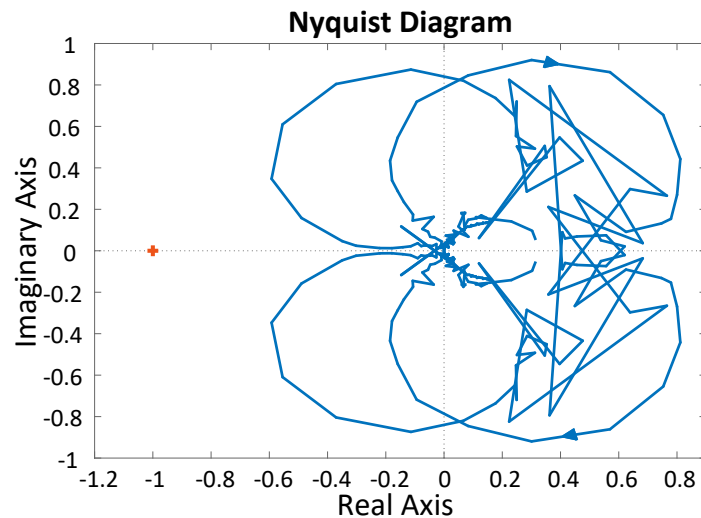


Figure 6.40 Nyquist contour for WPP 1 interconnection under normal condition.

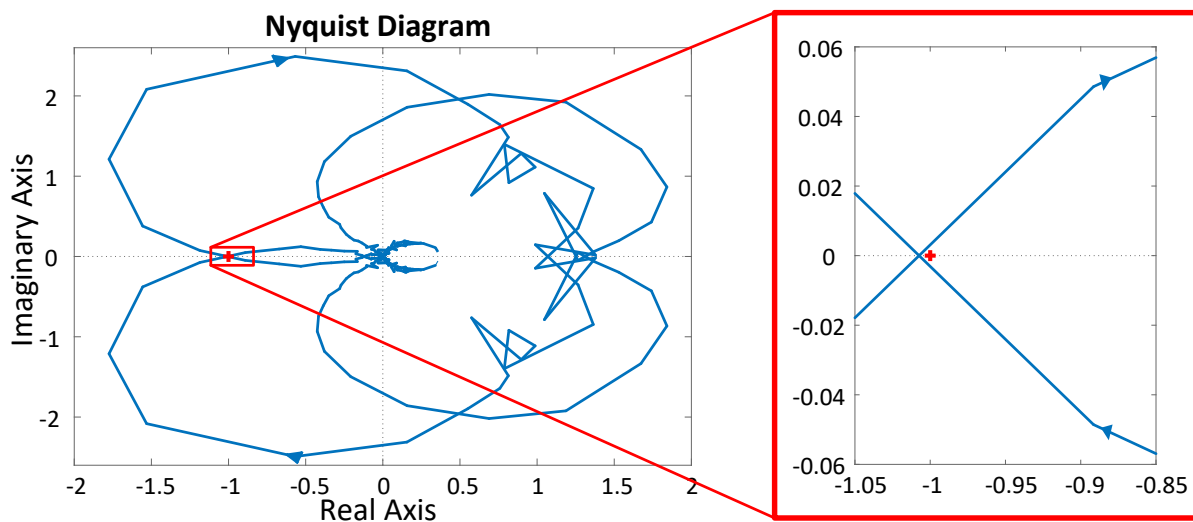


Figure 6.41 Nyquist contour for WPP 1 interconnection under contingency condition.

It is observed in Figure 6.40 that the interconnection of the new wind farm WPP 1 does not indicate any potential risks when the grid is considered in normal operating condition, since the Nyquist contour does not encircle the critical point. On the other hand, once the contingency condition is assumed (Figure 6.41), it can be seen that the Nyquist contour encircles the critical point  $(-1,0)$ , thus, indicating a potential interaction risks between the wind farm and the grid.

To validate these results, the corresponding detailed representation of the above scenarios has been simulated in EMTP. Initially, the grid is assumed in its normal condition and, then, at time  $t =$

10s, the ac line interconnector to the neighbor connecting grid is lost (three-phase breaker opens), leaving the grid in its contingency case. The resulting expected positive sequence voltage and powers measured at the PCC of WPP 1 are illustrated in Figure 6.42.

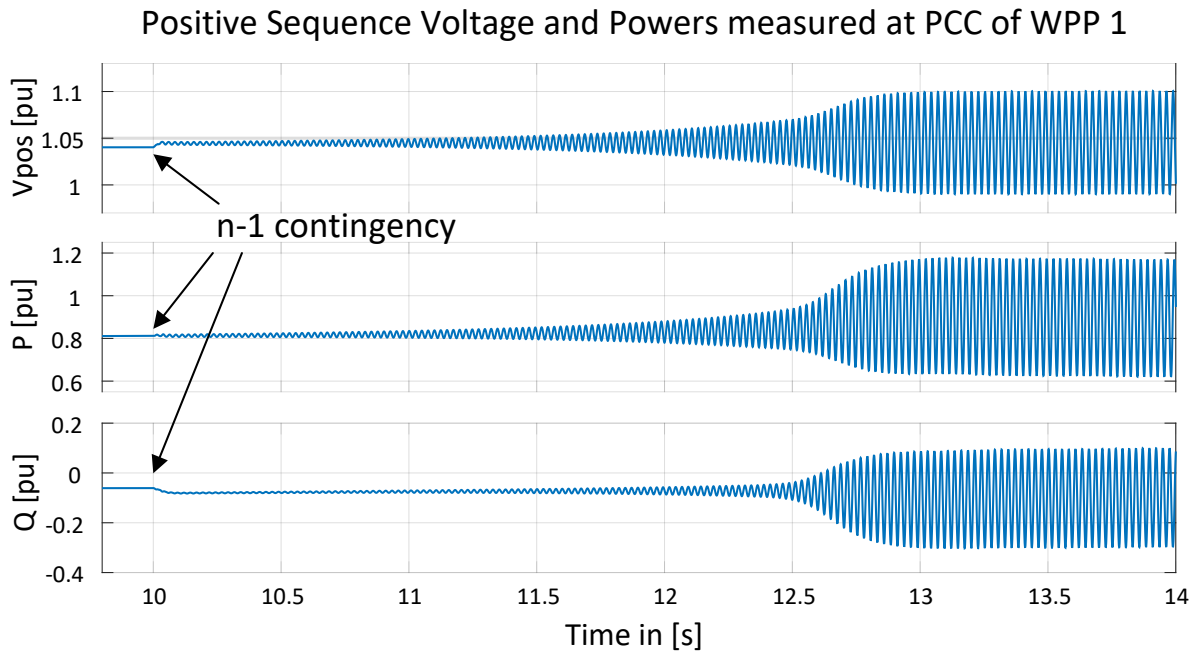


Figure 6.42 Large-scale grid: effect of n-1 contingency at PCC of WPP 1.

It is evident from Figure 6.42 that the considered n-1 contingency, namely, the loss of the ac interconnector to a neighbor grid, leads to sustained low frequency oscillations measured at the PCC of the wind farm WPP 1. These results, thus, confirm the DQ-Scanning predictions illustrated in Figure 6.40 and Figure 6.41.

#### 6.10.4 Large-Scale Grid: Stability under High and Low Wind Conditions

This subchapter investigates the stability of the large-scale SSCI-Benchmark I ([37]) under the perspective of different operating conditions imposed by intermittent renewable generation. More specifically, system stability is addressed under high and low wind conditions.

The interconnection of wind farm WPP 5 is studied. It is assumed that WPP 5 lies geographically far from the other four wind farms, such that wind variations at WPP 5 are not necessarily correlated to those of WPP 1, 2, 3 and 4. This allows a separate investigation of wind variations in the grid area of WPP 5.

Stability is assessed for two cases: i) for nominal wind conditions (i.e., wind speed is assumed equal 11.24 m/s); and ii) a low wind conditions, for which wind speed is assumed equal 8 m/s. The DQ-Scanning technique is used to investigate the impact of wind variations. For this, the grid input  $dq$ -impedances are obtained assuming that WPP 5 is injecting nominal power. Additionally, the input  $dq$ -admittances of wind farm WPP 5 are extracted for the two aforementioned conditions, namely, considering high and low wind speeds.

The resulting Nyquist contours for the high and low wind scenarios are shown in Figure 6.43 and Figure 6.44 respectively.

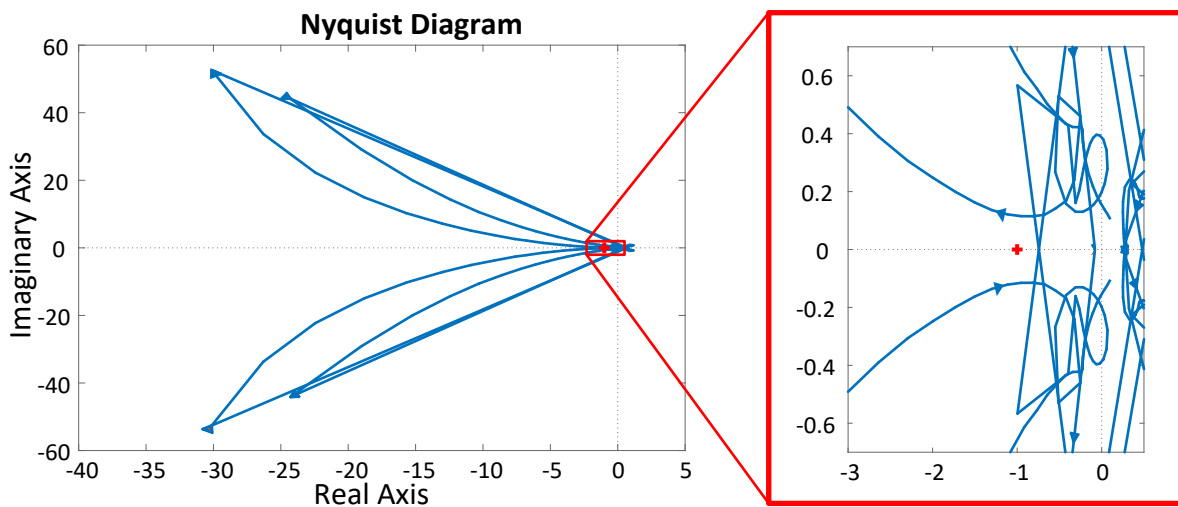


Figure 6.43 Nyquist contour for WPP 5 interconnection considering nominal wind speed.

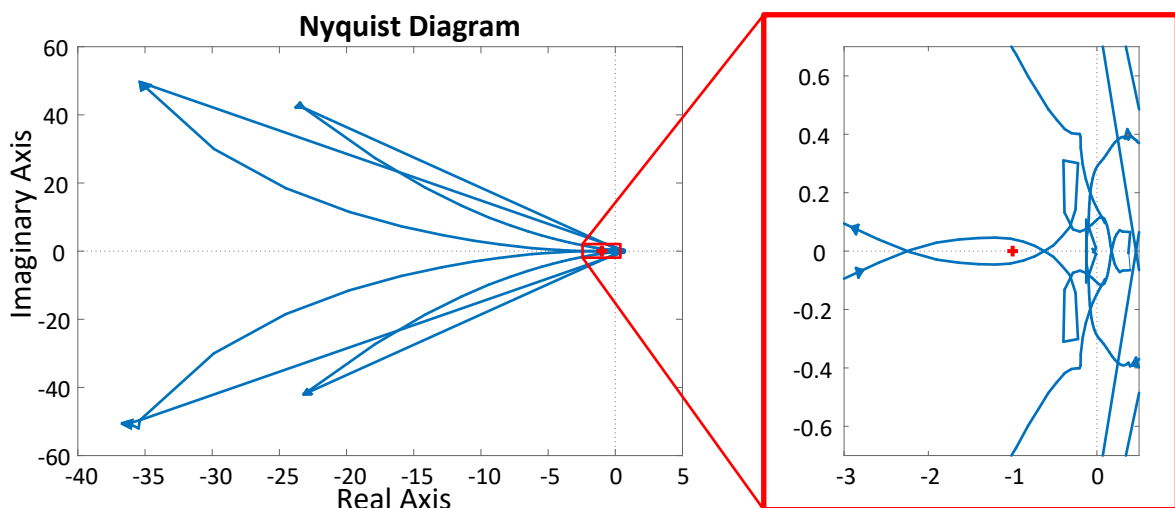


Figure 6.44 Nyquist contour for WPP 5 interconnection with low wind speed (8 m/s).

It can be seen from Figure 6.43 that the interconnection of WPP 5 considering the wind farm operating at nominal wind conditions is not expected to lead to any instabilities. Interestingly, however, the consideration of a lower wind speed, namely, 8 m/s, affects the small-signal input  $dq$ -admittances in such a way that the stability of the interconnection is affected. It is observed in Figure 6.44 that the Nyquist contour encircles the critical point  $(-1,0)$ , so that an unstable condition for WPP 5 is expected if wind speed is low.

To verify these results, the detailed EMTP representation of SSCI-Benchmark I is used. Wind farm WPP 5 is initialized at nominal wind speed. Then, at time  $t = 3\text{s}$ , wind speed is reduced stepwise for WPP 5 from 11.24 m/s to 8 m/s. The resulting voltages and powers measured at the point-of-common-coupling (PCC) of WPP 5 are illustrated in Figure 6.45.

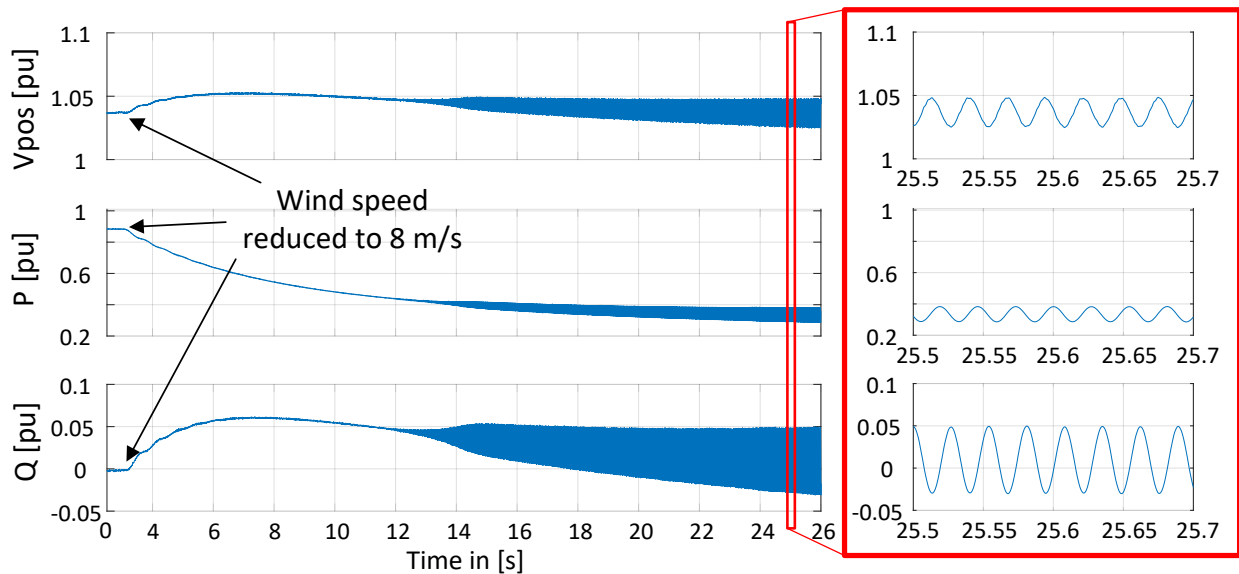


Figure 6.45 Positive sequence voltage and powers at PCC after wind speed change.

It can be seen in Figure 6.45 that reducing the wind speed of WPP 5 to 8 m/s has the effect of pushing the system to a new operating condition that is not stable. After a certain level of power is achieved, it can be observed that an increased oscillatory behavior starts. Oscillations have a frequency of approximately 38 Hz and can be observed not only in the injected powers, but also in the grid voltage measured at the PCC.

These results therefore corroborate those obtained previously through the application of the DQ-Scanning technique, which predicted an unstable operating condition for low wind speeds at the wind farm WPP 5 (indicated by the encirclements of the critical point in Figure 6.44).

Finally, it is emphasized that the analyzed grid contains not only meshed structure of classical components (transmission lines, series-capacitors, transformers, loads), but also an important share of grid-connected inverters (four wind farms, HVDC link) as well as synchronous condensers. These results are, thus, also an indication that the DQ-Scanning is capable of properly extracting and assessing the small-signal characteristics of all these components only by having their detailed models, which could have been protected (i.e., black-boxes), and without requiring any further detailed information.

## CHAPTER 7 CONCLUSION AND RECOMMENDATIONS

### 7.1 Summary

This thesis focuses on the analysis of low frequency phenomena and stability assessment of energy systems with realistic consideration of power equipment.

It starts with a review of relevant and recent field events resulting from the adverse interaction of generating units in existing grid infrastructures. They involve not only conventional power plants, but, in recent years, mostly grid-connected inverters, strongly represented by wind and photovoltaic power plants as well as HVDC interconnectors. These events are treated as evidence that planning and study of modern power systems require reconsideration.

An overview is provided for the classification and definition of the different types of low frequency power system oscillations. It has been noted that grid-connected inverters add new dynamics into existing grids and, thus, introduce new types of possible interactions and instabilities.

A review of existing models and benchmark grids for low frequency phenomena is given. Moreover, a new benchmark system is proposed for low frequency interaction studies involving wind farms in series compensated grids. It considers realistic representation of grid equipment with their corresponding nonlinear characteristics, such as surge-arresters and transformer saturation.

A generic manufacturer specific EMT-type wind turbine model is proposed. It addresses a system based on a directly-coupled (gearless) externally-excited synchronous generator, which is connected to a three-stage full-converter system consisting of a six-pulse diode rectifier, a dc-dc boost converter and a two-level VSC. All wind turbine controllers are developed and explained. This detailed model has been validated against field tests conducted in the framework of this research in a real wind turbine, with focus on fault-ride-through strategies. It has been observed that the proposed model provides sufficiently accurate and adequate performance.

Moreover, an EMT-type hybrid model is developed for the same wind turbine system by combining average value models and switched equivalent circuits for the power electronic stages. The hybrid model allows for much larger simulation time-steps under some acceptable assumptions. As a result, faster computation times are achieved, also making the model suitable for real-time applications.

An in-depth analytical analysis of low frequency interaction phenomena involving grid-connected inverters is made. For this, modal analysis is applied. Linearized state-space representations are developed for a simple VSC system, as well as for the proposed benchmark system in conjunction with detailed type-III and type-IV wind turbine models. The methodology used for developing and validating separate analytical subsystems into a complete linearized state-space representation is outlined. Additionally, eigenvalue sensitivity and participation factor analysis are applied to support investigations and understanding of low frequency phenomena, with emphasis on adverse interactions found in case of type-III based wind farms.

A literature review of stability assessment methods is provided. The capabilities of the methodology with the current largest industry relevance, namely, the combined scan technique, are assessed. This is done by applying it to the same systems previously investigated by means of modal analysis. Limitations are found and demonstrated. More specifically, it has been observed that the combined scan technique was capable of properly predicting stability in the case of type-III wind farm, however provided incorrect stability prediction in the cases of a simple VSC system consisting of only a PLL and a current regulator, and of a type-IV wind farm. Detailed analysis of these cases indicated that the inherent asymmetric input impedance characteristics of grid-connected inverters are not properly considered in the combined scan technique, yielding therefore the need for a multi-variable framework for the analysis of modern power system structures.

To address the aforementioned limitations, a new screening technique for stability assessment is proposed, namely, the DQ-Scanning technique. It is based on the already existing multivariable impedance-based theory in the  $dq$ -frame, however it has been further improved to address realistic grid structures and equipment considerations. For this, an enhanced perturbation signal structure is proposed for the extraction of small-signal input  $dq$ -admittance and impedance characteristics of grid-connected inverters and electrical grids, which in turn can also contain grid-connected inverters. It is highlighted that attention is required when extracting such characteristics from realistic equipment representations, for instance with detailed consideration of transformer characteristics, especially in the low frequency region. This is demonstrated based on a thorough validation conducted against rigorous analytical representation of the investigated systems. Finally, stability assessment is proposed based on the use of the resulting admittance and impedance representations in conjunction with the framework provided by the well-established Generalized Nyquist criterion.

It is noted that the DQ-Scanning technique relies on the separate extraction of the small-signal input admittance and impedance characteristics of grid-connected inverters and electrical grids, respectively. From an industrial perspective, it is emphasized that this consists in one of the main advantages of the proposed methodology, since their extraction can be assigned to different parties of a project, which may help accelerate stability analyses and identification of possible critical scenarios in practical interconnection processes. It is assumed that the exchange of frequency dependent input impedance and admittance characteristics of grid and grid-connected inverters, which result from the DQ-Scanning application, is less prone to intellectual property issues if compared to the exchange of detailed grid information and equipment models. This becomes even more relevant in multi-converter scenarios, which may involve different manufacturers. Therefore, it may even help establishing another language between power system operators and manufacturers (or project developers).

Additionally, it is also revealed that the separate analysis of grid and grid-connected inverters allows the consideration of proper perturbation variables for these subsystems. More specifically, it is demonstrated that current perturbations are more appropriate to extract the input impedance of grid subsystems, whereas voltage perturbations are more adequate for grid-connected inverters, since help avoiding constraints imposed by right-half-plane poles during stability analysis.

Finally, the capabilities of the proposed DQ-Scanning technique are investigated for different cases in different grid structures with focus on the stability assessment of new interconnections. It has been observed that it was capable of properly predicting the stability in all scenarios, even under consideration of multi-converter large-scale grids, thus, providing strong evidence for its efficient and reliable use in the context of modern power system structures, including when protected (i.e., black-box) models are used.

## **7.2 Recommendations for Future Works**

It is emphasized that this thesis dealt with the small-signal stability analysis of power systems. Future works could further explore the small-signal impedance representations obtained through application of the DQ-Scanning in several aspects.

From a power system perspective, it would certainly be relevant to further investigate the characteristics of typical plant controllers and map them in the  $dq$ -frame. For instance, the impacts of different wind farm controllers, e.g. voltage droop control or power-frequency control, which aim at controlling active and reactive power or voltage at the point of common coupling, could be further assessed, also taking into consideration different choices of partition points for the DQ-Scanning application and providing recommendations in this sense.

Additionally, it is reinforced that the DQ-Scanning technique is based on an impedance and admittance representation of grid and grid-connected inverters in  $dq$ -frame and neglects their zero-sequence representations. The effect of adding the zero-sequence in these representations is left for future research. By doing so, a more complete representation of assessed subsystems is expected, and it would be relevant to verify what role the zero-sequence may play in low-frequency phenomena in power systems.

From a linear control perspective, the question of admittance (or impedance) oriented design of grid-connected inverter controllers could be raised. For instance, a mapping of the impact of different typical controllers in the input  $dq$ -admittances could support fast mitigation of adverse interaction issues in the case of new interconnection projects, by providing engineers with valuable information of which controllers and variables to manipulate in order to achieve compliance.

To enhance this perspective, the robust control theory could also be addressed. It is noted that the small-signal characteristics of grids and grid-connected inverters are only valid for small variations around the investigated operating point. Additionally, it has been observed that, for instance, the input admittance characteristics of grid-connected inverters can significantly vary from one operating point to the other. This has been confirmed in subchapter 6.10.4 in which the impact of low wind in wind farm operating conditions was sufficient to change its input admittances characteristics in such a manner that a stable operation was not possible anymore. Therefore, it is assumed that the application of robust control theory could support the development of conditions on the input admittances characteristics of grid-connected inverters (or on the input impedance characteristics of grids) to guarantee stable operation. Such conditions could be directly applied to the input admittances (or impedances) representations, avoiding, for instance, the necessity of applying the Generalized Nyquist Criterion.

Also, the optimization of the perturbation technique and the code implementation of the DQ-Scanning technique with focus on the reduction of computation efforts could be investigated. It is noted that the DQ-Scanning technique relies on the use of single-tone perturbations, i.e., on the perturbation of one of the  $dq$ -channel at one single frequency at a time. Moreover, the settings of the perturbation (ramp times, perturbation length and amplitudes, among others) are currently left to the engineering judgement, based on available information on the subsystems. Thus, the effect of automated routines for defining the best perturbation signals depending on the systems and the effects of other perturbation signals as well as multi-tone perturbations, for instance, based on white-noise injection or on the simultaneous non-correlated signals, could be assessed. Additionally, software package specific optimizations, for example, the ones allowing the use of snapshots of system states or numerical solutions could be considered.

Another aspect of interest is the equivalence of frames. This thesis focused on the small-signal representations of input admittance and impedance characteristics in the  $dq$ -frame. Moreover, it also provided the detailed mathematical base for converting the  $dq$ -frame results into the  $\alpha\beta$ -frame. Nevertheless, given the fact that other existing methodologies are based on the representation of the impedances (or admittances) in the sequence domain, it would be of importance to find the required mathematical relations and assumptions to relate the  $dq$ -frame results to the ones obtained in the sequence domain. Such analysis could further help understanding the limitations found, for instance, for the combined scan technique.

## REFERENCES

- [1] United Nations, “Paris Agreement,” *21st Conference of the Parties of the United Nations Framework Convention on Climate Change (UNFCCC)*. United Nations Treaty Collection. 8 July 2016. Archived from the original on 21 August 2016. Retrieved 02 February 2020, Paris, France, 2015.
- [2] IEA, “Average auction price by project commissioning date, 2012-2022.” available at <https://www.iea.org/data-and-statistics/charts/average-auction-price-by-project-commissioning-date-2012-2022>, Accessed on May 27th 2020, IEA, Paris, 2020.
- [3] IRENA (2019), “Renewable Energy Statistics 2019.” The International Renewable Energy Agency, Abu Dhabi.
- [4] L. Harnefors, X. Wang, A. G. Yepes, and F. Blaabjerg, “Passivity-Based Stability Assessment of Grid-Connected VSCs—An Overview,” *IEEE J. Emerg. Sel. Top. Power Electron.*, vol. 4, no. 1, pp. 116–125, Mar. 2016.
- [5] R. G. Farmer, A. L. Schwalb, and E. Katz, “Navajo project report on subsynchronous resonance analysis and solutions,” *IEEE Trans. Power Appar. Syst.*, vol. 96, no. 4, pp. 1226–1232, Jul. 1977.
- [6] M. Bahrman, E. V. Larsen, R. J. Piwko, and H. S. Patel, “Experience with HVDC - Turbine-Generator Torsional Interaction at Square Butte,” *IEEE Trans. Power Appar. Syst.*, vol. PAS-99, no. 3, pp. 966–975, May 1980.
- [7] C. Sihler, A. M. Miri, A. Harada, and U. Team, “Damping of Torsional Resonances in Generator Shafts Using a Feedback Controlled Buffer Storage of Magnetic Energy,” in *International Conference on Power Systems Transients - IPST*, 2003, no. 1, pp. 1–6.
- [8] A. M. Miri, C. Sihler, and T. Zöller, “Active damping of torsional modes in turbine-generator shafts,” in *Proc. IEEE PESC*, 2009, vol. 1, no. 1, pp. 2–7.
- [9] A. Mulawarman and P. Mysore, “Detection of undamped sub-synchronous oscillations of wind generators with series compensated lines,” in *Minnesota Power Systems Conference*, 2011.
- [10] NERC, “Online Report: Lessons learned - Sub-synchronous interaction between series-

- compensated transmission lines and generation,” 2011.
- [11] G. D. Irwin, A. K. Jindal, and A. L. Isaacs, “Sub-synchronous control interactions between type 3 wind turbines and series compensated AC transmission systems,” in *2011 IEEE Power and Energy Society General Meeting*, 2011, vol. 44, no. 2, pp. 1–6.
- [12] L. Wang, X. Xie, Q. Jiang, H. Liu, Y. Li, and H. Liu, “Investigation of SSR in Practical DFIG-Based Wind Farms Connected to a Series-Compensated Power System,” *IEEE Trans. Power Syst.*, vol. 30, no. 5, pp. 2772–2779, Sep. 2015.
- [13] H. Liu *et al.*, “Subsynchronous Interaction Between Direct-Drive PMSG Based Wind Farms and Weak AC Networks,” *IEEE Trans. Power Syst.*, vol. 32, no. 6, pp. 4708–4720, Nov. 2017.
- [14] I. Vieto, H. Liu, S. Rogalla, and J. Sun, “On the Potential of Subsynchronous Resonance of Voltage-Source Converters with the Grid,” in *Proceedings of 14th Wind Integration Workshop*, 2015, pp. 438–443.
- [15] C. Buchhagen, C. Rauscher, A. Menze, and J. Jung, “BorWin1 - First experiences with harmonic interactions in converter dominated grids,” in *International ETG Congress 2015: Die Energiewende - Blueprints for the New Energy Age*, 2015, pp. 1–7.
- [16] C. Li, “Unstable Operation of Photovoltaic Inverter From Field Experiences,” *IEEE Trans. Power Deliv.*, vol. 33, no. 2, pp. 1013–1015, Apr. 2018.
- [17] Y. Cheng, M. Sahni, D. Muthumuni, and B. Badrzadeh, “Reactance Scan Crossover-Based Approach for Investigating SSCI Concerns for DFIG-Based Wind Turbines,” *IEEE Trans. Power Deliv.*, vol. 28, no. 2, pp. 742–751, Apr. 2013.
- [18] Y. Cheng, S. H. (Fred) Huang, J. Rose, V. A. Pappu, and J. Conto, “Subsynchronous resonance assessment for a large system with multiple series compensated transmission circuits,” *IET Renew. Power Gener.*, vol. 13, no. 1, pp. 27–32, Jan. 2019.
- [19] IEEE PES Task Force, “Modeling Subsynchronous Oscillations in Wind Energy Interconnected Systems.” Chair: Yunzhi Cheng (ERCOT); Co-Chair: Lingling Fan (USF), 2019.

- [20] A. S. Trevisan, A. A. El-Deib, R. Gagnon, J. Mahseredjian, and M. Fecteau, "Field Validated Generic EMT-Type Model of a Full Converter Wind Turbine Based on a Gearless Externally Excited Synchronous Generator," *IEEE Trans. Power Deliv.*, vol. 33, no. 5, pp. 2284–2293, Oct. 2018.
- [21] Hydro-Québec TransÉnergie, "Transmission Provider Technical Requirements for the Connection of Power Plants to the Hydro Québec Transmission System." 2009.
- [22] BC Hydro for Generations, "60 kV to 500 kV Technical Interconnection Requirements for Power Generators." Revision 1.4. Effective Date: June 02, 2014.
- [23] AEMO, "Power System Model Guidelines." Final Report and Determination, 2018.
- [24] RTE, "Code Réseau." .
- [25] IEC, "Wind Turbines - Part 27-1: Electrical Simulation Models - Wind Turbines, IEC Standard 61400-27-1 ed. 1." 2015.
- [26] WECC, "Type 3 Wind Turbine Generator Model - Phase II," Jan. 23, 2014.
- [27] U. Karaagac, H. Saad, J. Peralta, and J. Mahseredjian, "Doubly-fed induction generator based wind park models in EMTP-RV." Polytechnique Montréal, 2016.
- [28] Manitoba Hydro International, "Type-3 Wind Turbine Model." For PSCAD Version v4.6. Revision 3. December 3, 2018.
- [29] A. Y. Goharrizi, J. C. Garcia Alonso, E. Borisova, F. Mosallat, and D. Muthumuni, "Benchmark Model of Type-III Wind Turbine for Research and Development Applications," in *2018 IEEE Canadian Conference on Electrical & Computer Engineering (CCECE)*, 2018, vol. 2018-May, pp. 1–6.
- [30] U. Karaagac, J. Mahseredjian, H. Saad, J. Peralta, and L. D. Bellomo, "Simulation Models for Wind Parks with Variabel Speed Wind Turbines in EMTP-RV," 2015.
- [31] Manitoba Hydro International, "Type-4 Wind Turbine Model." For PSCAD Version v4.6. Revision 3. December 3, 2018.
- [32] U. Karaagac *et al.*, "A Generic EMT-Type Model for Wind Parks With Permanent Magnet Synchronous Generator Full Size Converter Wind Turbines," *IEEE Power Energy Technol.*

- Syst. J.*, vol. 6, no. 3, pp. 131–141, Sep. 2019.
- [33] R. Gagnon, G. Turmel, C. Larose, J. Brochu, G. Sybille, and M. Fecteau, “Large-Scale Real-Time Simulation of Wind Power Plants into Hydro-Québec Power System,” in *Proceedings of the 9th International Workshop on Large-Scale Integration of Wind Power into Power Systems as well as on Transmission Networks for Offshore Wind Power Plants*, 2010.
- [34] R. Gagnon *et al.*, “Hydro-Québec Strategy to Evaluate Electrical Transients Following Wind Power Plant Integration in the Gaspésie Transmission System,” *IEEE Trans. Sustain. Energy*, vol. 3, no. 4, pp. 880–889, Oct. 2012.
- [35] R. Teodorescu, M. Liserre, and P. Rogríguez, *Grid Converters for Photovoltaic and Wind Power Systems*. John Wiley & Sons, Inc., 2011.
- [36] O. Anaya-Lara, N. Jenkins, J. Ekanayake, P. Cartwright, and M. Hughes, *Wind Energy Generation: Modelling and Control*. John Wiley & Sons, Ltd, 2009.
- [37] U. Karaagac, “Subsynchronous Control Interaction (SSCI) in DFIG based Wind Parks [Presentation Slides].” Task Force on EMT-type Modeling of Wind Turbine Generators and Parks at IEEE PES General Meeting 2015 in Denver, CO, US, 2015.
- [38] A. Yazdani and R. Iravani, *Voltage-Sourced Converters in Power Systems*. Hoboken, NJ, USA: John Wiley & Sons, Inc., 2010.
- [39] T. Ackermann, Ed., *Wind Power in Power Systems*. Chichester, UK: John Wiley & Sons, Ltd, 2012.
- [40] S. Heier, *Grid Integration of Wind Energy*. Chichester, UK: John Wiley & Sons, Ltd, 2014.
- [41] R. Gasch and J. Twele, Eds., *Wind Power Plants*. Berlin, Heidelberg: Springer Berlin Heidelberg, 2012.
- [42] R. W. Erickson and D. Maksimović, *Fundamentals of Power Electronics*. Boston, MA: Springer US, 2001.
- [43] R. N. Beres, X. Wang, M. Liserre, F. Blaabjerg, and C. L. Bak, “A Review of Passive Power Filters for Three-Phase Grid-Connected Voltage-Source Converters,” *IEEE J. Emerg. Sel. Top. Power Electron.*, vol. 4, no. 1, pp. 54–69, Mar. 2016.

- [44] R. N. Beres, X. Wang, F. Blaabjerg, M. Liserre, and C. L. Bak, “Optimal Design of High-Order Passive-Damped Filters for Grid-Connected Applications,” *IEEE Trans. Power Electron.*, vol. 31, no. 3, pp. 2083–2098, Mar. 2016.
- [45] ENTSO-E - European Network of Transmission System Operators for Electricity, “Official Journal of the European Union - Legislation: Commission Regulation (EU) 2016/631 of 14 april 2016 establishing a network code on requirements for grid connection of generators.” Official Journal of the European Union—Legislation: Commission Regulation (EU) 2016/631, Apr.14, 2016.
- [46] TAB-HS-Germany, “Technical requirements for the connection and operation of customer installations to the high-voltage network (TCC High-Voltage).” 2016.
- [47] National-Grid (UK), “The Grid Code.” 2013.
- [48] ONS - Operador Nacional do Sistema Elétrico (Brazil), “Submódulo 3.6—Requisitos técnicos mínimos para a conexão às instalações de transmissão.” Submódulo 3.6, Revisão 1.1, 2010.
- [49] P. Giroux, “Simscape power systems: Power converter modeling techniques.” MathWorks Matlab 2016a, 2016.
- [50] C. Langlois, M. Asmine, M. Fischer, and S. Adloff, “On-site Under Voltage Ride Through performance tests — Assessment of ENERCON Wind Energy converters based on Hydro-Québec Transénergie requirements,” in *2012 IEEE Power and Energy Society General Meeting*, 2012, pp. 1–8.
- [51] A. S. Trevisan, M. Fecteau, Â. Mendonça, R. Gagnon, and J. Mahseredjian, “Analysis of low frequency interactions between DFIG wind turbines and series compensated systems,” in *IPST '19 - International Conference on Power System Transients*, 2019.
- [52] B. Pal and B. Chaudhuri, *Robust Control in Power Systems*. Boston: Kluwer Academic Publishers, 2005.
- [53] P. Kundur, *Power System Stability and Control*. McGraw-Hill, 1994.
- [54] IEEE SSR Working Group of the System Dynamic Performance Subcommittee, “Reader’s

- guide to subsynchronous resonance,” *IEEE Trans. Power Syst.*, vol. 7, no. 1, pp. 150–157, 1992.
- [55] R. A. Achilles, “SSR countermeasure impact on system induction-generator effect,” *IEEE Trans. Power Syst.*, vol. 3, no. 2, pp. 383–391, May 1988.
- [56] IEEE SSR Working Group of the System Dynamic Performance Subcommittee, “A bibliography for the study of subsynchronous resonance between rotating machines and power systems,” *IEEE Trans. Power Appar. Syst.*, vol. 95, no. 1, pp. 216–218, Jan. 1976.
- [57] IEEE SSR Working Group of the System Dynamic Performance Subcommittee, “First Supplement to a Bibliography for the Study of Subsynchronous Resonance Between Rotating Machines and Power Systems,” *IEEE Trans. Power Appar. Syst.*, vol. PAS-98, no. 6, pp. 1872–1875, Nov. 1979.
- [58] IEEE SSR Working Group of the System Dynamic Performance Subcommittee, “Second Supplement to a Bibliography for the Study of Subsynchronous Resonance Between Rotating Machines and Power Systems,” *IEEE Power Eng. Rev.*, vol. PER-5, no. 2, pp. 34–34, Feb. 1985.
- [59] IEEE SSR Working Group of the System Dynamic Performance Subcommittee, “Third supplement to a bibliography for the study of subsynchronous resonance between rotating machines and power systems,” *IEEE Trans. Power Syst.*, vol. 6, no. 2, pp. 830–834, May 1991.
- [60] M. R. Iravani *et al.*, “Fourth supplement to a bibliography for the study of subsynchronous resonance between rotating machines and power systems,” *IEEE Trans. Power Syst.*, vol. 12, no. 3, pp. 1276–1282, Aug. 1997.
- [61] IEEE-Report, “Terms, Definitions and Symbols for Subsynchronous Oscillations,” *IEEE Trans. Power Appar. Syst.*, vol. PAS-104, no. 6, pp. 1326–1334, 1985.
- [62] P. M. Anderson, B. L. Agrawal, and J. E. Van Ness, *Subsynchronous Resonance in Power Systems*, no. 1. IEEE, 1990.
- [63] K. R. Padiyar, *Analysis of Subsynchronous Resonance in Power Systems*. Boston, MA: Springer US, 1999.

- [64] IEEE SSR Working Group of the System Dynamic Performance Subcommittee, "First benchmark model for computer simulation of subsynchronous resonance," *IEEE Trans. Power Appar. Syst.*, vol. 96, no. 5, pp. 1565–1572, Sep. 1977.
- [65] M. R. Iravani and R. M. Mathur, "Two Countermeasures for Damping Torsional Interactions and Transient Torques of Turbine-Generators," *IEEE Trans. Power Syst.*, vol. 2, no. 2, pp. 406–412, 1987.
- [66] G. N. Pillai, A. Ghosh, and A. Joshi, "Robust control of SSSC to improve torsional damping," in *2001 IEEE Power Engineering Society Winter Meeting. Conference Proceedings (Cat. No.01CH37194)*, 2001, vol. 3, no. C, pp. 1115–1120.
- [67] A. Tabesh and R. Iravani, "Frequency-Response Analysis of Torsional Dynamics," *IEEE Trans. Power Syst.*, vol. 19, no. 3, pp. 1430–1437, Aug. 2004.
- [68] R. P. Carpanen and B. S. Rigby, "A FACTS-Based Power Flow Controller Model for The IEEE SSR First Benchmark Model," in *2007 IEEE Power Engineering Society Conference and Exposition in Africa - PowerAfrica*, 2007, no. July, pp. 1–8.
- [69] F. D. de Jesus, E. H. Watanabe, L. F. W. de Souza, and J. E. R. Alves, "SSR and Power Oscillation Damping Using Gate-Controlled Series Capacitors (GCSC)," *IEEE Trans. Power Deliv.*, vol. 22, no. 3, pp. 1806–1812, Jul. 2007.
- [70] R. K. Varma, S. Auddy, and Y. Semsedini, "Mitigation of Subsynchronous Resonance in a Series-Compensated Wind Farm Using FACTS Controllers," *IEEE Trans. Power Deliv.*, vol. 23, no. 3, pp. 1645–1654, Jul. 2008.
- [71] M. S. El-Moursi, B. Bak-Jensen, and M. H. Abdel-Rahman, "Novel STATCOM Controller for Mitigating SSR and Damping Power System Oscillations in a Series Compensated Wind Park," *IEEE Trans. Power Electron.*, vol. 25, no. 2, pp. 429–441, Feb. 2010.
- [72] L. Fan, R. Kavasseri, Z. L. Miao, and C. Zhu, "Modeling of DFIG-Based Wind Farms for SSR Analysis," *IEEE Trans. Power Deliv.*, vol. 25, no. 4, pp. 2073–2082, Oct. 2010.
- [73] Z. Wu, C. Zhu, and M. Hu, "Supplementary Controller Design for SSR Damping in a Series-Compensated DFIG-Based Wind Farm," *Energies*, vol. 5, no. 11, pp. 4481–4496, Nov. 2012.

- [74] R. Thirumalaivasan, M. Janaki, and N. Prabhu, "Damping of SSR Using Subsynchronous Current Suppressor With SSSC," *IEEE Trans. Power Syst.*, vol. 28, no. 1, pp. 64–74, Feb. 2013.
- [75] R. G. Farmer *et al.*, "Second Benchmark Model for Computer Simulation of Subsynchronous Resonance," *IEEE Trans. Power Appar. Syst.*, vol. PAS-104, no. 5, pp. 1057–1066, 1985.
- [76] H. Kuisti and T. Rauhala, "Frequency Scanning Program for SSR Studies Implemented To Function in Connection of PSS/E Power Flow Analysis Program," in *Proceedings of 15th Power System Computing Conference (PSCC)*, 2005, no. August, pp. 22–26.
- [77] K. R. Padiyar and N. Prabhu, "Analysis of SSR With Three-Level Twelve-Pulse VSC-Based Interline Power-Flow Controller," *IEEE Trans. Power Deliv.*, vol. 22, no. 3, pp. 1688–1695, Jul. 2007.
- [78] A. El-deib, A. Trevisan, A. Mendonca, and M. Fischer, "Assessment of Full-Converter Wind Turbines' Immunity against Subsynchronous Interaction using Eigenvalue Analysis," in *Proceedings of the 14th Wind Integration Workshop*, 2015.
- [79] CIGRE WG C4.503, "Power System Test Cases for EMT-Type Simulation Studies." CIGRE, Paris, France, August, 2018.
- [80] G. Andersson, R. Atmuri, R. Rosenqvist, and S. Torseng, "Influence of Hydro Units' Generator-to-Turbine Inertia Ratio on Damping of Subsynchronous Oscillations," *IEEE Trans. Power Appar. Syst.*, vol. PAS-103, no. 8, pp. 2352–2361, Aug. 1984.
- [81] J. Brochu, C. Larose, and R. Gagnon, "Generic Equivalent Collector System Parameters for Large Wind Power Plants," *IEEE Trans. Energy Convers.*, vol. 26, no. 2, pp. 542–549, Jun. 2011.
- [82] B. Badrzadeh and S. Saylor, "Susceptibility of wind turbines to sub-synchronous control and torsional interaction," in *PES T&D 2012*, 2012, pp. 1–8.
- [83] H. T. Ma and P. B. Brogan, "Sub-Synchronous Control Interaction studies between full-converter wind turbines and series-compensated AC transmission lines," in *2012 IEEE Power and Energy Society General Meeting*, 2012, pp. 1–5.

- [84] A. Schwanka Trevisan, M. Fecteau, Â. Mendonça, and J. Mahseredjian, “Analysis of low frequency interactions of DFIG wind turbine systems in series compensated grids,” *Submitt. to EPSR - Electr. Power Syst. Res.*, 2020.
- [85] P. J. Nolan, N. K. Sinha, and R. T. H. Alden, “Eigenvalue sensitivities of power systems including network and shaft dynamics,” *IEEE Trans. Power Appar. Syst.*, vol. 95, no. 4, pp. 1318–1324, Jul. 1976.
- [86] P. L. Dandeno and P. Kundur, “Practical application of eigenvalue techniques in the analysis of power system dynamic stability problems,” *Can. Electr. Eng. J.*, vol. 1, no. 1, pp. 35–46, Jan. 1976.
- [87] A. A. Fouad and K. T. Khu, “Subsynchronous Resonance Zones in the IEEE ‘Bench Mark’ Power System,” *IEEE Trans. Power Appar. Syst.*, vol. PAS-97, no. 3, pp. 754–762, May 1978.
- [88] A. A. Fouad and K. T. Khu, “Damping of Torsional Oscillations in Power Systems with Series-Compensated Lines,” *IEEE Trans. Power Appar. Syst.*, vol. PAS-97, no. 3, pp. 744–753, May 1978.
- [89] N. Kakimoto and A. Phongphanphane, “Subsynchronous resonance damping control of thyristor-controlled series capacitor,” *IEEE Trans. Power Deliv.*, vol. 18, no. 3, pp. 1051–1059, Jul. 2003.
- [90] D. Rai, S. O. Faried, G. Ramakrishna, and A.-A. Edris, “Damping Inter-Area Oscillations Using Phase Imbalanced Series Compensation Schemes,” *IEEE Trans. Power Syst.*, vol. 26, no. 3, pp. 1753–1761, Aug. 2011.
- [91] D. Jovcic, N. Pahalawaththa, and M. Zavahir, “Analytical modelling of HVDC-HVAC systems,” *IEEE Trans. Power Deliv.*, vol. 14, no. 2, pp. 506–511, Apr. 1999.
- [92] D. Jovcic, N. Pahalawaththa, and M. Zavahir, “Stability analysis of HVDC control loops,” *IEE Proceedings-Generation, ...*, 1999.
- [93] D. Jovcic, N. Pahalawaththa, and M. Zavahir, “Small signal analysis of HVDC-HVAC interactions,” *IEEE Trans. Power Deliv.*, vol. 14, no. 2, pp. 525–530, Apr. 1999.

- [94] H. Saad, J. Mahseredjian, S. Denetière, and S. Nguefeu, “Interactions studies of HVDC–MMC link embedded in an AC grid,” *Electr. Power Syst. Res.*, vol. 138, pp. 202–209, Sep. 2016.
- [95] A. Ostadi, A. Yazdani, and R. K. Varma, “Modeling and Stability Analysis of a DFIG-Based Wind-Power Generator Interfaced With a Series-Compensated Line,” *IEEE Trans. Power Deliv.*, vol. 24, no. 3, pp. 1504–1514, Jul. 2009.
- [96] R. K. Varma and A. Moharana, “SSR in Double-Cage Induction Generator-Based Wind Farm Connected to Series-Compensated Transmission Line,” *IEEE Trans. Power Syst.*, vol. 28, no. 3, pp. 2573–2583, Aug. 2013.
- [97] L. Fan and Z. Miao, “Mitigating SSR Using DFIG-Based Wind Generation,” *IEEE Trans. Sustain. Energy*, vol. 3, no. 3, pp. 349–358, Jul. 2012.
- [98] H. A. Mohammadpour, Y.-J. Shin, and E. Santi, “SSR analysis of a DFIG-based wind farm interfaced with a gate-controlled series capacitor,” in *2014 IEEE Applied Power Electronics Conference and Exposition - APEC 2014*, 2014, pp. 3110–3117.
- [99] H. Huang, C. Mao, J. Lu, and D. Wang, “Small-signal modelling and analysis of wind turbine with direct drive permanent magnet synchronous generator connected to power grid,” *IET Renew. Power Gener.*, vol. 6, no. 1, p. 48, 2012.
- [100] N. P. W. Strachan and D. Jovcic, “Stability of a Variable-Speed Permanent Magnet Wind Generator With Weak AC Grids,” *IEEE Trans. Power Deliv.*, vol. 25, no. 4, pp. 2779–2788, Oct. 2010.
- [101] N. Pogaku, M. Prodanovic, and T. C. Green, “Modeling, Analysis and Testing of Autonomous Operation of an Inverter-Based Microgrid,” *IEEE Trans. Power Electron.*, vol. 22, no. 2, pp. 613–625, Mar. 2007.
- [102] P. C. Krause, O. Wasynczuk, and S. D. Sudhoff, *Analysis of Electric Machinery and Drive Systems*. Hoboken, NJ, USA: John Wiley & Sons, Inc., 2002.
- [103] G. Gaba, S. Lefebvre, and D. Mukhedkar, “Comparative analysis and study of the dynamic stability of AC/DC systems,” *IEEE Trans. Power Syst.*, vol. 3, no. 3, pp. 978–985, Aug. 1988.

- [104] MathWorks, “Connect - Block Diagram Interconnections of Dynamic Systems.” available at <https://de.mathworks.com/help/control/ref/connect.html>. Retrieved on March 31, 2020., 2020.
- [105] A. S. Trevisan, “Codes and Simulation Files.” in Contribution to Assessment Methods for Low-Frequency Interactions in Inverter Dominated Power Systems, Ph.D. Thesis, Polytechnique Montreal, 2020. Available at: [Polymtl-OneDrive/Data/Aramis/Thesis/Codes\\_and\\_Simulation\\_Files](#).
- [106] MathWorks, “MATLAB, Simulink and Simscape Power Systems Toolbox.” Release 2016a, The MathWorks, Inc., Natick, Massachusetts, United States., 2020.
- [107] W. J. Rugh, *Linear System Theory*. Upper Saddle River, NJ: Prentice Hall, 1996.
- [108] I. J. Perez-Arriaga, G. C. Verghese, and F. C. Schewpe, “Selective Modal Analysis with Applications to Electric Power Systems, Part I: Heuristic Introduction,” *IEEE Power Eng. Rev.*, vol. PER-2, no. 9, pp. 29–30, Sep. 1982.
- [109] G. C. Verghese, I. J. Perez-Arriaga, and F. C. Schewpe, “Selective Modal Analysis with Applications to Electric Power Systems, Part II: The Dynamic Stability Problem,” *IEEE Power Eng. Rev.*, vol. PER-2, no. 9, pp. 30–31, Sep. 1982.
- [110] A. Schwanka Trevisan, A. Mendonca, R. Gagnon, J. Mahseredjian, and M. Fecteau, “Analytically Validated SSCI Assessment Technique for Wind Parks in Series Compensated Grids,” *IEEE Trans. Power Syst.*, vol. 8950, no. c, pp. 1–1, 2020.
- [111] S. Denetiere, H. Saad, Y. Vernay, P. Rault, C. Martin, and B. Clerc, “Supporting Energy Transition in Transmission Systems: An Operator’s Experience Using Electromagnetic Transient Simulation,” *IEEE Power Energy Mag.*, vol. 17, no. 3, pp. 48–60, May 2019.
- [112] B. L. Agrawal and R. G. Farmer, “Use of Frequency Scanning Techniques for Subsynchronous Resonance Analysis,” *IEEE Trans. Power Appar. Syst.*, vol. PAS-98, no. 2, pp. 341–349, Mar. 1979.
- [113] I. M. Canay, “A Novel Approach to the Torsional Interaction and Electrical Damping of the Synchronous Machine Part I: Theory,” *IEEE Trans. Power Appar. Syst.*, vol. PAS-101, no. 10, pp. 3630–3638, Oct. 1982.

- [114] I. M. Canay, "A Novel Approach to the Torsional Interaction and Electrical Damping of the Synchronous Machine Part II: Application to an arbitrary network," *IEEE Trans. Power Appar. Syst.*, vol. PAS-101, no. 10, pp. 3639–3647, Oct. 1982.
- [115] J. Mahseredjian, S. Denetière, L. Dubé, B. Khodabakhchian, and L. Gérin-Lajoie, "On a new approach for the simulation of transients in power systems," *Electr. Power Syst. Res.*, vol. 77, no. 11, pp. 1514–1520, Sep. 2007.
- [116] M. Elfayoumy and C. G. Moran, "A Comprehensive Approach for Sub-Synchronous Resonance Screening Analysis Using Frequency scanning Technique," *2003 IEEE Bol. PowerTech Conf.*, pp. 1–5, 2003.
- [117] P. Vuorenää, T. Rauhala, and P. Järventausta, "Applying TCSC frequency response data derived using electromagnetic transient analysis in SSR frequency scanning studies," *2009 IEEE Bucharest PowerTech Innov. Ideas Towar. Electr. Grid Futur.*, pp. 1–6, 2009.
- [118] Xiao Jiang and A. M. Gole, "A frequency scanning method for the identification of harmonic instabilities in HVDC systems," *IEEE Trans. Power Deliv.*, vol. 10, no. 4, pp. 1875–1881, 1995.
- [119] R. Nath and C. Grande-Moran, "Study of Sub-Synchronous Control Interaction due to the interconnection of wind farms to a series compensated transmission system," in *PES T&D 2012*, 2012, pp. 1–6.
- [120] D. H. R. Suriyaarachchi, U. D. Annakkage, C. Karawita, and D. A. Jacobson, "A Procedure to Study Sub-Synchronous Interactions in Wind Integrated Power Systems," *IEEE Trans. Power Syst.*, vol. 28, no. 1, pp. 377–384, Feb. 2013.
- [121] T. Rauhala and P. Järventausta, "Frequency scanning techniques for analysis of the effect of device dependent subsynchronous oscillations on subsynchronous damping," in *16th PSCC Proceedings*, 2008, pp. 1–7.
- [122] B. Badrzadeh and Y. Zhou, "Sub-synchronous interaction in wind power plants part I: Study tools and techniques," in *2012 IEEE Power and Energy Society General Meeting*, 2012, pp. 1–9.
- [123] M. Sahni *et al.*, "Sub-synchronous interaction in wind power plants- part II: An ercot case

- study,” *IEEE Power Energy Soc. Gen. Meet.*, pp. 1–9, 2012.
- [124] M. Sahni, D. Muthumuni, B. Badrzadeh, A. Gole, and A. Kulkarni, “Advanced screening techniques for Sub-Synchronous Interaction in wind farms,” *Proc. IEEE Power Eng. Soc. Transm. Distrib. Conf.*, pp. 1–9, 2012.
- [125] G. T. Wrate, B. A. Mork, and K. K. Mustaphi, “A new method to determine frequency characteristics of a power system including nonlinear effects,” in *Proceedings of IPST’97*, 1997, pp. 5–10.
- [126] R. D. Middlebrook, “Input filter considerations in design and application of switching regulators,” in *IEEE Conf Rec Annu Meet Ind Appl Soc*, 1976, pp. 366–382.
- [127] M. Belkhat, “Stability Criteria for AC Power Systems with Regulated Loads,” George Washington University, 1997.
- [128] L. Harnefors, M. Bongiorno, and S. Lundberg, “Input-admittance calculation and shaping for controlled voltage-source converters,” *IEEE Trans. Ind. Electron.*, vol. 54, no. 6, pp. 3323–3334, 2007.
- [129] L. Harnefors, “Analysis of subsynchronous torsional interaction with power electronic converters,” *IEEE Trans. Power Syst.*, vol. 22, no. 1, pp. 305–313, 2007.
- [130] J. Sun, “Small-signal methods for AC distributed power systems-A review,” *IEEE Trans. Power Electron.*, vol. 24, no. 11, pp. 2545–2554, 2009.
- [131] J. Sun, “Impedance-based stability criterion for grid-connected inverters,” *IEEE Trans. Power Electron.*, vol. 26, no. 11, pp. 3075–3078, 2011.
- [132] U. Karaagac, J. Mahseredjian, S. Jensen, R. Gagnon, M. Fecteau, and I. Kocar, “Safe Operation of DFIG-Based Wind Parks in Series-Compensated Systems,” *IEEE Trans. Power Deliv.*, vol. 33, no. 2, pp. 709–718, Apr. 2018.
- [133] H. Saad, Y. Fillion, S. Deschanvres, Y. Vernay, and S. Dennetiere, “On resonances and harmonics in HVDC-MMC station connected to AC grid,” *IEEE Trans. Power Deliv.*, vol. 32, no. 3, pp. 1565–1573, 2017.
- [134] N. Karnik, D. Novosad, H. K. Nia, M. Sahni, M. Ghavami, and H. Yin, “An evaluation of

- critical impact factors for SSCI analysis for wind power plants: A utility perspective,” in *2017 IEEE Power & Energy Society General Meeting*, 2017, pp. 1–5.
- [135] L. A. Kilgore, D. G. Ramey, and M. C. Hall, “Simplified transmission and generation system analysis procedures for subsynchronous resonance problems,” *IEEE Trans. Power Appar. Syst.*, vol. 96, no. 6, pp. 1840–1846, Nov. 1977.
- [136] H. Liu, X. Xie, and W. Liu, “An Oscillatory Stability Criterion Based on the Unified dq-Frame Impedance Network Model for Power Systems With High-Penetration Renewables,” *IEEE Trans. Power Syst.*, vol. 33, no. 3, pp. 3472–3485, May 2018.
- [137] W. Liu, X. Xie, J. Shair, and J. He, “Frequency-coupled Impedance Model based Subsynchronous Oscillation Analysis for Direct-drive Wind Turbines Connected to a Weak AC Power System,” in *IET Renewable Power Generation Conference*, 2018.
- [138] D. Shu, X. Xie, H. Rao, X. Gao, Q. Jiang, and Y. Huang, “Sub-and Super-Synchronous Interactions between STATCOMs and Weak AC/DC Transmissions with Series Compensations,” *IEEE Trans. Power Electron.*, vol. 33, no. 9, pp. 7424–7437, 2018.
- [139] A. Rygg, M. Molinas, C. Zhang, and X. Cai, “A Modified Sequence-Domain Impedance Definition and Its Equivalence to the dq-Domain Impedance Definition for the Stability Analysis of AC Power Electronic Systems,” *IEEE J. Emerg. Sel. Top. Power Electron.*, vol. 4, no. 4, pp. 1383–1396, Dec. 2016.
- [140] M. K. Bakhshizadeh *et al.*, “Couplings in Phase Domain Impedance Modelling of Grid-Connected Converters,” *IEEE Trans. Power Electron.*, vol. 31, no. 10, pp. 1–1, 2016.
- [141] Y. Xu, H. Nian, and J. Sun, “Cross coupling of grid-connected inverter impedance over frequency - Phenomena, effects and modeling,” in *Proceedings of 15th Wind Integration Workshop*, 2016.
- [142] Y. Xu, H. Nian, G. Xu, and J. Qiu, “Cross-coupling over frequency and sequence in impedance modelling of grid-connected inverter,” *J. Eng.*, vol. 2017, no. 13, pp. 990–995, Jan. 2017.
- [143] B. Wen, “Stability Analysis of Three-phase AC Power Systems Based on Measured D-Q Frame Impedances,” Virginia Polytechnic Institute and State University, 2014.

- [144] B. Wen, D. Boroyevich, R. Burgos, P. Mattavelli, and Z. Shen, "Small-Signal Stability Analysis of Three-Phase AC Systems in the Presence of Constant Power Loads Based on Measured d-q Frame Impedances," *IEEE Trans. Power Electron.*, vol. 30, no. 10, pp. 5952–5963, Oct. 2015.
- [145] B. Wen, D. Dong, D. Boroyevich, R. Burgos, P. Mattavelli, and Z. Shen, "Impedance-based analysis of grid-synchronization stability for three-phase paralleled converters," *IEEE Trans. Power Electron.*, vol. 31, no. 1, pp. 26–38, 2016.
- [146] L. Harnefors, "Modeling of Three-Phase Dynamic Systems Using Complex Transfer Functions and Transfer Matrices," *IEEE Trans. Ind. Electron.*, vol. 54, no. 4, pp. 2239–2248, 2007.
- [147] M. Cespedes, "Impedance modeling, analysis, and adaptation of grid-connected inverters with PLL," Rensselaer Polytechnic Institute, 2014.
- [148] M. Cespedes and J. Sun, "Impedance modeling and analysis of grid-connected voltage-source converters," *IEEE Trans. Power Electron.*, vol. 29, no. 3, pp. 1254–1261, 2014.
- [149] A. Rygg, "Impedance-based methods for small-signal analysis of systems dominated by power electronics," Norwegian University of Science and Technology, 2018.
- [150] X. Wang, L. Harnefors, and F. Blaabjerg, "Unified Impedance Model of Grid-Connected Voltage-Source Converters," *IEEE Trans. Power Electron.*, vol. 33, no. 2, pp. 1775–1787, Feb. 2018.
- [151] F. Liu, J. Liu, H. Zhang, and D. Xue, "Stability Issues of Z + Z Type Cascade System in Hybrid Energy Storage System (HESS)," *IEEE Trans. Power Electron.*, vol. 29, no. 11, pp. 5846–5859, Nov. 2014.
- [152] A. Rygg and M. Molinas, "Apparent Impedance Analysis: A Small-Signal Method for Stability Analysis of Power Electronic-Based Systems," *IEEE J. Emerg. Sel. Top. Power Electron.*, vol. 5, no. 4, pp. 1474–1486, Dec. 2017.
- [153] M. K. Bakhshizadeh, F. Blaabjerg, J. Hjerrild, L. Kocewiak, and C. L. Bak, "Improving the impedance-based stability criterion by using the vector fitting method," *IEEE Trans. Energy Convers.*, vol. 33, no. 4, pp. 1739–1747, 2018.

- [154] B. Badrzadeh, M. Sahni, Y. Zhou, D. Muthumuni, and A. Gole, "General Methodology for Analysis of Sub-Synchronous Interaction in Wind Power Plants," *IEEE Trans. Power Syst.*, vol. 28, no. 2, pp. 1858–1869, 2013.
- [155] G. Francis, R. Burgos, D. Boroyevich, F. Wang, and K. Karimi, "An algorithm and implementation system for measuring impedance in the D-Q domain," *IEEE Energy Convers. Congr. Expo. Energy Convers. Innov. a Clean Energy Futur. ECCE 2011, Proc.*, pp. 3221–3228, 2011.
- [156] M. Lwin, R. Kazemi, and D. Howard, "Frequency Scan Considerations for SSCI Analysis of Wind Power Plants," in *2019 IEEE Power & Energy Society General Meeting (PESGM)*, 2019, pp. 1–5.
- [157] A. G. J. Macfarlane and I. Postlethwaite, "The generalized Nyquist stability criterion and multivariable root loci," *Int. J. Control*, vol. 25, no. 1, pp. 81–127, Jan. 1977.
- [158] C. Zhang, M. Molinas, A. Rygg, and X. Cai, "Impedance-based Analysis of Interconnected Power Electronics Systems: Impedance Network Modeling and Comparative Studies of Stability Criteria," *IEEE J. Emerg. Sel. Top. Power Electron.*, vol. PP, no. c, pp. 1–1, 2019.
- [159] Y. Liao and X. Wang, "Impedance-Based Stability Analysis for Interconnected Converter Systems With Open-Loop RHP Poles," *IEEE Trans. Power Electron.*, vol. 35, no. 4, pp. 4388–4397, Apr. 2020.
- [160] N. S. Nise, *Control Systems Engineering*. Wiley, 2015.
- [161] S. Skogestad and I. Postlethwaite, *Multivariable Feedback Control - Analysis and design*. 2001.
- [162] B. Gustavsen and A. Semlyen, "Rational approximation of frequency domain responses by vector fitting," *IEEE Trans. Power Deliv.*, vol. 14, no. 3, pp. 1052–1061, Jul. 1999.
- [163] A. Stepanov, "Sub-synchronous Oscillation with type 3 WT and MMC-HVDC," in *EMTP User Conference, Atlanta, US*, 2019.

## APPENDIX A GENERIC TYPE-IV WIND TURBINE PARAMETERS

The proposed values of the constants  $c_1$  to  $c_9$  used to describe the power coefficients of the proposed generic type-IV wind turbine model are given in Table A.1.

Table A.1 Power coefficient values

$c_1$	$c_2$	$c_3$	$c_4$	$c_5$	$c_6$	$c_7$	$c_8$	$c_9$
0.2065	200	0.15	0.05	2.14	13.2	13	-0.02	-0.003

The proposed rated values for the wind turbine system are given in Table A.2.

Table A.2 Wind Turbine Parameters

Parameter	Name	Value	Unit
$R_r$	Wind turbine rotor radius	42	m
$\lambda_{opt}$	Optimal tip-speed ratio	7.1	-
$v_{rated}$	Nominal wind speed	11	m/s
$v_{cut-in}$	Cut-in wind speed	3.5	m/s

Moreover, the assumed parameters for the synchronous machines are given in Table A.3.

Table A.3 Synchronous machine parameters

Parameter	Name	Value	Unit
$P_{SG}$	Nominal power	2	MVA
$v_{SG}$	Nominal stator phase-to-phase voltage	830	V
$f_{SG}$	Nominal stator frequency	10.8	Hz
$i_{fn,SG}$	Nominal excitation current	31.7	A
$R_{s,SG}$	Stator resistance per phase	0.0726	pu
$L_{ls,SG}$	Stator leakage inductance	1.3790	pu
$L_{md,SG}$	Direct-axis magnetizing inductance	1.9701	pu
$L_{mq,SG}$	Quadrature-axis magnetizing inductance	1.9701	pu
$R_{f,SG}$	Field resistance	0.0102	pu
$L_{lf,SG}$	Field leakage inductance	0.0167	pu
$H_{SG}$	Inertia coefficient	6.7	s
$p_{SG}$	Pole pairs	36	-

## APPENDIX B DQ-TRANSFORMATION

This appendix provides a review of the *abc-to-dq*-transformation used throughout the thesis is provided. Moreover, an example of the application of a *dq*-transformation is provided based on a simple RL-circuit to illustrate the *dq*-couplings existent in the *dq*-frame even for balanced systems.

### a) *dq-to-abc*-Transformation

The *dq-to-abc*-transformation denoted as  $\mathbf{T}_{dq}$  and used throughout this thesis is given by

$$\begin{bmatrix} x_a \\ x_b \\ x_c \end{bmatrix} = \begin{bmatrix} \sin(\omega t) & \cos(\omega t) & 1 \\ \sin\left(\omega t - \frac{2\pi}{3}\right) & \cos\left(\omega t - \frac{2\pi}{3}\right) & 1 \\ \sin\left(\omega t + \frac{2\pi}{3}\right) & \cos\left(\omega t + \frac{2\pi}{3}\right) & 1 \end{bmatrix} \begin{bmatrix} x_d \\ x_q \\ x_0 \end{bmatrix} \quad (\text{B.1})$$

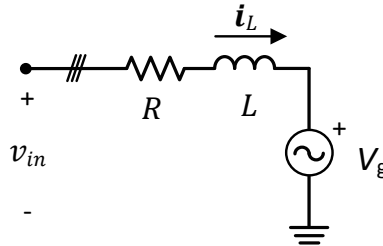
### b) *abc-to-dq*-Transformation

The *abc-to-dq*-transformation denoted as  $\mathbf{T}_{dq}^{-1}$  is the inverse of  $\mathbf{T}_{dq}$  above and is given as

$$\begin{bmatrix} x_d \\ x_q \\ x_0 \end{bmatrix} = \frac{2}{3} \begin{bmatrix} \sin(\omega t) & \sin\left(\omega t - \frac{2\pi}{3}\right) & \sin\left(\omega t + \frac{2\pi}{3}\right) \\ \cos(\omega t) & \cos\left(\omega t - \frac{2\pi}{3}\right) & \cos\left(\omega t + \frac{2\pi}{3}\right) \\ \frac{1}{2} & \frac{1}{2} & \frac{1}{2} \end{bmatrix} \begin{bmatrix} x_a \\ x_b \\ x_c \end{bmatrix} \quad (\text{B.2})$$

### c) Example of the application of the *dq*-Transformation on a three-phase RL-Circuit

The *abc-to-dq*-transformation is now demonstrated for the case of a simple RL-circuit. The circuit is illustrated in the next figure.



For the RL-circuit illustrated above, we can write following differential equation

$$\begin{bmatrix} v_{in,a} \\ v_{in,b} \\ v_{in,c} \end{bmatrix} = \begin{bmatrix} R & 0 & 0 \\ 0 & R & 0 \\ 0 & 0 & R \end{bmatrix} \begin{bmatrix} i_{L,a} \\ i_{L,b} \\ i_{L,c} \end{bmatrix} + \begin{bmatrix} L & 0 & 0 \\ 0 & L & 0 \\ 0 & 0 & L \end{bmatrix} \frac{d}{dt} \left\{ \begin{bmatrix} i_{L,a} \\ i_{L,b} \\ i_{L,c} \end{bmatrix} \right\} + \begin{bmatrix} v_{g,a} \\ v_{g,b} \\ v_{g,c} \end{bmatrix} \quad (\text{B.3})$$

where  $v_{in,i}$  is the input voltage to the three-phase RL-circuit,  $R$  and  $L$  the circuit parameters,  $i_{L,i}$  the current through the inductor and  $v_{g,i}$  the grid voltage. The subscript  $i$  indicates the phase for which equation B.3 is valid, i.e.,  $i$  corresponds to either  $a$ ,  $b$  or  $c$ .

Applying the  $abc$ -to- $dq$ -transformation  $\mathbf{T}_{dq}^{-1}$  to the  $abc$ -variables of B.3 gives

$$\mathbf{T}_{dq}^{-1} \begin{bmatrix} v_{in,a} \\ v_{in,b} \\ v_{in,c} \end{bmatrix} = \begin{bmatrix} R & 0 & 0 \\ 0 & R & 0 \\ 0 & 0 & R \end{bmatrix} \mathbf{T}_{dq}^{-1} \begin{bmatrix} i_{L,a} \\ i_{L,b} \\ i_{L,c} \end{bmatrix} + \begin{bmatrix} L & 0 & 0 \\ 0 & L & 0 \\ 0 & 0 & L \end{bmatrix} \mathbf{T}_{dq}^{-1} \frac{d}{dt} \left\{ \begin{bmatrix} i_{L,a} \\ i_{L,b} \\ i_{L,c} \end{bmatrix} \right\} + \mathbf{T}_{dq}^{-1} \begin{bmatrix} v_{g,a} \\ v_{g,b} \\ v_{g,c} \end{bmatrix} \quad (\text{B.4})$$

Before further developing equation B.4, a closer look is given at its derivative term. By applying the chain rule, it can be written that

$$\frac{d}{dt} \left\{ \begin{bmatrix} i_{L,a} \\ i_{L,b} \\ i_{L,c} \end{bmatrix} \right\} = \frac{d}{dt} \left\{ \mathbf{T}_{dq} \begin{bmatrix} i_d \\ i_q \\ i_0 \end{bmatrix} \right\} = \frac{d}{dt} \{ \mathbf{T}_{dq} \} \begin{bmatrix} i_d \\ i_q \\ i_0 \end{bmatrix} + \mathbf{T}_{dq} \frac{d}{dt} \left\{ \begin{bmatrix} i_d \\ i_q \\ i_0 \end{bmatrix} \right\} \quad (\text{B.5})$$

It is seen that there is a derivative term of the transformation matrix  $\frac{d}{dt} \{ \mathbf{T}_{dq} \}$  which is given by

$$\frac{d}{dt} \{ \mathbf{T}_{dq} \} \begin{bmatrix} i_d \\ i_q \\ i_0 \end{bmatrix} = \omega \begin{bmatrix} \cos(\omega t) & -\sin(\omega t) & 0 \\ \cos\left(\omega t - \frac{2\pi}{3}\right) & -\sin\left(\omega t - \frac{2\pi}{3}\right) & 0 \\ \cos\left(\omega t + \frac{2\pi}{3}\right) & -\sin\left(\omega t + \frac{2\pi}{3}\right) & 0 \end{bmatrix} \begin{bmatrix} i_d \\ i_q \\ i_0 \end{bmatrix} \quad (\text{B.6})$$

For balanced systems it can be assumed that there is no zero sequence component. The last column of equation (B.6) has no importance and it can be written that

$$\frac{d}{dt} \{ \mathbf{T}_{dq} \} = \omega \begin{bmatrix} \cos(\omega t) & -\sin(\omega t) & 1 \\ \cos\left(\omega t - \frac{2\pi}{3}\right) & -\sin\left(\omega t - \frac{2\pi}{3}\right) & 1 \\ \cos\left(\omega t + \frac{2\pi}{3}\right) & -\sin\left(\omega t + \frac{2\pi}{3}\right) & 1 \end{bmatrix} \begin{bmatrix} i_d \\ i_q \\ 0 \end{bmatrix} = \omega \mathbf{T}_{dq} \begin{bmatrix} -i_q \\ i_d \\ 0 \end{bmatrix} \quad (\text{B.7})$$

Finally, substituting (B.7) in (B.4) gives

$$\begin{aligned}
\begin{bmatrix} v_{in,d} \\ v_{in,q} \\ 0 \end{bmatrix} &= \begin{bmatrix} R & 0 & 0 \\ 0 & R & 0 \\ 0 & 0 & R \end{bmatrix} \begin{bmatrix} i_d \\ i_q \\ 0 \end{bmatrix} + \begin{bmatrix} L & 0 & 0 \\ 0 & L & 0 \\ 0 & 0 & L \end{bmatrix} \frac{d}{dt} \begin{bmatrix} i_d \\ i_q \\ 0 \end{bmatrix} + \begin{bmatrix} 0 & -\omega L & 0 \\ \omega L & 0 & 0 \\ 0 & 0 & 0 \end{bmatrix} \begin{bmatrix} i_d \\ i_q \\ 0 \end{bmatrix} \\
&+ \begin{bmatrix} v_{g,d} \\ v_{g,q} \\ 0 \end{bmatrix}
\end{aligned} \tag{B.8}$$

Equation (B.8) can be simplified by eliminating the last row corresponding to a non-existent zero sequence component, which leads in equation form to

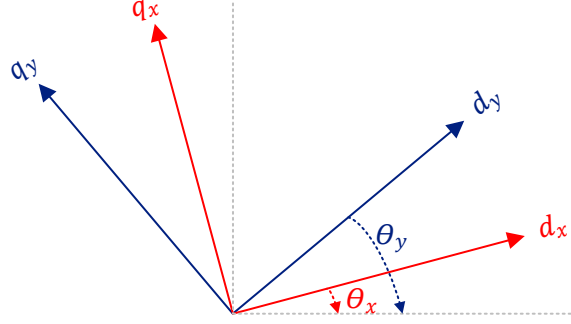
$$\begin{cases} v_{in,d} = Ri_d + L \frac{di_d}{dt} - \omega Li_q + v_{g,d} \\ v_{in,q} = Ri_q + L \frac{di_q}{dt} + \omega Li_d + v_{g,q} \end{cases} \tag{B.9}$$

As can be seen from equation (B.9), although the original RL-circuit has been considered symmetric, i.e.,  $R$  and  $L$  have been equally considered in all three phases, in  $dq$ -frame a coupling term appears  $-\omega Li_q$  or  $\omega Li_d$ , respectively, for the  $d$  and  $q$  components.

Nevertheless, it is noted that if the phase of the  $dq$ -transformation rotates with the same rotational speed as the grid,  $i_d$  and  $i_q$  are constants in steady-state.

## APPENDIX C FRAME ROTATION IN DQ-FRAME

In order to establish the transformation between any two frames of reference, let  $x$  denote the reference frame from which the variables are being transformed and  $y$  the reference frame to which the variables are being transformed. A snapshot of  $x$  and  $y$   $dq$ -frames is illustrated next.



It can then be written that

$$f_{dq0}^y = K_{xy} f_{dq0}^x \quad (\text{C.1})$$

where  $f_{dq0}^y$  and  $f_{dq0}^x$  represent a set of variables in two different  $dq0$ -frames and  $K_{xy}$  the transformation matrix from  $x$  to  $y$  frame.

It can also be written that

$$f_{dq0}^x = K_s^x f_{abc} \quad (\text{C.2})$$

where  $f_{abc}$  represent the variables of  $f_{dq0}^x$  in the stationary  $abc$ -frame.  $K_s^x$  is the transformation matrix that transforms that  $abc$ -variables into their  $dq$ -variables.  $K_s^x$  is equal equation (B.2).

Substituting equation (C.2) in (C.1) gives

$$f_{dq0}^y = K_{xy} K_s^x f_{abc} \quad (\text{C.3})$$

However, we have also that

$$f_{dq0}^y = K_s^y f_{abc} \quad (\text{C.4})$$

By comparing (C.3) with (C.4) it is evident that

$$K_{xy} K_s^x = K_s^y \quad (\text{C.5})$$

From (C.5) it is now, finally, possible to state that

$$K_{xy} = K_s^y (K_s^x)^{-1} \quad (\text{C.6})$$

It is noted from equation (C.6) that the transformation matrices  $K_s^y$  and  $(K_s^x)^{-1}$  correspond to equations (B.2) and (B.1), respectively. The only difference is that the angle  $\omega t$  is replaced by the corresponding angles  $\theta_x(t)$  and  $\theta_y(t)$  of each rotation frame  $x$  and  $y$ . For a given instant  $t = t_0$  corresponding to the figure above, we have  $\theta_x$  and  $\theta_y$  and we can write

$$K_{xy} = \frac{2}{3} \begin{bmatrix} \sin(\theta_y) & \sin\left(\theta_y - \frac{2\pi}{3}\right) & \sin\left(\theta_y + \frac{2\pi}{3}\right) \\ \cos(\theta_y) & \cos\left(\theta_y - \frac{2\pi}{3}\right) & \cos\left(\theta_y + \frac{2\pi}{3}\right) \\ \frac{1}{2} & \frac{1}{2} & \frac{1}{2} \end{bmatrix} \begin{bmatrix} \sin(\theta_x) & \cos(\theta_x) & 1 \\ \sin\left(\theta_x - \frac{2\pi}{3}\right) & \cos\left(\theta_x - \frac{2\pi}{3}\right) & 1 \\ \sin\left(\theta_x + \frac{2\pi}{3}\right) & \cos\left(\theta_x + \frac{2\pi}{3}\right) & 1 \end{bmatrix} \quad (\text{C.7})$$

And equation (C.7) can, after some trigonometric manipulations, be rearranged to

$$K_{xy} = \begin{bmatrix} \cos(\theta_y - \theta_x) & \sin(\theta_y - \theta_x) & 0 \\ -\sin(\theta_y - \theta_x) & \cos(\theta_y - \theta_x) & 0 \\ 0 & 0 & 1 \end{bmatrix} \quad (\text{C.8})$$

In cases which the zero sequence is not relevant and only a relation between the dq-components is searched between frames  $x$  and  $y$ , it can be written that

$$f_{dq0}^y = \begin{bmatrix} \cos(\theta_y - \theta_x) & \sin(\theta_y - \theta_x) \\ -\sin(\theta_y - \theta_x) & \cos(\theta_y - \theta_x) \end{bmatrix} f_{dq0}^x \quad (\text{C.9})$$

## APPENDIX D MATLAB CODE – STATE SPACE DEVELOPMENT OF SIMPLE VSC SYSTEM

```

%% Aramis Schwanka Trevisan - 28.07.2019
% Code to obtain a state-space representation of a simple VSC consisting of only
a PLL and current regulator connected to a simple RL-grid representation.

%% Initialize variables (not shown here)

%% RL-Grid:

A_grid = [-(Rg+Rinf)/Lg      w0;
          -w0      -(Rg+Rinf)/Lg];
B_grid = [Rinf/Lg  0  -1/Lg  0;
          0  Rinf/Lg  0  -1/Lg ];
C_grid = [-Rinf  0;
          0  -Rinf;
          1  0;
          0  1];
D_grid = [Rinf 0  0 0;
          0  Rinf 0 0;
          0  0  0 0;
          0  0  0 0];

SS_grid = ss(A_grid,B_grid,C_grid,D_grid);
SS_grid.InputName = {'ic_d','ic_q','vg_d','vg_q'};
SS_grid.StateName = {'ig_d','ig_q'};
SS_grid.OutputName = {'vpcc_d','vpcc_q','ig_d','ig_q'};

%% RL-Output Filter:

A_filt = [-Rc/Lc  w0;
          -w0  -Rc/Lc];
B_filt = [1/Lc 0  -1/Lc 0;
          0  1/Lc 0  -1/Lc];
C_filt = [1 0;
          0 1];
D_filt = [0 0 0 0;
          0 0 0 0];

SS_filt = ss(A_filt,B_filt,C_filt,D_filt);
SS_filt.InputName = {'vconv_d','vconv_q','vpcc_d','vpcc_q'};
SS_filt.StateName = {'ic_d','ic_q'};
SS_filt.OutputName = {'ic_d','ic_q'};

%% Linearized PLL:

Kv2pu = 1/(sqrt(2/3)*V_rated);

phi_g0 = 0; % common ref.-frame aligned with grid source voltage
Kphi = -cos(phi_PLL0-phi_g0)*vpcc_d0*Kv2pu - ...
        sin(phi_PLL0-phi_g0)*vpcc_q0*Kv2pu;
Kvd = -sin(phi_PLL0-phi_g0);
Kvq = cos(phi_PLL0-phi_g0);

```

```

A_pll = [Kp_pll*Kphi Ki_pll
         Kphi      0];
B_pll = Kv2pu*[Kp_pll*Kvd Kp_pll*Kvq;
              Kvd      Kvq ];
C_pll = [1 0];
D_pll = [0 0];

SS_pll = ss(A_pll,B_pll,C_pll,D_pll);
SS_pll.InputName = {'vpcc_d','vpcc_q'};
SS_pll.StateName = {'phi_pll','grosteta_pll'};
SS_pll.OutputName = {'phi_pll'};

%% Reference-frame conversion: vpcc from common ref.-frame (CRF) to converter
frame.

Kv2pu = 1/(sqrt(2/3)*V_rated);

A_conv_vpcc = [0];
B_conv_vpcc = [0 0 0];
C_conv_vpcc = [0;
              0];
D_conv_vpcc = Kv2pu*[ vpcc_q0_c cos(phi_PLL0) sin(phi_PLL0);
                    -vpcc_d0_c -sin(phi_PLL0) cos(phi_PLL0)];

SS_conv_vpcc = ss(A_conv_vpcc,B_conv_vpcc,C_conv_vpcc,D_conv_vpcc);
SS_conv_vpcc.InputName = {'phi_pll','vpcc_d','vpcc_q'};
SS_conv_vpcc.StateName = {'dummy_conv_vpcc'};
SS_conv_vpcc.OutputName = {'vpcc_d_pu_c','vpcc_q_pu_c'};

%% Reference-frame conversion: ic from common ref.-frame (CRF) to converter
frame.

Ki2pu = 1/i_base;

A_conv_ic = [0];
B_conv_ic = [0 0 0];
C_conv_ic = [0;
            0];
D_conv_ic = Ki2pu*[ iq_ref0*i_base cos(phi_PLL0) sin(phi_PLL0);
                  -id_ref0*i_base -sin(phi_PLL0) cos(phi_PLL0)];

SS_conv_ic = ss(A_conv_ic,B_conv_ic,C_conv_ic,D_conv_ic);
SS_conv_ic.InputName = {'phi_pll','ic_d','ic_q'};
SS_conv_ic.StateName = {'dummy_conv_ic'};
SS_conv_ic.OutputName = {'ic_d_pu_c','ic_q_pu_c'};

%% Current-control:

A_CC = [0 0 0 0;
        0 0 0 0;
        0 0 0 0;
        0 0 0 0];

```

```

B_CC = [1 0 0 0 0 0;
        0 0 1 0 0 0;
        0 1 0 0 0 0;
        0 0 0 1 0 0];

C_CC = [ Ki_d -Ki_d 0 0;
         0 0 Ki_q -Ki_q];
D_CC = [Kp_d 0 -Kp_d -w0*Lc/Z_base 1 0;
        0 Kp_q w0*Lc/Z_base -Kp_q 0 1];

SS_CC = ss(A_CC,B_CC,C_CC,D_CC);
SS_CC.InputName =
{'id_ref','iq_ref','ic_d_pu_c','ic_q_pu_c','vpcc_d_pu_c','vpcc_q_pu_c'};
SS_CC.StateName = {'Yd_ref','Yd_meas','Yq_ref','Yq_meas'};
SS_CC.OutputName = {'vconv_d_pu_c','vconv_q_pu_c'};

%% Reference-frame conversion: vconv from converter to common ref.-frame.

Kv2pu = 1/(sqrt(2/3)*V_rated);
Kpu2v = (sqrt(2/3)*V_rated);

A_conv_vconv = [0];
B_conv_vconv = [0 0 0];
C_conv_vconv = [0;
                0];
D_conv_vconv = Kpu2v*[-vconv_q0*Kv2pu cos(-phi_PLL0) sin(-phi_PLL0);
                    vconv_d0*Kv2pu -sin(-phi_PLL0) cos(-phi_PLL0)];

SS_conv_vconv = ss(A_conv_vconv,B_conv_vconv,C_conv_vconv,D_conv_vconv);
SS_conv_vconv.InputName = {'phi_pll','vconv_d_pu_c','vconv_q_pu_c'};
SS_conv_vconv.StateName = {'dummy_conv_vconv'};
SS_conv_vconv.OutputName = {'vconv_d','vconv_q'};

%% Create Complete State-Space Representation:

opt = connectOptions('Simplify',false); % this avoids smaller realization
ss_VSC = connect(SS_grid,SS_filt,SS_pll,SS_conv_vpcc,SS_conv_ic,...
                SS_CC,SS_conv_vconv,...
                {'vg_d','vg_q','id_ref','iq_ref'},...
                {'vpcc_d','vpcc_q','ig_d','ig_q','ic_d','ic_q','phi_pll',...
                'vpcc_d_pu_c','vpcc_q_pu_c','ic_d_pu_c','ic_q_pu_c',...
                'vconv_d_pu_c','vconv_q_pu_c','vconv_d','vconv_q'});

[A_VSC,B_VSC,C_VSC,D_VSC] = ssdata(ss_VSC);

% End.

```